UNCLASSIFIED

SECURITY CLASSIFICATION OF THIS PAGE *(When Data Entered)*

REPORT DOCUMENTATION PAGE		READ INSTRUCTIONS BEFORE COMPLETING FORM
1. REPORT NUMBER NORDA Report 21	2. GOVT ACCESSION NO.	3. RECIPIENT'S CATALOG NUMBER
4. TITLE *(and Subtitle)* Effective Low-Frequency Geoacoustic Properties Inferred from Measurements in the Northeast Atlantic		5. TYPE OF REPORT & PERIOD COVERED Final 6. PERFORMING ORG. REPORT NUMBER
7. AUTHOR*(s)* Ronald L. Dicus Rockne S. Anderson		8. CONTRACT OR GRANT NUMBER*(s)*
9. PERFORMING ORGANIZATION NAME AND ADDRESS Naval Ocean Research & Development Activity Ocean Acoustics Division, OSTL NSTL Station, Mississippi 39529		10. PROGRAM ELEMENT, PROJECT, TASK AREA & WORK UNIT NUMBERS 62759
11. CONTROLLING OFFICE NAME AND ADDRESS Same		12. REPORT DATE September 1982 13. NUMBER OF PAGES 155
14. MONITORING AGENCY NAME & ADDRESS*(if different from Controlling Office)*		15. SECURITY CLASS. *(of this report)* UNCLASSIFIED 15a. DECLASSIFICATION/DOWNGRADING SCHEDULE

16. DISTRIBUTION STATEMENT *(of this Report)*

Approved for Public Release
Distribution Unlimited

17. DISTRIBUTION STATEMENT *(of the abstract entered in Block 20, if different from Report)*

18. SUPPLEMENTARY NOTES

19. KEY WORDS *(Continue on reverse side if necessary and identify by block number)*

Geoacoustic models
Acoustic sediment-bottom interaction

20. ABSTRACT *(Continue on reverse side if necessary and identify by block number)*

The performance of surveillance systems mounted, suspended, or towed near the bottom is governed in part by the nature of the acoustic bottom interaction. Bottom properties affecting this interaction include, among others, the spatial variation of sound speed, density, and attenuation. Specification of these bottom properties is generally referred to as a geoacoustic model. Research to date has, to a large degree, involved the quest for appropriate geoacoustic models and their validation by comparison of measured and model-predicted bottom-loss functions.

(Continued)

DD FORM 1 JAN 73 1473 EDITION OF 1 NOV 65 IS OBSOLETE
S/N 0102-LF-014-6601

UNCLASSIFIED

SECURITY CLASSIFICATION OF THIS PAGE *(When Data Entered)*

20. Abstract (Continued)

At frequencies of significance for long range surveillance systems (5 to 100 Hz) data for model building is often insufficient or too poorly resolved. In spite of the vast quantity of marine geological and geophysical data generally available to the acoustician, a majority of the data describe sediments and crustal structure at depths greater than a few hundred meters or less than 10 meters. Correspondingly, these depths are important at frequencies below a few Hertz or greater than a few hundred Hertz.

The purpose of the study documented in this report was to develop geoacoustic models capable of predicting the essential bottom reflectivity behavior relevant to long-range, low-frequency surveillance systems from acoustic survey measurements and available marine geological data.

It was found that at five thickly sedimented bottom sites, simple geoacoustic models could be derived from measurements of bottom reflectivity data taken at grazing angles from 5° to 80°. Deconvolution processing and analysis of the resultant bottom impulse responses led to the form of the models and to quantitative values of model parameters. Specifically, amplitude and arrival time analysis of dominant peaks in the impulse responses was employed. Model-predicted arrival times differed from measured arrival times by 3.1 msec on the average. This difference is small compared to the processing pulse duration of 14.2 msec. Accurate arrival time prediction such as exhibited here is one requirement of a geoacoustic model if it is to be incorporated into a propagation model for detailed predictions of acoustic field intensity.

Geological analyses of available environmental data were conducted to develop estimates of sediment sound speed, density and attenuation profiles. Geological data were obtained from (1) cores, (2) seismic profiler records, (3) 3.5 kHz profiler records, (4) wide angle reflection profiling (sonobuoy data), and (5) Deep Sea Drilling Project (DSD) holes drilled in locations with sediment analogous to the site of interest. Information relevant to acoustic properties are summarized including: water depth, bottom and water sound speed, sediment thickness, and reflectors within the sediments. General discussions of geological features affecting acoustic properties at several of the stations are presented in Appendix D.

Geologically inferred predictions of sediment surface sound speed and density were in agreement with the acoustical estimates but the total sediment sound-speed model was inadequate, as judged by errors in the predicted arrival times. Both the acoustical and geological estimates of attenuation were subject to large uncertainties, and the geological estimate was consistenly higher than the acoustical estimate.

The acoustical model results of this study suggest generalization to other deep ocean abyssal-plain and abyssal-hills bottom sites. However, since the geological data base was of the type that is generally available, the difficulties with geological model prediction may also be encountered at other sites.

Recommendations for improving accuracy of geologically inferred models include (1) recording and analyzing full dynamic range of amplitude information in normal-incidence profiler data; (2) pulse compression and dereverberation processing (deconvolution) of profiler and wide-angle reflectivity data; and (3) improved sampling in DSDP cores of the top few hundred meters.

NORDA Report 21

Effective Low-Frequency Geoacoustic Properties Inferred from Measurements in the Northeast Atlantic

Ronald L. Dicus†
Rockne S. Anderson*

Acoustics Division
Ocean Science and Technology Laboratory

September 1982

Naval Ocean Research and Development Activity
NSTL Station, Mississippi 39529

† Present address: Naval Research Laboratory,
Code 5160,
Washington, DC 20375

*Present address: Sensors and Avionics Technology Directorate,
Code 3031, Naval Air Development Center,
Warminster, Pennsylvania 18974

Foreword

This report documents geoacoustic models designed to predict the nature of acoustic boundary interaction. For five sites involving thickly sedimented bottoms, simple models are derived from measurements of reflectivity. Also, recommendations are provided for improving the accuracy of geoacoustic models in general.

G.T. Phelps

G.T. Phelps, Captain, USN
Commanding Officer, NORDA

ERRATA

"Effective Low-Frequency Geoacoustic Properties
Inferred from Measurements in the Northeast Atlantic"

NORDA Report 21

1. Page iv: "List of Tables xiii" (not xii)
2. Page x: "Figure 61 ...at Station 8." (not Station B)
3. Page x: "Figure 65. add "Site 136." at end (should read: "...determined at Site 136.")
4. Page xiv: "$C_{o,i}$ Sound speed in water o..." (not "water a...")
5. Page 14: Second column, line 4: "...on attenuation frequency" should read "...of attenuation on frequency."
6. Page 100: $t_{nt} = 2\sin^3\theta_{RT}/(3V_{gT})$ should read $t_{nt} = 2\sin^3\theta_{RT}/(3g_T)$
7. Page 109: Second column, third sentence of first full paragraph should read: "Between 0500 and 0700Z, a thick section of sediment exists as a transition zone between the flat plain to the west and the rough fault-block relief of the continental margin to the east."
8. Last page: (page 2 of DD1473) Fourth paragraph, fifth line: "DSDP" (not "DSD").

NOTE: Long explanatory captions for Figures 52 through 73 have been omitted from the figures themselves but appear in the List of Illustrations on pages viii-xii.

Executive Summary

The performance of surveillance systems mounted, suspended, or towed near the bottom is governed in part by the nature of the acoustic bottom interaction. Bottom properties affecting this interaction include, among others, the spatial variation of sound speed, density, and attenuation. Specification of these bottom properties is generally referred to as a geoacoustic model. Research to date has, to a large degree, involved the quest for appropriate geoacoustic models and their validation by comparison of measured and model-predicted bottom-loss functions.

At frequencies of significance for long range surveillance systems (5 to 100 Hz) data for model building is often insufficient or too poorly resolved. In spite of the vast quantity of marine geological and geophysical data generally available to the acoustician, a majority of the data describe sediments and crustal structure at depths greater than a few hundred meters or less than 10 meters. Correspondingly, these depths are important at frequencies below a few Hertz or greater than a few hundred Hertz.

The purpose of the study documented in this report was to develop geoacoustic models capable of predicting the essential bottom reflectivity behavior relevant to long-range, low-frequency surveillance systems from acoustic survey measurements and available marine geological data.

It was found that at five thickly sedimented bottom sites, simple geoacoustic models could be derived from measurements of bottom reflectivity data taken at grazing angles from 5° to 80°. Deconvolution processing and analysis of the resultant bottom impulse responses lead to the form of the models and to quantitative values of model parameters. Specifically, amplitude and arrival time analysis of dominant peaks in the impulse responses was employed. Model-predicted arrival times differed from measured arrival times by 3.1 msec on the average. This difference is small compared to the processing pulse duration of 14.2 msec. Accurate arrival time prediction such as exhibited here is one requirement of a geoacoustic model if it is to be incorporated into a propagation model for detailed predictions of acoustic field intensity.

Executive Summary

Geological analyses of available environmental data were conducted to develop estimates of sediment sound speed, density and attenuation profiles. Geological data were obtained from (1) cores, (2) seismic profiler records, (3) 3.5 kHz profiler records, (4) wide angle reflection profiling (sonobuoy data) and (5) Deep Sea Drilling Project (DSDP) holes drilled in locations with sediment analogous to the site of interest. Information relevant to acoustic properties are summarized including: water depth, bottom and water sound speed, sediment thickness and reflectors within the sediments. General discussions of geological features affecting acoustic properties at several of the stations are presented in Appendix D.

Geologically inferred predictions of sediment surface sound speed and density were in agreement with the acoustical estimates but the total sediment sound-speed model was inadequate, as judged by errors in the predicted arrival times. Both the acoustical and geological estimates of attenuation were subject to large uncertainties, and the geological estimate was consistently higher than the acoustical estimate.

The acoustical model results of this study suggest generalization to other deep ocean abyssal-plain and abyssal-hills bottom sites. However, since the geological data base was of the type that is generally available, the difficulties with geological model prediction may also be encountered at other sites.

Recommendations for improving accuracy of geologically inferred models include: (1) recording and analyzing full dynamic range of amplitude information in normal-incidence profiler data; (2) pulse compression and dereverberation processing (deconvolution) of profiler and wide-angle reflectivity data; and (3) improved sampling in DSDP cores of the top few hundred meters.

Acknowledgments

We are indebted to many for their cooperation in planning and executing the field experiment. We wish to thank Robert S. Winokur for his support and encouragement of the project and Samuel W. Marshall, who continued the support during the writing phase. The data were acquired through the expertise provided by the Acoustic Surveys Division of the Naval Oceanographic Office, headed by Wilburt Geddes. Orest Diachok, through many helpful discussions, provided several ideas for this report. Peter Shen, William Cronin, and Robin Martin assisted in the required computer work. The geological analysis was provided by William F. Ruddiman and Linda K. Glover for Stations 4 and 5 in the Tagus Abyssal Plain, and by Larry Reynolds for Station 2 in the Iberian Abyssal Plain. James Matthews offered many suggestions, which were based largely on unpublished work. Kenneth V. Mackenzie and Burlie Brunson reviewed parts of the paper. We especially wish to thank Gerald Morris who critically reviewed the entire paper and Linda McRaney, who edited the entire final manuscript.

This work was supported by program element 62759.

Contents

Contents

Illustrations

Illustrations

Illustrations

Illustrations

Illustrations

Illustrations

Tables

Symbols and Abbreviations

$C_{o,i}$	Sound speed in water a or sediment layer i, m/sec.
CR	Sound speed ratio at first interface, used without subscript when it is clear that it derives from Rayleigh or arrival-time analysis. CR = $C_{sediment}/C_{water}$.
CR_i	Sound speed ratio at interface i, from acoustic arrival time analysis. $CR_i = C_i/C_{i-1}$.
$CR_{G,R,T}$	CR determined from geological data (G), from Rayleigh coefficient analysis of acoustic data (R), or from time of arrival analysis of acoustic data (T).
CRIC	Surface sediment sound speed and interval sound speed method of determining g.
DR	Density ratio at first interface, used without subscript when it is clear that the acoustically inferred value from Rayleigh-coefficient analysis is intended. DR = ρ sediment/ρ water.
$DR_{G,R}$	DR determined from geological data (G) or from the Rayleigh-coefficient analysis of the acoustic data (R).
DSDP	Deep Sea Drilling Project.
f	Frequency.
g	Sound speed gradient in a layer (positive for sound speed increasing with depth) sec^{-1}.
h	Thickness of a layer, m.
HF	High Frequency.
IC	Interval or average sound speed of a layer.
i	Layer index increasing with depth starting with the water as layer zero. Also used for the unit imaginary symbol $i = (-1)^{1/2}$.

Symbols and Abbreviations

k	Wave number, $2\pi/\lambda$.
LF	Low Frequency
p	Amplitude of an arrival in the unit impulse response of the bottom.
r	Slant range, i.e., total path length from source to receiver along bottom interacting ray path.
R	Plane wave reflection coefficient at the top of a layer.
RMS	Root Mean Square.
S_n	Total two-way ray path-length through the sediments
S_{ni}	Two-way ray path-length of nth arrival propagation path through layer i.
T	Plane wave transmission coefficient at top of a layer
Δ_t	Measured two-way travel time difference; i.e., the time difference between an observed arrival and the first bottom reflected arrival.
t_{ni}	Two-way travel time elapsed in propagation of nth arrival through layer i.
t_n	Two-way travel time differences between first and nth arrival.
$t_{A,G}$	Root-mean-square difference between measured and computed arrival times for a given station and acoustically inferred model (A) or geologically inferred model (G).
z	Depth below water-sediment interface.
α	Plane-wave attenuation coefficient, dB/m.
$\theta_{o,i}$	Grazing angle at the water-sediment interface (o), or at bottom of ith layer (i).

arrival times to obtain estimates of sediment sound speed, density, and attenuation.

Results of the analyses indicated the utility of the experimental design and deconvolution processing for the investigation of bottom-interaction phenomena. Wide-angle seismic reflection techniques are usually limited to layers more than approximately 200 m thick in deep water [39]. The deconvolution techniques employed here for sediment sound-speed analysis extend the capability to layers as thin as 10 m.

The low-frequency impulse response behavior (at all but the sediment-free bottom site, station 7) was modeled by simple refracting- and/or reflecting-layer models. The average root-mean-square (RMS) arrival-time error (predicted arrival time versus observed) for all the models was 3.1 msec, with a maximum RMS error of 8.6 msec (Station 2, model 6). These RMS errors are smaller than the 14.2 msec, 3 dB, full-width pulse duration for the low-frequency impulse responses. The sediment sound-speed structure at shallow depths, as determined from two-layer modeling of high-frequency impulse responses, was suggestive of higher sound speeds than would be expected on the basis of geological information.

Geological analyses of available environmental data were conducted to develop estimates of sediment sound-speed, density and attenuation profiles. Geological data were obtained from (1) cores, (2) seismic-profiler records, (3) 3.5 kHz profiler records, (4) wide-angle reflection profiling (sonobuoy data) and (5) Deep Sea Drilling Project (DSDP) holes drilled in locations with sediments analogous to the site of interest. Whenever possible the sound-speed profile was specified in terms of an effective constant gradient and determined from DSDP sites with a sedimentary structure similar to that of the station as determined from other geological considerations. Other methods for deriving the gradient are also discussed in Appendix E.

Sediment density and surficial sound-speed were generally measured from core samples. Attenuation estimates were based on core samples and relationships presented by Hamilton [45]. In addition, other information relevant to the acoustic properties are summarized including: water depth, bottom-water sound-speed, sediment thickness, and reflectors within the sediments. General discussions of geological features affecting acoustic properties at several of the stations are presented in Appendix D.

Geologically inferred predictions of sediment surface sound-speed and density were in agreement with the acoustical estimates (DR_R, and CR_R), but the overall sound-speed model was inadequate, as judged by errors in the predicted arrival times (RMS $t_G \cong 50$ msec). Both the acoustical and geological estimates of attenuation were subject to large uncertainties, and the geological estimate was consistently higher than the acoustical estimate.

The acoustical model results of this study suggest generalization to other deep ocean abyssal-plain and abyssal-hills bottom sites. However, since the geological data base was of the type that is generally available, the difficulties with geological model prediction may also be encountered at other sites.

Recommendations for improving accuracy of geologically inferred models include: (1) recording and analyzing full dynamic range of amplitude information in normal-incidence profiler data; (2) pulse compression and dereverberation processing (deconvolution) of profiler and wide-angle-reflectivity data; and, (3) improved sampling in DSDP cores of the top few hundred meters.

In the organization of the report, many details have been included which the reader may wish to skip on first reading. Section II is a brief historical

review of progress in the study of the acoustic bottom-interaction problem. Section III describes the usual two-ship experiments often used for collecting bottom-reflectivity data. Section IV.A may be skipped by the reader familiar with deconvolution processing. In Section IV.B, the geoacoustic models are described together with the analysis procedures for determining model parameters from the measured data. Section IV.C gives the detailed acoustic results, and Section V gives the detailed geological results for each station. A table summarizing the most significant results is located at the end of these last two sections. A detailed comparison of the acoustical and geological results is discussed in Section VI, and condensed statements of conclusions and recommendations are given in Sections VII and VIII. References and illustrations constitute Sections IX and X followed by several appendices with more detailed information. Appendix A begins with a summary of formulas used in the acoustical analyses. A fuller discussion of the characteristics of the acoustic data is reserved for Appendix B. The available geological and geophysical information relevant to acoustic properties at each site is discussed in Appendix C. Additional information explaining the effects of marine geological processes on the bottom acoustic response and describing presently available techniques for measurement and prediction of geoacoustic parameters is included in Appendices D and E. The paper concludes with Appendix F, which gives a brief discussion of the structure of the sound-speed profiles at each of the stations. It is suggested that a rapid reading of the paper include Sections IV.B, IV.C, V, VI, VII, and VIII.

II. Background

One of the earliest theories to be applied to the bottom-interaction problem was that of Lord Rayleigh [1] during the 1890's. Rayleigh derived the reflection coefficient for plane waves incident at arbitrary angles on the boundary separating two homogeneous fluid half-spaces. According to Sergeev [2], continuous ultrasonic echo-sounding measurements were made from a moving ship during the period 1918-1920 to evaluate bottom topography and to determine whether the bottom was hard or soft. Liebermann [3] recorded 24 kHz signals that were received via direct and bottom-reflection paths at a 9^{o} grazing angle. By measuring the maximum and minimum intensities as the source height was varied, he was able to determine the bottom-reflection coefficient. He concluded that the reflectivity depended on sediment grain size and sorting. By 1949 Sergeev also began to utilize echo pulse amplitude and waveform information to correlate with bottom type.

During seismic refraction studies, Hill [4] observed arrivals which he attributed to refraction within a sound-speed gradient in the bottom. Several of the later studies of the sound speed gradient are discussed in Appendix E.

Hamilton et al. [5] measured in situ and laboratory values of sediment density, porosity, grain size, sound-speed, and attenuation at 100 kHz. They discussed the honeycomb and honeycomb flocculant sediment structures formed by deposition of small particles, the bridging effect of platey minerals, and the attendant relationship between sediment porosity and grain size. From measurements of sediment density and sound-speed, normal-incidence bottom-loss values were calculated and found to be in good agreement with bottom-loss measurements taken by Mackenzie [6]. Breslau's [7] work on 12 kHz normal-incidence bottom-reflectivity data statistically demonstrated highly significant correlations between bottom loss and: (1) porosity; (2) amount of sand, silt or clay; and (3) sorting.

In the work of Mackenzie [6], the fluid half-space model of the bottom was brought to full quantitative development. In his measurements of bottom reflectivity at grazing angles from 12 to 90^{o} and at frequencies of 4, 7.5, and 16 kHz, Mackenzie found that the

Rayleigh-Morse theory (in which the Rayleigh equation is modified for bottom absorption by inclusion of a complex sound-speed) provided a good theoretical description of the data. He thus demonstrated that an older theory of normally reacting surfaces [8] was inappropriate for bottom sediments. In addition, the theory fit the data best when attenuation coefficients were extrapolated from measurements at 30 kHz according to a linear or first-power dependence on frequency.

A flurry of research activity (Jones et al. [9], Barnard et al. [10] in 1964, Brown and Ricard [11], Bucker et al. [12], Menotti et al. [13], Cole [14] in 1965, Smith and Li [15] in 1966, and Winokur and Bohn [16] in 1968) was concerned with the next logical step for improving bottom-loss models: multilayered fluid and viscoelastic models. These models permitted more accurate bottom-loss curve fitting and explained some of the variability observed as a function of grazing angle. An important step was taken by Morris [17], who demonstrated that better data fits were obtained after incorporating sound-speed gradients. In particular, they provided an explanation for low losses observed at low grazing angles.

In 1970, Hastrup [18] and Hovem [19] introduced the technique of deconvolution for processing bottom-reflectivity data. Deconvolution removes bubble-pulse reflections from bottom-reflected traces generated by explosive charges, and increases the resolution or spikiness of primary reflected pulses. Sediment-reflecting horizons are more easily identified, thereby aiding in the synthesis of layered models. Hastrup computed theoretical impulse responses from sediment core measurements and found that they compared favorably with the experimentally measured impulse responses. Frequency domain deconvolution techniques were also employed by Van der Veen and Santaniello [20] and refined by Lackoff and LeBlanc [21], Dicus [22], and Herstein [23]. Homomorphic deconvolution was demonstrated by Stoffa et al. [24, 25].

Interest in the effects of a sound-speed gradient continued. Hanna [26] showed how the bottom gradient could be estimated from the obeservation of interference nulls due to superposition of the reflected and refracted ray at a bottom-mounted hydrophone using a CW source. Christensen et al. [27] identified the refracted arrival associated with a bottom sound-speed gradient by comparing high-pass and low-pass filtered bottom-reflected traces. In addition, they showed that the refracted pulse arrival times for varying source-to-receiver ranges were predicted by ray trace computations with a suitably chosen gradient value. Dicus [28] measured bottom impulse responses for a gradient bottom and demonstrated precise quantitative modeling of the impulse responses and associated bottom-loss functions. Santaniello et al. [29] discussed the focusing of sound rays in a gradient bottom, the contribution of lateral (head) waves, and the effect of different measurement geometries in connection with bottom-loss data that showed significant negative losses over a restricted grazing angle range. Stickler [30, 31] pointed out the inadequacy of analyzing data with the assumption of incident plane waves, and showed numerical examples of the shift in apparent critical angle and occurrence of negative losses associated with different measurement geometries. For an isospeed bottom, he presented a new method for measuring bottom sound speed with bottom-mounted sensors in the case of a point source [32].

III. Description of Experiment

The acoustic data were obtained during a two-ship operation conducted by the Naval Oceanographic Office (NAVOCEANO) in the northeast Atlantic from 25 September to 17 October 1973 between Barry, Wales, and Las Palmas, Canary Islands.

The locations of the acoustic stations are shown in Figure 1 and listed in

Table 1. Station locations and times

Station	Province	Time/Date (1973)	Latitude/Longitude
2	Northern Iberian	0110/29 Sep	42°49.0'N/13°43.5'W
	Abyssal Plain	0503/29 Sep	42°55.3'N/13°01.0'W
4	Southeast Tagus	2255/1 Oct	37°10.7'N/11°15.0'W
	Abyssal Plain	0250/2 Oct	37°30.0'N/11°38.9'W
5	Southwest Tagus	2246/3 Oct	37°7.4'N/12°25.4'W
	Abyssal Plain	0224/4 Oct	37°24.2'N/11°59.1'W
7	Dragon Seamount	1900/7 Oct	34°59.9'N/16°28.5'W
		2118/7 Oct	34°40.0'N/16°27.8'W
8	Dragon Seamount Plateau	1111/8 Oct	34°55.4'N/16°37.2'W
		1349/8 Oct	34°39.5'N/16°52.5'W
9	Lower Continental Rise	0635/11 Oct	29°0.0'N/20°49.5'W
	South of Madeira	0930/11 Oct	29°11.4'N/20°27.5'W

Table 1. Of the six stations, four are in deep ocean basins (2,4,5, and 9), one is on an extremely rough basement outcrop, a seamount (Station 7), and one is on a shallow, thickly sedimented feature distant from shore (Station 8).

Bottom-reflectivity measurements were obtained using the experimental geometry shown in Figure 2. USNS WILKES was anchored during the experiment in order to receive signals at a deep hydrophone from SUS charges launched from USNS KANE while traveling away from WILKES along a track referred to as the bomb run. Explosive source charges (MK 61 SUS, 0.8 kgm TNT) were detonated at 244 m depth. Signals were received on an omnidirectional hydrophone at approximate depths of 2500 m for stations 2, 4, and 5; 1700 m for stations 8 and 9; and 244 m for station 7. The depth of the source was chosen as a compromise between greater low-frequency energy at shallow depths and greater multipath resolution at greater depths. Receiver depths were chosen to optimize reception of direct-water-path signals except at station 7. At station 7 a shallow receiver was chosen to inhibit multipath separation and allow integration over all surface-reflected multipaths. Multipath resolution at station 7 was impossible for any experimental geometry because of the long response time of the reverberant bottom.

Charges were detonated at spacings ranging from 2 to 10 minutes; the interval was chosen to give a grazing-angle increment of about 3^{o} for each geometry. The initial charge was detonated at a distance from the receiver, which provided a bottom-reflected ray path at near-normal grazing angle. The minimum grazing angle was obtained at the maximum range near the first convergence zone. The actual grazing angles were computed during data analysis by using a ray-trace program [33] incorporating sound-speed profiles obtained from SVSTD (sound velocity/salinity/temperature/depth) measurements taken either immediately before or after the experiment.

The hydrophone used was a Clevite Model CH-1A. The system response was flat within 1 dB below 2.2 kHz and 4 dB down at 4 kHz. All measurements utilized the self-calibration property of the synthetic-replica deconvolution technique [22].

The received signals were fed into a high impedance (500 megohm in parallel with 100 pfd) Ithaco 453 amplifier.

The amplified signal was monitored and adjusted in 5 dB increments to keep the input signal to the recorder at about -6 dB re/1 v. Two identical Lockheed 7-track recorders with a dynamic range of 35 dB were used with a 10 dB gain separation. The data were recorded in both FM and direct modes at 7-1/2 ips. The FM response was 0-2500 Hz; the direct response was 100-25,000 Hz. Two other channels were used: one for verbal annotations and the other to record a Systron Donner 8150 time-code generator signal. The remaining channel was unrecorded.

IV. Acoustical Data Analysis

A. Digital Processing

1. Deconvolution

The data were processed digitally to obtain the ocean-bottom impulse response. Once accomplished, little additional effort was required to obtain bottom-loss results digitally. Prior to digitization, the analog data tapes were pre-edited by listening to the data and voice tracks simultaneously and decoding the recorded time code. In this way absolute start and stop times were determined, which bracketed the desired data for digitizing. The analog tapes were then digitized at the computer center of the Naval Ship Research and Development Center, Carderock, Maryland. The start times determined during the pre-editing were preset in a time decoder for initiating digitization. Following digitization, the newly created digital tapes were processed on a Control Data Corporation Model 3800 computer at the Naval Research Laboratory, Washington, D.C.

Impulse responses were calculated using a synthetic-deconvolution technique [22]. With the synthetic method, a replica of the acoustic signal incident at the ocean bottom is generated by a time expansion/contraction transformation of a directly measured source signal. The direct signal is measured only once, while the amount of expansion or contraction is varied on a shot-by-shot basis. The expansion factor adjusts the bubble-pulse period of the direct signal to that of the particular shot being processed. The bubble-pulse period is measured as the time between the peak of the shock pulse and the peak of the first bubble pulse.

Bubble-pulse periods were generally measured to an accuracy of $\pm 0.1\%$ using the inverse filter technique on measured direct-path signals. At the longer ranges corresponding to grazing angles of less than approximately 20^{o}, suitable direct-path signals were not available because of refractive shadowing, distortion, or excessive noise. In most of these instances, the bottom-reflected signal was used for bubble-pulse-period determination. Primary reflected pulses were separated in time from the bubble pulses and hence did not interfere with them. At Station 7, bottom-reflected signals could not be used with the inverse-filter technique because of interference between bubble pulses and primary reflected pulses. In this case, the cepstrum technique was applied.

The deconvolutions were accomplished in the frequency domain via discrete finite Fourier transforms. The effects of noise were minimized and the impulse responses stabilized by linear, minimum-mean-square-error estimation. Geometric spreading and absorption losses incurred along the water paths were removed in order that the impulse responses represent only the contribution of the bottom interaction.

An eigen-ray computation was made for each station using the Naval Research Laboratory program, Trimain [33], with modification for printing bottom grazing angles and ray slant ranges. For each station, Trimain provided the transmission-loss and slant-range information needed to make the geometric-spreading and absorption-loss corrections.

A zero-phase filter with Gaussian-shaped amplitude spectrum was applied to the impulse responses to obtain a desirable pulse shape free of side-lobes.

The 3 dB points of the filter response were set to 43 and 87 Hz for the low-frequency traces and to 2.1 kHz for the low-pass filtered broadband traces. For the low frequency band, the lower cutoff frequency was chosen to exclude low-frequency noise and the upper cutoff frequency was chosen to limit the complication of additional layering resolved at greater band-widths. The cutoff frequency for the broadband or high-frequency band was chosen to eliminate high-frequency noise imposed by the high-frequency roll-off of the tape-recorder frequency-modulation circuitry. The impulse-response amplitudes were normalized to the output corresponding to a unit amplitude band-limited input.

2. Bottom Loss Computations

Bottom-loss can be defined as the ratio of the plane wave energy incident on the ocean bottom to the reflected energy expressed in decibels as a function of frequency and grazing angle. In calculating bottom-loss from the experimental data, geometric spreading and absorption losses must be calculated from the ray path associated with specular reflection. In the case of a rough bottom, there are many possible bottom-reflecting rays connecting the source and receiver for any geometry. For Stations 7 and 8 the bathymetry was variable about a mean slope. The geometric spreading and absorption losses were then computed based on the ray path associated with specular reflection from a plane inclined at the mean slope.

For all the stations except 7, the single bottom-interacting signals were easily time-separated from water surface reflected multiples. At Station 7, time separation was impossible both before and after deconvolution. In this case, however, the four main arrivals associated with a single bottom bounce could be separated from the next group of arrivals associated with two bottom bounces. Therefore, the first group of arrivals were isolated and a 6 db correction applied to remove the average effect of the four arrivals.

Bottom-loss versus grazing-angle functions were computed for each station in one-third-octave frequency bands. The squared magnitudes of the Fourier coefficients of direct and bottom-reflected signals were summed separately in one-third-octave frequency bands. Each sum is proportional to the respective acoustic energy. After correction for water-column geometric spreading and absorption losses, and correction of the bottom-reflected energy for error due to noise, bottom-loss was computed as the ratio of direct to bottom-reflected energy expressed in decibels. No corrections were made for noise in the direct signal because the signal-to-noise ratio was much higher than that for the bottom-reflected signals.

The noise was assumed to be colored Gaussian noise having an approximately flat spectrum within each one-third-octave frequency band. The energy within a one-third-octave band is, then, the sum of squares of non-zero mean Gaussian variates which have equal variances. If there were no signal and only noise, then the variates would be zero mean and the one-third-octave band energy would be distributed as the familiar Chi-Square variate. With signal energy, the probability distribution function becomes a noncentral Chi-Square distribution.

At low frequencies, a lengthy sample of noise is required to allow for spectral smoothing. This step was prohibitive because of machine computation time. As an alternative, from 10 to 20 short noise samples already taken for the deconvolution noise filtering were ensemble averaged to obtain a spectrum. The amplitude of the relative noise spectrum was adjusted for each shot by measuring the energy in a short noise sample that was taken ahead of each shot.

The error-bar curves that bracket the bottom-loss data correspond to three standard deviations. Although the non-normal distribution precludes simple identification of confidence limits, error bars corresponding to three

standard deviations should give good order of magnitude estimates of the error with approximately the same confidence limit (97%) as that for a normal distribution.

B. Geoacoustical Modeling

1. Models

Three single-layer and four double-layer sediment models with reflecting or refracting layers, with or without an underlying half-space, are employed to describe the observed impulse responses. In Figures 3-9 the ray diagrams and the sound-speed profiles corresponding to the models are shown. The rays numbered from 1 to 3 correspond to the first three arrivals in order of increasing arrival time arising from reflections from layer interfaces or turning rays within a layer. All the hypothesized models are particular cases of total internal reflection; that is, sound rays are totally returned to the water column by either refraction or reflection.

The first model is simply a constant sound-speed layer overlying a half-space with reflection coefficient $R = \exp(i\pi/2)$. The second model is the same, except for an additional constant sound-speed layer. The third model is a layer with a sound-speed gradient and an assumed thickness several wavelengths greater than the deepest turning point. The sound-speed profile in the sediment is assumed to be the well-known, pseudo-linear profile [17] with interface gradient g. For the pseudo-linear profile the sound speed is given by

$$C(z) = C_T\,(1-2g(z-z_T)/C_T)^{-1/2} \qquad (1)$$

where C(z) is the sound speed at depth z, z_T is the depth at which the pseudo-linear profile begins, C_T is the sound-speed at depth z_T, and g is the sound-speed gradient at depth z_T.

The fourth model is a layer with a gradient in which deeper penetrating rays are intercepted by reflection from half-space with reflection coefficient $R = \exp(i\pi/2)$. Model 5 is a constant sound-speed layer overlying a half-space with a gradient. Model 6 consists of a layer with a gradient overlying a half-space with a gradient. Model 7 is a layer with a gradient above a constant sound-speed layer overlying a half-space with reflection coefficient $R = \exp(i\pi/2)$.

In each case, the model is applied over a restricted grazing-angle range from a low grazing angle consistent with a high-frequency asymptotic or ray-theory approximation, to a high grazing-angle at which the model fails to fit the data.

When a pseudo-linear sound-speed half-space is involved, it is assumed that the applicable grazing-angle range limits the turning points to well above the critical depth. The critical depth is the depth at which the sound speed approaches infinity. From (1) the critical depth is given by

$$z_C = z_T + C_T/2g \qquad (2)$$

The pseudo-linear half-space is a physically unrealistic model because of the sound-speed singularity [34]. However, the problem is effectively eliminated when the critical depth occurs in the region of "hidden depths" [35], i.e., a few wavelengths below the turning depth. This condition is easily satisfied for sufficiently small grazing angles.

It should be noted that some of the models actually revert to one of the simpler models over some portion of the lower angular range. In Model 2 at grazing-angles below the second-layer critical angle (if there is one), the reflection process is the same as for Model 1. Model 4 reverts to Model 3 when the turning point of the refracted ray is above the bottom of the layer. Model 5 reverts to Model 1 at low angles if there is a critical angle for the second layer. Similarly, Models 6 and 7 become

Model 4 at low angles if there is a critical angle for the second layer.

2. Parameter Extraction

The models and the analyses which follow are based on plane waves; i.e., the geometry is specified by the grazing angle independent of the source and receiver positions. The plane wave assumption is an approximation that greatly simplifies the problem. However, care must be exercised to limit its application to geometries for which the approximation is valid. Rudnick [36] pointed out that plane waves never really exist in any real measurement. More recently, Stickler [31] has shown numerical examples of errors induced by the plane-wave assumption for the case of reflection from a half-space with a sound-speed gradient. In particular, the observed critical angle may be shifted significantly from the plane-wave value.

In spite of these difficulties, it can be shown that the plane-wave approximation may be applied under certain restrictions regarding the measurement geometry and the wavelength. The reflected field of a point-source spherical wave interacting with a horizontally stratified bottom can be treated by the method of steepest descents in order to give an asymptotic approximation valid at high frequencies and at large distances. The calculation shows that the point-source reflected field is just a spherical wave radiating from the source-point image multiplied by the plane wave reflection coefficient, plus a correction term which may be kept as small as desired by choosing sufficiently large values of kR (where $k = 2\pi/\lambda$ and R is distance from the receiver to the source-point image) and by choosing grazing-angles that are not too near critical. Details of the calculation for the case of a constant-sound-speed halfspace may be found in Officer [37] and Brekovskikh [38]. The case of a reflecting layer and a pseudo-linear-sound-speed halfspace can be treated in a similar manner. The results of these calculations are summarized in Appendix A, Tables 5 and 6.

In the plane-wave-approximation model, parameters may be extracted from the data by analysis of arrival times and arrival-pulse amplitudes. Formulas for fitting arrival times are given for each the models in Table 7. The arrival-time analysis yields an estimate of the sediment sound-speed at the water-sediment interface, as well as sound-speed parameters and layer thickness for succeeding layers. First, arrival-peak amplitudes (water-sediment interface reflection coefficients R_1) are used to obtain the sediment density and a second independent estimate of the sound-speed at the water-sediment interface by application of the Rayleigh reflection equation. In each case, certain functions of measured quantities are plotted and a straight line curve is fitted. Model parameters are determined from the slope and the intercept of the fitted line. Formulas giving the quantities to be plotted and the meaning of the slope and the intercept parameters are found in Table 8.

Average attenuation coefficients are estimated from the peak amplitudes of the last arrival that passed through a turning point. When the last arrival comes from a reflection, it is assumed (as part of the model definition) that the reflection is total with a $\pi/2$ phase change (i.e., $R = \exp i\pi/2$). Formulas for the attenuation analysis are given in Table 9.

The parameter-extraction methods are based on assumed simple sediment sound-speed models that were chosen to fit arrival times and peak heights of the processed impulse responses. Justification for this model approach is based on the results given in Reference 28 in which Station 5 data for the present study was analyzed in terms of Model 3. It was shown that not only did the model fit the arrival times observed, but the entire set of impulse responses and bottom-loss curves were in striking

agreement with theoretical curves generated by the model. The agreement included observed pulse shapes and some subtle features in the loss curves. Furthermore, the model used in the analysis was consistent with well-documented geological evidence for the general existence of sediment sound-speed gradients [39, 40, 41].

Some of the data in the present study were found to fit reflecting- and some refracting-type behaviors. Arrival-time behavior for pulses reflected from an interface differs markedly from that of refracted pulses within a layer with a sound-speed gradient. In those cases where reflecting behavior was observed, the arrival-time fit was even better than the average, as judged by the RMS travel-time error t_A. Thus, because of the success in modeling the refracting case when a good time-of-arrival fit was obtained, sediment parameters were also derived from good time-of-arrival fits in reflecting cases. The seven models analyzed included combinations of reflecting- and refracting-type layers and half-spaces.

C. Acoustical Results

Except for Station 7, the geometry of the experiment permitted time separation of the bottom-interacting arrival from the subsequent water-surface-reflected arrivals. The traces were truncated in time to exclude the surface arrivals before the deconvolution processing was applied. The effect of the truncation can be seen, for example, in the Station 2 traces (see Appendix B) beginning at approximately 200 msec in the first eight high-angle traces, and then decreasing steadily to approximately 100 msec in the lowest-angle trace. The effect is seen as an apparent sudden decrease in the random noise level.

The effectiveness of the deconvolution at all the stations may be judged by the degree to which bubble-pulse energy is removed and by the resultant noise background as seen in the figures in Appendix B. At each of the stations except for Station 7, the reflectors are seen to correlate well from trace to trace. The complexity of reflectors is apparent in the high-frequency traces; however, at low frequencies a single penetrating arrival dominates over all others.

The decay times of the impulse responses of Stations 2, 4, 5, 8 and 9 are on the order of 0.1 sec and are attributed to multiple reflections within the sediment layers. In the geological discussions that follow in later sections it is shown that at these stations the bottom is relatively smooth and thickly sedimented. That is, the sediment cover is thick enough that the dominant bottom-reflected energy interacts via bottom paths located wholly within the sedimentary cover.

At Station 7, on the other hand, the impulse responses reveal no coherent pattern of peaks. Decay times of the impulse responses are on the order of 1 sec and are attributed to random scattering from a rough, sediment-free bottom. This hypothesis is supported by the fact that the core sample showed no penetration.

The intent of the data processing and modeling was to apply inversion techniques to obtain information about the bottom environment. The coherence and regularity of the impulse responses for Stations 2, 4, 5, 8, and 9 permitted detailed modeling and parameter extraction. This was not possible for Station 7. Once effective models are in hand, the bottom response as a function of frequency and source-receiver geometry may be computed directly within the limits of the models. Questions regarding surveillance system performance may then be addressed.

The major results of the analysis are presented in Table 2 in which the inferred sediment parameters are given for the Rayleigh-reflection-coefficient analysis and the time-of-arrival analysis.

Table 2. Summary of acoustically inferred model parameters

Sound-speed of the water C_w is in meters/second, gradients g_1, g_2 are in sec^{-1}, thickness h_1, h_2 in meters, attenuation κ_A in dB/meter/kHz, and time t_A in msec. The parameters DR and CR_R are based on Rayleigh-reflection-coefficient analysis; the remaining parameters are derived from time-of-arrival analysis for each model.

Station	Model	C_W	DR	CR_R	h_1	CR_1	g_1	h_2	CR_2	g_2	κ_A	t_A
2	3	1549.0	1.4	0.97	280	1.05	0.8				0.05	6.1
2	5	1549.0	1.4	0.97	12	1.00		260	1.05	0.8	0.05	8.4
2	6	1549.0	1.4	0.97	13	0.96	10.4	260	1.00	0.8	0.06	8.6
4	1	1548.5	1.3	1.04	75	1.06					0.04	0.5
4	4	1548.5	1.3	1.04	76	1.04	0.6				0.06	0.9
4	3	1548.5	1.3	1.04	81	1.00	2.1				0.07	0.5
5	3	1548.6	1.6	0.99	200	1.03	0.8				0.02	4.8
5	6	1548.6	1.6	0.99	37	0.99	2.5	170	1.00	0.8	0.03	4.0
8	1	1504.8	1.4	0.99	50	1.08					0.51	1.9
8	2	1504.8	1.4	0.99	12	1.03		36	1.07		0.51	1.0
8	4	1504.8	1.4	0.99	49	1.01	4.3				0.27	0.9
9	1	1525.5	1.5	0.97	80	1.06					0.27	1.2
9	7	1525.5	1.5	0.97	29	0.97	4.4	42	1.00		0.30	1.4

Average = 3.1

The parameters specified include: (1) density ratio DR, (2) sound-speed ratio CR, (3) layer thickness h, (4) sound-speed-gradient parameter g, and (5) attenuation constant κ_A. The water sound-speed CW was from a direct measurement and t_A is the root-mean-square difference between the measured and the predicted arrival times. The detailed acoustical results are presented in Appendix B. Plots of impulse responses and bottom-loss curves are given together with a discussion of their features. Plots of the straight-line curve fits are also given for each of the model analyses.

V. Geological Data Analysis

For each station geoacoustic properties of the sea floor were inferred from geological data obtained from (1) cores, (2) seismic-profiler records, (3) 3.5 kHz profiler records, (4) wide-angle reflection profiling (sonobuoy data) and (5) Deep Sea Drilling Project (DSDP) holes drilled in locations with sediments analogous to the site of interest. Although several methods for estimating sound-speed profiles were used, whenever possible an effective constant gradient was determined from DSDP sites with a sedimentary structure similar to that of

the station as determined from other geological considerations. An average interval sound speed, IC, was calculated from the acoustic travel time measured on the seismic-profiler record to a reflecting horizon correlated with a drilled interface at a known depth. The gradient was easily obtained from the relationship involving IC and the ratio of sediment surface sound speed to that of the bottom water, CR. This method of determining a gradient is referred to as the CRIC method and is used at Stations 2, 4, 5, and 8. The gradient thus determined is assumed constant in depth and is the same parameter as the "linear gradient" of Hamilton et al. [42].

A distinction should be noted between the definition of the gradient employed in the geological analysis and in the acoustical analysis. In the geological analysis the sound-speed gradient is assumed constant independent of depth and is denoted by the symbol g. In the acoustical analysis the term gradient and the symbol g refer to a parameter in the sound-speed formula for the pseudo-linear profile (see Section IV.B.1). In particular g is the sound-speed gradient at the top interface of the pseudo-linear layer. The sound-speed gradient continues to increase with depth, but for layer thicknesses and turning-point depths much less than the critical depth, the gradient is approximately constant--hence the term pseudo-linear sound-speed profile. In the acoustical analysis, layers were thin in the above sense; therefore, g values geologically inferred may reasonably be compared with g values acoustically inferred.

The environmental data from the stations are presented in Appendix C. Each station analysis contains a bathymetric map of the vicinity in addition to just the station site in order to provide information useful in extrapolating the acoustic results beyond the immediate station site. A general discussion of geological features that affect the acoustic properties at several of the stations is deferred to Appendix D.

Table 3 summarizes the acoustical properties of the sediments discussed in the geological analysis in the appendices. In addition, other information relevant to the acoustic properties are summarized: water depth, bottom-water sound-speed, sediment thickness and reflectors within the sediments.

The water depth is listed where the first and last charges were dropped, except for Station 7 where the minimum depth along the track is also indicated. Uncorrected depths are those read directly off the depth recorder and calibrated for a water sound speed of 1500 m/sec. The corrected values are derived from the tables of Gold and Audet [43].

The water sound-speed listed in Table 3 is that at the maximum depth reached by the SVSTD. Actual bottom-water sound-speed used elsewhere in this report is determined by extrapolating this value of sound-speed to the ocean bottom by using Reference [44]. The complete water sound-speed profiles are shown in Figure 73.

The sediment thickness is given in units of two-way travel time to the geologic basement as determined from the sparker-profiler records. The value is the average along the track of the reflectivity experiment as best determined from recordings in the vicinity. The sparker could not be operated during the acoustic experiment because the low-frequency signal (50-150 Hz) of the sparker source would interfere with the acoustic measurements. The actual thickness is a function of the sound-speed profile; however, for purposes of a rough estimate, the values list approximate thickness in kilometers (assumed sound-speed of 2000 m/sec).

The depth of the LF (low frequency) reflectors in two-way travel time are read from the sparker-profiler records at the closest point to the acoustic station that the sparker was operating. For values of less than 0.5 seconds, a rough estimate of the depth can be made using an assumed sediment sound speed of

Table 3. Geologic data and inferred acoustic parameters

Station	Province	Water depth (m) uncor.	Water depth (m) cor.	Bottom water sound speed (m/sec)	Sediment thickness (sec)	Depth of LF reflectors (sec)	No. of HF reflectors per meter	Density (gm/cm^3)	CR_G	g (sec^{-1})	κ_G dB/m/kHz
2	Northern Iberian Abyssal Plain	5250–5250	5306–5306	1551.0 @ 5291 m	1.2 1.2	0.11 0.38	0.3-03	1.51	0.977	0.7	0.078
4	Southeast Tagus Abyssal Plain	5075–5065	5131–5121	1548.5 @ 5115 m	2.0	0.09 0.35 1.09	0.45–0.6	1.53	0.994	0.7	0.076
5	Southwest Tagus Abyssal Plain	5066–5065	5121–5120	1548.6 @ 5120 m	2.0	0.05 0.13 0.30 1.00	0.35–0.6	1.54	0.996	0.7	0.077
7	Dragon Seamount	1950–1210–2700	1957–1218–2711	1503.6 @ 2264 m	0.001			2.5–2.9	2.5–3.4		
8	Dragon Seamount Plateau	2410–2085	2420–2094	1504.8 @ 2480 m	0.9	0.14 0.51 0.85	0.2–0.3	1.60	1.013	2.3	0.250
9	Lower Continental Rise South of Madeira	4685–4654	4724–4693	1525.5 @ 4000 m	1.3	0.05 0.11 0.23	0.5–0.3	1.52	0.984	1.1	0.100

1500 m/sec. The choice of the reflectors is somewhat subjective, but appears to correlate with the layer interfaces determined from the acoustic data.

Two values for the number of discrete reflectors per meter as determined from the 3.5 kHz (HF) depth recorder are given. These values are where the first and last charges were dropped, respectively. The maximum depth of penetration observed in the records is about 50 m (assuming a sound speed of 1500 m/sec in the sediment). The listed values are determined from approximately the upper 25 m. This parameter is further discussed in Appendix D.2.

The final four columns list the geoacoustic parameters of the sediments. The justification for choosing the particular values is given in Appendix C.

A comparison of these parameters as derived from the geological and acoustical data will be discussed in Section VI of this report.

The wet density, ρ, is measured for core samples or is estimated from the known geological properties of the sediments.

The ratio of the sound-speed of the sediment to that of the bottom water (CR) was generally estimated from core data. The average sound speed for the upper 5 m of the sea floor is used for this value. The sediment sound-speed is, in general, lower than that of the bottom water. Exceptions are the sediments with high carbonate content at Station 8 and the basalt outcrop with a negligible sedimentary cover at Station 7.

The sound-speed gradient, g, is defined in this report as the difference in sound-speed at 200 m and at the sediment surface divided by 200 m. Various methods used to derive this value are discussed in detail in the appendices. Sonobuoy data are used in the Station 9 determination. At the other stations, the two-way travel time to a reflector of known depth from a DSDP drill hole was used to determine the gradient.

The last column is the attenuation constant κ. This parameter is the proportionality constant in the equation that assumes a linear dependence on attenuation frequency: $\alpha = \kappa f$. The values listed are based on core samples and relationships presented by Hamilton [45].

VI. Comparison of Acoustical and Geological Results

Values of the sediment-to-water density ratio (DR) and sound-speed ratio (CR) as estimated from the acoustical and geological results are given in Table 4. Absolute differences between the acoustically inferred sediment-to-water density ratio using the Rayleigh-equation method (DR_R) and the core-measured values averaged over the top 5 m of sediment (DR_G) averaged 8%. The density ratio is probably the least sensitive acoustic parameter, and a value of 1.5 for all of the stations is probably as good a choice as either the DR_R or DR_G values.

Similarly, the sediment-to-water sound-speed ratio determined by application of the Rayleigh-reflection equation (CR_R) and time-of-arrival methods (CR_T) may be compared with the geological value (CR_G). Absolute differences between CR_R and CR_G averaged 2%, whereas absolute differences between CR_T and CR_G averaged 4%. The larger differences for CR_T may be expected, since CR_T is obtained from extrapolations of the behavior at depth. CR_R, on the other hand, is sensitive to just the reflection at the water-sediment interface.

The differences between CR_R and CR_T were largely reconciled at Stations 2 and 8 by the inclusion of a thin layer at the top of the sediments. The extra layer provided a CR_T value more nearly equal to CR_R, and, at the same time, gave correct arrival-times for both the high-frequency and low-frequency impulse responses. Presumably the differences at the other stations could also be reconciled by more complicated layered models.

Table 4. Comparison of acoustical and geological results

Acoustic Station	Model	DR_R	DR_G	CR_R	CR_T	CR_G	t_A (msec)	t_G (msec)	κ_A dB/m/kHz	κ_G
2	3	1.4	1.5	0.97	1.05	0.98	6.1	103	0.05	0.08
2	5	1.4	1.5	0.97	1.00	0.98	8.4	103	0.05	0.08
2	6	1.4	1.5	0.97	0.96	0.98	8.6	103	0.06	0.08
4	1	1.3	1.5	1.04	1.06	0.99	0.5	33	0.04	0.08
4	4	1.3	1.5	1.04	1.04	0.99	0.9	33	0.06	0.08
4	3	1.3	1.5	1.04	1.00	0.99	0.5	33	0.07	0.08
5	3	1.6	1.5	0.99	1.03	1.00	4.8	50	0.02	0.08
5	6	1.6	1.5	0.99	0.99	1.00	4.0	50	0.03	0.08
8	1	1.4	1.6	0.99	1.08	1.01	1.9	42	0.51	0.25
8	2	1.4	1.6	0.99	1.03	1.01	1.0	42	0.51	0.25
8	4	1.4	1.6	0.99	1.01	1.01	0.9	42	0.27	0.25
9	1	1.5	1.5	0.97	1.06	0.98	1.2	64	0.27	0.10
9	7	1.5	1.5	0.97	0.97	0.98	1.4	64	0.30	0.10

For a single-layer model at low frequencies, CR_T should be used rather than CR_R. The use of CR_T generates small errors in the amplitude of the first reflected pulse, but gives the correct arrival times. Alternatively, the use of CR_R gives the correct amplitude for the first reflected pulse, but causes significant errors in the arrival-times.

The best estimate of sediment sound-speed structure based solely on geological data at each station is described as a single layer with a gradient as defined in Section V. The gradients are listed in Table 3. The corresponding sound-speed profiles are indicated by arrows in Figure 10. The acoustic models are more complex; the corresponding parameters are listed in Table 4 and profiles illustrated in Figure 10. An appropriate means to compare geological and acoustical models is by the arrival times. Arrival-time differences between the predicted and actually observed times were calculated and the RMS differences t_A and t_G presented in Table 4.

For each of the stations, the acoustical RMS arrival-time error t_A was less than 9 msec. In consideration of the pulse width (14.2 msec corresponding to full width at 3 dB points), the theoretical-bottom-loss pattern would be expected to match the observed pattern to within half an oscillation period. The RMS time difference was largest for Stations 2 and 5. This might be expected, since the model at these stations was forced to describe a much thicker sediment layer. The geologically predicted arrival times yielded errors t_G that were much greater than the pulse width; therefore, there would be no hope in reproducing the bottom-loss oscillation pattern.

The uniqueness of modeling tends to be more of a problem at shallow depths. For example, at Stations 2 and 8 where additional modeling of the high-frequency impulse responses was attempted, the

time-of-arrival behavior did not clearly separate into constant-sound-speed or sound-speed-gradient behavior at shallow depths (<10 m). This difficulty, however, is not serious (as it would be at greater depths) because the absolute differences in sound speed for the different candidate models are small over a thin layer. At greater depths, the models are clearly differentiated by the arrival-time behavior as demonstrated at Stations 2 and 5.

Details of the shallow sediment structure (<10 m) are relatively unimportant at low frequencies (wavelength >>10 m). It primarily contributes to the effective low-frequency Rayleigh-type reflection at the water-sediment interface. At higher frequencies (wavelength <<10 m), shallow penetrating rays are well resolved from the water-sediment reflected pulse, and the details of the sound-speed structure are important.

The shallow sediment structure inferred at Stations 2 and 8 (Fig. 10) indicated a rapid initial increase in sound-speed at the top of the sediments. As discussed previously, more than one model gave a reasonable time-of-arrival fit. The shallow structure could be modeled by either a constant or a gradient sound-speed layer. The gradient layer permitted a lower value of CR_T and gave approximately the same average sound speed as the constant-sound-speed model. Although the exact form of the sound-speed profile could not be unambiguously decided, the models were consistent with a sound-speed which rose rapidly to values on the order of 1600-1700 m/sec within the first 10 m for Station 2, and within the first 50 m for Station 8.

From the geological point of view, the shallow sound-speeds are higher than would be expected for the sediments involved. In addition, the associated sound-speed gradients are much higher than any previously measured. On this basis, one might drop the gradient-layer interpretation and choose the constant-sound-speed-layer model. In that case, however, the sound-speed just takes discontinuous jumps and still arrives at the high sound-speeds.

Although a variety of bottom sediment structures could account for the observed high sound-speeds, their occurrence is not readily predicted on the basis of the available geological data alone. Nevertheless, geological observations are often suggestive or supportive of acoustic findings. For example, a very hard clay interface was sampled in the core cutter from a core taken south of Station 2. Likewise, near Station 8, there was an indication of a highly reflective buried layer at the start of the seismic profile track. This evidence of high-sound-speed layers from the core samples may indicate the cause of the acoustically inferred high-sound-speeds at shallow depths observed at Stations 2 and 8.

Comparison of the shallow sediment acoustical results with geological theory is not direct. Deep-water sound-speed gradients determined from sonobuoy interval-velocity measurements are only available for sediment depths more than a few hundred meters. It would hardly seem reliable to extrapolate these values for use at 0-50 m. Gravity- and piston-type cores cannot provide the desired information because they typically penetrate less than 5 m of sediment.

Effective shallow sound-speed gradients need not be explained entirely in terms of sediment compaction, temperature gradients, or pressure effects. A distribution of high-sound-speed sediment layers among other low-speed layers could produce apparent high gradients at shallow depths, particularly when there are geological reasons to expect the most recent sediment deposition to be of the slower sound-speed type. At greater depths where the comparison was more direct (e.g., Stations 2 and 5), the acoustically inferred sound-speed gradients fell well within the range of previously reported values and were completely consistent with geological expectations for the particular sites.

The geologically inferred sound-speed gradient using an interval-velocity measurement, deep-drill core-measured depth, and core-measured CR value (CRIC method) was in good agreement with the acoustically determined gradient for acoustic ray paths which penetrated 200-300 m in depth (Stations 2 and 5). This suggests that extrapolation of deep sediment gradients can be made from remote sites having similar sedimentological histories. Although gradients were accurately predicted, the predicted arrival times t_G were in error by much more than a pulse width (see Table 4). In other cases (Stations 8 and 9), the geological prediction of a deep gradient was not applicable because either significant reflection or total reflection was occurring at a much shallower layer.

Estimates of acoustic attenuation are compared in Table 4 where $^{K}_{A}$ is the acoustical estimate and $^{K}_{G}$ is the geological estimate. For each set of values, Stations 2, 4, and 5 have the lowest values and Station 8 has the highest, although the acoustic results have a greater range of values. The attenuation parameter is the most difficult parameter to estimate in either approach. The geological estimate is based on data for which there is much scatter and the acoustical estimate is based on so few points it is difficult to estimate its probable error.

Many sources of error may contribute to discrepancies between acoustically and geologically inferred model parameters. The acoustical analysis is limited by the imposition of a priori model types to which the data is fitted. Simple models were chosen to describe the behavior of dominant features in the received signals. Many details of the signals are not included and, of course, even the dominant features are not modeled exactly.

Some sources of error in the geological analysis may stem from the following considerations of the way that geological survey data is collected: (1) On seismic-profile surveys clipped signals are recorded in order to reveal deep reflecting horizons. The accompanying disadvantage is that differences in layer reflectivities may not be differentiated. (2) Surface reflections and bubble pulses in profiler and sonobuoy data limit depth resolution and preclude accurate measurement at depths of 0 to 200 m--the depth range that is most influential in low-frequency, low-grazing-angle, bottom-sediment interaction. (3) Surficial sound speeds measured in cores or extrapolated from deeper measurements may not be the same as the effective low-frequency, interface-sound-speed parameter required by the models. (4) Sound-speed gradients predicted from interval-velocity analyses of layers deeper than 200 m may not be applicable at shallower depths. (5) Sediment sampling in DSDP cores is often insufficient at depths of 0 to 200 m.

VII. Conclusions

A deep water experiment employing a deep hydrophone and 0.8 kg SUS charges detonated at 244 m depth provides data useful for modeling low-frequency, low-grazing-angle, bottom-interaction phenomena. Deconvolution processing of bottom reflectivity data eliminates multiple bubble pulses which otherwise interfere with the data analysis and interpretation.

We draw the following conclusions about the specific sites analyzed in this report:

(1) Impulse responses from thick-sediment bottom sites displayed sequences of pulses in an easily discerned pattern varying with grazing-angle. Decay times for the overall pattern were on the order of 0.1 sec. At low frequencies (40 to 90 Hz) and over some restricted range of grazing-angles bottom impulse responses could be interpreted in terms of simple layered sediment models consisting of one to three refracting and/or reflecting layers. The RMS error in the model-predicted arrival time along the

dominant bottom interacting path t_A ranged from 1 to 9 msec--less than the 14.2 msec acoustic pulse width.

(2) In marked contrast the impulse responses from a sediment-free bottom site showed no distinctive pattern (suggestive of roughness scattering) and decayed in times on the order of 1 sec. No modeling was attempted.

(3) Geological and acoustical estimates of the sediment-to-water density ratio (DR_R, DR_G) and the sound-speed ratios (CR_R, CR_G) agreed to within 5%.

(4) Differences between the geologically and acoustically inferred sound-speed profiles were on the order of 100 msec and varied considerably with model and depth. The geologically inferred sound speed was always lower, with an RMS error in predicted arrival time along the dominant bottom-interacting path t_G of 33 to 103 msec, i.e., from 1 to 5 times the acoustic pulse width.

(5) In all cases relatively low bottom-losses were measured over angular ranges for which a large, dominant peak was observed in the impulse response. The dominant peak was attributed to a totally refracting or reflecting sediment path that penetrated the sediments to less than 200 m depth. The only loss mechanism was hypothesized to be an effective attenuation along the dominant path.

(6) Acoustically inferred, effective attenuation coefficients, estimated to be uncertain by at least a factor of 2, ranged from 0.02 to 0.05 dB/m/kHz. Although the geological and acoustical values showed the same trend from station to station, ratios of the two inferred values ranged from 1 to 4.

Because of the geographical and geological diversity of the thick-sediment sites analyzed in this study, it is expected that the same types of low-frequency bottom-interaction behavior would be observed at many other thick sediment sites. When this is the case, simple geoacoustic models are possible for predicting those aspects of surveillance-system performance that depend on bottom reflectivity. In the absence of detailed wide-angle reflectivity measurements, such as those analyzed in this study, the derivation of accurate geoacoustic models on the basis of generally available geological data is limited. Nevertheless, the utility of such data could be significantly enhanced, as suggested in the recommendations that follow.

VIII. Recommendations

The following recommendations are suggested for improving the utility of normal-incidence subbottom-profiler and deep-drill-core data for the prediction of accurate geoacoustic models:

1. Record undistorted signal amplitude of normal-incidence profiler returns, i.e., without clipping.

2. Apply signal processing techniques of deconvolution and deghosting to remove interference due to bubble pulses and water-surface reflections.

3. Measure sound-speed and density in the upper few hundred meters of a deep-drill core (DSDP) at sample spacings small relative to a wavelength.

4. Develop mathematical inversion techniques of sound-speed-profile reconstruction that are sensitive at the relevant depths of penetration (0-200 m) and to the averaging effects of low frequencies and low grazing angles.

IX. References

[1] Rayleigh, W. S., The Theory of Sound, 2nd ed., Dover, New York Publications (1955), para. 270.

[2] Sergeev, L. A., "Ultrasonic Echo Soundings for Geophysical Purposes," Applied Geophysics 20, 141-154 (1958), Trans. 115 by M. Slessers, Naval Oceanographic Office, NSTL Station, MS(1963).

[3] Liebermann, L. N., "Reflection of Sound from Coastal Sea Bottoms," J. Acoust. Soc. Am. 20(3), 305-309 (1948).

[4] Hill, H. M., "Seismic Refraction Shooting in an Area of the Eastern Atlantic," Phil. Trans. Roy. Soc. Lond., A244, 561-569 (1952).

[5] Hamilton, E. L., G. Shumway, H. W. Menard, and C. J. Shipek, "Acoustic and Other Physical Properties of Shallow-water Sediments Off San Diego," J. Acoust. Soc. Am. 28, 1-15 (1956).

[6] Mackenzie, K. V., "Reflection of Sound from Coastal Bottoms," J. Acoust. Soc. Am. 32, 221-231 (1960).

[7] Breslau, L. R., "The Normally-Incident Reflectivity of the Sea Floor at 12 Kc and Its Correlation with Physical Geological Properties of Naturally-Occurring Sediments," Woods Hole Oceanographic Institution Reference 67-16 (1967).

[8] Morse, P. M., Vibration and Sound, 2nd ed., McGraw-Hill Book Co. New York, (1948) p. 367.

[9] Jones, J. L., C. B. Leslie, and L. E. Barton, "Acoustic Characteristics of Underwater Bottoms," J. Acoust. Soc. Am. 36(1), 154-157 (1964).

[10] Barnard, G. R., J. L. Bardin, and W. B. Hempkins, "Underwater Sound Reflection from Layered Media," J. Acoust. Soc. Am. 36, 2119-2123 (1964).

[11] Brown, M. V., and J. H. Richard, "Interference Pattern Observed in Reflections from the Ocean Bottom," J. Acoust. Soc. Am. 37, 1033-1036 (1965).

[12] Bucker, H. B., J. A. Whitney, G. S. Yee and R. R. Gardner, "Reflection of Low-Frequency Sonar Signals from a Smooth Ocean Bottom," J. Acoust. Soc. Am. 37, 1037-1051 (1965).

[13] Menotti, F. R., S. R. Santaniello, and W. R. Schumacher, "Studies of Observed and Predicted Values of Bottom Reflectivity as a Function of Incident Angle," J. Acoust. Soc. Am. 38, 707-714 (1965).

[14] Cole, B. F., "Marine Sediment Attenuation and Ocean-Bottom Reflected Sound," J. Acoust. Soc. Am. 38, 291-297 (1965).

[15] Smith, D. T. and W. N. Li, "Echo-Sounding and Sea-Floor Sediments," Marine Geology 4, 353-364 (1966).

[16] Winokur, R. S. and J. C. Bohn, "Sound Reflection from a Low-Velocity Bottom," J. Acoust. Soc. Am. 44, 1130-1138 (1968).

[17] Morris, H. E., "Bottom-Reflection-Loss Model with a Velocity Gradient," J. Acoust. Soc. Am. 48, 1198-1202 (1970).

[18] Hastrup, O. E., "Digital Analysis of Acoustical Reflectivity in the Tyrrhenian Abyssal Plain," J. Acoust. Soc. Am. 47 (1), 181-190 (1970).

[19] Hovem, J. M., "Deconvolution for Removing the Effects of the Bubble Pulses of Explosive Charges," J. Acoust. Soc. Am. 47 (1), 281-284 (1970).

[20] Van der Veen, S. R. and S. R. Santaniello, "Digital Processing of Explosive Source Ocean-Bottom Reflected Acoustical Signals," U. S. Naval Underwater Systems Center, Technical Report 4337, (1972).

[21] Lackoff, M. R. and L. R. LeBlanc, "Frequency Domain Seismic Deconvolution Filtering," J. Acoust. Soc. Am. 57, 151-159 (1975).

[22] Dicus, R. L., "Impulse Response Estimation With Underwater Explosive Charge Acoustic Signals," J. Acoust. Soc. Am 70, 122-133 (1981).

[23] Herstein, P. D., "The Effect of Noise on the Deconvolution of Ocean Sediment Interacted Acoustic Signals," Naval Underwater Systems Center Tech. Rep. 5373 (1976).

[24] Stoffa, P. L., P. Buhl, and G. M. Bryan, "The Application of Homomorphic Deconvolution to Shallow Water Marine Seismology - Part I: Models," Geophysics 39 (4), 401-416 (1974).

[25] Buhl, P., P. L. Stoffa, and G. M. Bryan, "The Application of Homomorphic Deconvolution to Shallow Water Marine Seismology - Part II: Real Data," Geophysics 39 (4), 417-426, (1974).

[26] Hanna, J. S., "Short Range Transmission Loss and the Evidence for Bottom-Refracted Energy," J. Acoust. Soc. Am. 53 (6), 1686-1690 (1973).

[27] Christensen, R. E., J. A. Frank, and W. M. Geddes, "Low Frequency Propagation Via Shallow Refracted Paths Through Deep Ocean Unconsolidated Sediments," J. Acoust. Soc. Am. 57 (6), 1421-1426 (1975).

[28] Dicus, R. L., "Preliminary Investigations of the Ocean Bottom Impulse Response at Low Frequencies," Naval Oceanographic Office, Tech. Note 6130-4-76 (1976).

[29] Santaneillo, S. R., F. R. DiNapoli, R. K. Dullea, and P. D. Herstein, "Studies on the Interaction of Low-Frequency Acoustic Signals with the Ocean Bottom," Geophysics 44 (12), 1922-1940 (1979).

[30] Stickler, D. C., "The Principles Involved in the Measurement of Bottom Loss," Western Electric, New York, Rep. 72, R245 (1972).

[31] Stickler, D. C., "Negative Bottom Loss, Critical Angle Shift and the Interpretation of the Bottom Reflection Coefficient," J. Acoust. Soc. Am. 61 (3), 707-710 (1977).

[32] Stickler, D. C., "Measurement of the Sound Speed in Bottom Layers," J. Acoust. Soc. Am. 57 (3), 585-590 (1975).

[33] Roberts, B. G., Jr., "Horizontal-Gradient Acoustical Ray-Trace Program Trimain," Naval Research Laboratory, Report 7827 (1974).

[34] Williams, A. O., Jr., "Acoustic Reflection from a Structured Sea Bottom," J. Acoust. Soc. Am. 59 (1), 62-68, (1976).

[35] Williams, A. O., Jr., "Hidden Depths: Acceptable Ignorance about Ocean Bottoms," J. Acoust. Soc. Am. 59 (5), 1175-1179 (1976).

[36] Rudnick, I., "The Propagation of an Acoustic Wave Along a Boundary," J. Acoust. Soc. Am. 19 (2), 348-356 (1947).

[37] Officer, C. B., Introduction to the Theory of Sound Transmission with Application to the Ocean, (McGraw-Hill Book Company, New York, 1958).

[38] Brekhovskikh, L. M., "Waves in Layered Media," Academic Press, New York, (1960).

[39] Houtz, R. E. and J. I. Ewing, "Sedimentary Velocities of the Western North Atlantic Margin," Bull. Seismol. Soc. Am. 54, 867-895 (1964).

[40] Laughton, A. S., "Sound Propagation in Compacted Ocean Sediments." Geophysics 22, 233-260 (1957).

[41] Hamilton, Edwin L., "Prediction of Deep-Sea Sediment Properties: State-of-the-Art," In: Deep-Sea Sediments, Physical and Mechanical Properties, Anton L. Inderbitzen (ed.), (Plenum Press, New York, 1974).

[42] Hamilton, Edwin L., David G. Moore, Edwin C. Buffington, Philip L. Sherrer, and Joseph R. Curray, "Sediment Velocities from Sonobuoys: Bay of Bengal, Bering Sea, Japan Sea, and North Pacific," J. Geophys. Res. 79, 2653-2668 (1974).

[43] Gold, E. A. and J. J. Audet, Jr., "Computerized Depth Correction Data Bank for the North Atlantic Ocean and the Caribbean Sea and the Gulf of Mexico," Office of Naval Research, Acoustic

Environmental Support Detachment, Arlington, Virginia, and Naval Oceanographic Office, NSTL Station, MS, August, 151 p., 1973 (AESD Tech Note 73-03/NAVOCEANO Tech Note 6160-07-73).

[44] Naval Oceanographic Office, "Tables of Sound Speed in Sea Water," Special Publication SP-58 (1962).

[45] Hamilton, Edwin L., "Compressional-Wave Attenuation in Marine Sediments," Geophysics 37, 620-646, (1972).

[46] Reynolds, L. M., "Marine Geology of the Iberian Abyssal Plain," Unpublished manuscript, Naval Oceanographic Office, NSTL Station, MS, (1976).

[47] Laughton, A. S., "An Interplain Deep-Sea Channel System," Deep Sea Res. 7, 75-88 (1960).

[48] Laughton, A. S., "New Evidence of Errosion on the Deep Ocean Floor," Deep Sea Res. 15, 21-29 (1968).

[49] Laughton, A. S., W. A. Berggren et al., "Site 118," in: Initial Reports of the Deep Sea Drilling Project. vol. 12., pp. 673-751, U.S. Gov. Print. Off., Washington, (1972).

[50] Cernock, Paul J., "Sound Velocities in Gulf of Mexico Sediments as Related to Physical Properties and Simulated Overburden Pressure," Texas A&M University Tech. Report 70-5-T, College Station, Texas, (1970).

[51] Hamilton, Edwin L., Richard T. Bachman, Joseph R. Curray and David G. Moore, "Sediment Velocities from Sonobuoys: Bengal Fan, Sunda Trench, Andaman Sasin, and Nicobar Fan," J. Geophys. Res., 82, 3003-3012 (1977).

[52] Hamilton, Edwin L., "Sound Velocity and Related Properties of Marine Sediments, North Pacific," J. Geophys. Res., 75, 4423-4446 (1970).

[53] Ruddiman, W. F. and L. K. Glover, "Geology and Geophysics of the Tagus Basin," Naval Oceanographic Office, NSTL Station, MS, Tech. Note 6120-1-76, 37 p. (1976).

[54] Duplaix, S., W. D. Nesteroff, and B. C. Heezen, "Mineralogie Comparee des Sediments du Tage (Portugal) et de Quelques Sables Profonds de la Plaine Abyssale Correspondence," Deep Sea Res., 12, p. 211-217 (1965).

[55] Berger, Wolfgang H. and Ulrich von Rad, "Cretaceous and Cenozoic Sediments from the Atlantic Ocean, in: Initial Reports of the Deep Sea Drilling Project," v. 14, D. E. Hayes, A. C. Pimm and others, Washington, U.S. Gov. Print. Off., p. 787-954 (1972).

[56] Pimm, A. C. and D. E. Hayes, "General Synthesis," in: Initial Report of the Deep Sea Drilling Project, v. 14, D. E. Hayes, A. C. Pimm et al., Washington, U. S. Gov. Print. Off., p. 955-975 (1972).

[57] Hayes, D. E., A. C. Pimm, et al., "Site 142," in: Initial Reports of the Deep-Sea Drilling Project, v. 14, D. E. Hayes, A. C. Pimm et al., Washington, U. S. Gov. Print. Off., p. 249-282, (1972).

[58] Uchupi, Elazar, K. O. Emery, et al., "The Continental Margin off Western Africa: Senegal to Portugal," Woods Hole Tech. Report WHOI-75-43, 201 p. (1975).

[59] Hayes, D. E., A. C. Pimm, et al., "Site 136," in: Initial Reports of the Deep-Sea Drilling Project, v. 14, D. E. Hayes, A. C. Pimm et al., Washington, U.S. Gov. Print. Off., p. 49-83 (1972).

[60] Houtz, Robert, John Ewing, and P. Buhl, "Seismic Data from Sonobuoy Stations in the Northern and Equatorial Pacific," J. Geophys. Res., 75, 5093-5111 (1970).

[61] Embley, R. W.," New Evidence for Occurrence of Debris Flow Deposits in the Deep Sea," Geology, 4, 371-374 (1976).

[62] Anderson, Rockne S., "Statistical Correlation of Physical Properties and Sound Velocity in Sediments," in: Physics of Sound in Marine Sediments, Loyd Hampton (ed.), Plenum Press, New York, pp. 481-518, (1974).

[63] Laughton, A. S., M. N. Hill, and T. D. Allan, "Geophysical Investigations of a Seamount 150 Miles North of Madeira," Deep Sea Res. 7, 117-141, (1960).

[64] Fox, Paul J., E. Schreiber, and J. Peterson, "Compressional Wave Velocities in Basalt Recovered During Leg 14," U.S. Gov. Print. Off., Washington, pp. 773-775 (1972).

[65] Fox, Paul J., Edward Schreiber, and J. J. Peterson, "The Geology of the Oceanic Crust: Compressional Wave Velocities of Oceanic Rocks," J. Geophys. Res., 78, 5155-5172 (1973).

[66] Christensen, Nikolas I., "Compressional-Wave Velocities in Basalts from the Juan de Fuca Ridge," J. Geophys. Res. 75, 2773-2775 (1970).

[67] Berger, W. H., "Deep-Sea Sedimentation," in: The Geology of Continental Margins, C. A. Burk and C. L. Drake (eds.), Springer-Verlag, New York, pp. 213-241 (1974).

[68] Kanmera, Kametoshi, "Paleozoic and Mesozoic Geosynclinal Volcanism in the Japanese Islands and Associated Chert Sedimentation," in: Modern and Ancient Geosynclinal Sedimentation, R. H. Dott, Jr. and Robert H. Shaver (eds.), Society of Economic Paleontologists and Mineralogists, Tulsa (1974) Special Pub. No. 19, pp 161-173.

[69] Ewing, John I., Robert E. Houtz, and William J. Ludwig, "Sediment Distribution in the Coral Sea," J. Geophys. Res. 75, 1963-1972 (1970).

[70] Peterson, M. N. A. et al., "Cruise Leg Summary and Discussion," in: Reports of the Deep Sea Drilling Project, Vol. 2, ed. M. N. A. Peterson et al., (U.S. Gov. Print. Off., Washington, 1970), pp. 413-427.

[71] Bryan, A. M., "In Situ Indications of Gas Hydrate," in: Natural Gases in Marine Sediments, Isaac R. Kaplan, ed., (Plenum Press, New York, 1974).

[72] Berggren, W. A., "Late Pliocene-Pleistocene Glaciation," in: Initial Reports of the Deep Sea Drilling Project, Vol. 12, ed., A. S. Laughton, W. A. Berggren, et al., (U.S. Gov. Print. Off., Washington, 953-963, 1972).

[73] Houtz, Robert and John Ewing, "Upper Crystal Structure as a Function of Plate Age," J. Geophys. Res. 81, 2490-2498 (1976).

[74] Fry, John C. and Russell W. Raitt, "Sound Velocities at the Surface of Deep Sea Sediments," J. Geophys. Res., 66, 589-597 (1961).

[75] Urick, R. J., "A Sound Velocity Method for Determining the Compressibility of Finely Divided Substances," J. Appl. Phys. 18, 983-987 (1947).

[76] Countryman, Kenneth A., "Distribution of Deep Water Properties in the Northeast Atlantic Ocean," Naval Oceanographic Office, NSTL Station, MS, Tech. Note 3431-3-75, (1975).

[77] Schreiber, B. Charlotte, "Sound Velocity in Deep Sea Sediments," J. Geophys. Res. 73, 1259-1268 (1968).

[78] Horn, D. R., B. M. Horn, and M. N. Delach, "Correlation Between Acoustical and Other Physical Properties of Deep-Sea Cores," J. Geophys. Res. 73, 1939-1957 (1968).

[79] Hamilton, Edwin L., "Thickness and Consolidation of Deep-Sea Sediments," Bull. Geol. Soc. Am. 70, 1399-1424, (1959).

[80] Le Pichon, Xavier, John Ewing, and Robert E. Houtz, "Deep-Sea Sediment Vel-

ocity Determination Made While Reflection Profiling," J. Geophys. Res. 73, 2597-2614 (1968).

[81] Hamilton, Edwin L., "Variations of Density and Porosity with Depth in Deep-Sea Sediments," J. Sedim. Petrology, 46, 280-300 (1976).

[82] Bullard, E. C., "The Flow of Heat Through the Floor of the Ocean," in: The Sea, ed., M. N. Hill, (John Wiley & Sons, New York, 1963).

[83] Langseth, Marcus G., Jr., and Richard P. Von Herzen, "Heat Flow Through the Floor of the World Oceans," in: The Sea, Vol. 4, ed., Arthur E. Maxwell, (John Wiley & Sons, New York, 1970).

[84] Fenner, Don F. and Paul J. Bucca, "The Upper and Deep Sound Channel in the Northeast Atlantic," Naval Oceanographic Office, NSTL Station, MS, IR No. 69-94 (1969).

[85] Fenner, Don F. and Paul J. Bucca, "The Sound Velocity Structure of the North Atlantic Ocean," Naval Oceanographic Office, NSTL Station, MS, IR No. 71-13, (1971).

X. Illustrations

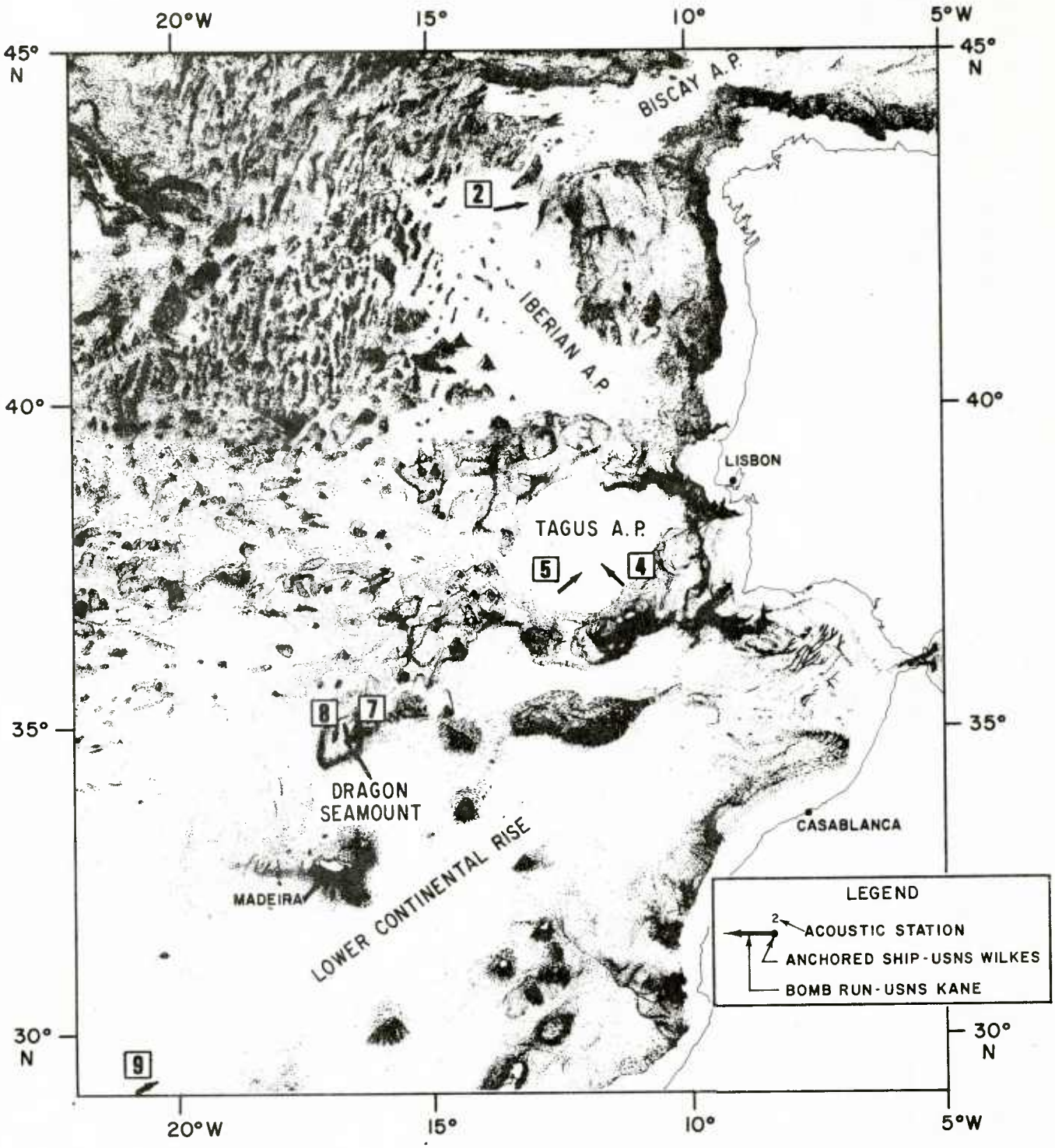

Figure 1. Physiographic map of the Northeast Atlantic Ocean with locations of bomb runs for stations.

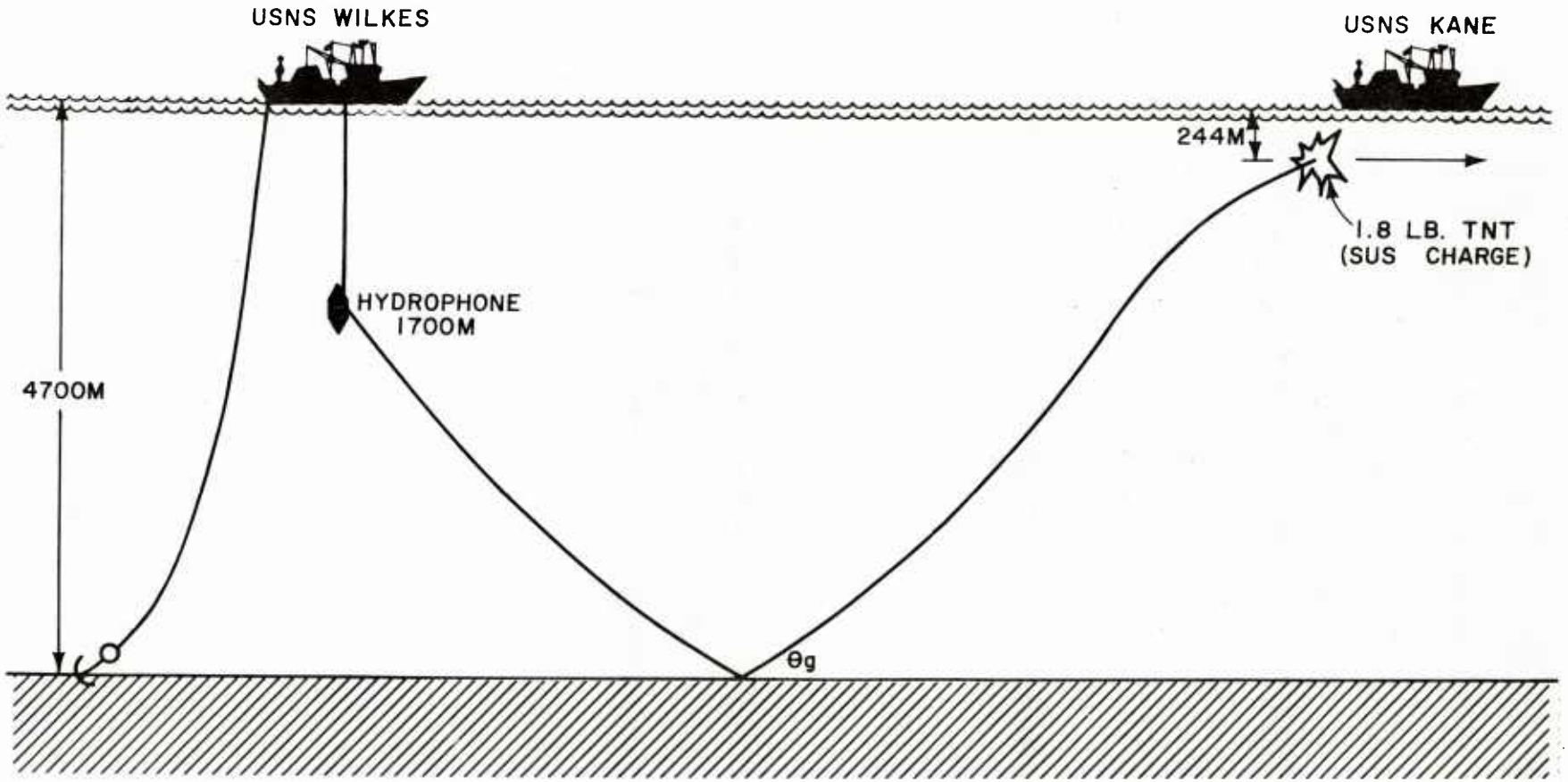

Figure 2. Typical geometry of bomb run for reflectivity experiment.

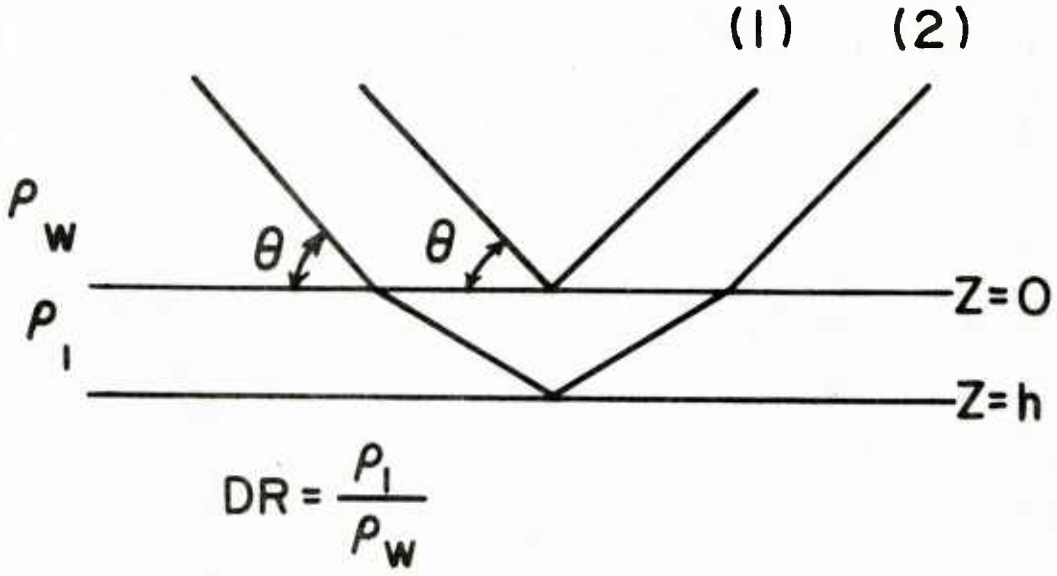

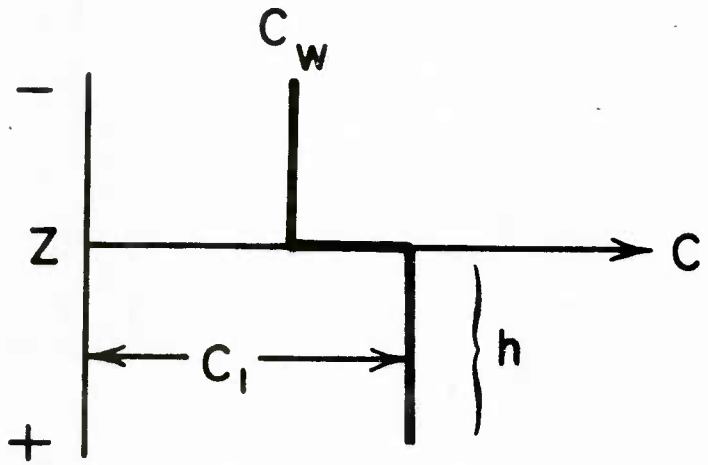

$$C(Z) = C_w \quad Z < O$$

$$C(Z) = C_1 \quad O \leq Z < h$$

$$CR = C_1 / C_w$$

Figure 3. Model 1: Constant-sound-speed layer overlying half-space with reflection coefficient R = i.

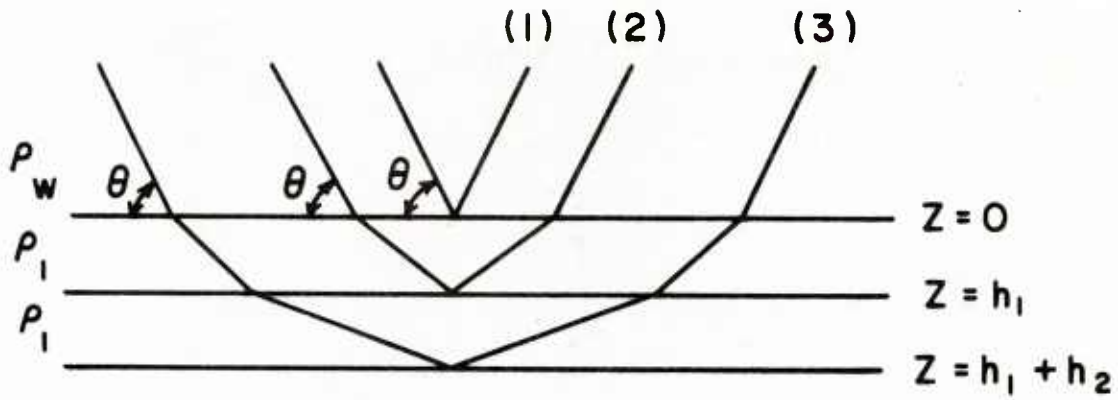

$$DR = \rho_1 / \rho_w$$

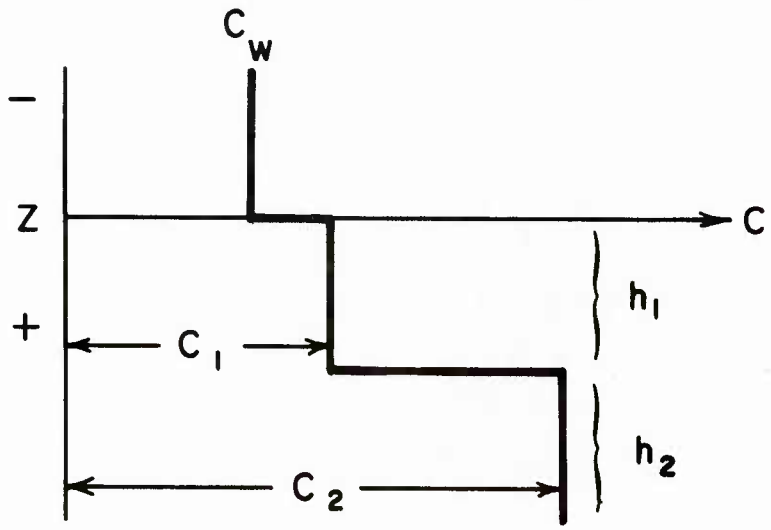

$$C(Z) = C_w \quad Z < 0$$

$$C(Z) = C_1 \quad 0 \leq Z < h_1$$

$$C(Z) = C_2 \quad h_1 \leq Z < h_1 + h_2$$

$$CR_1 = C_1 / C_w \quad CR_2 = C_2 / C_1$$

Figure 4. Model 2: Two constant-sound-speed layers overlying half-space with reflection coefficient R = i.

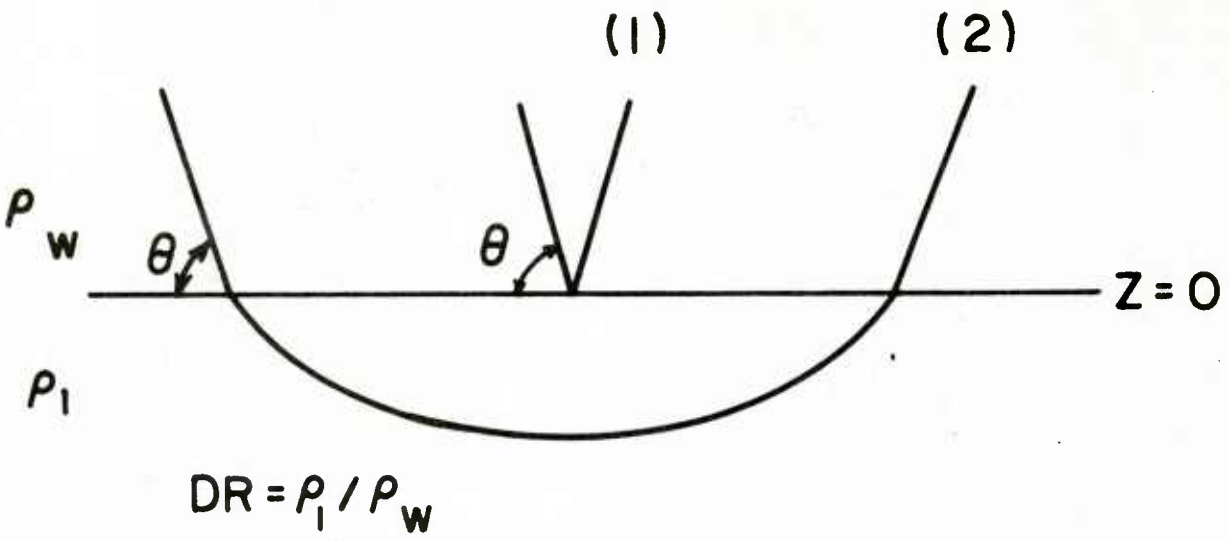

$$DR = \rho_1 / \rho_w$$

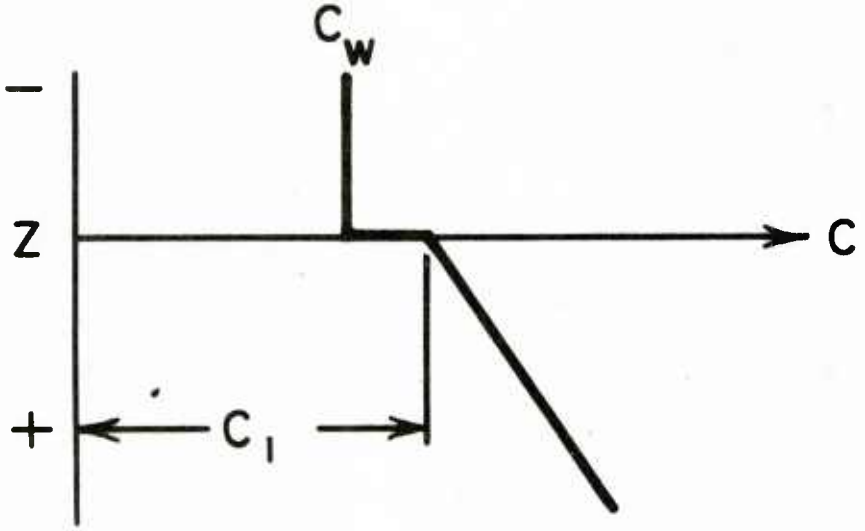

$$C(Z) = C_w \quad Z < 0$$

$$C(Z) = C_1 (1 - 2gZ / C_1)^{-1/2} \quad Z \geq 0$$

$$CR = C_1 / C_w$$

Figure 5. Model 3: Pseudo-linear-sound-speed half-space.

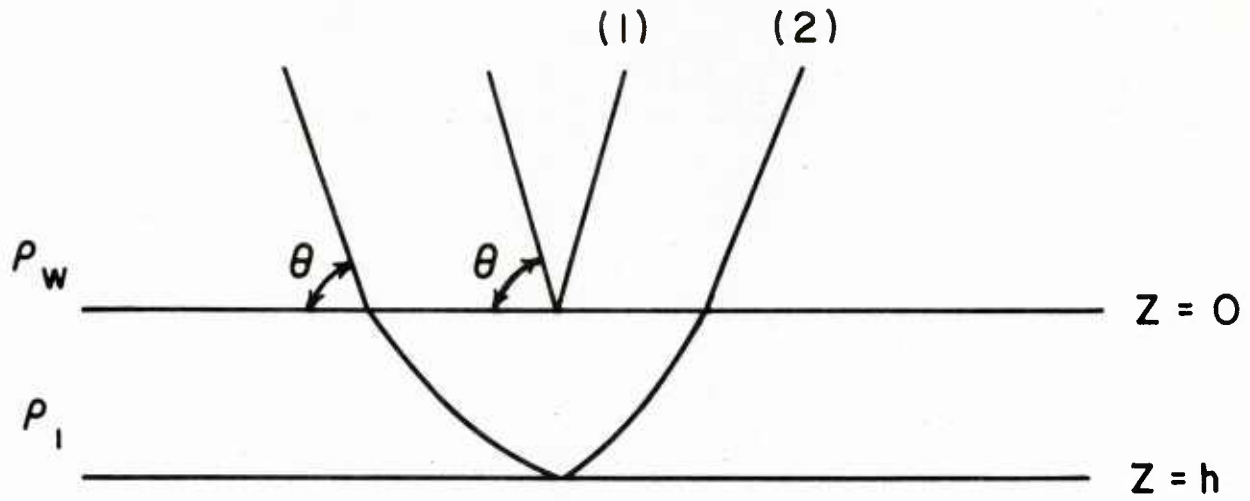

$$DR = \rho_1 / \rho_w$$

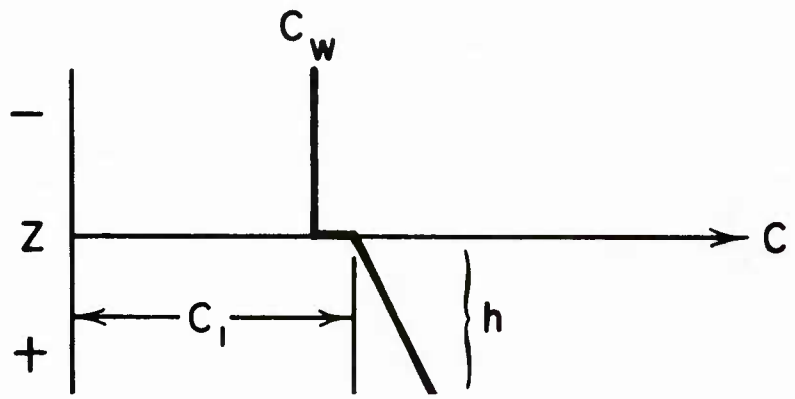

$$CR = C_1 / C_w$$

$$C(Z) = C_w \quad Z < 0$$

$$C(Z) = C_1 (1 - 2gZ/C_1)^{-1/2} \quad 0 \leq Z < h$$

Figure 6. Model 4: Pseudo-linear-sound-speed layer overlying half-space with reflection coefficient R = i.

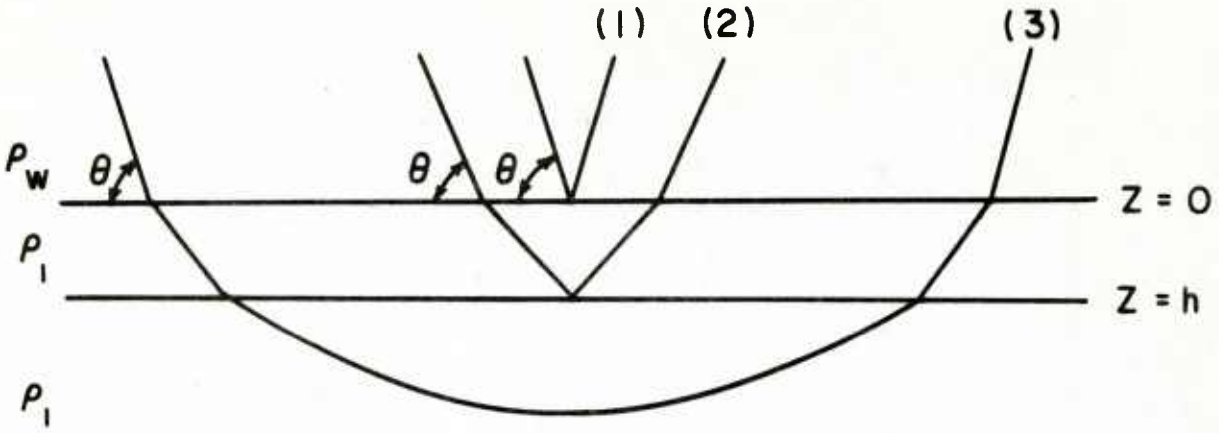

$$DR = \rho_1 / \rho_w$$

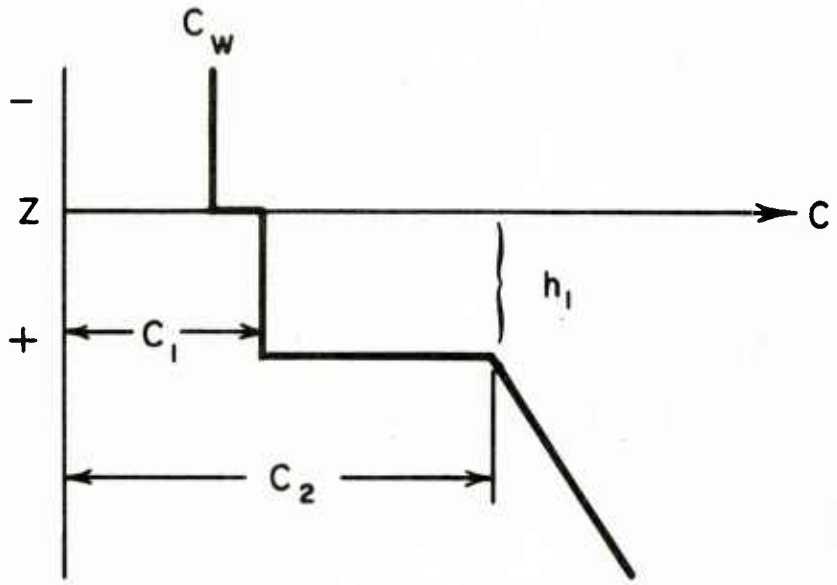

$$C(Z) = C_w \quad Z < 0$$

$$C(Z) = C_1 \quad 0 \le Z < h_1$$

$$C(Z) = C_2(1 - 2g(Z - h_1)/C_2)^{-1/2} \quad Z \ge h_1$$

$$CR_1 = C_1 / C_w$$

$$CR_2 = C_2 / C_1$$

Figure 7. Model 5: Constant-sound-speed layer overlying a pseudo-linear-sound-speed half-space.

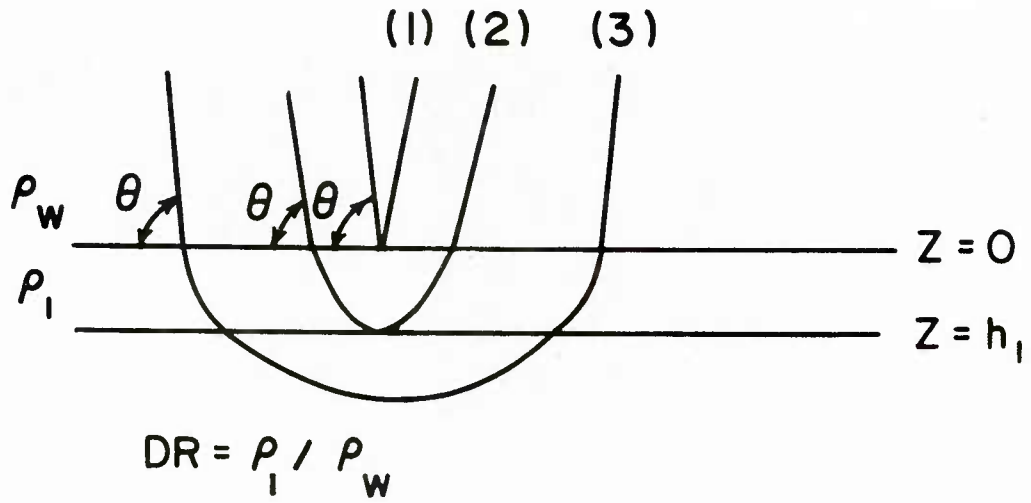

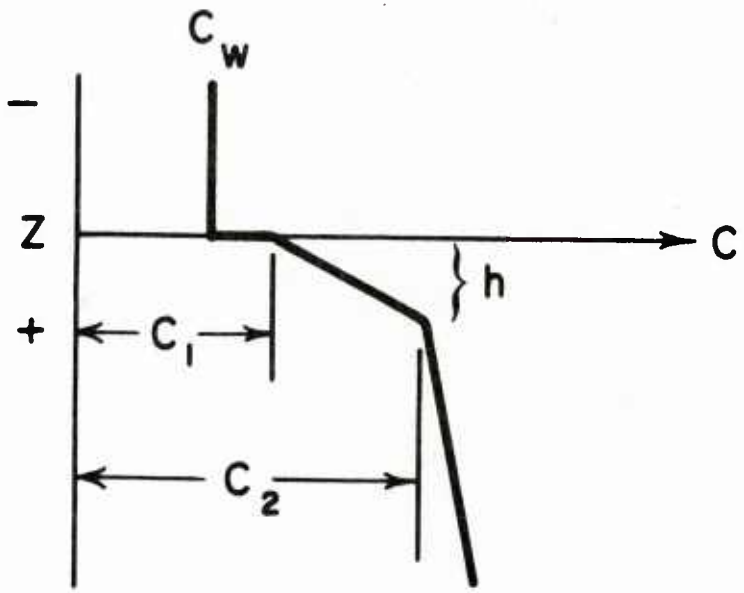

$$C(Z) = C_w \quad Z < 0$$

$$C(Z) = C_1 (1 - 2g_1 Z / C_1)^{-1/2} \quad 0 \leq Z < h_1$$

$$C(Z) = C_2 (1 - 2g_2 (Z - h_1) / C_2)^{-1/2} \quad Z \geq h_1$$

$$CR_1 = C_1 / C_w$$

Figure 8. Model 6: Pseudo-linear-sound-speed layer overlying pseudo-linear-sound-speed half-space.

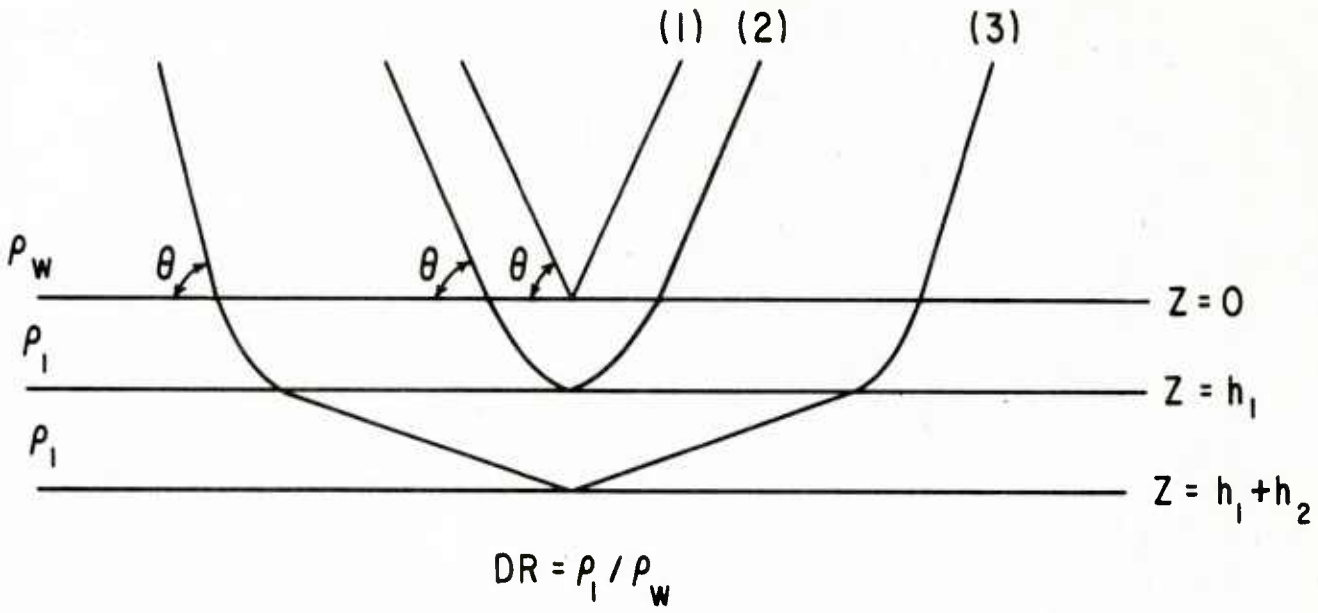

$$DR = \rho_1 / \rho_w$$

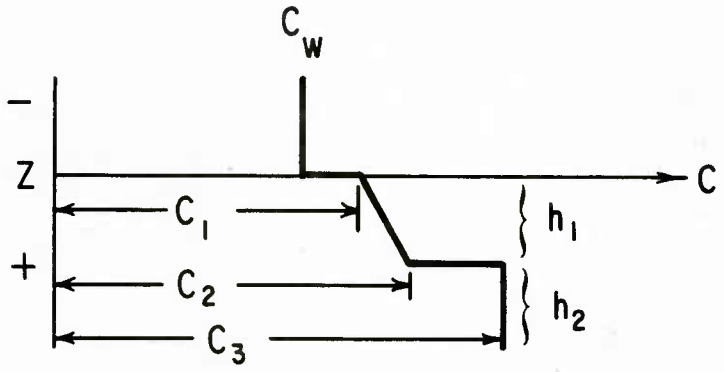

$$C(Z) = C_w \quad Z < 0$$

$$C(Z) = C_1 (1 - 2gZ/C_1)^{-1/2} \qquad 0 \le Z < h_1$$

$$C(Z) = C_3 \qquad h_1 \le Z < h_1 + h_2$$

$$CR_1 = C_1 / C_w \qquad CR_2 = C_3 / C_2 \qquad C_2 = C_1 (1 - 2gh_1 / C_1)^{-1/2}$$

Figure 9. Model 7: Pseudo-linear-sound-speed layer overlying a constant-sound-speed layer, overlying a half-space with reflection coefficient R = i.

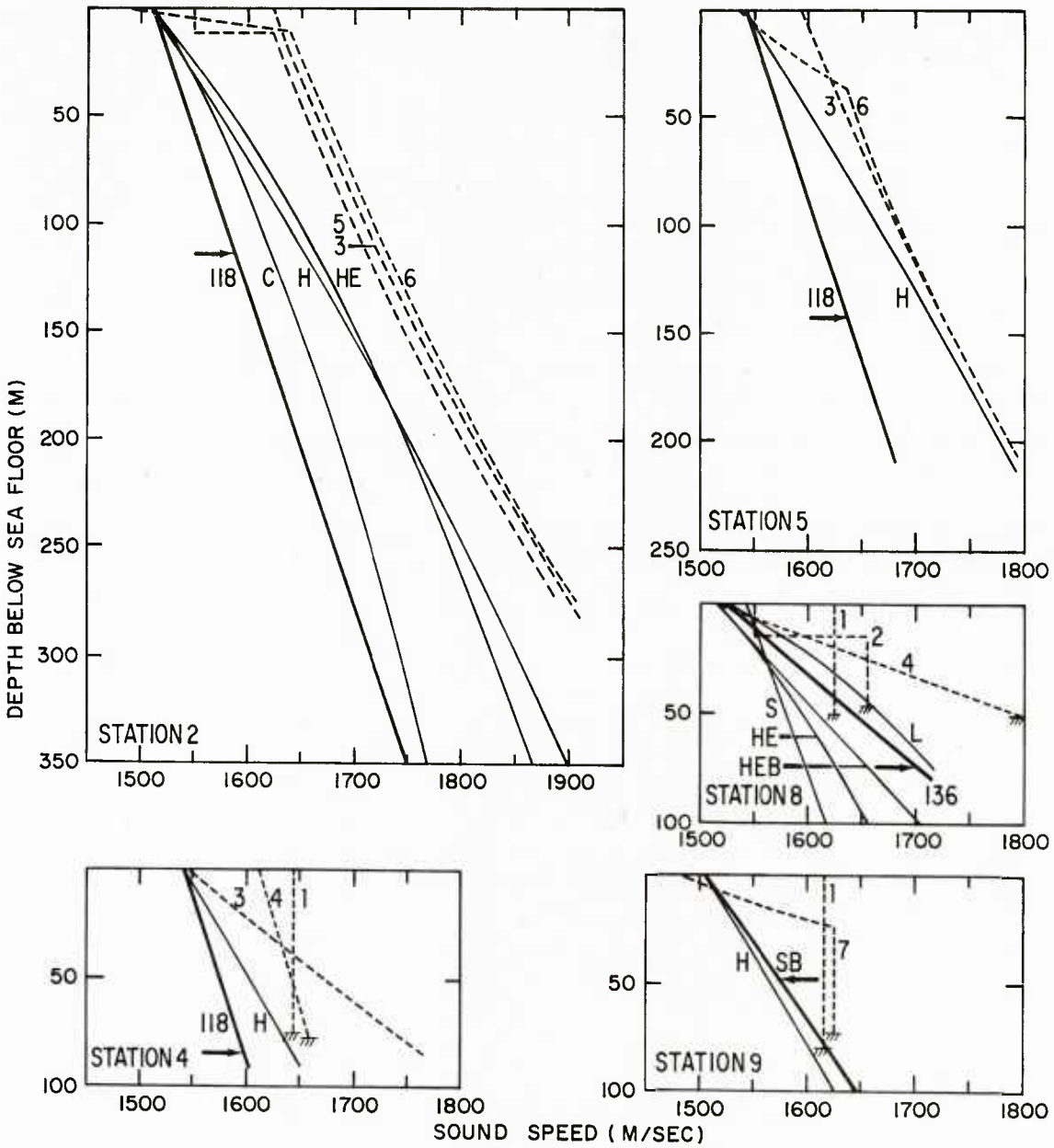

Figure 10. Predicted sound-speed profiles in sediments at each station. Solid lines represent models derived from geological/geophysical analyses and are discussed in Appendices C and E where: C = Cernock (50); H = Hamilton et al. (51); HE = Houtz and Ewing (39); HEB = Houtz, Ewing, and Buhl (60); L = modified after Laughton (40); S = based on surficial sediment data from Hamilton (82); SB = sonobuoy data from this report; 118 = based on DSDP Site 118 data (49); and 136 = based on DSDP Site 136 data (59). The arrow indicates the choice of profile based on geological considerations. Dashed lines represent models derived from acoustical analyses, with numbers corresponding to models in Figures 3-9. Hatch marks indicate an impenetrable interface.

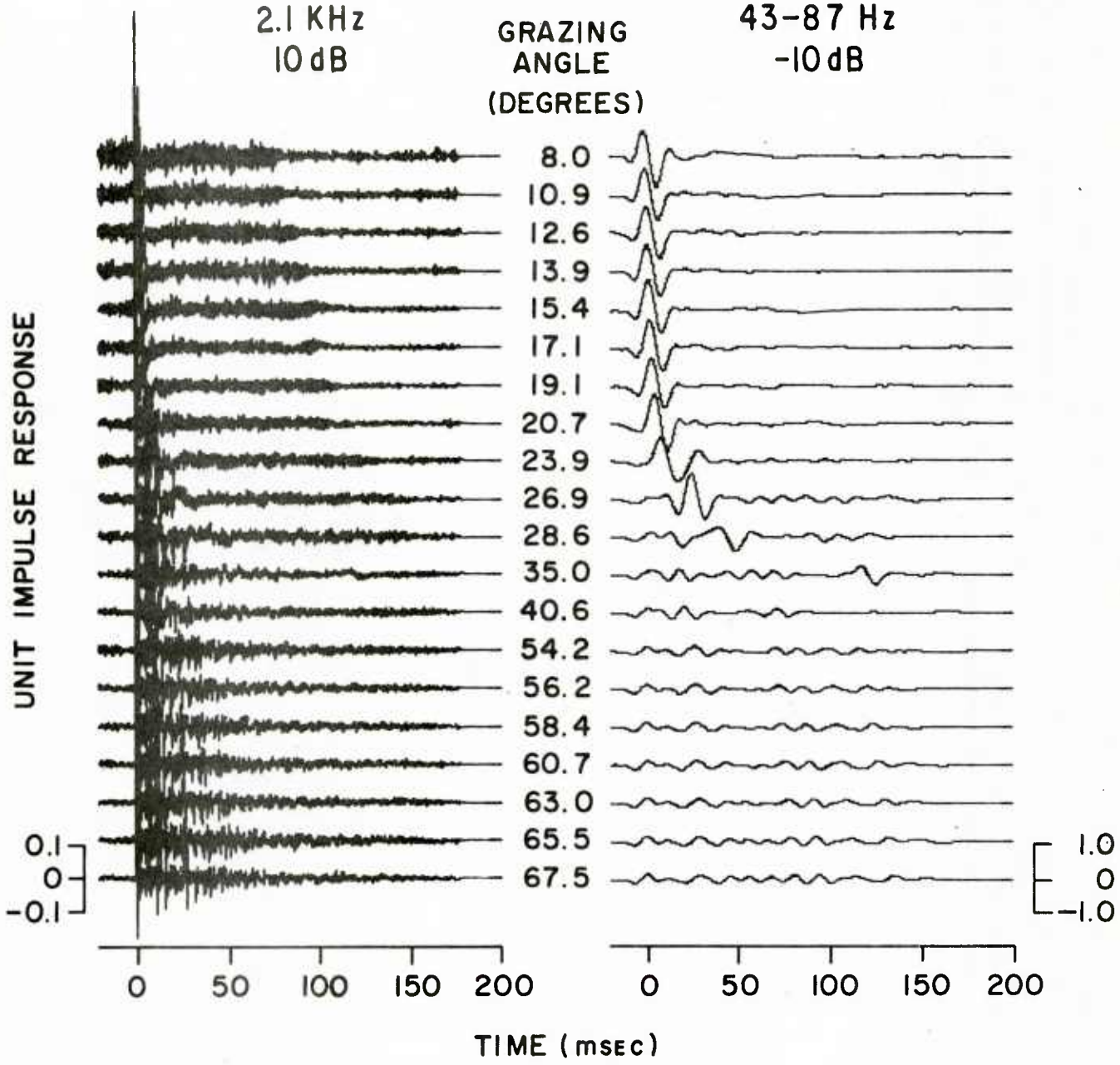

Figure 11. Station 2 impulse responses.

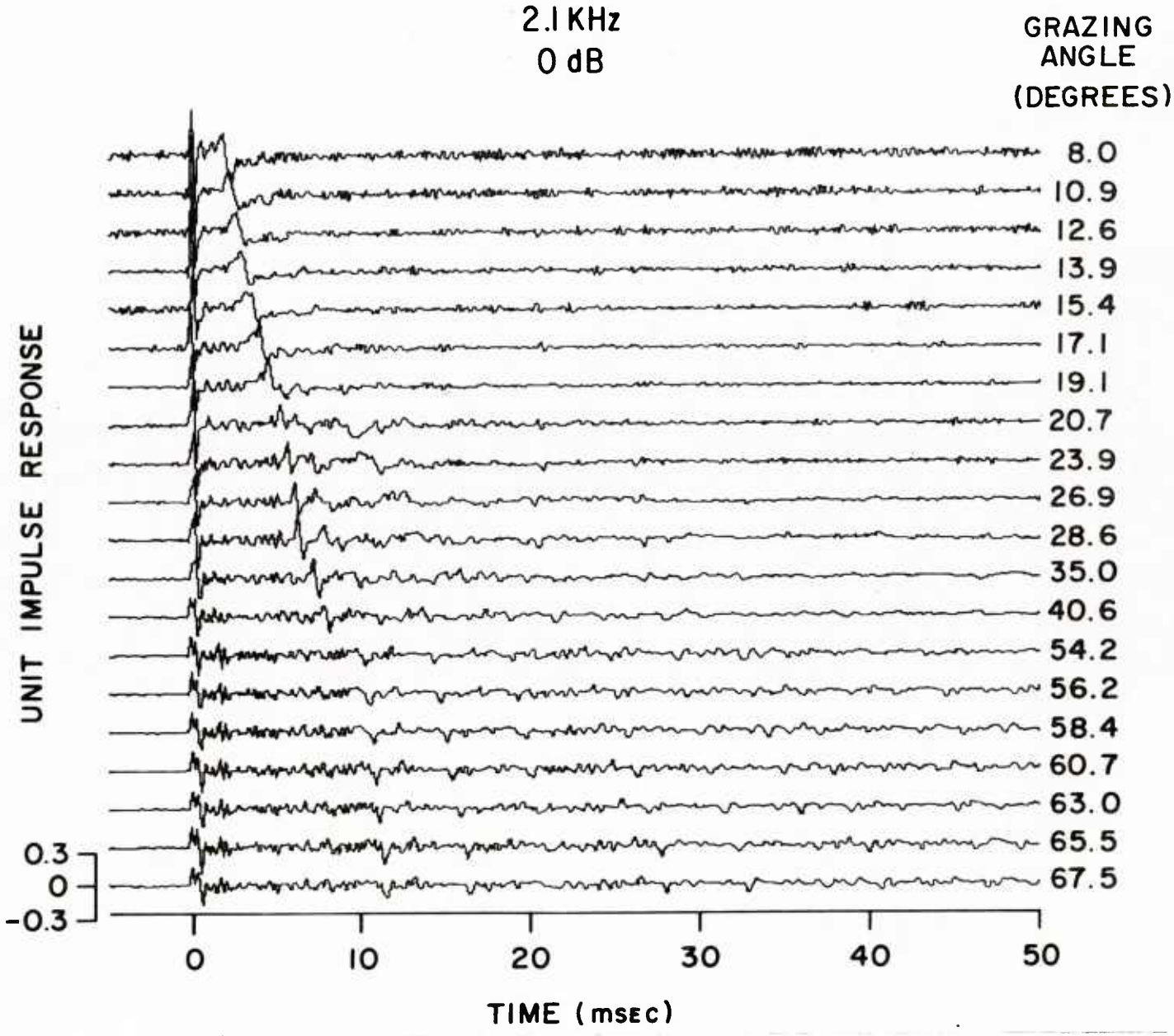

Figure 12. Station 2 impulse responses on expanded time axis.

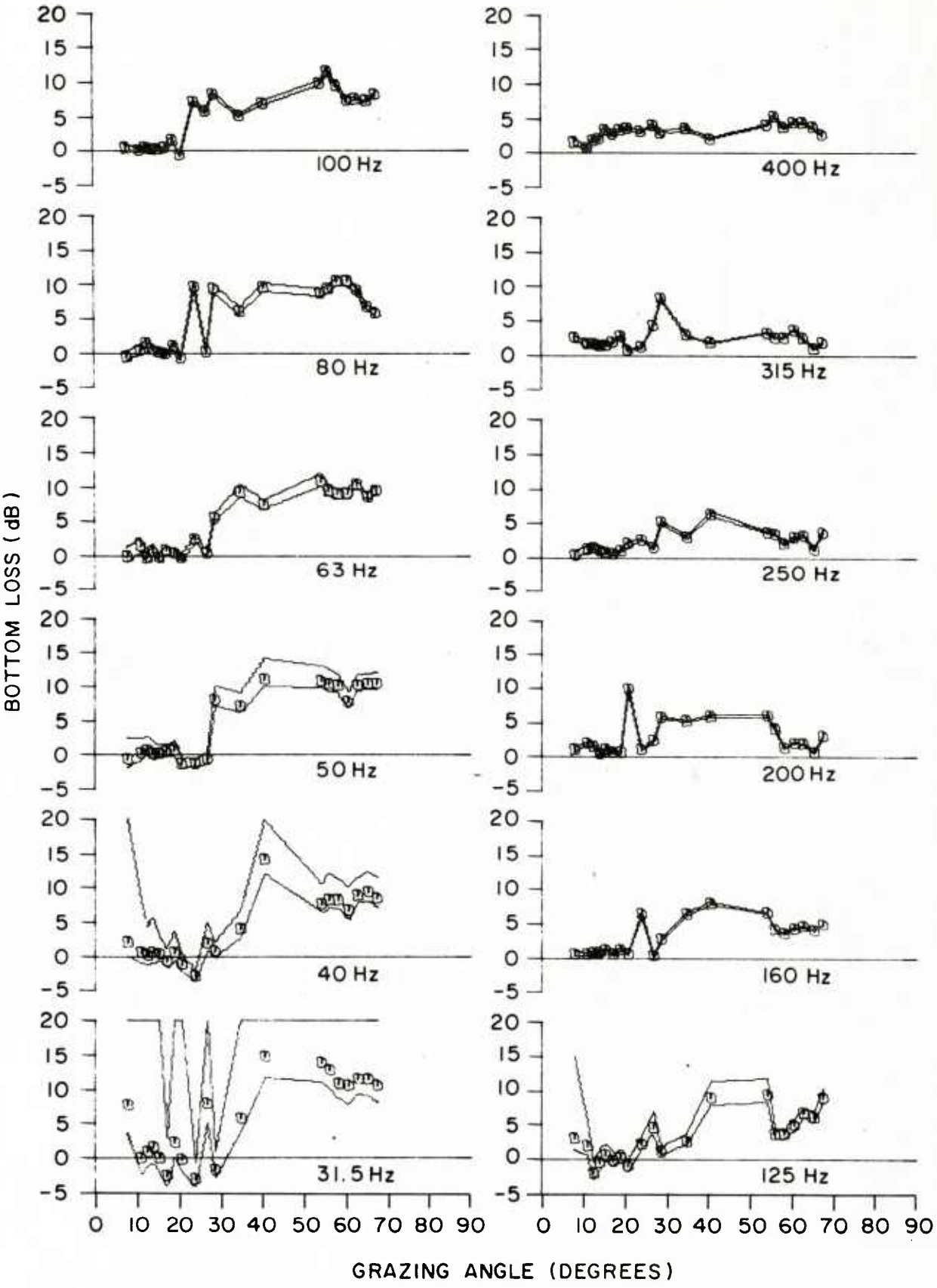

Figure 13. Station 2 one-third-octave bottom-loss curves.

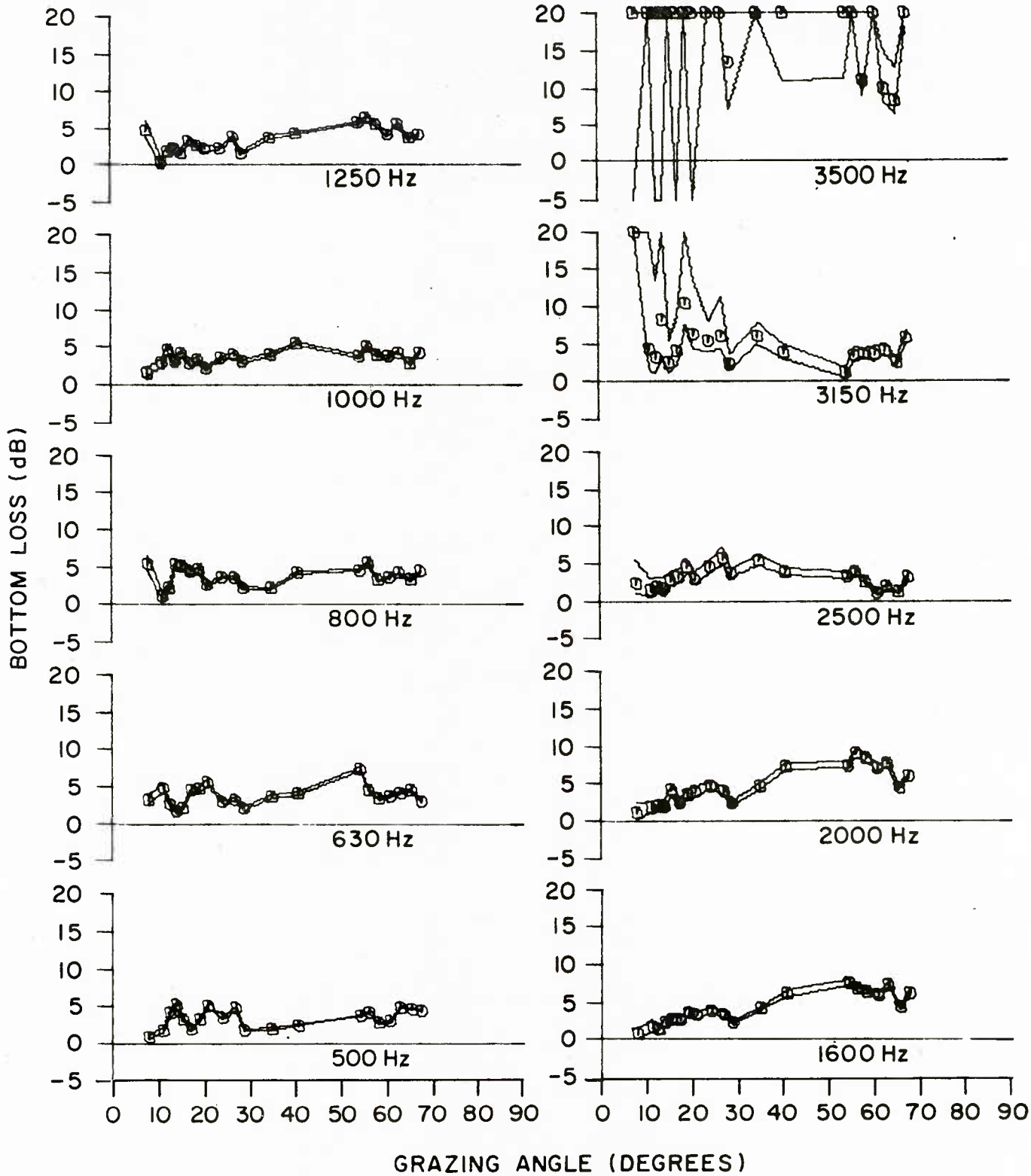

Figure 14. Station 2 one-third-octave bottom-loss curves.

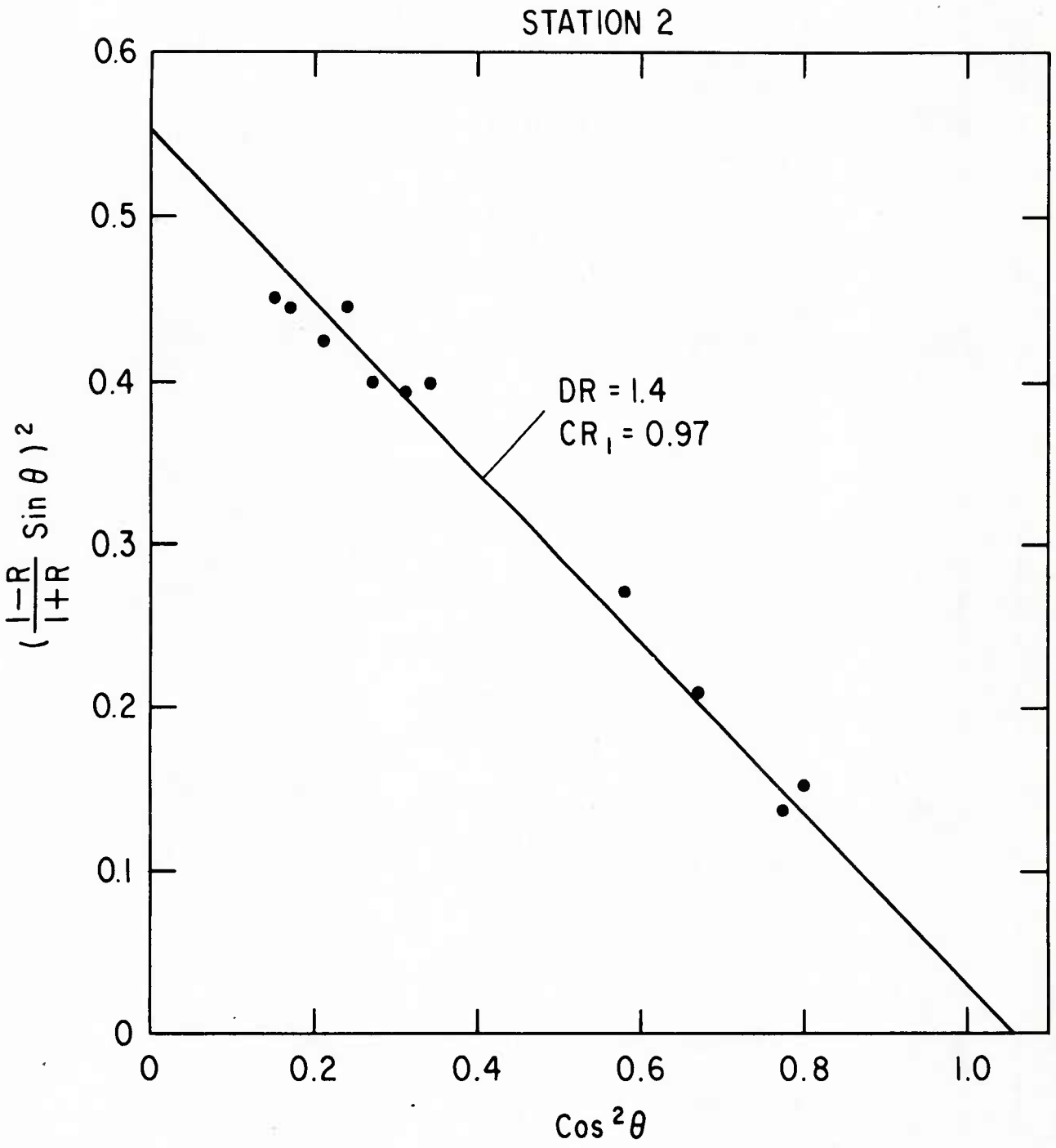

Figure 15. Station 2 Rayleigh-equation analysis.

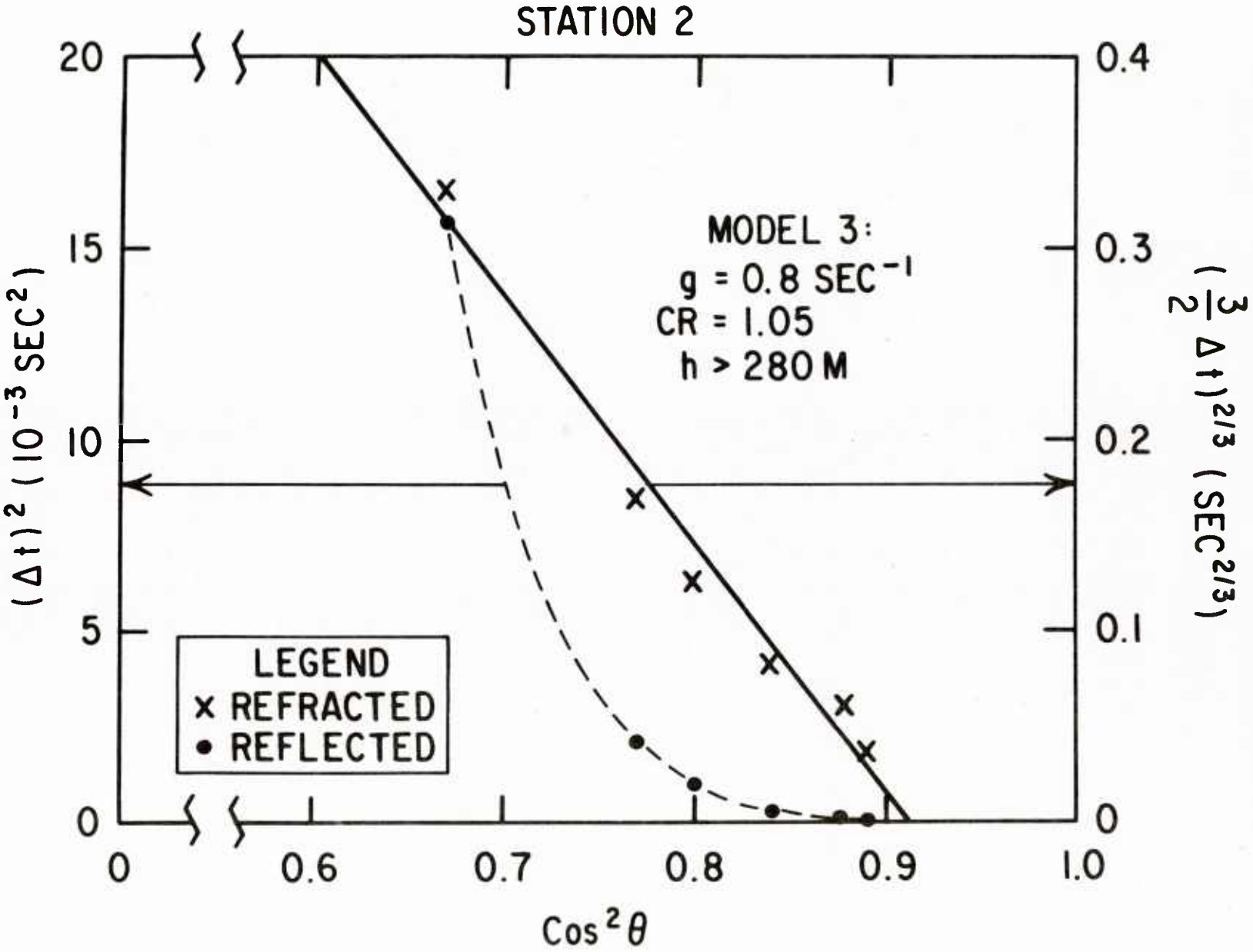

Figure 16. Station 2 model 3 analysis.

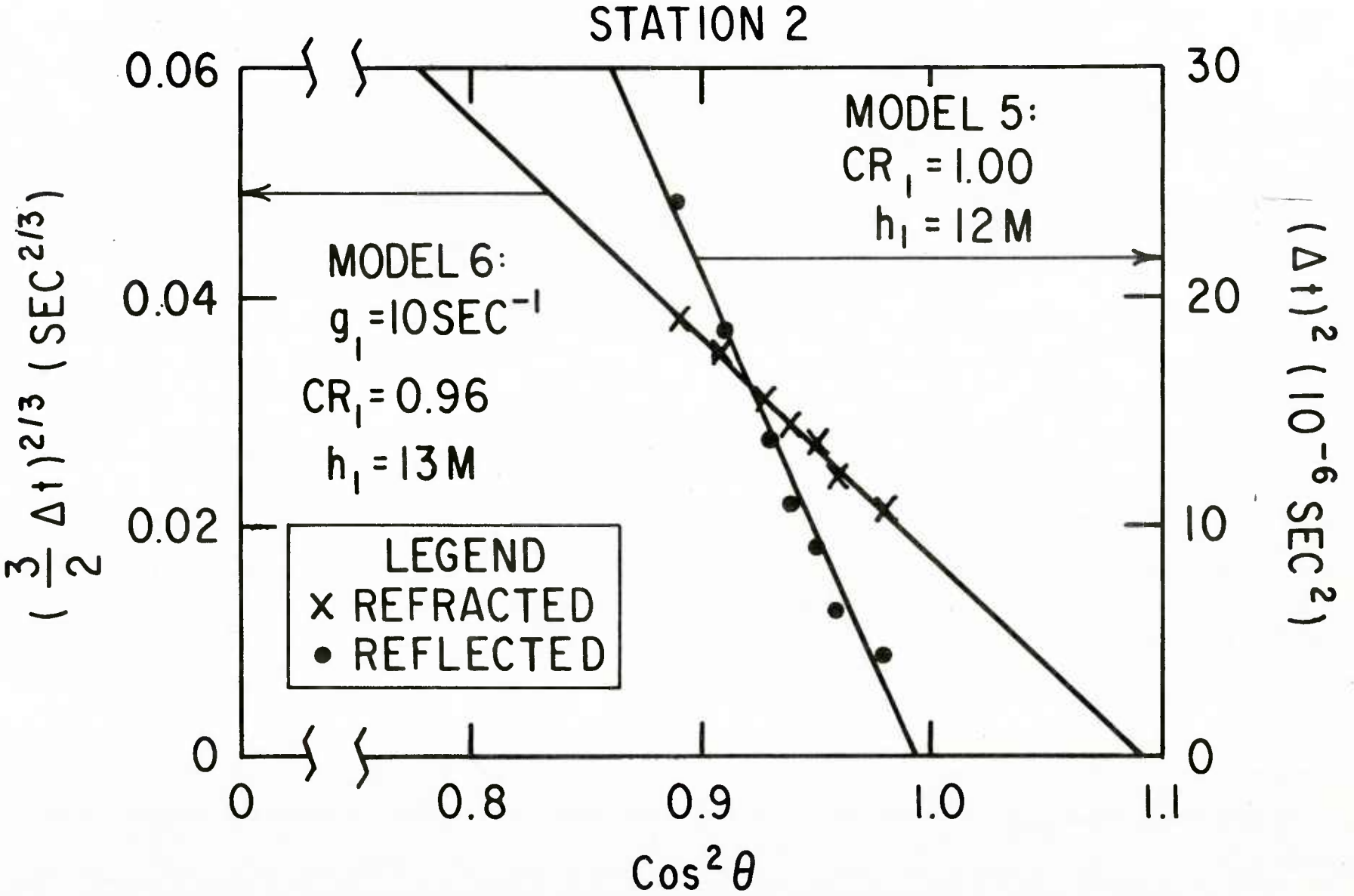

Figure 17. Station 2 models 5 and 6 analysis (upper layer).

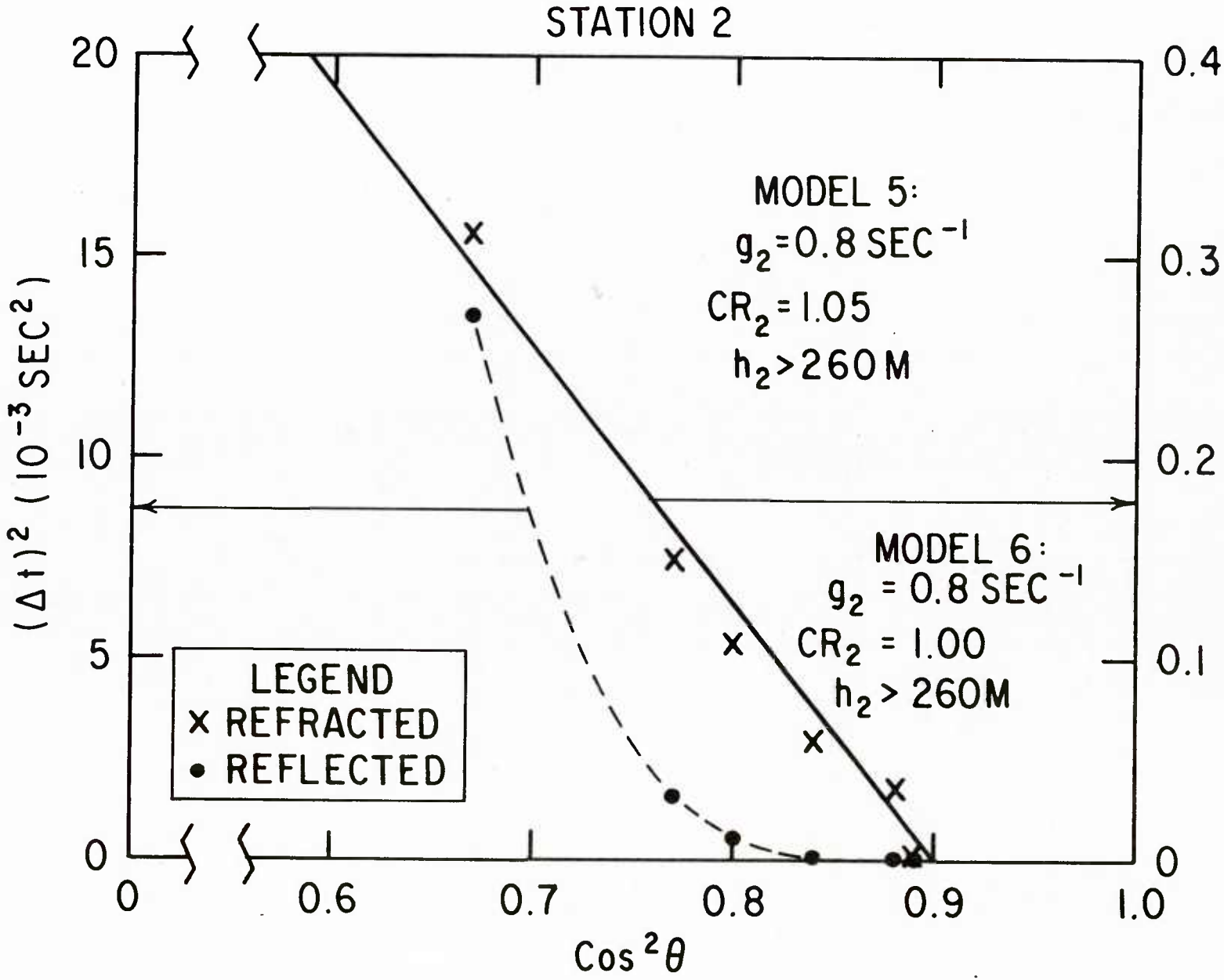

Figure 18. Station 2 models 5 and 6 analysis (deeper layer).

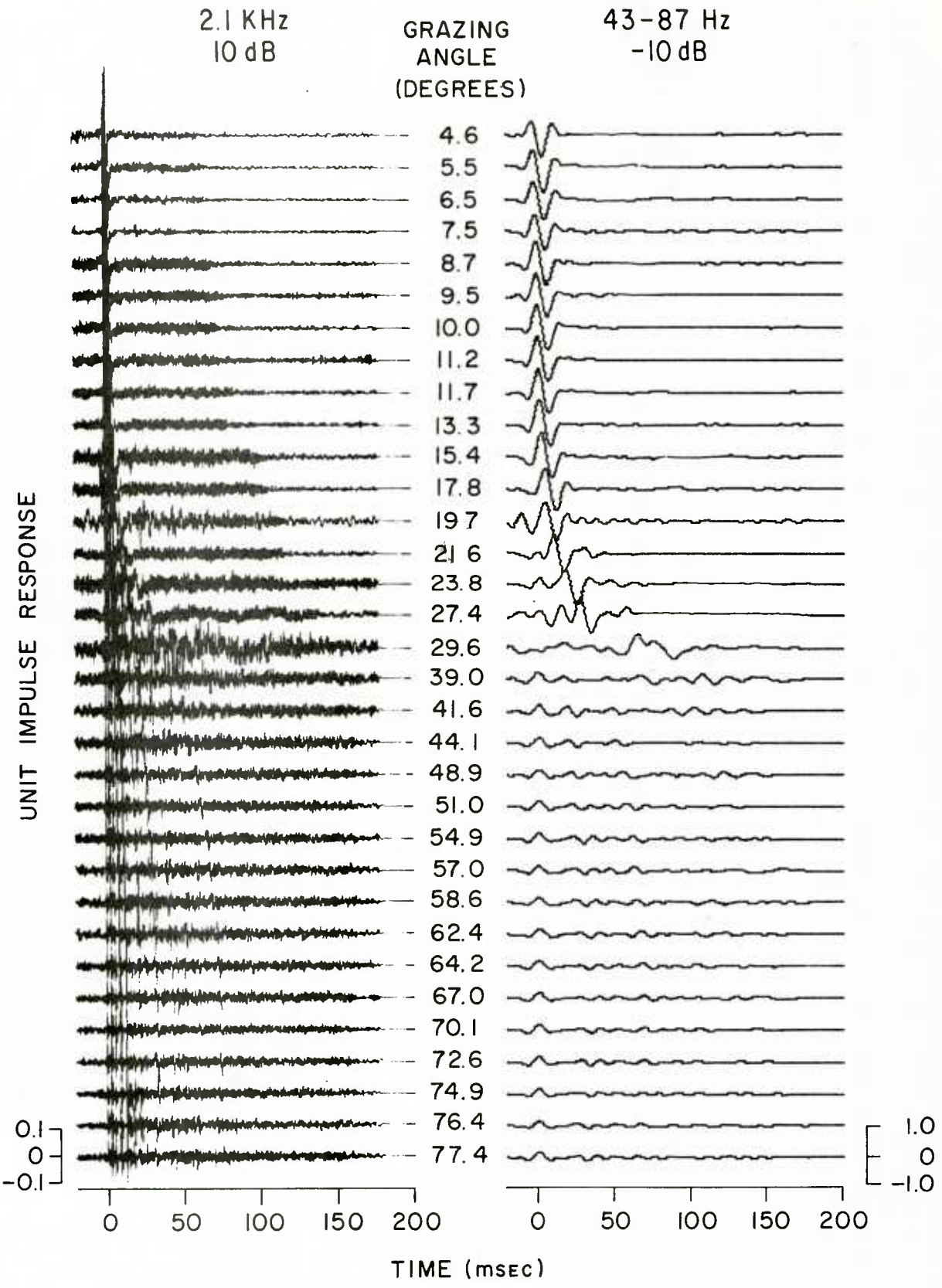

Figure 19. Station 4 impulse responses.

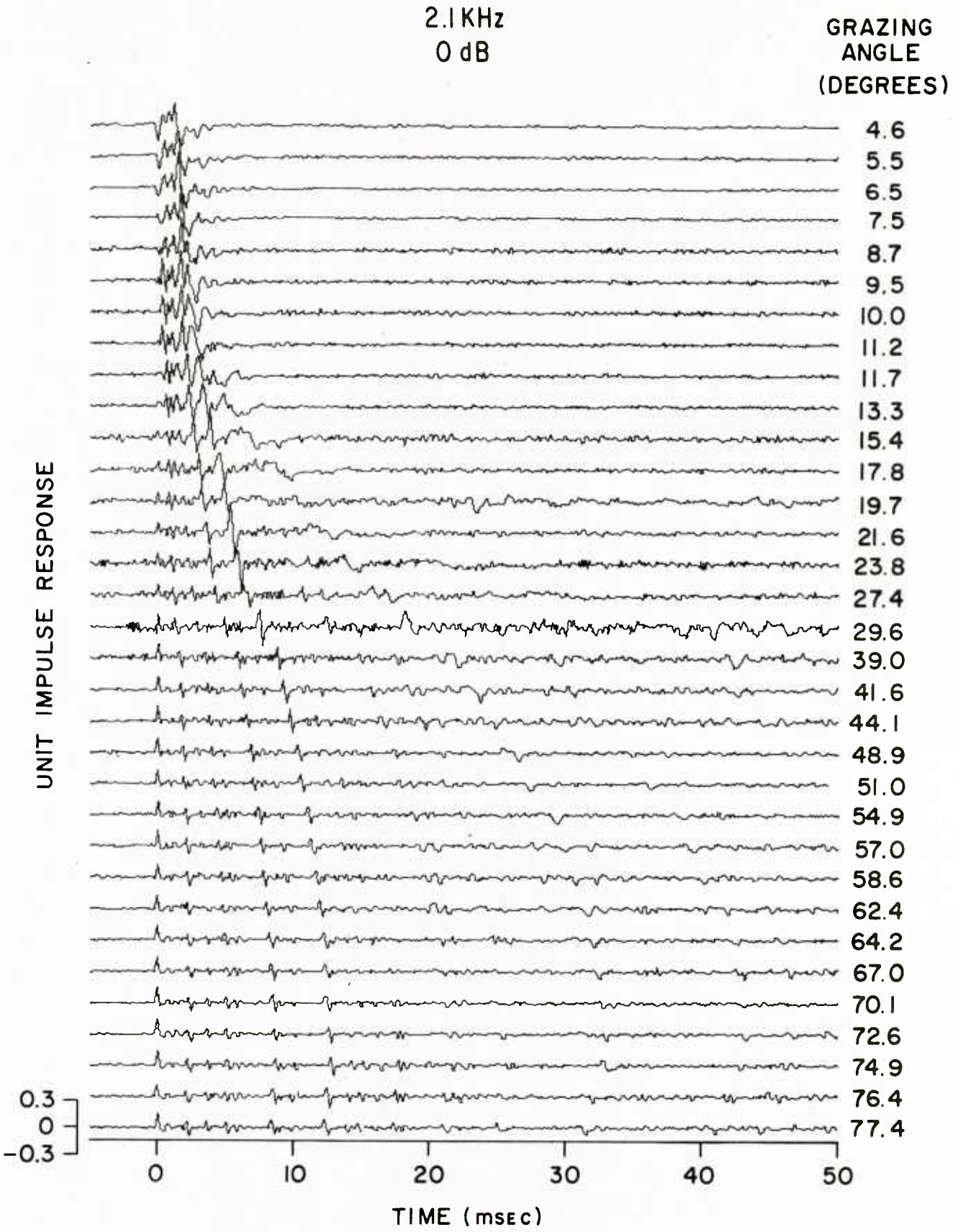

Figure 20. Station 4 impulse responses on expanded time axis.

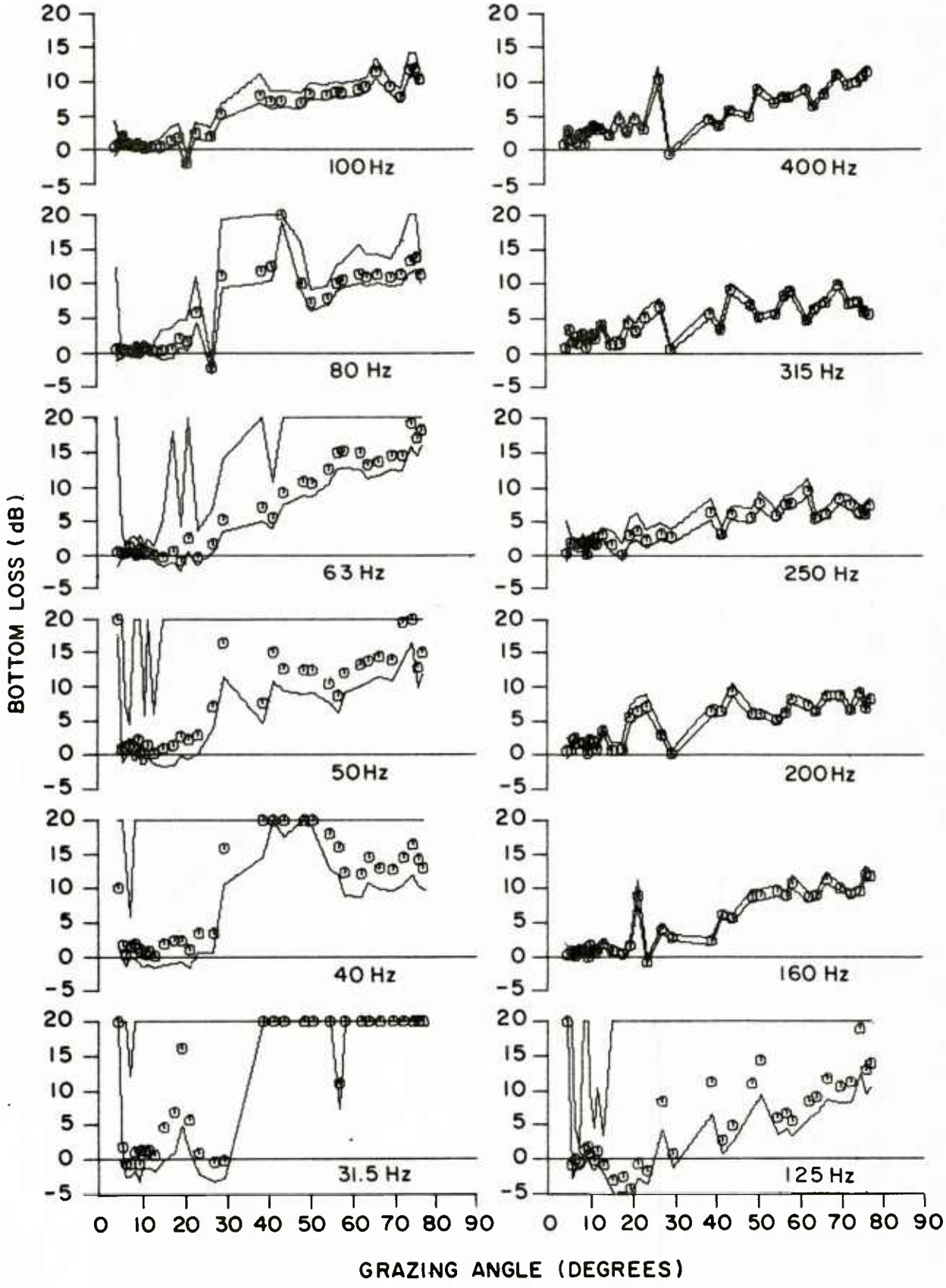

Figure 21. Station 4 one-third-octave bottom-loss curves.

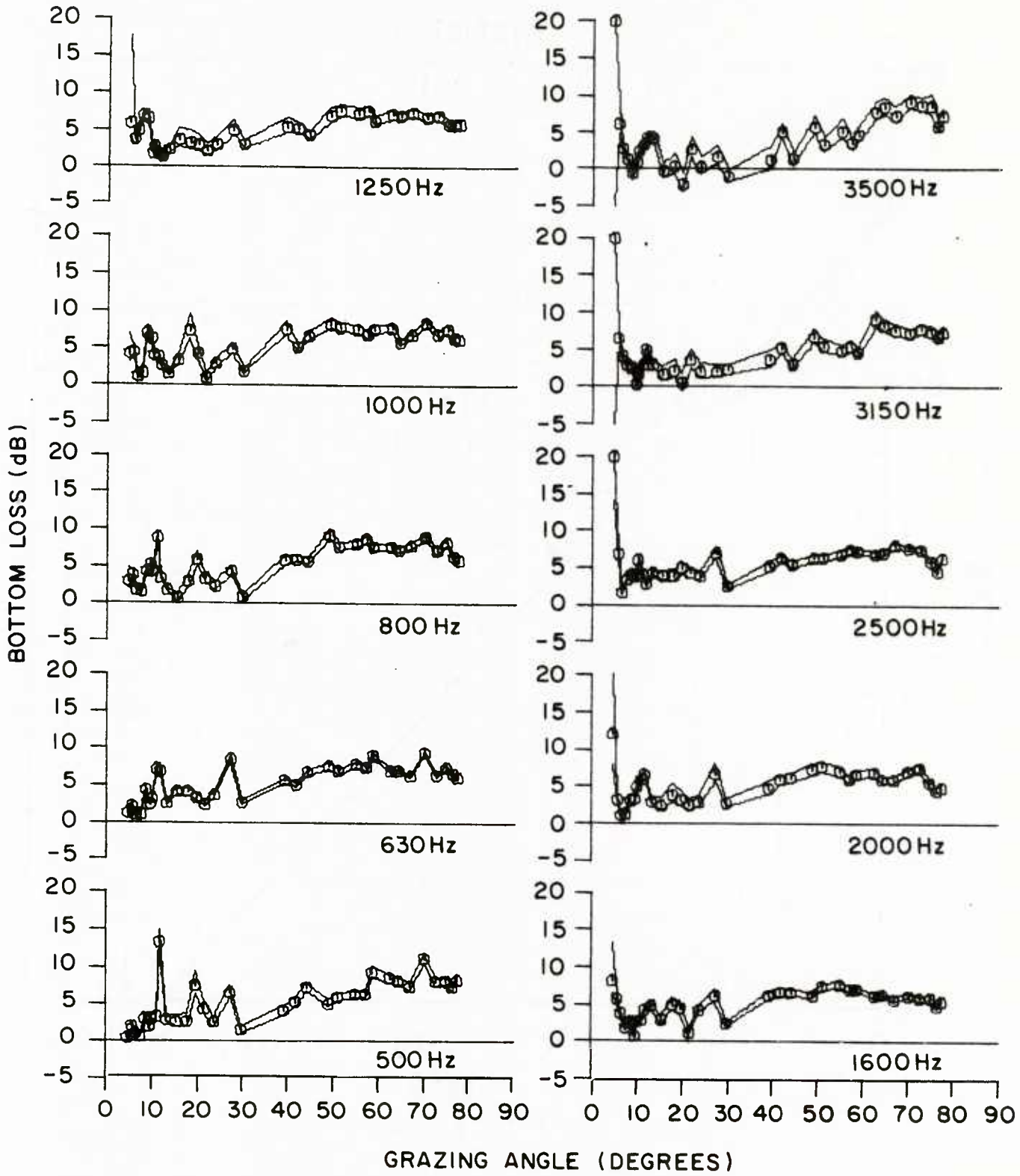

Figure 22. Station 4 one-third-octave bottom-loss curves.

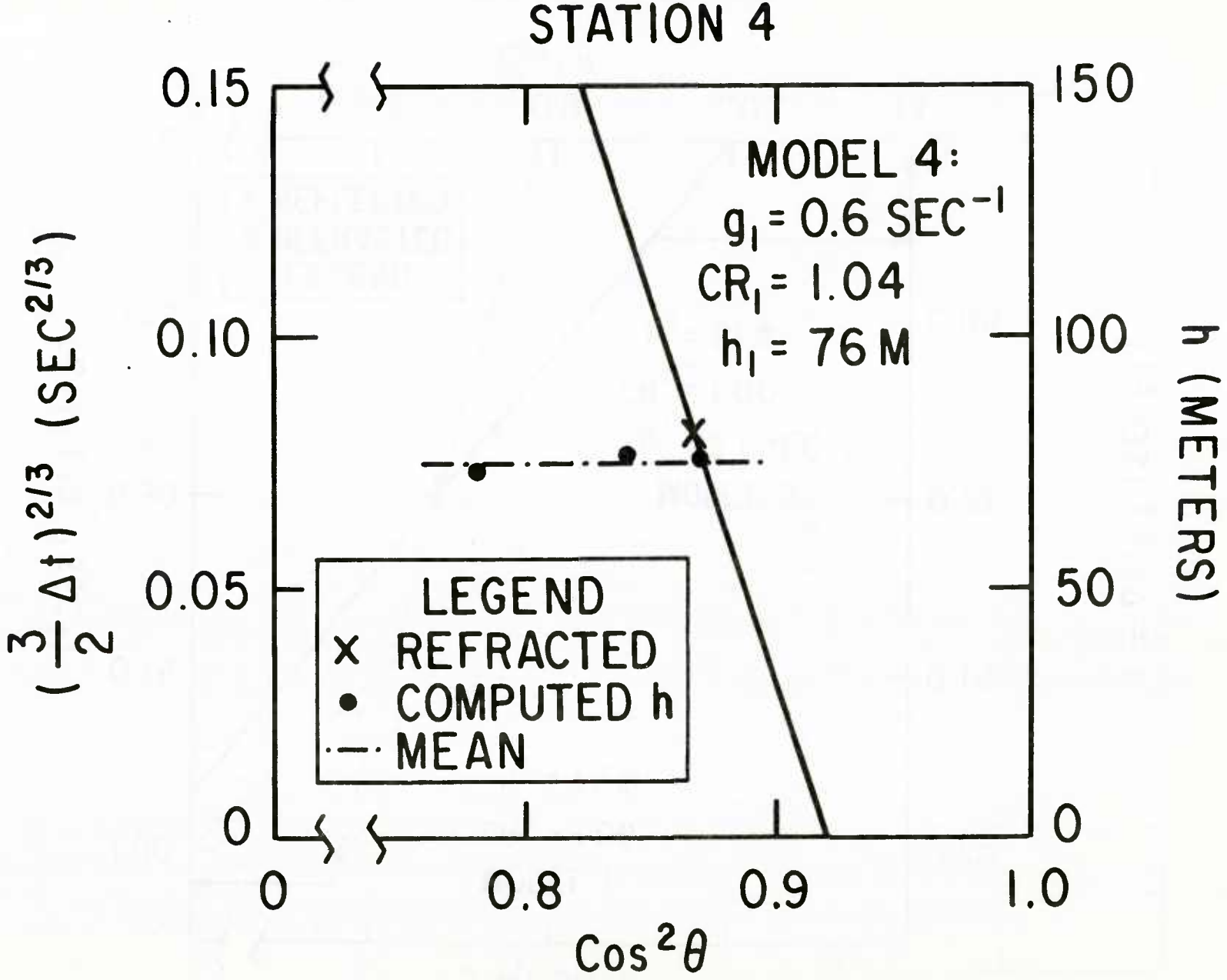

Figure 25. Station 4 model 4 analysis.

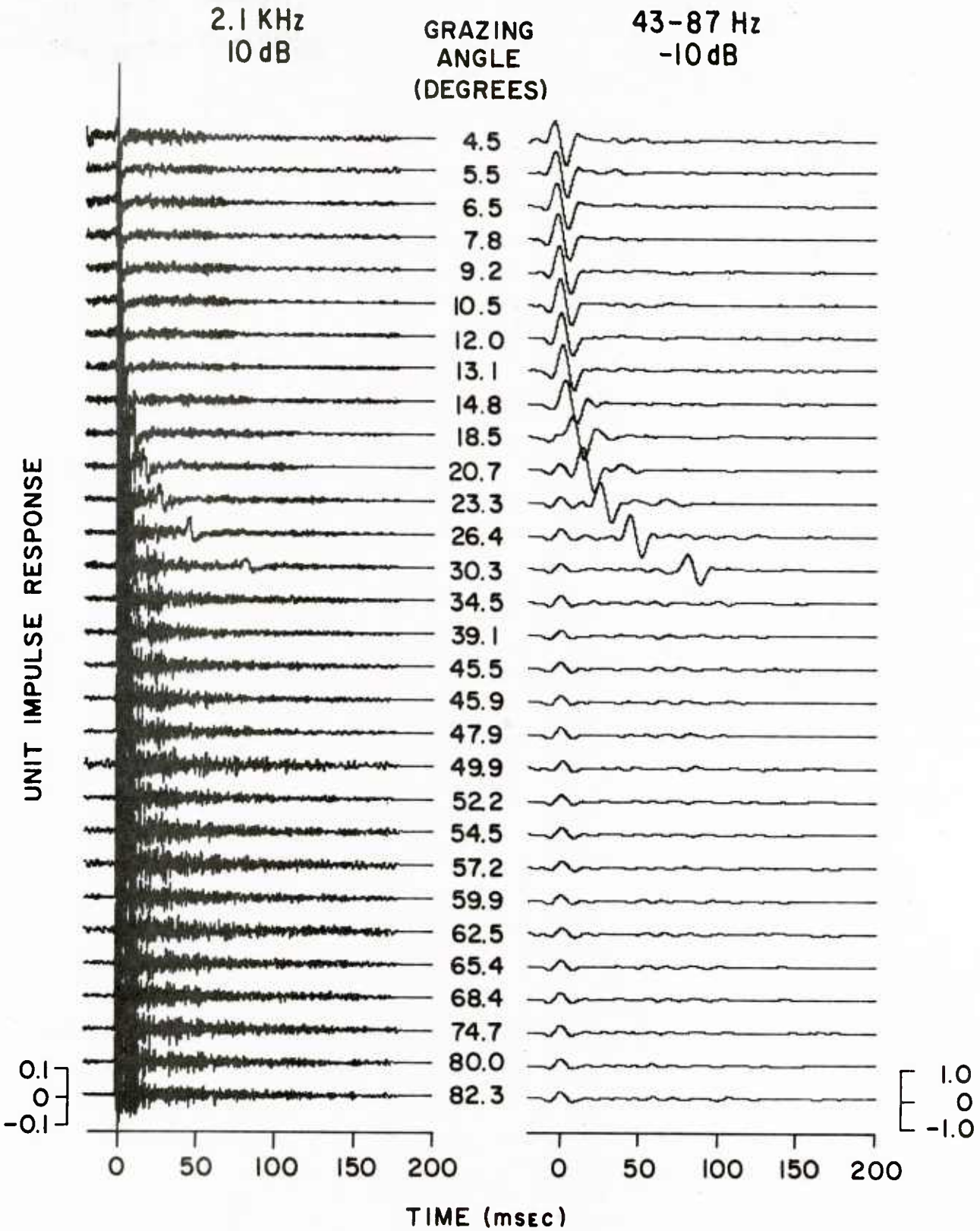

Figure 26. Station 5 impulse responses.

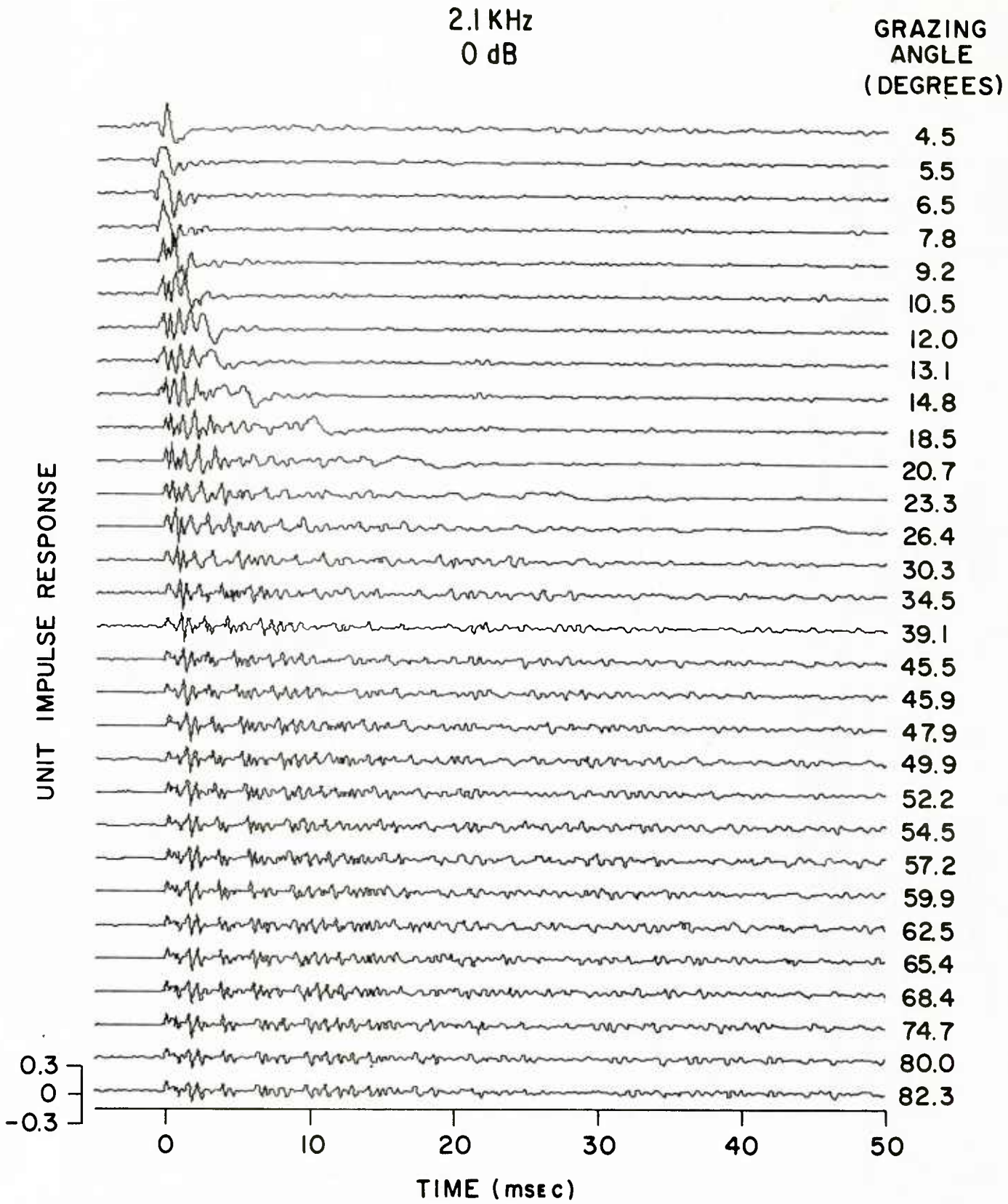

Figure 27. Station 5 impulse responses on expanded time axis.

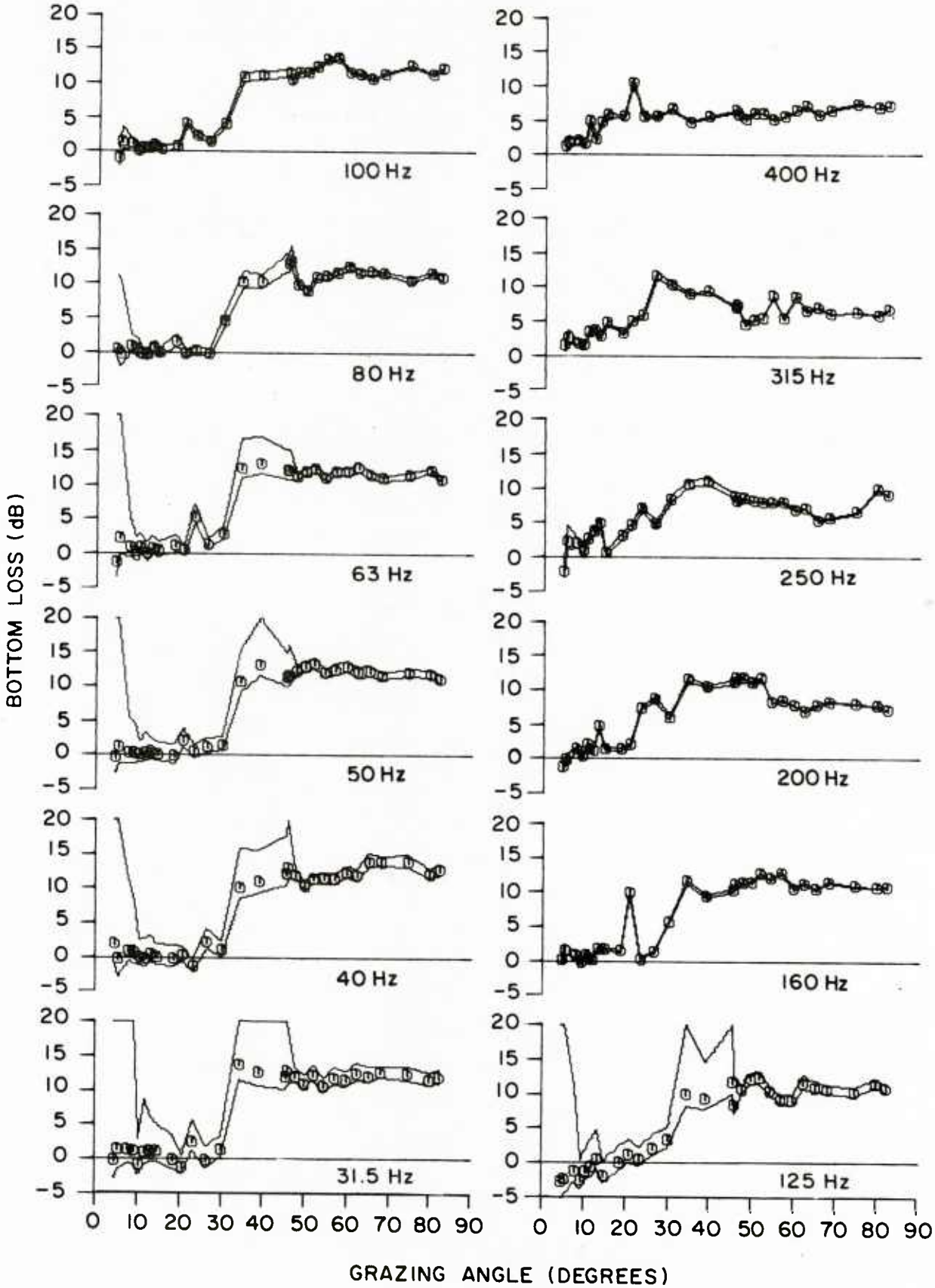

Figure 28. Station 5 one-third-octave bottom-loss curves.

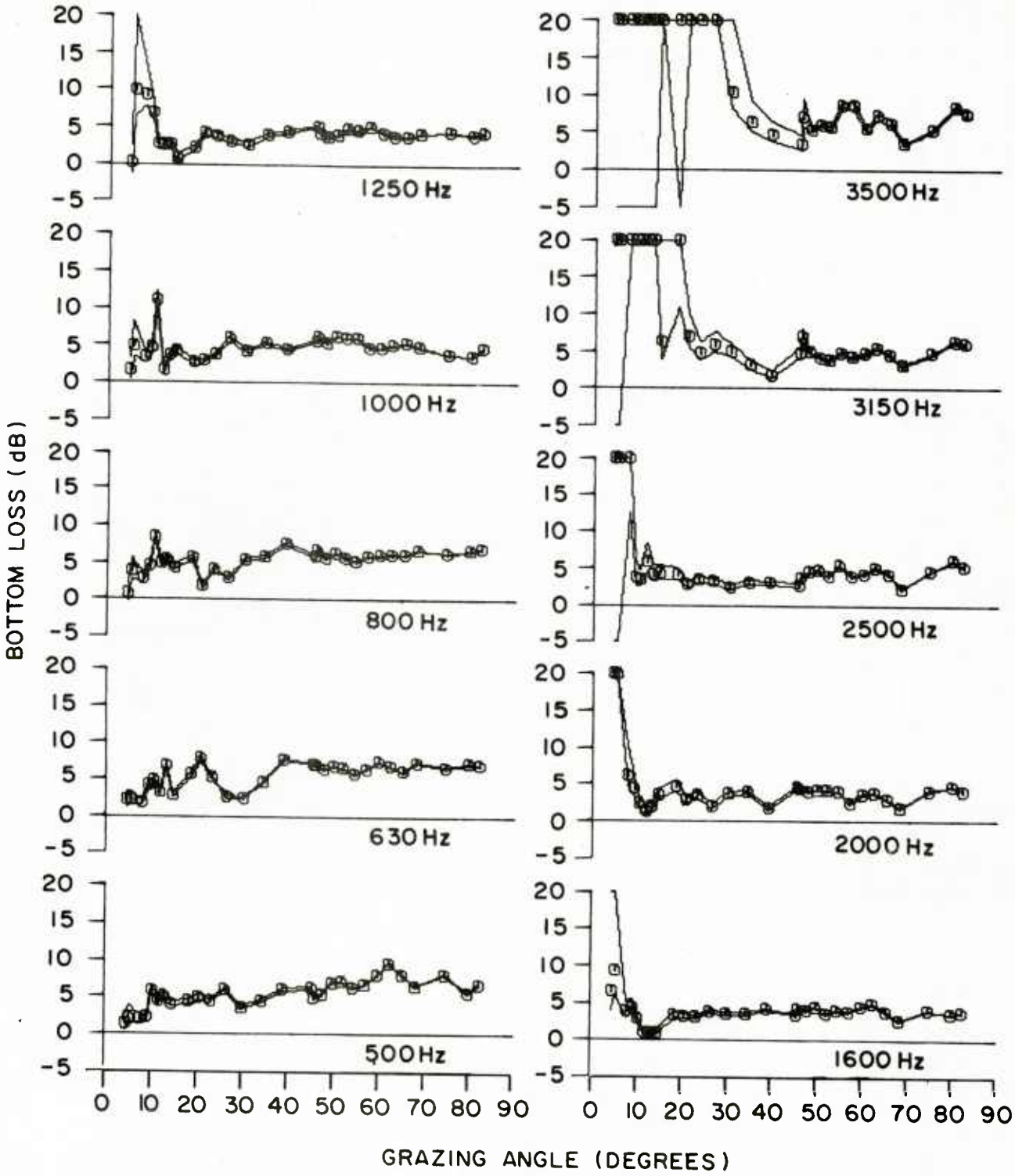

Figure 29. Station 5 one-third-octave bottom-loss curves.

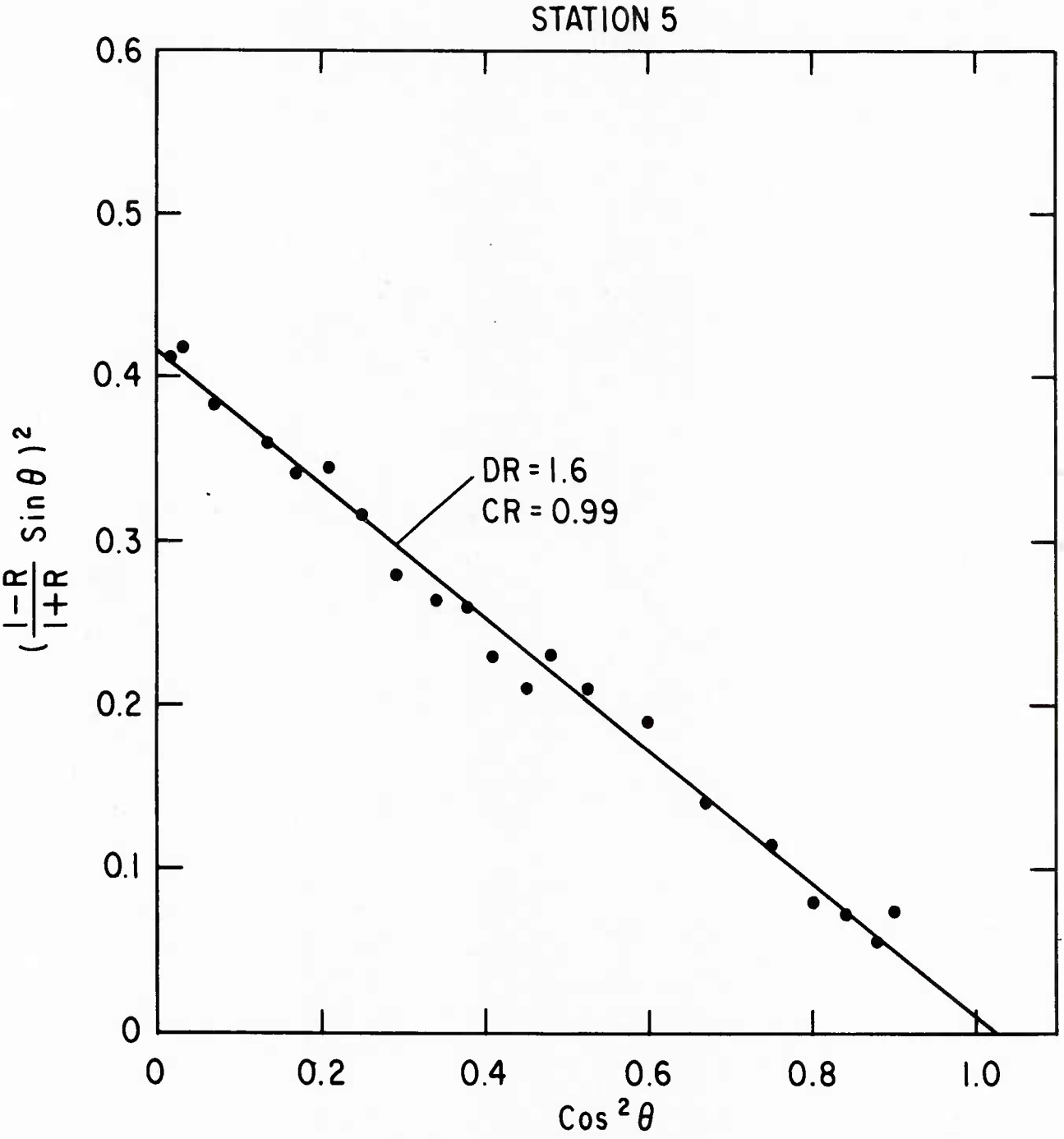

Figure 30. Station 5 Rayleigh-equation analysis.

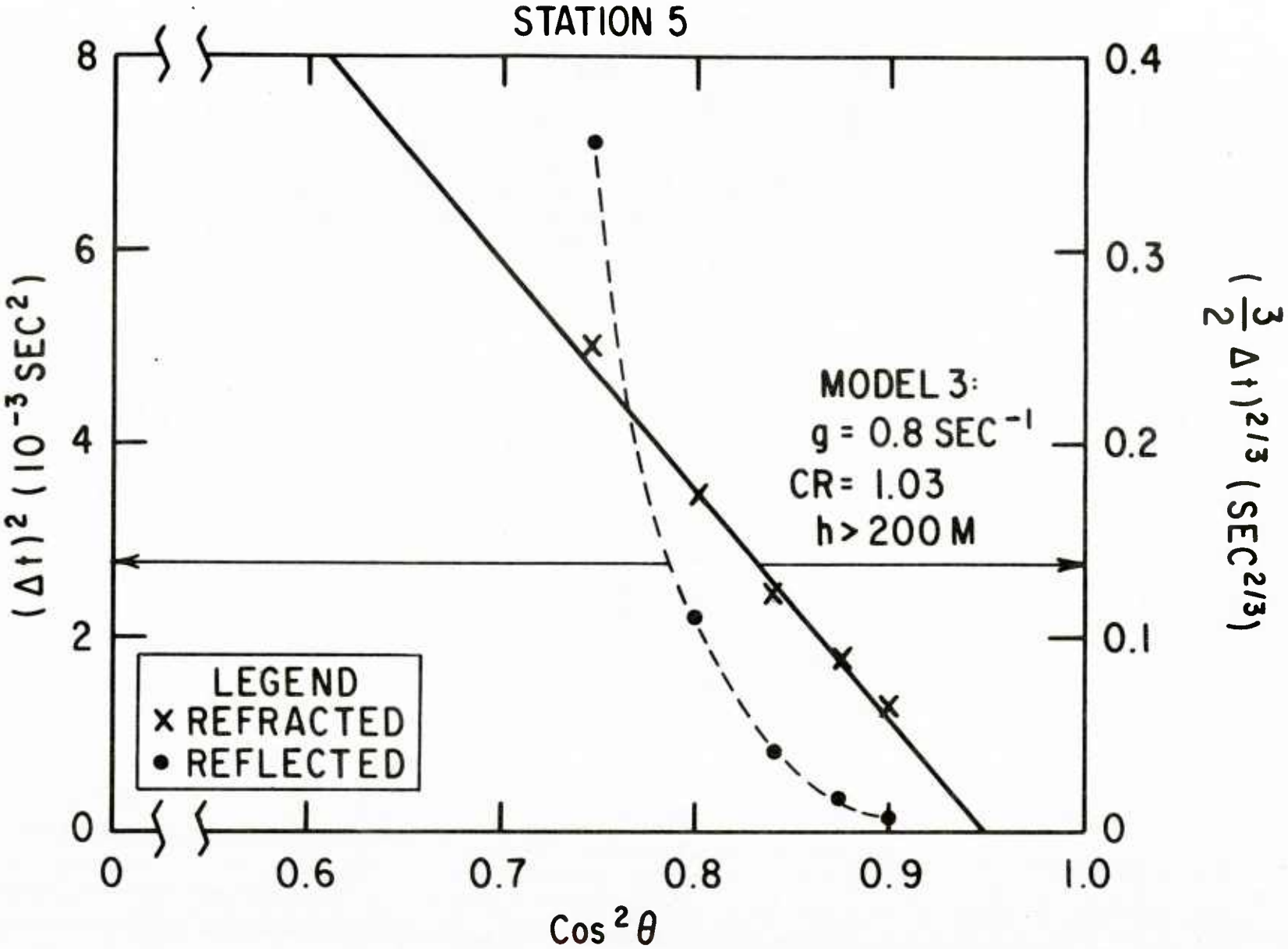

Figure 31. Station 5 model 3 analysis.

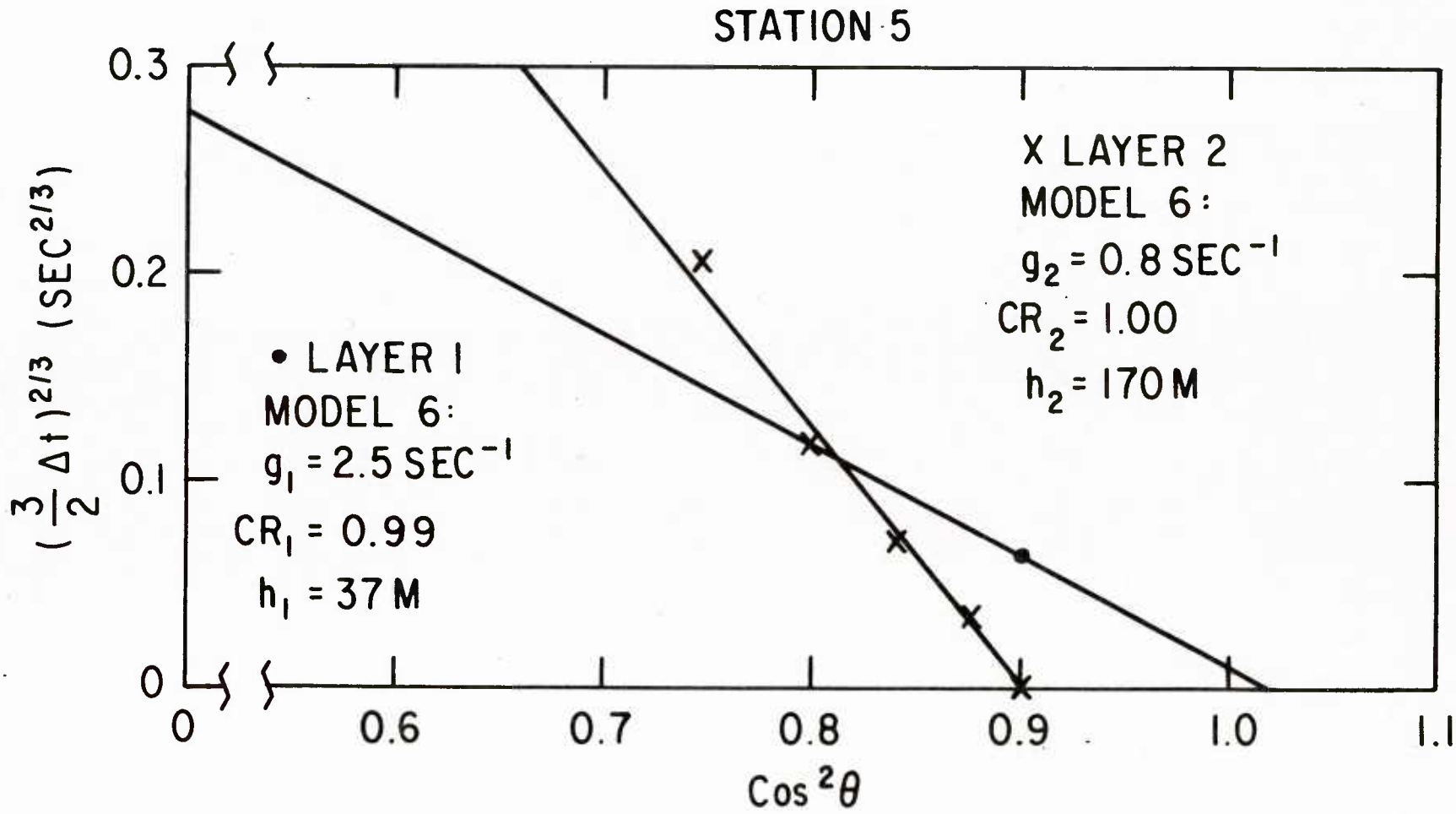

Figure 32. Station 5 model 6 analysis.

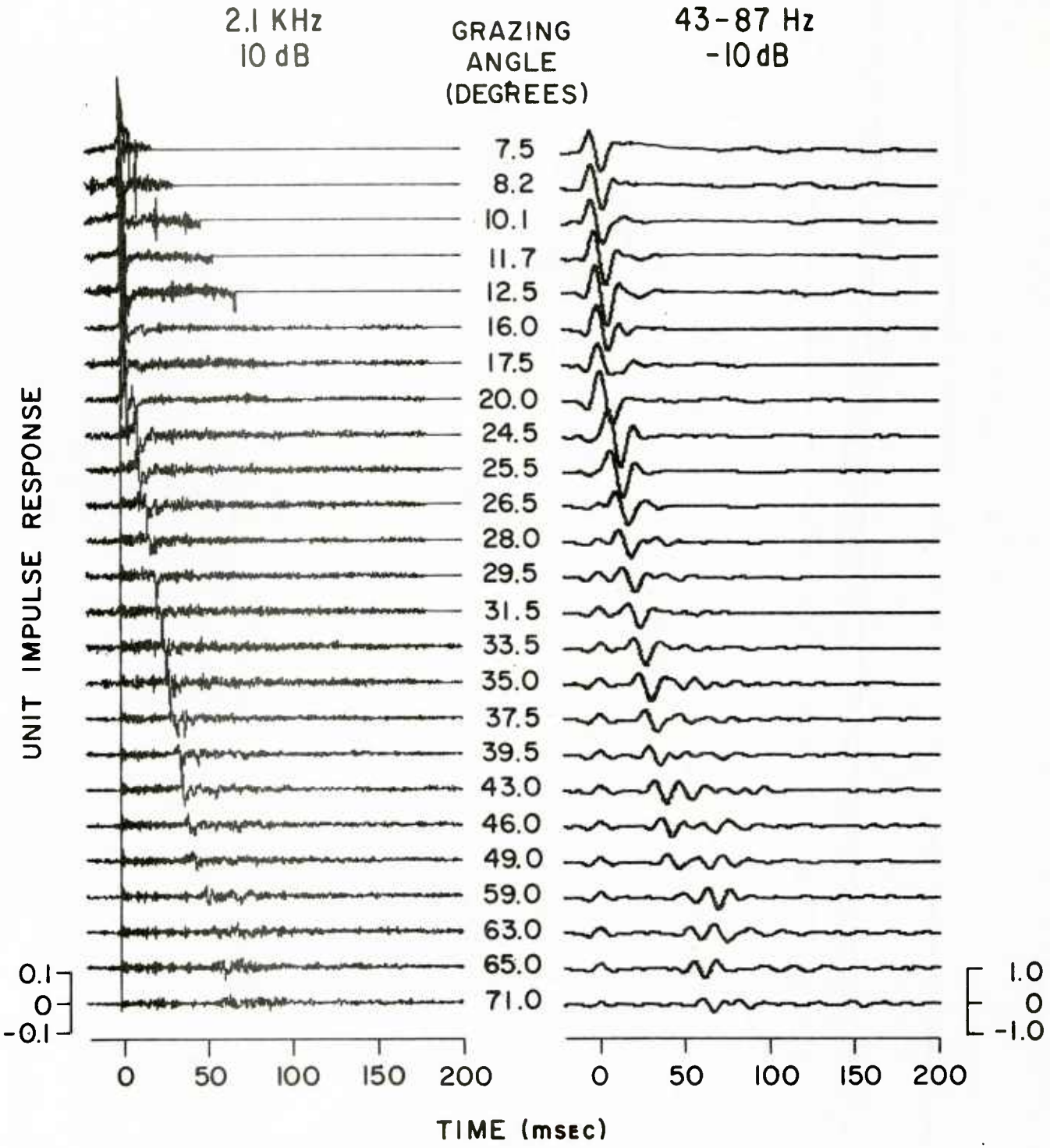

Figure 33. Station 8 impulse responses.

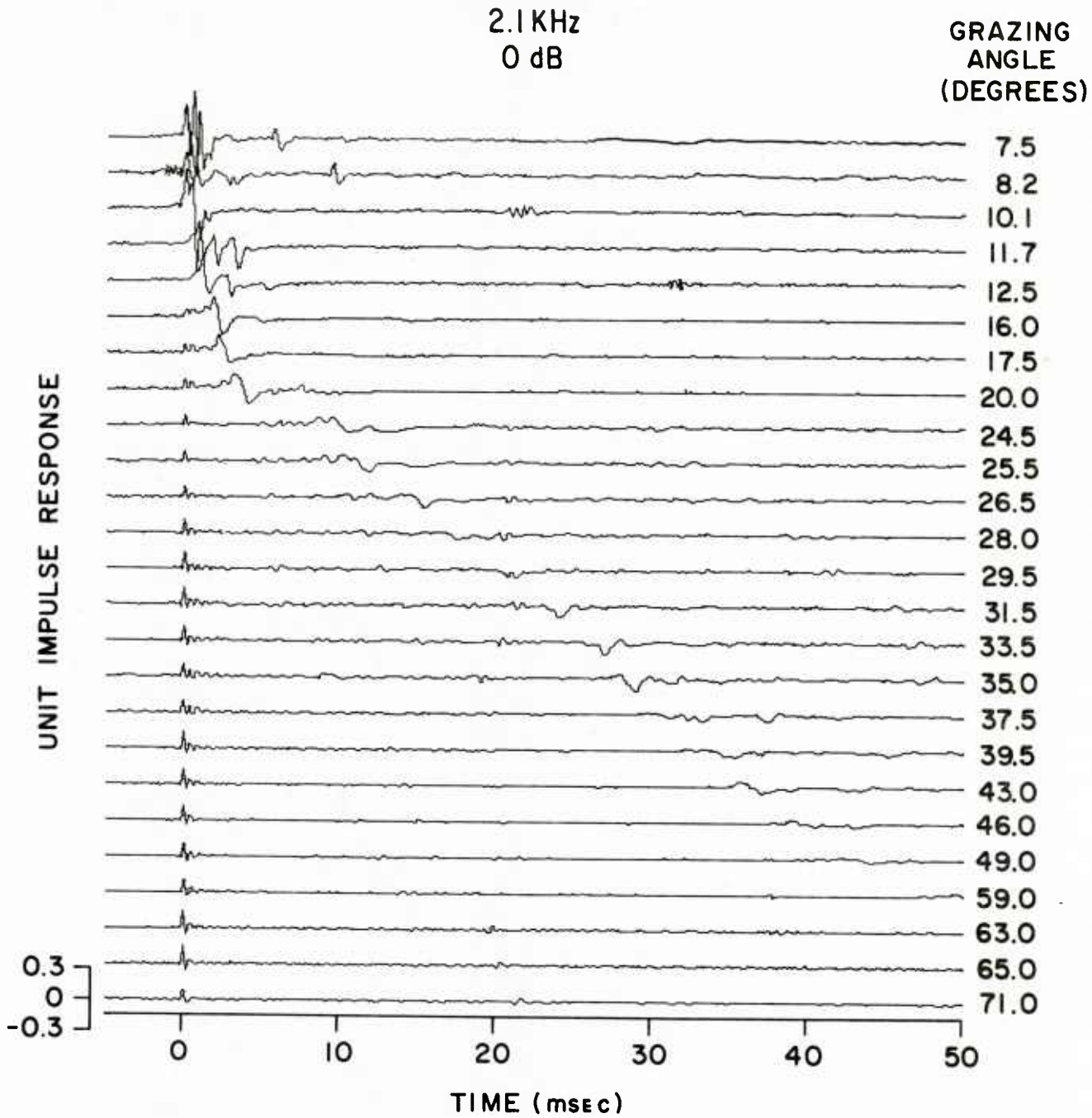

Figure 34. Station 8 impulse responses on expanded time axis.

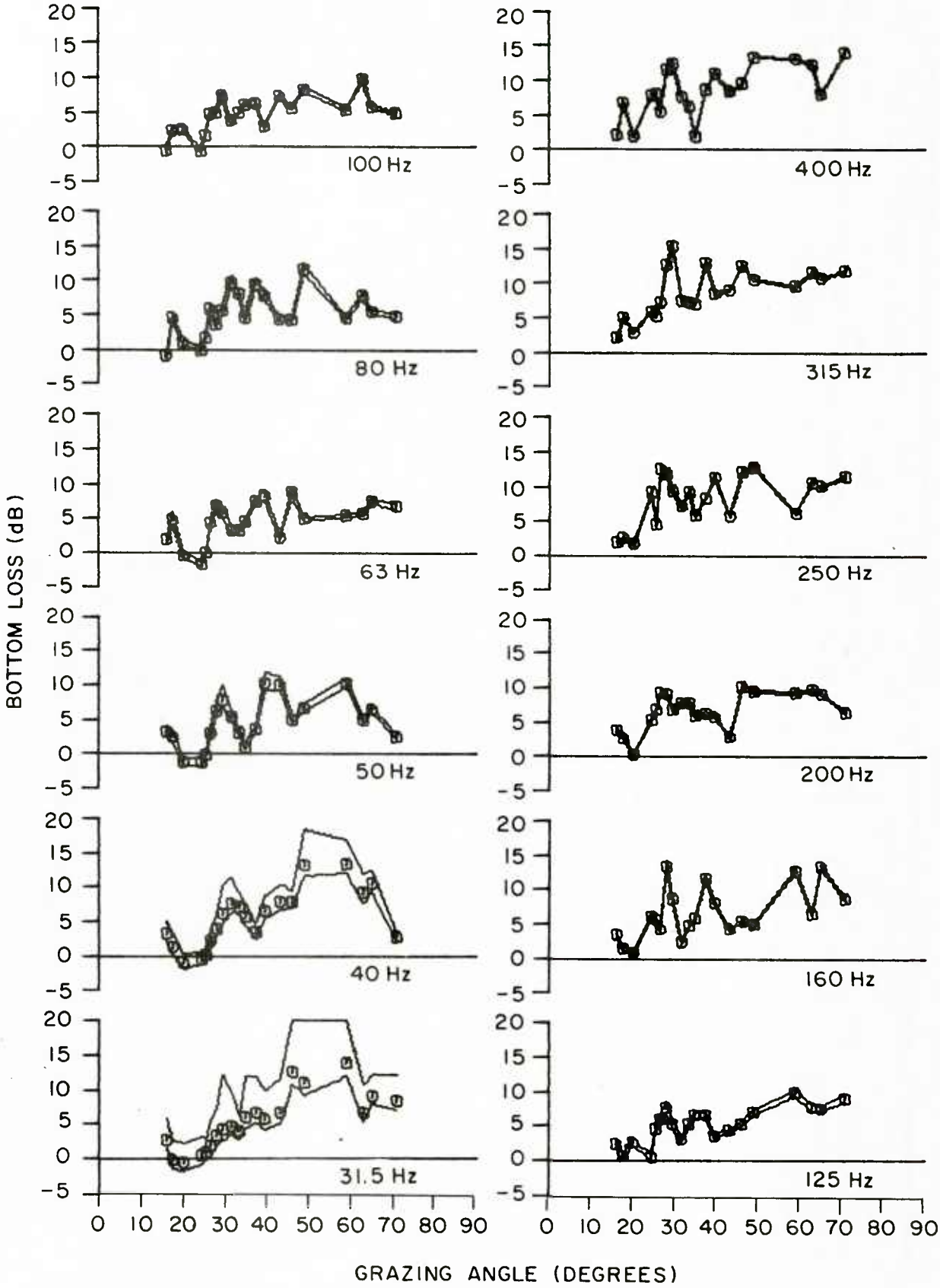

Figure 35. Station 8 one-third-octave bottom-loss curve.

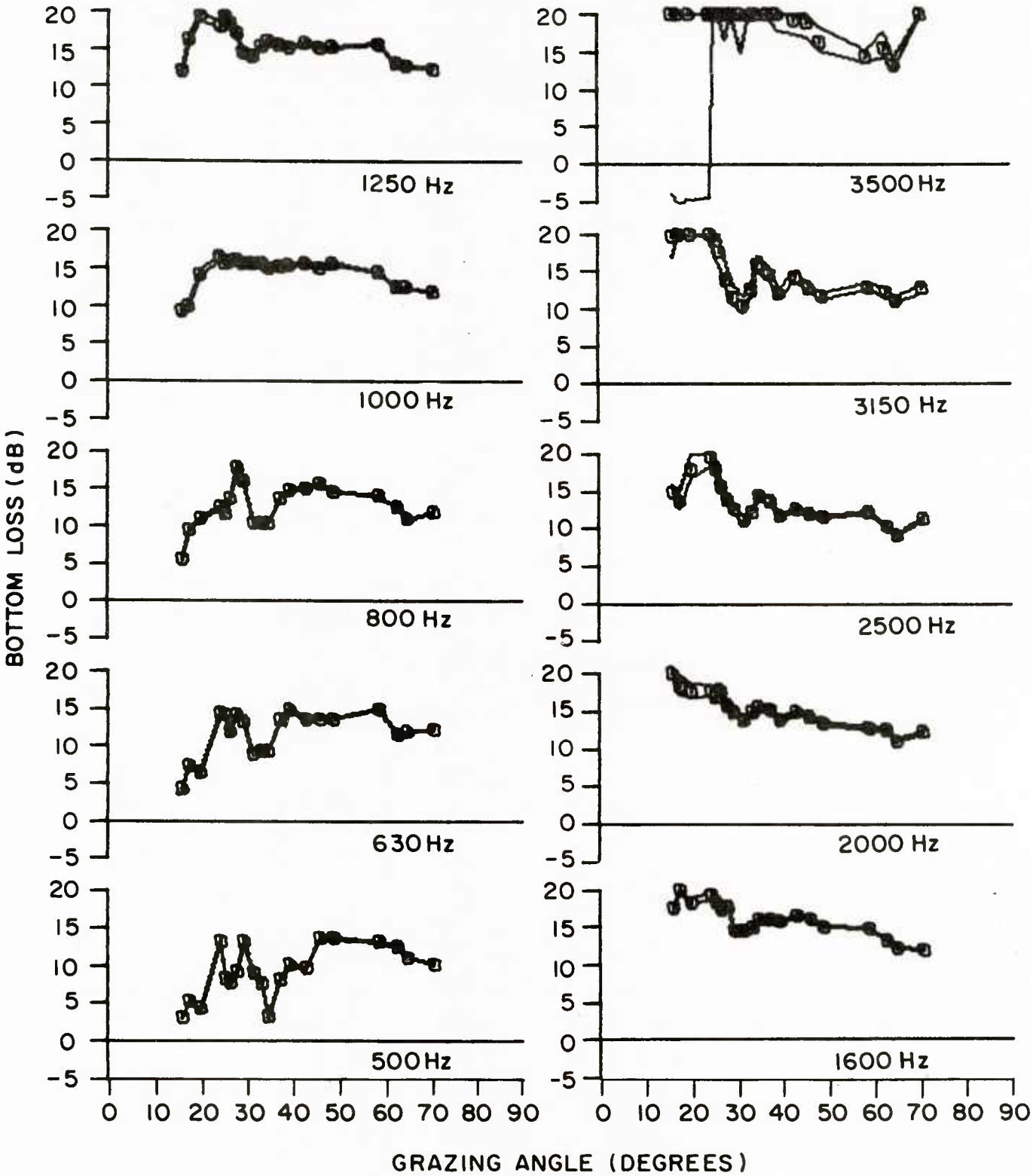

Figure 36. Station 8 one-third-octave bottom-loss curves.

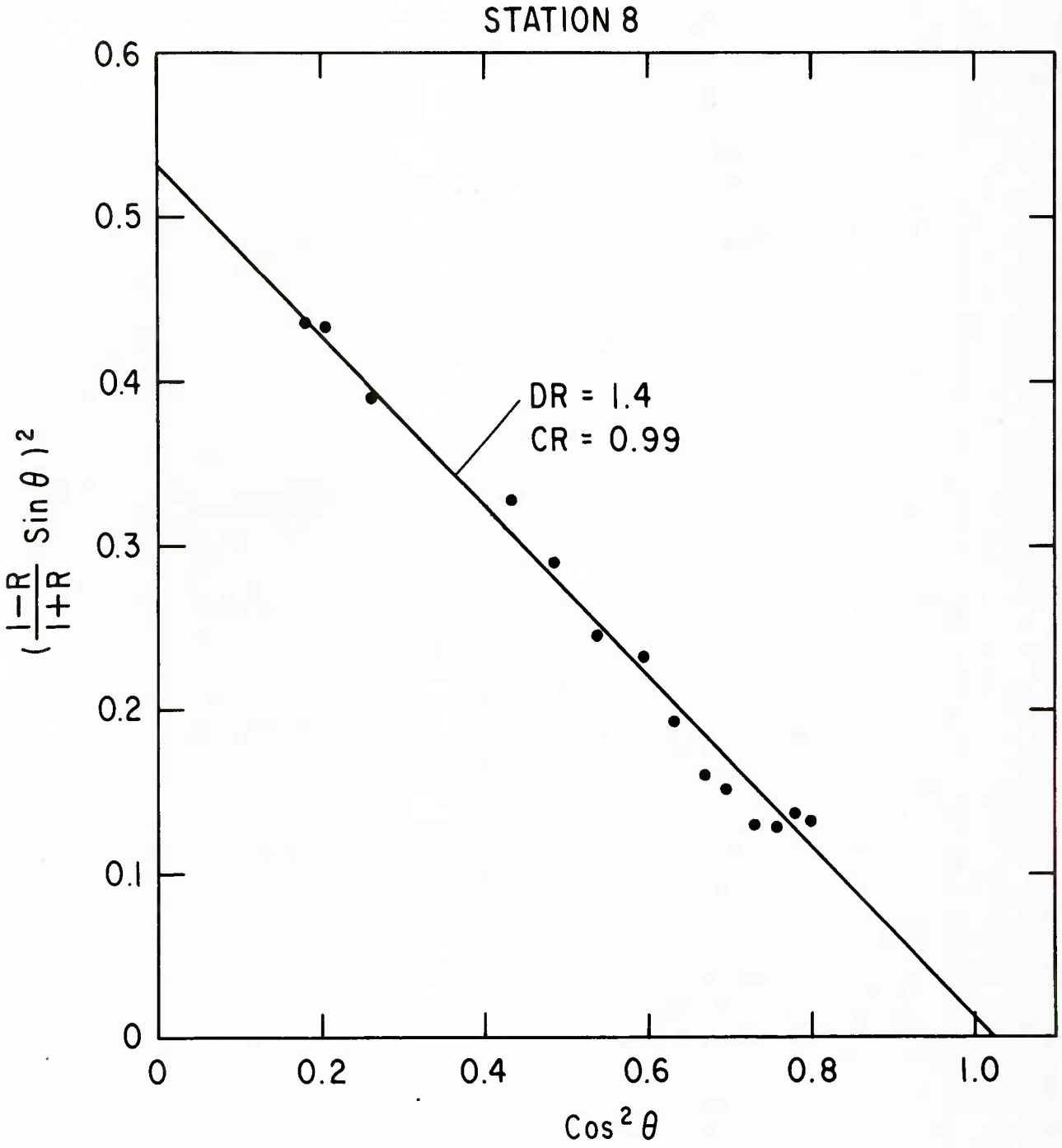

Figure 37. Station 8 Rayleigh-equation analysis.

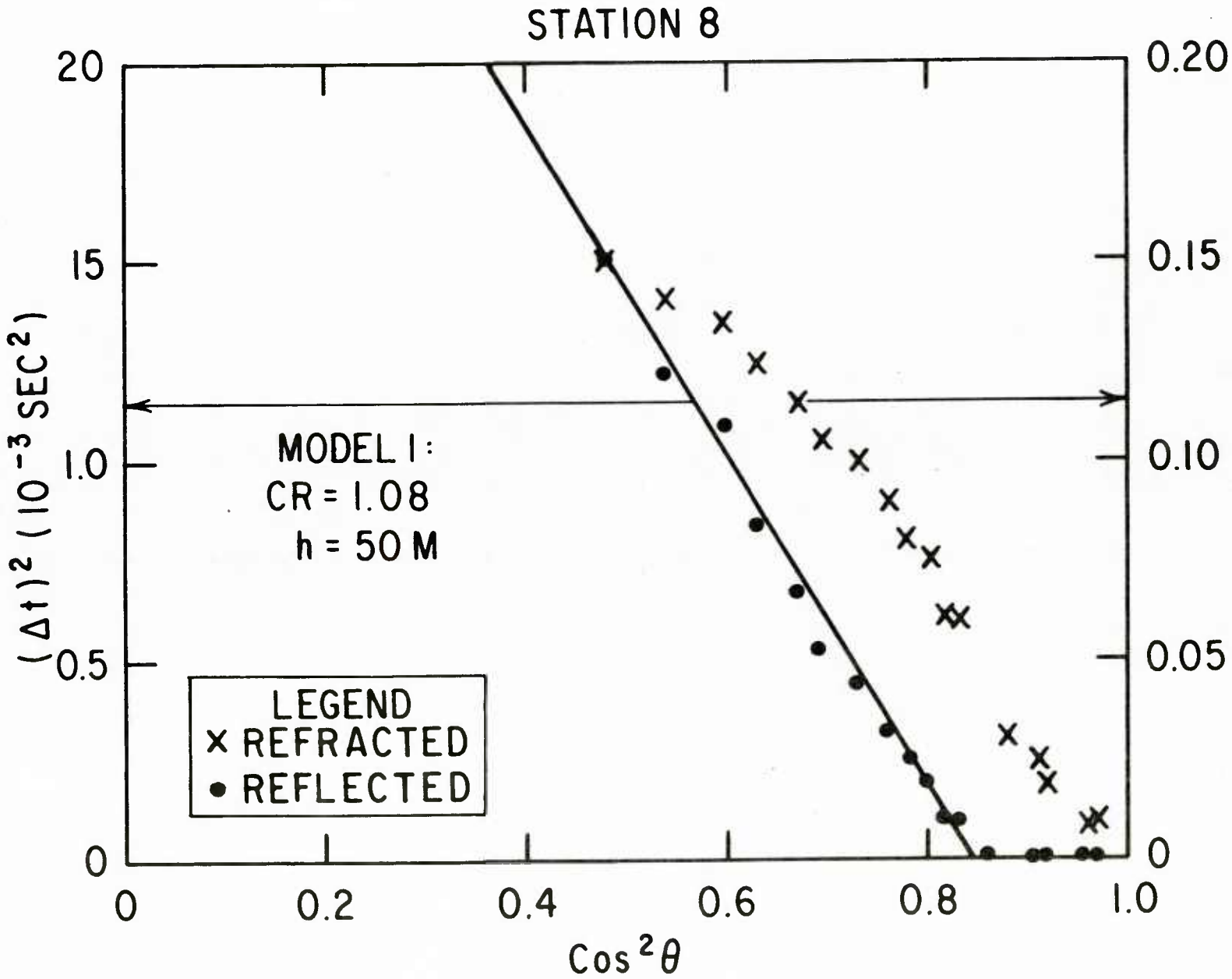

Figure 38. Station 8 model 1 analysis.

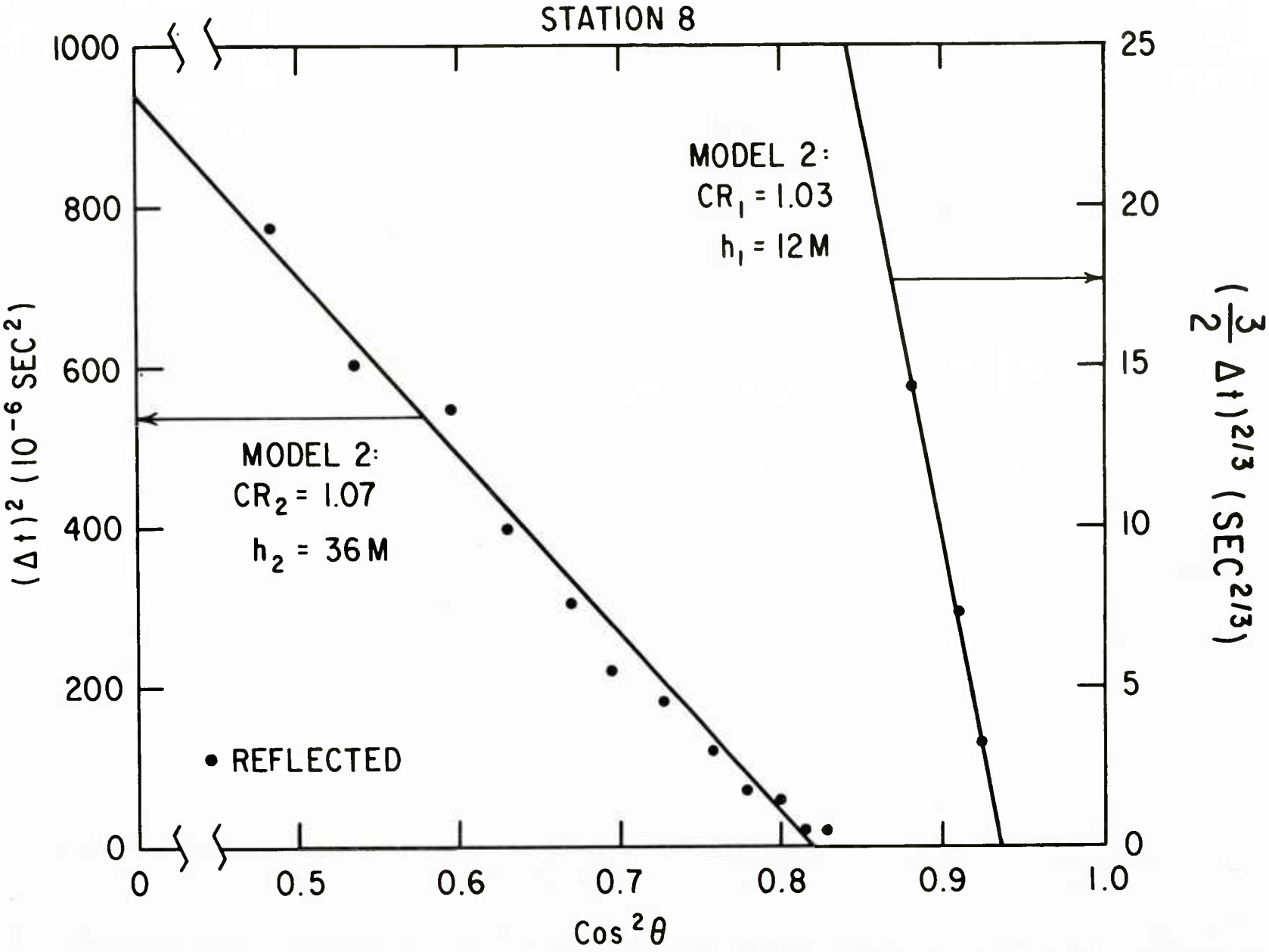

Figure 39. Station 8 model 2 analysis.

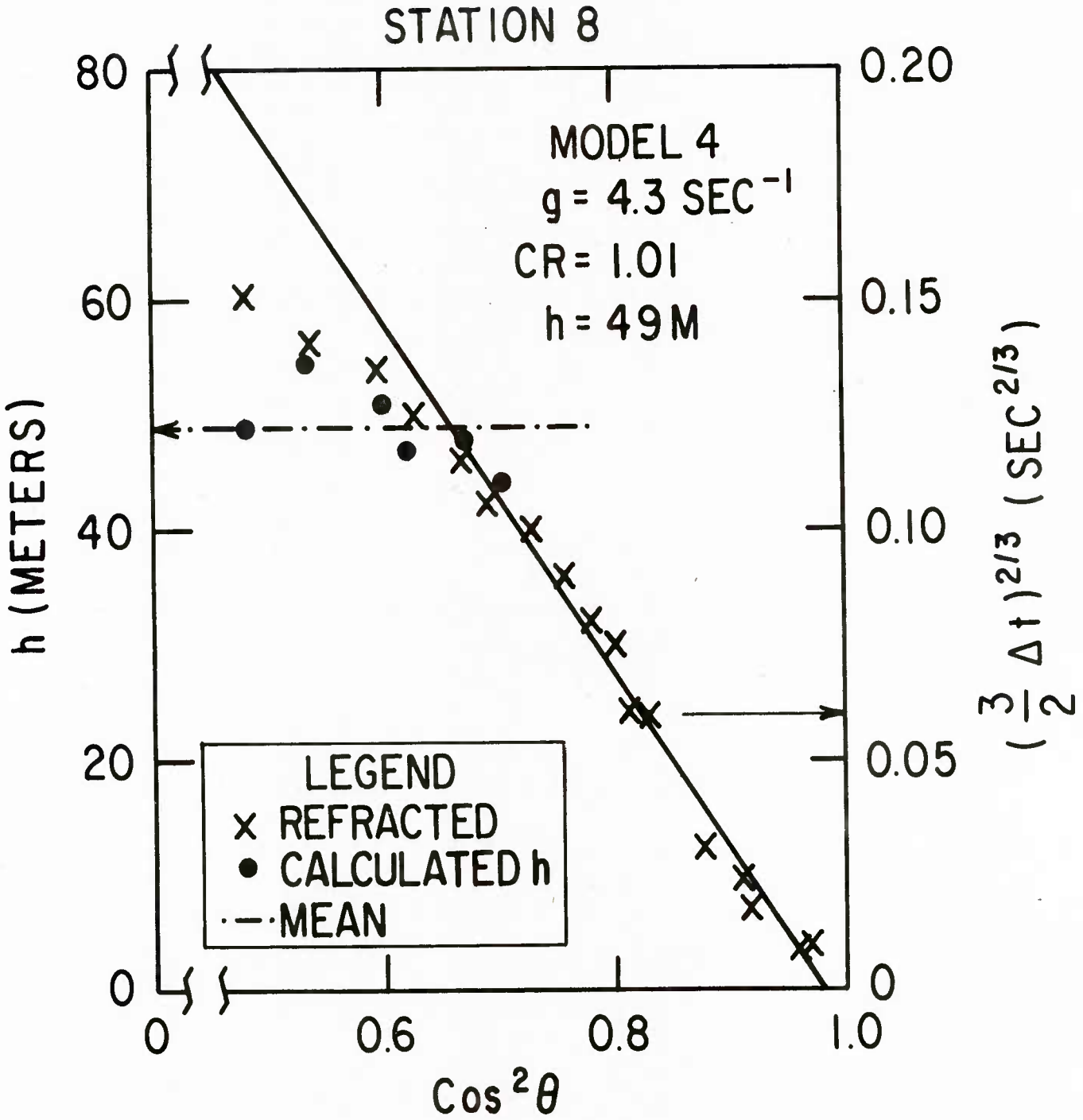

Figure 40. Station 8 model 4 analysis.

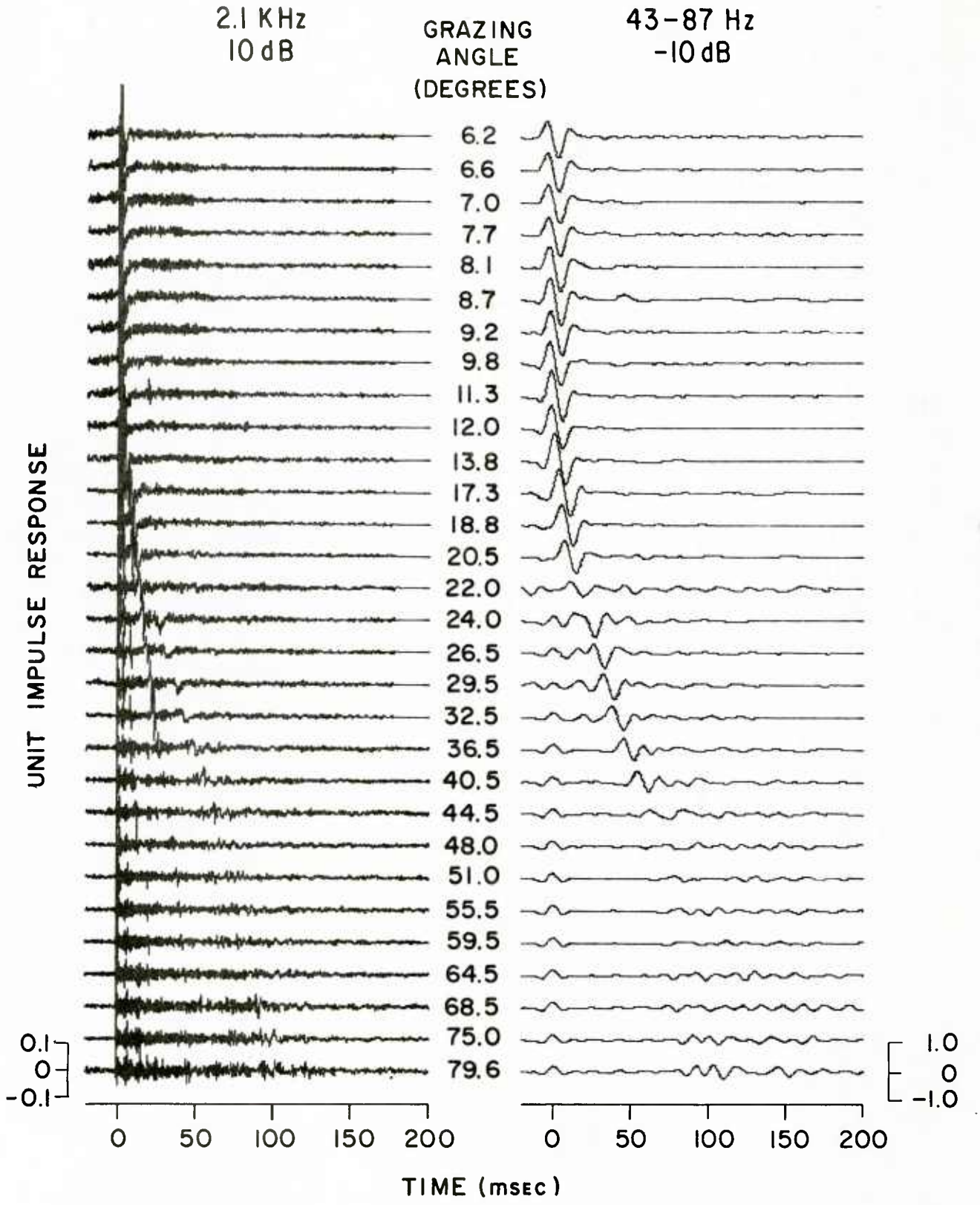

Figure 41. Station 9 impulse responses.

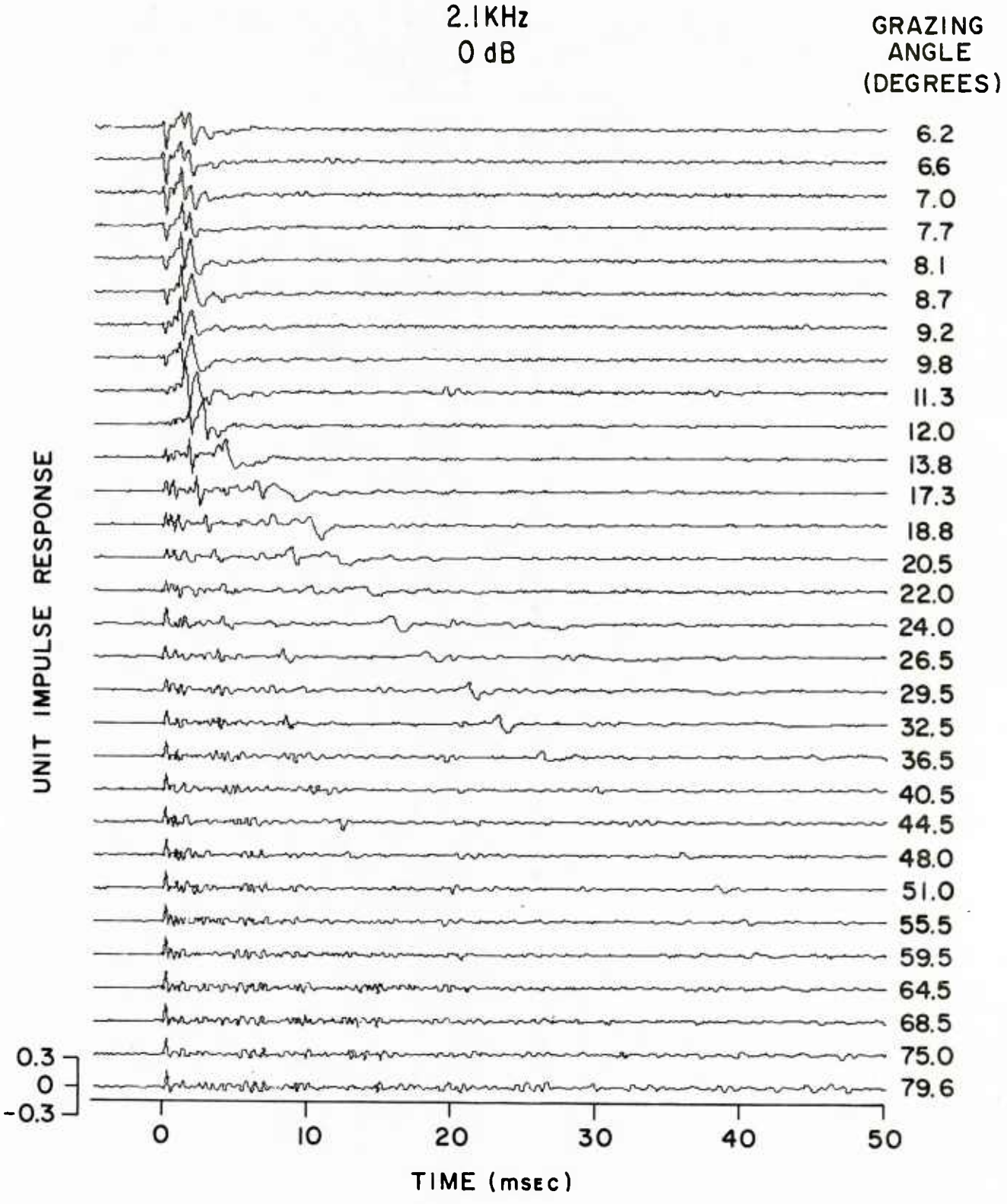

Figure 42. Station 9 impulse responses on expanded time axis.

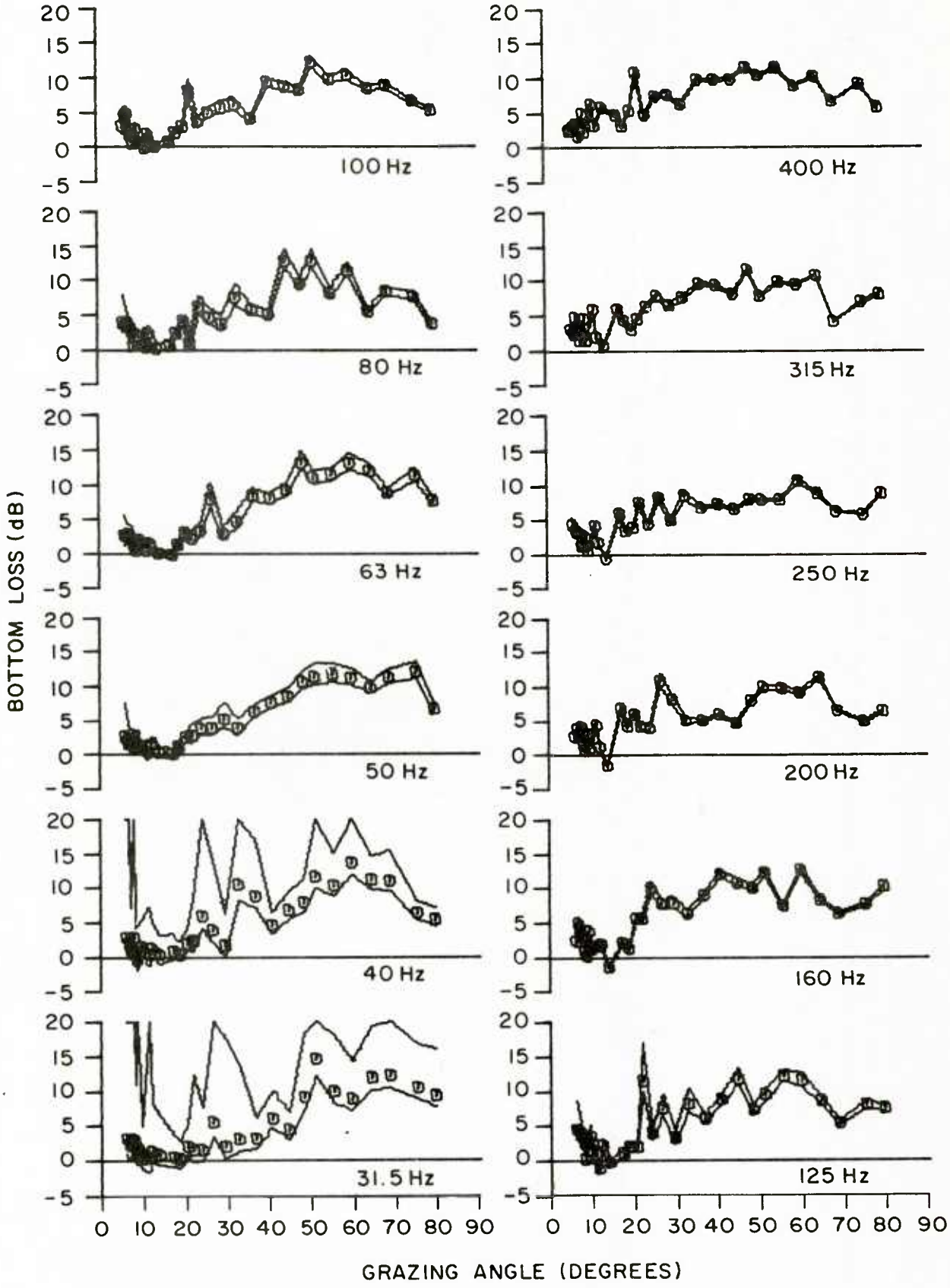

Figure 43. Station 9 one-third-octave bottom-loss curves.

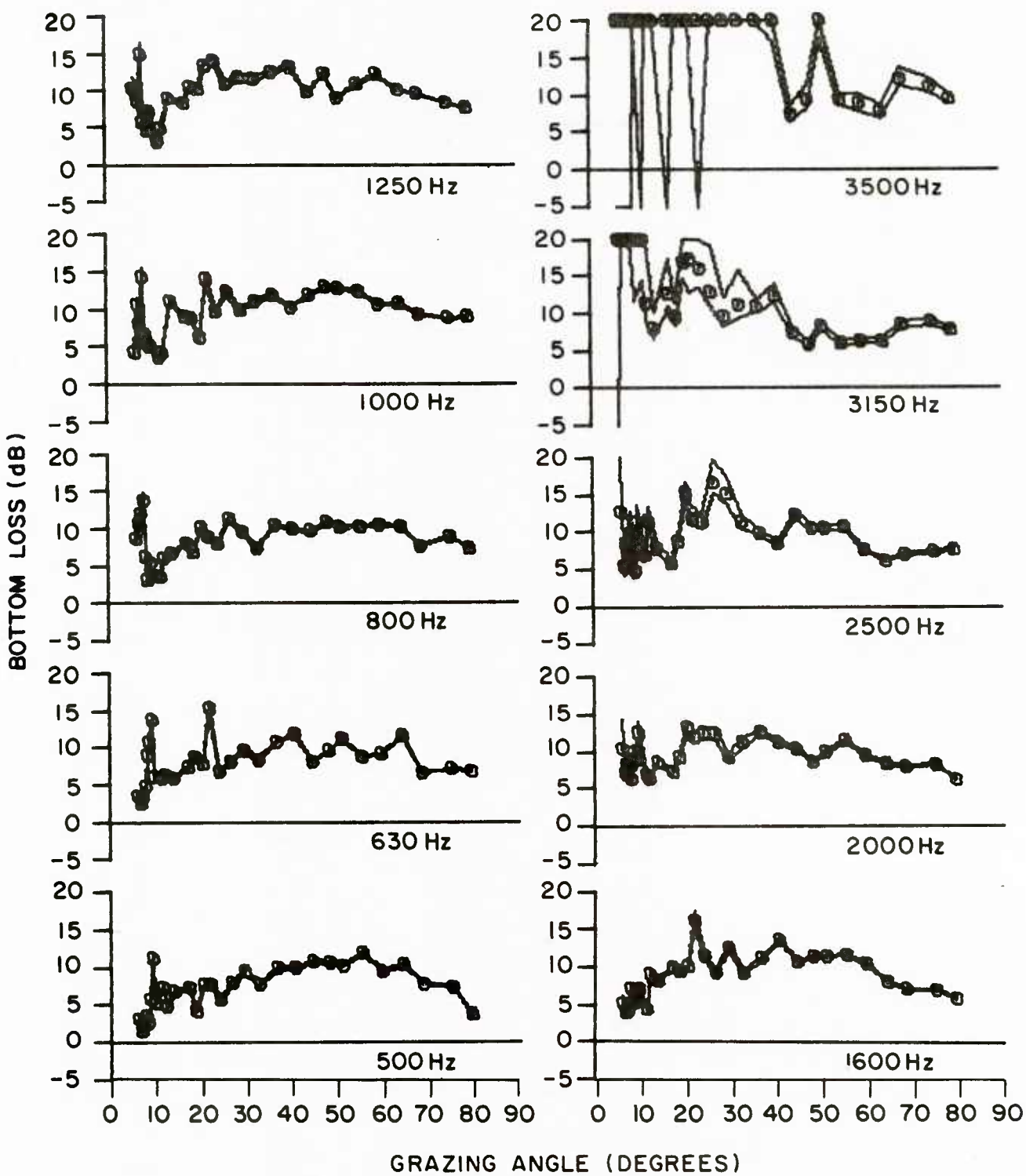

Figure 44. Station 9 one-third-octave bottom-loss curves.

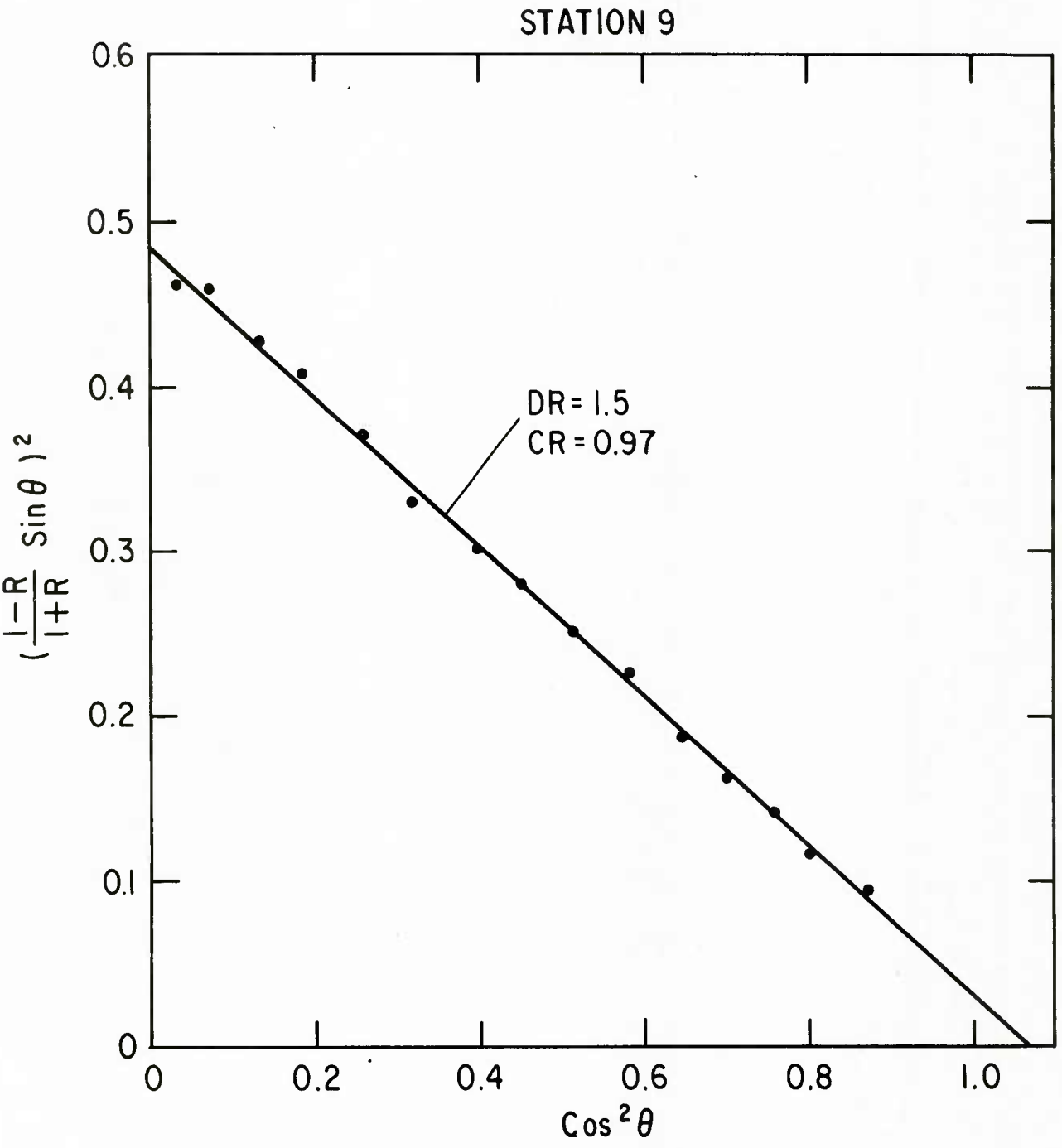

Figure 45. Station 9 Rayleigh-equation analysis.

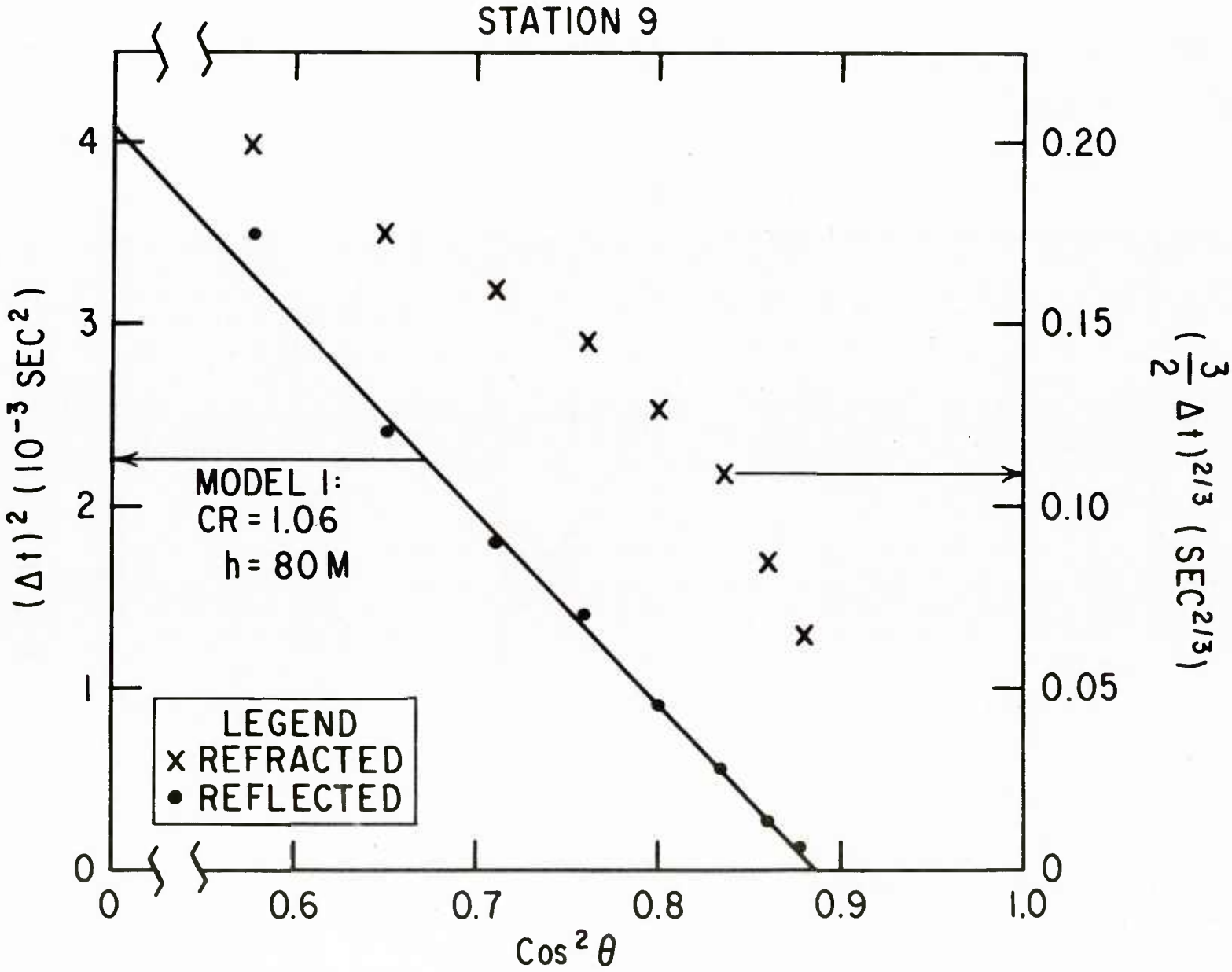

Figure 46. Station 9 model 1 analysis.

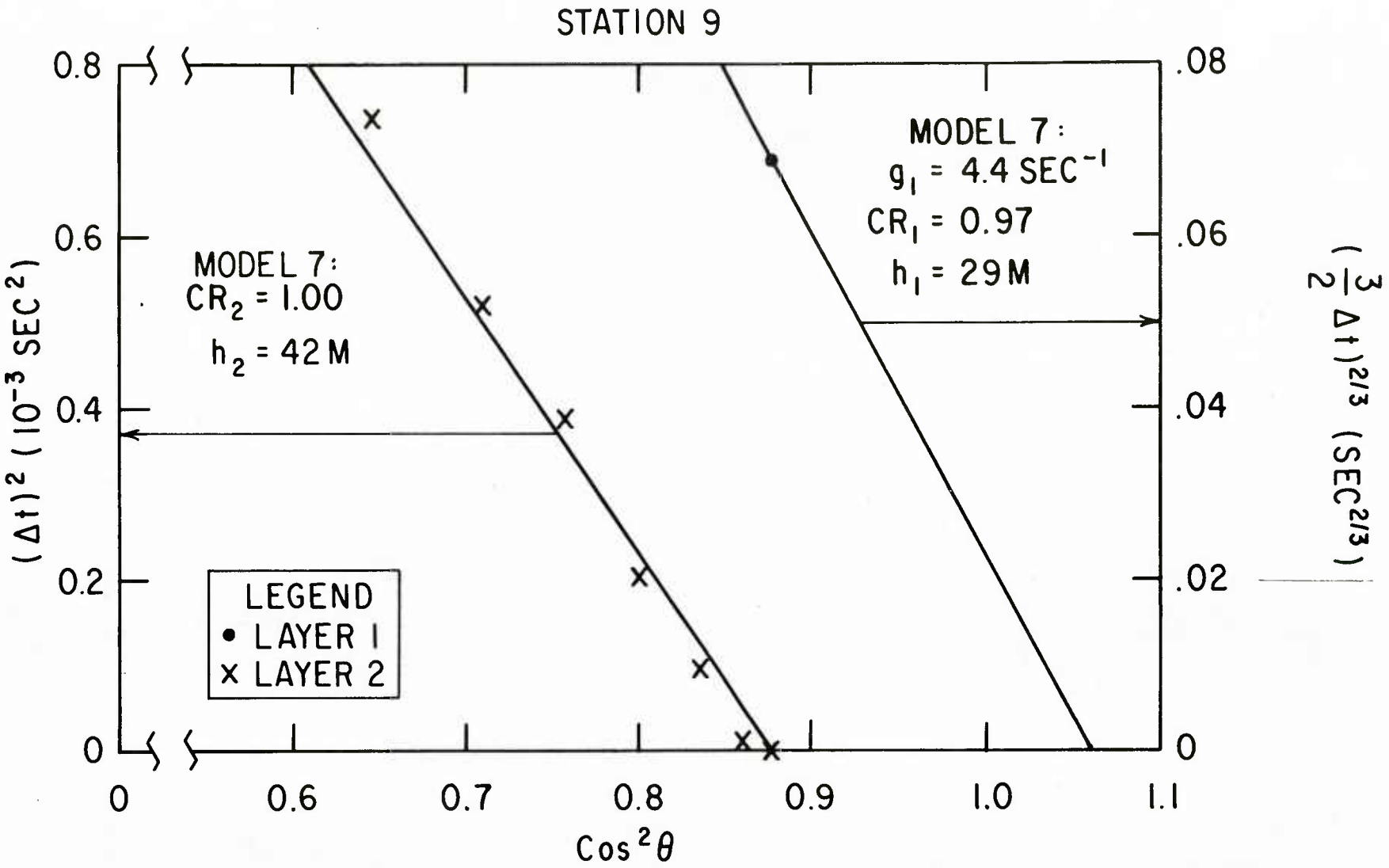

Figure 47. Station 9 model 7 analysis.

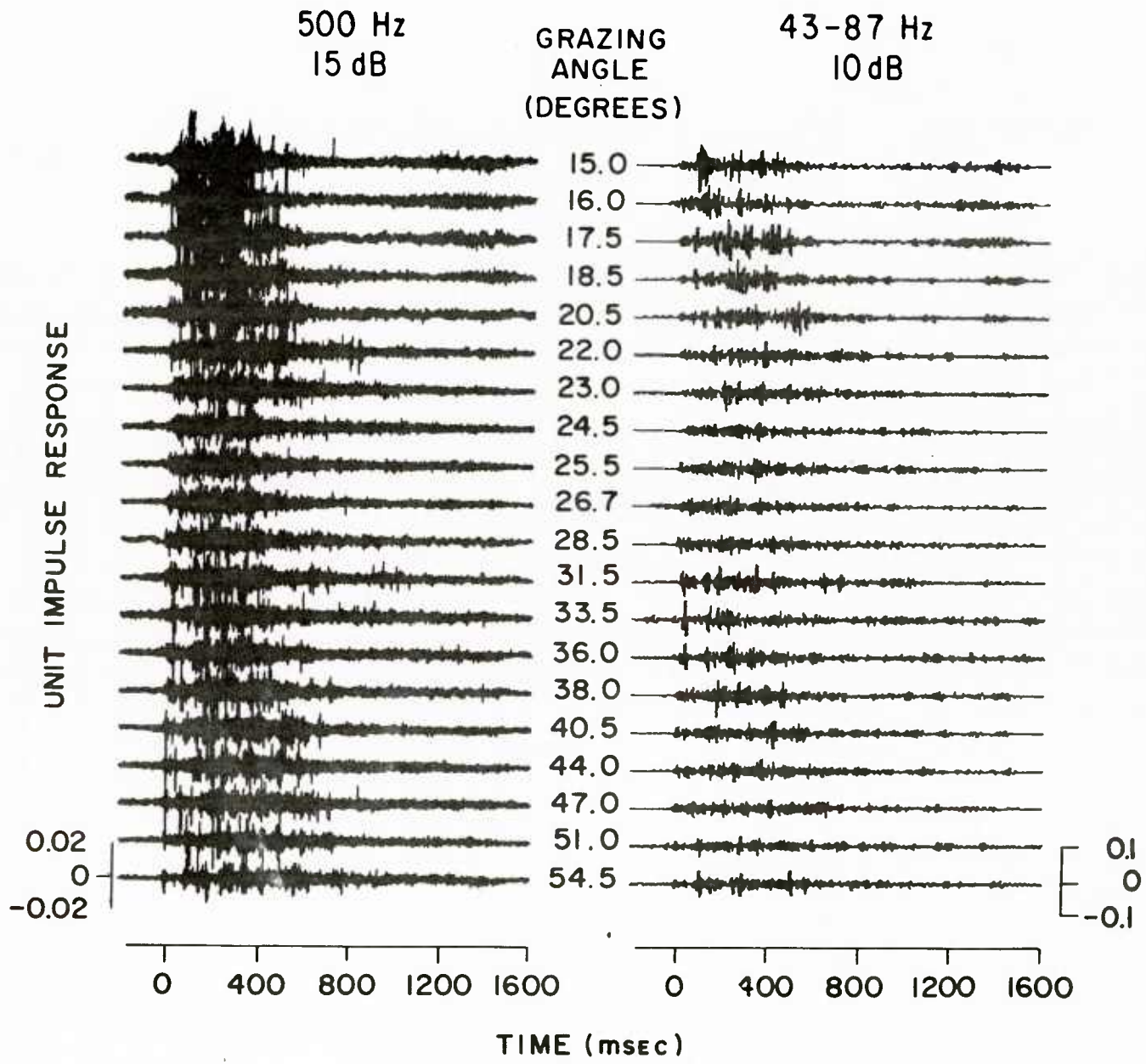

Figure 48. Station 7 impulse responses.

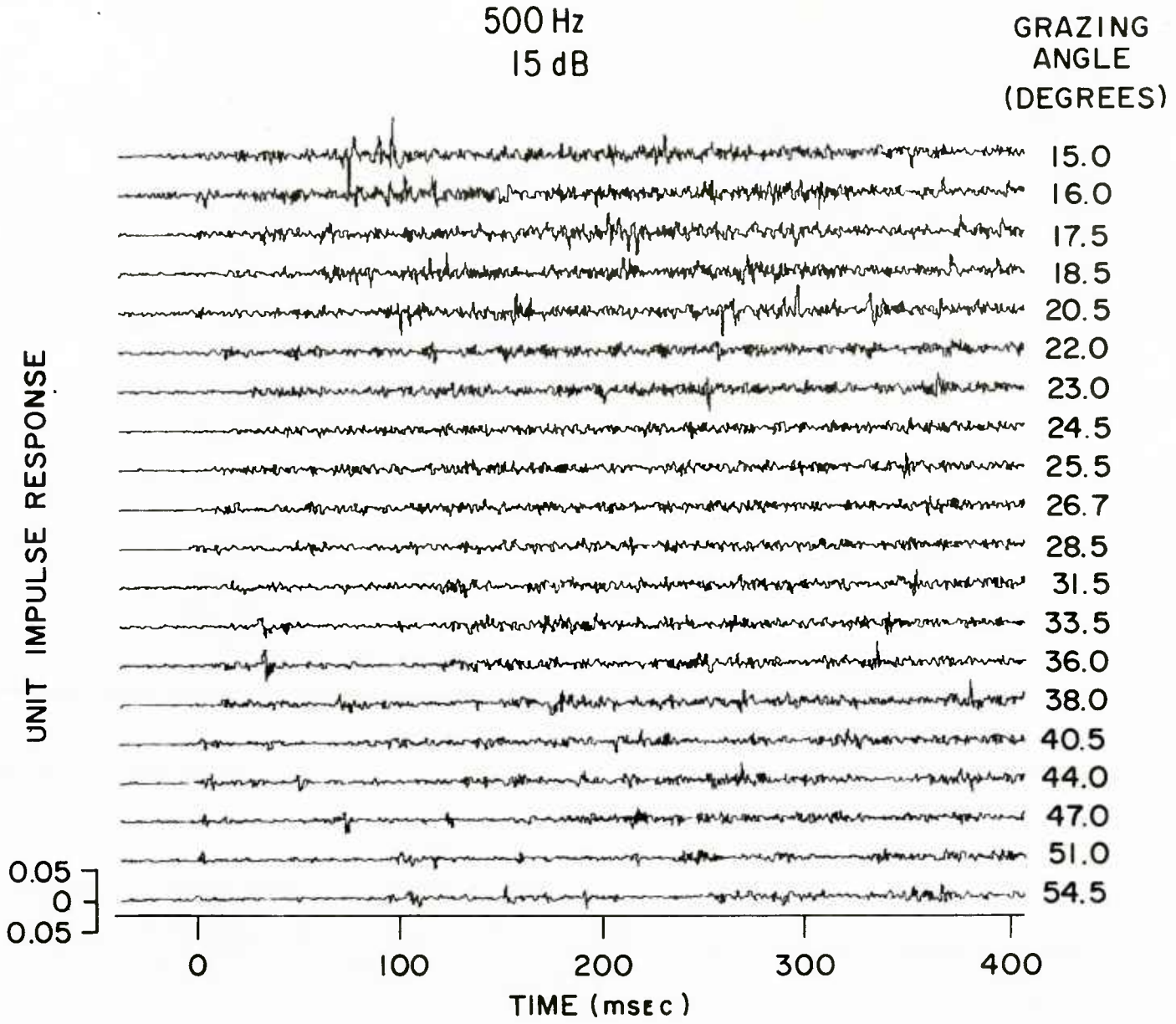

Figure 49. Station 7 impulse responses on expanded time axis.

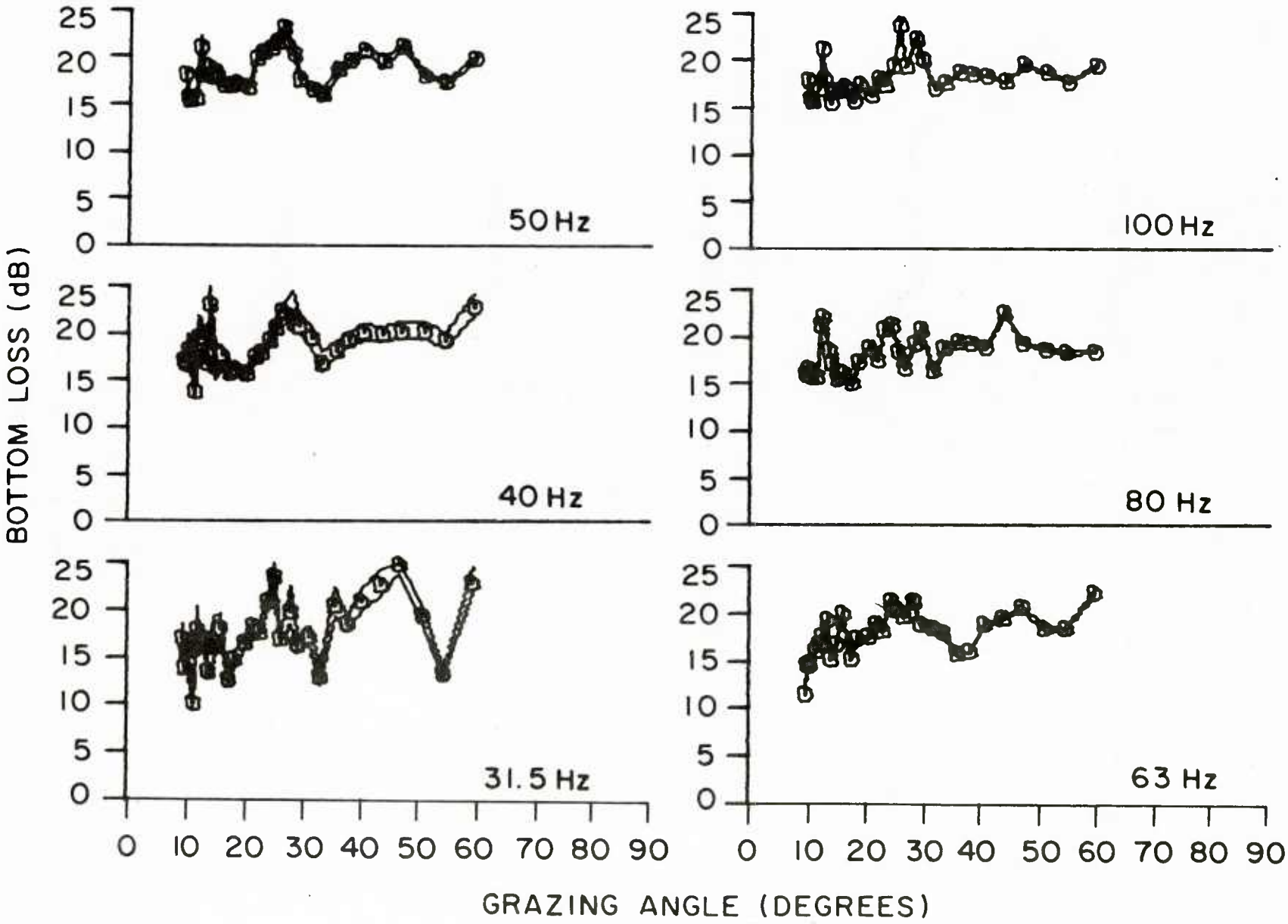

Figure 50. Station 7 one-third-octave bottom-loss curves.

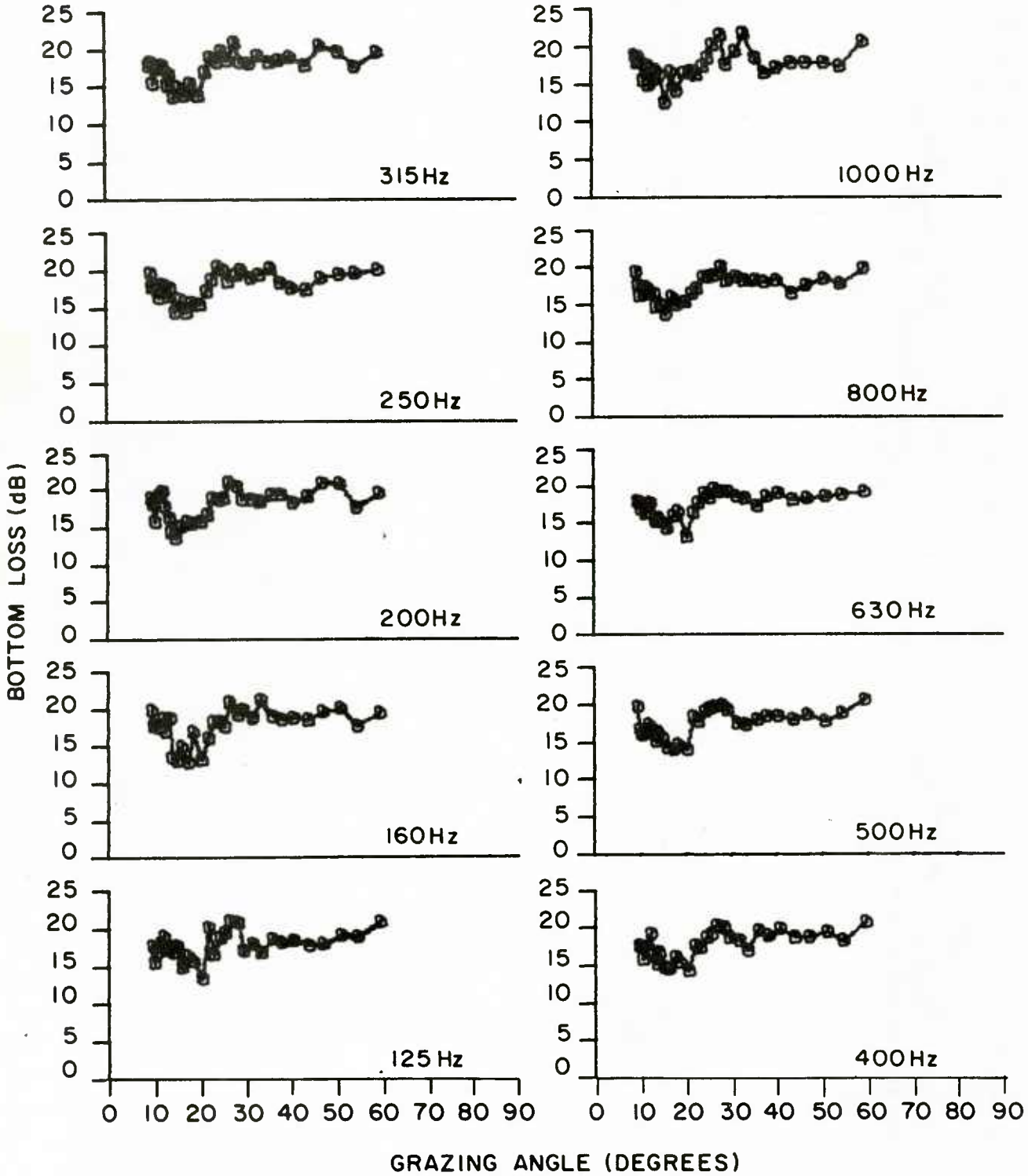

Figure 51. Station 7 one-third-octave bottom-loss curves.

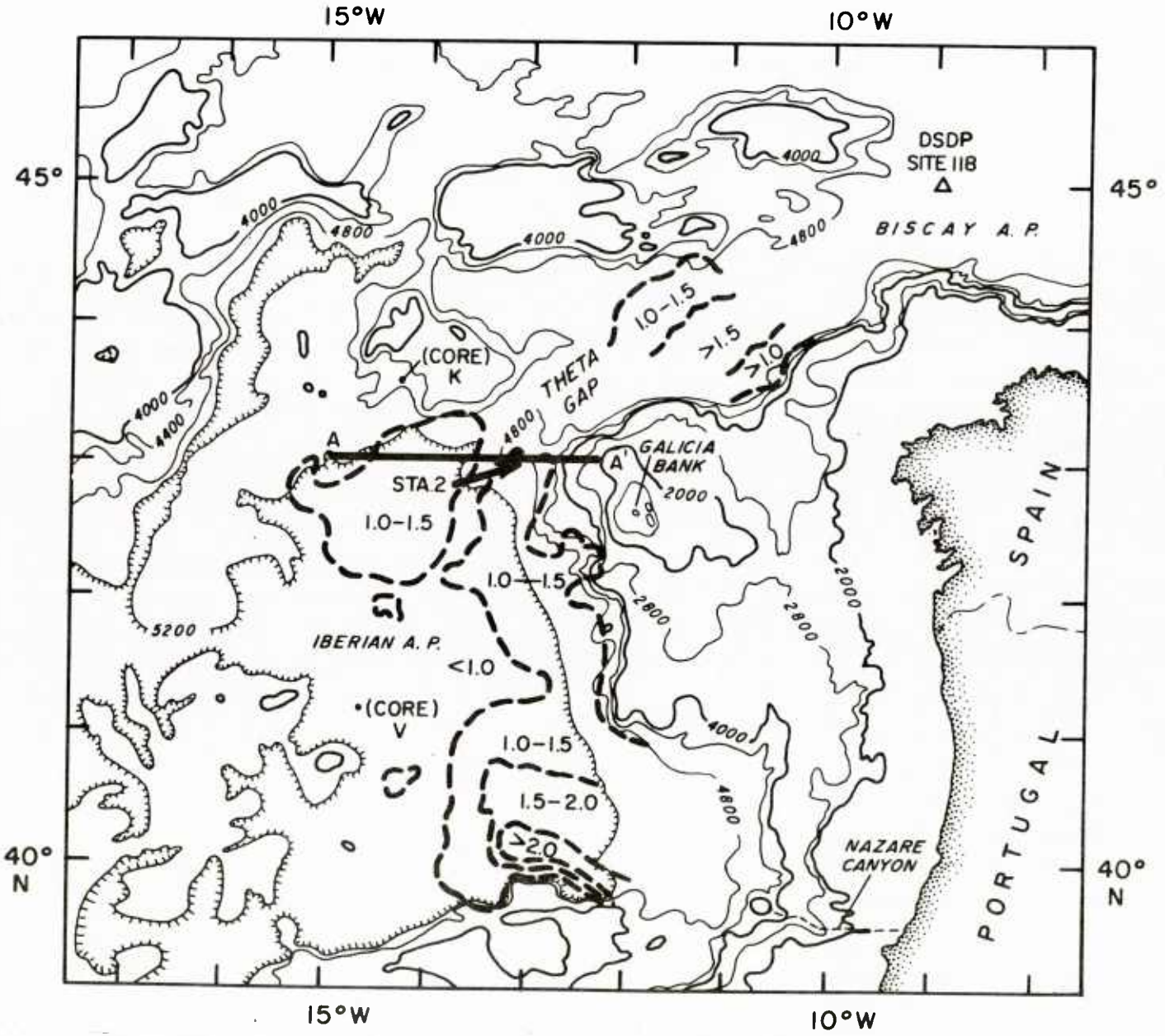

Figure 52. Area map of station 2 in the Iberian Abyssal Plain. Sediment thickness is indicated in seconds of two-way travel time.

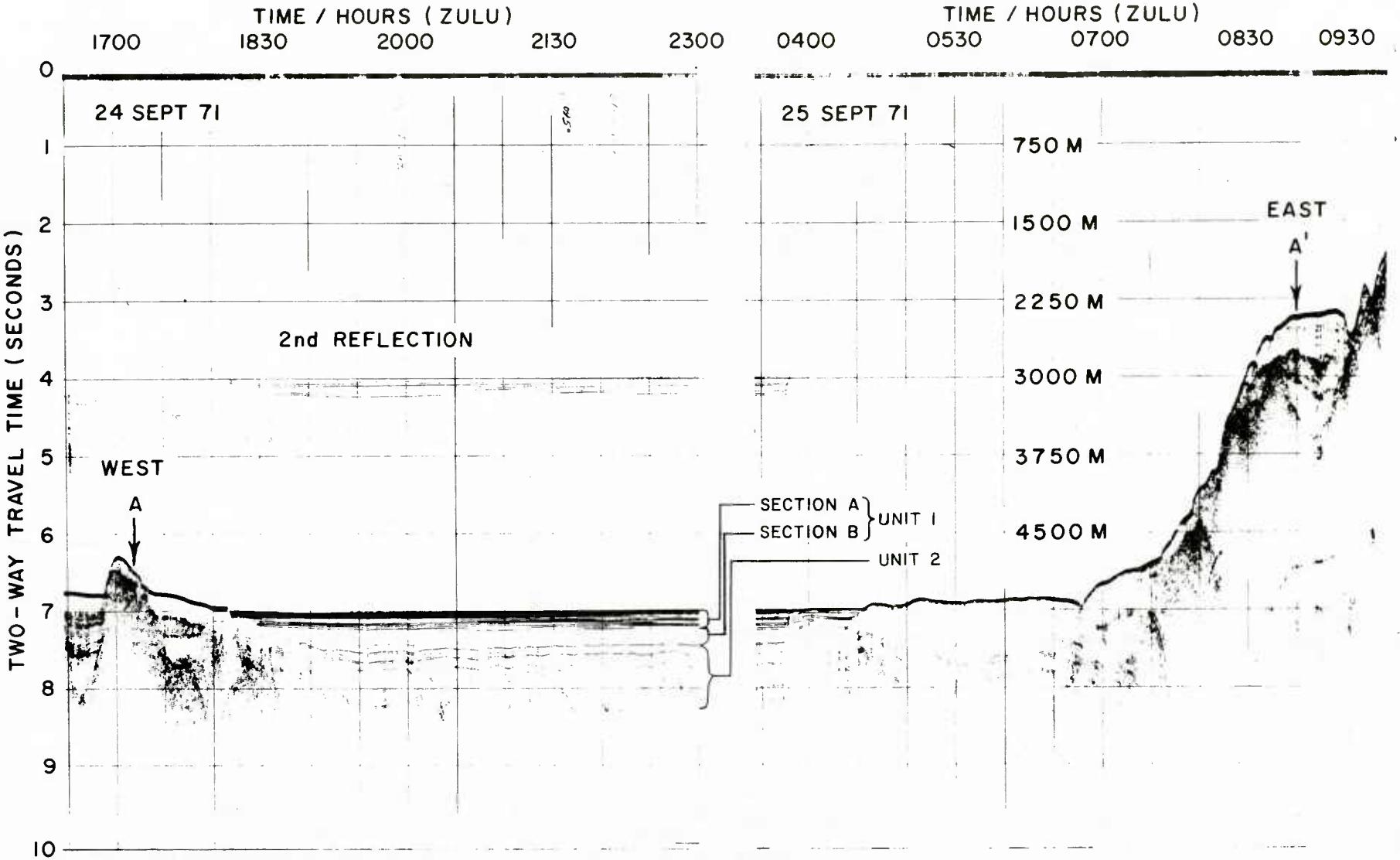

Figure 53. Seismic-profile records near station 2.

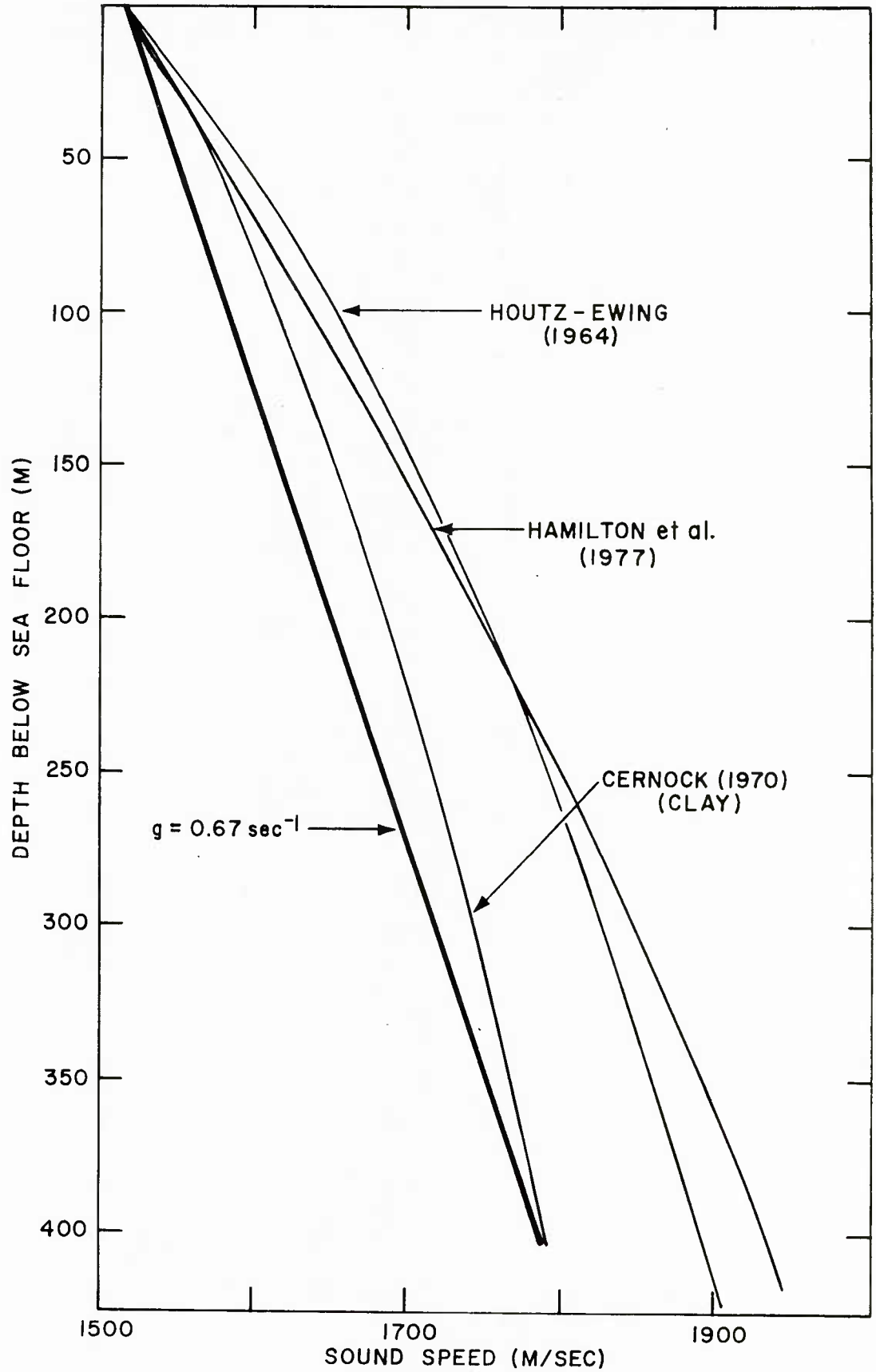

Figure 54. Predicted sediment sound-speed profiles at station 2.

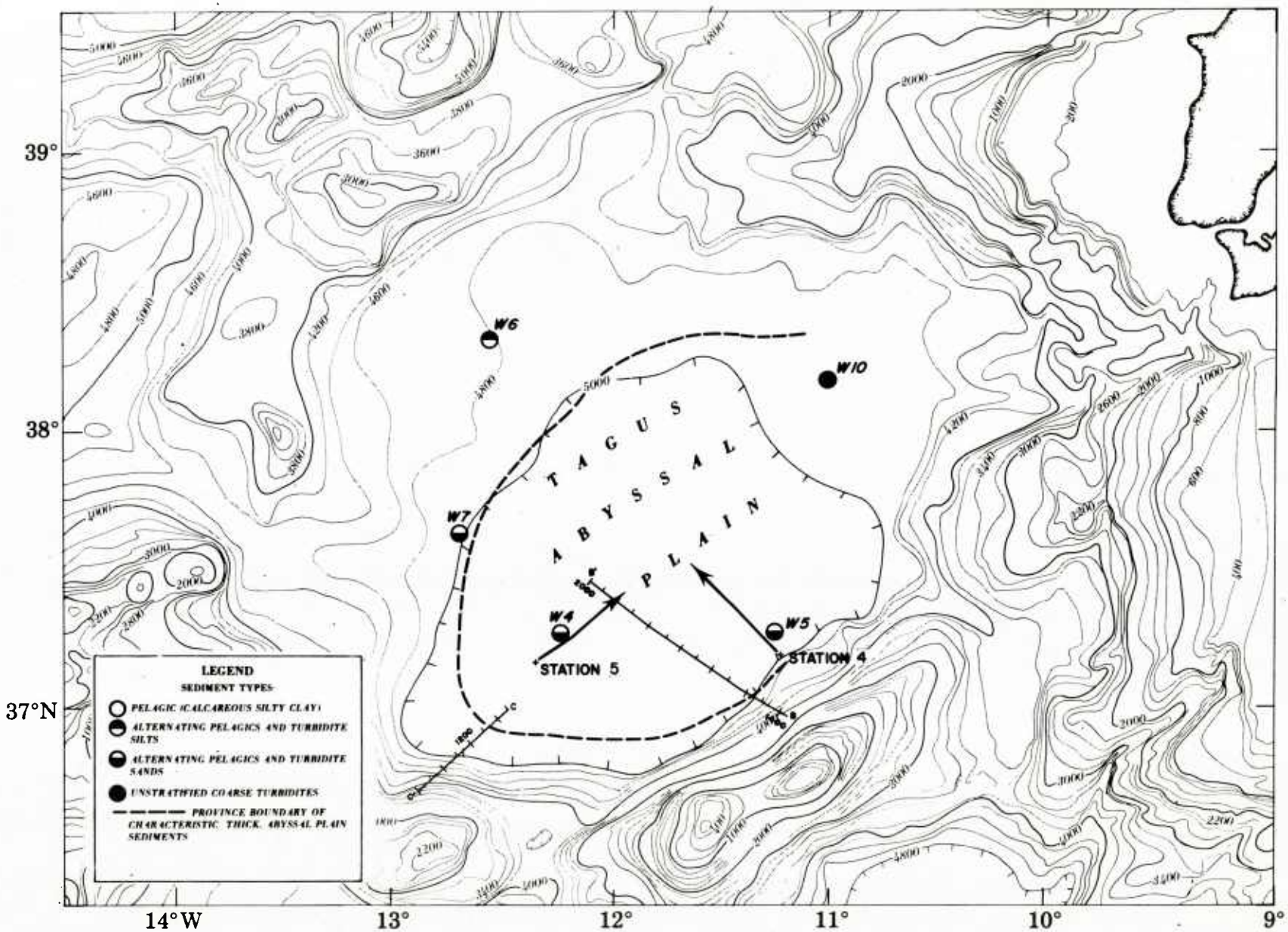

Figure 55. Area map of stations 4 and 5 in the Tagus Abyssal Plain.

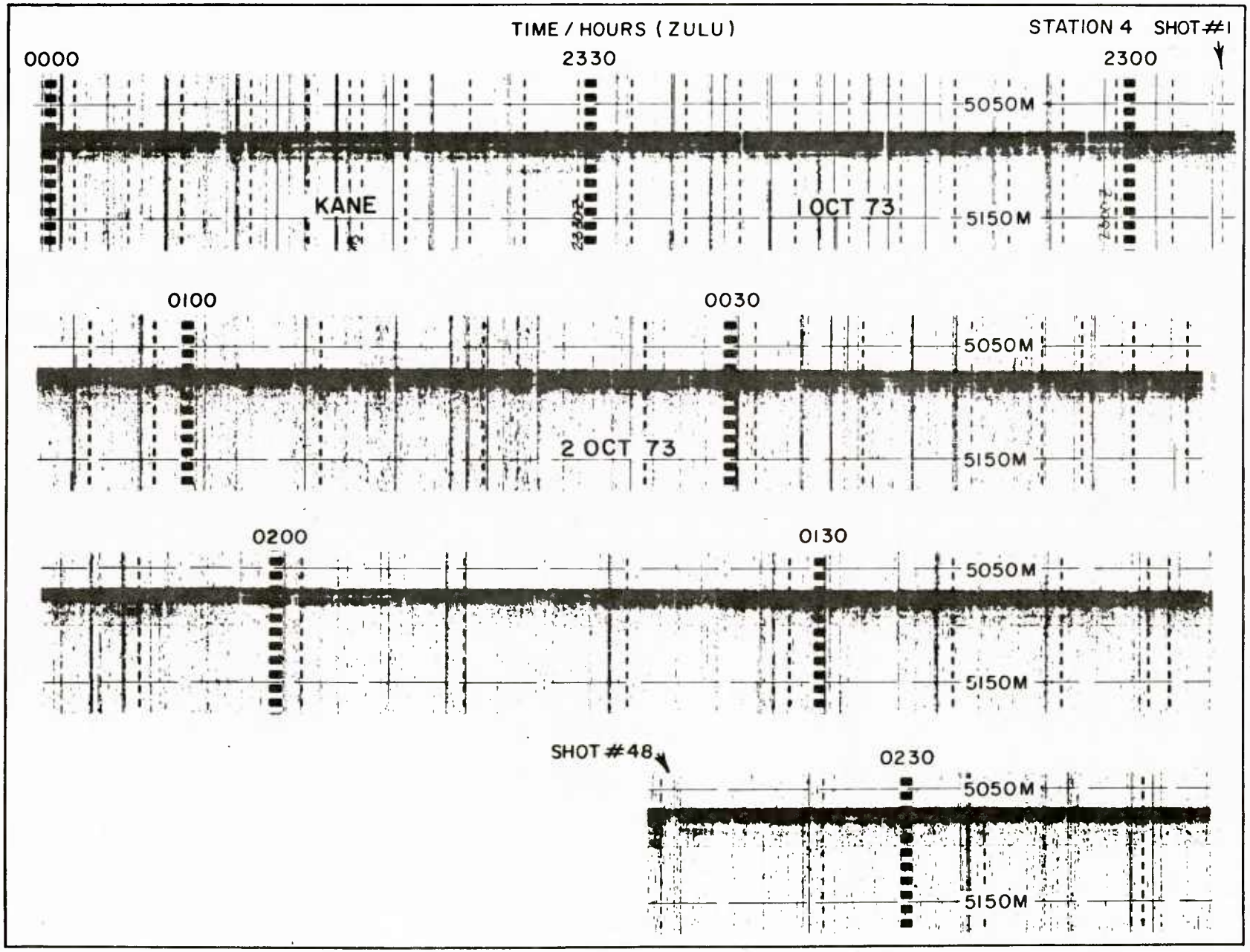

Figure 56. 3.5 kHz subbottom depth-recorder records along bomb run at station 4.

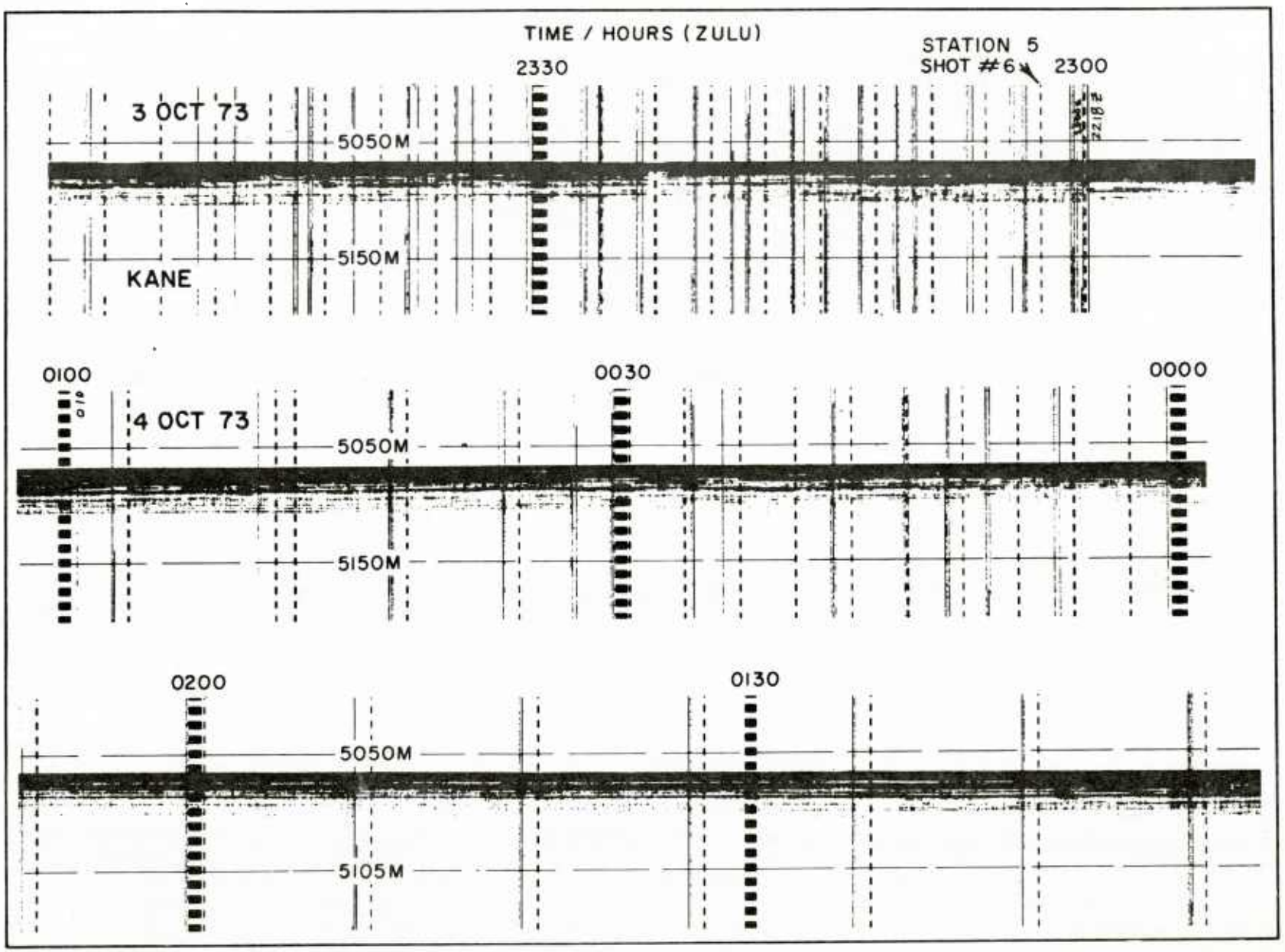

Figure 57. 3.5 kHz subbottom depth-recorder records along bomb run at station 5.

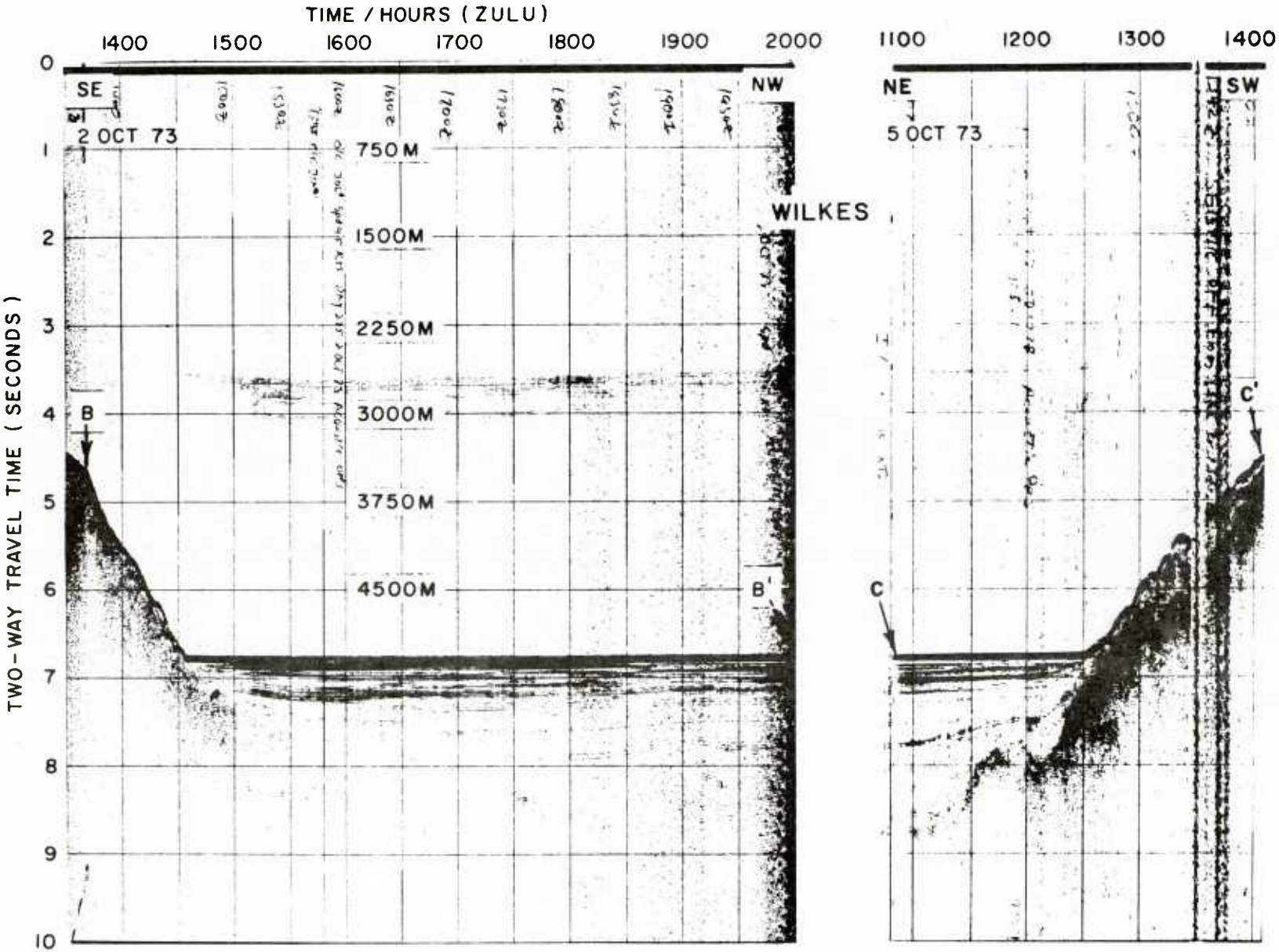

Figure 58. Seismic-profiler records near stations 4 and 5.

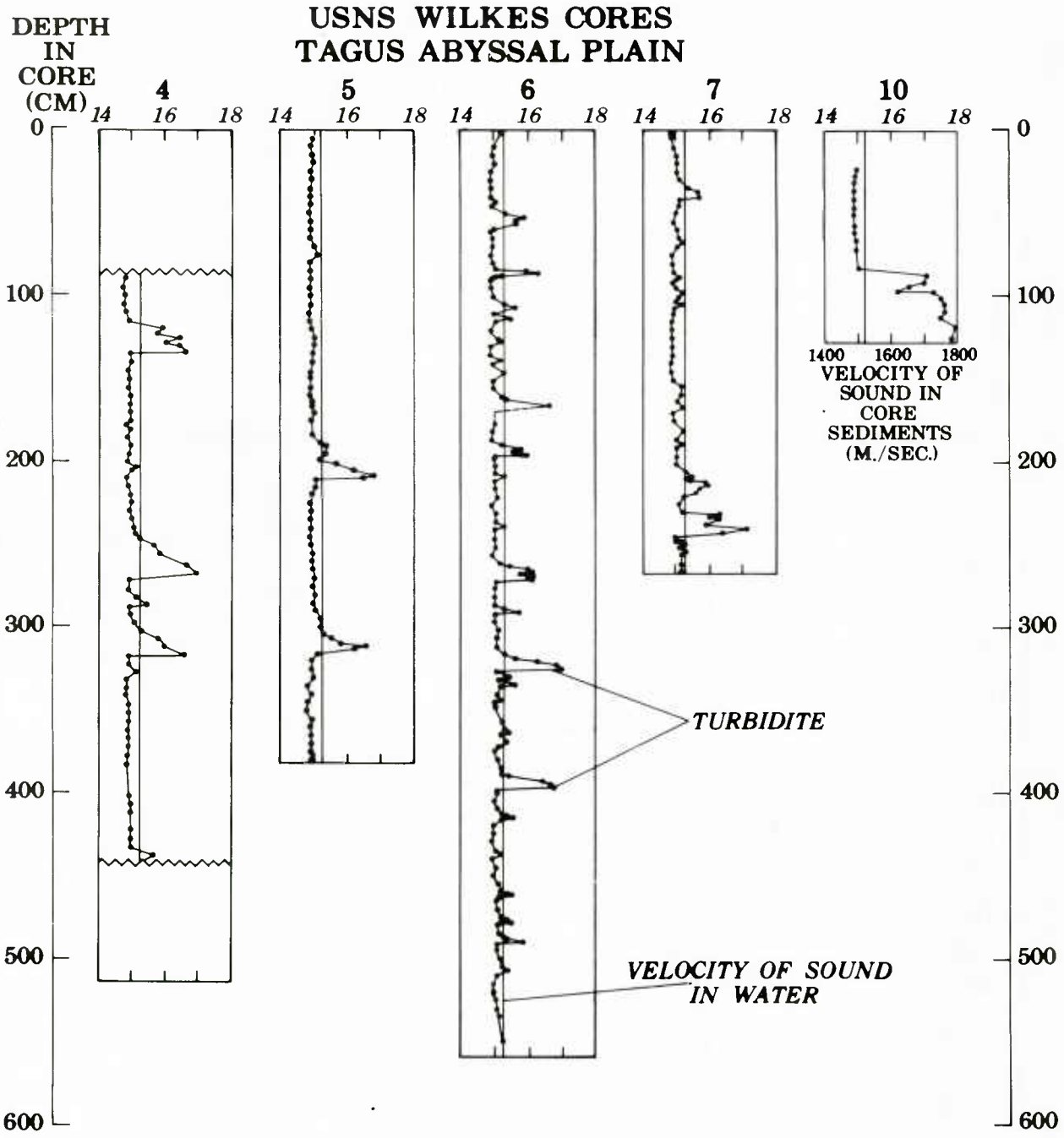

Figure 59. Sound-speed in cores from the Tagus Abyssal Plain.

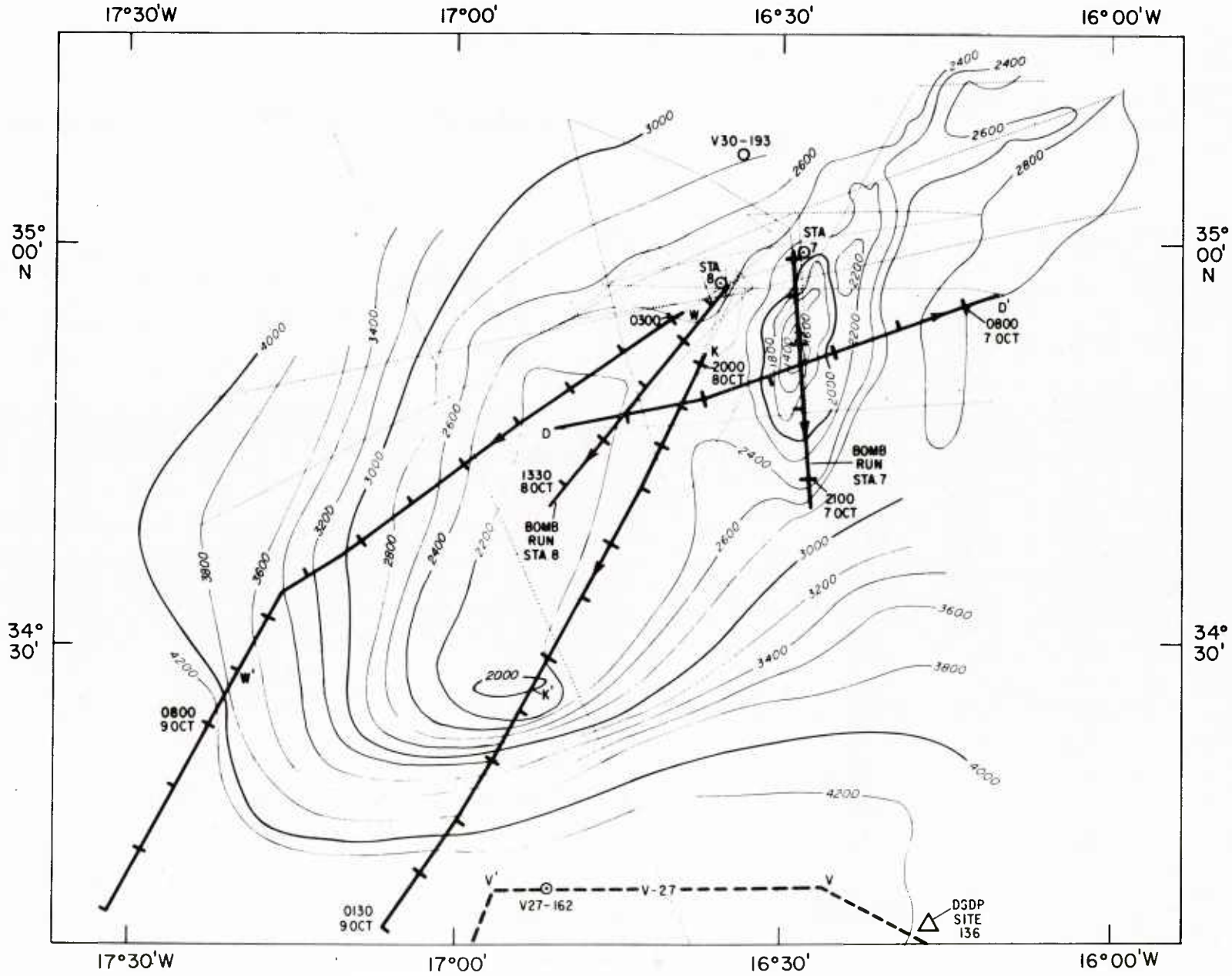

Figure 60. Area map of stations 7 and 8 at Dragon Seamount.

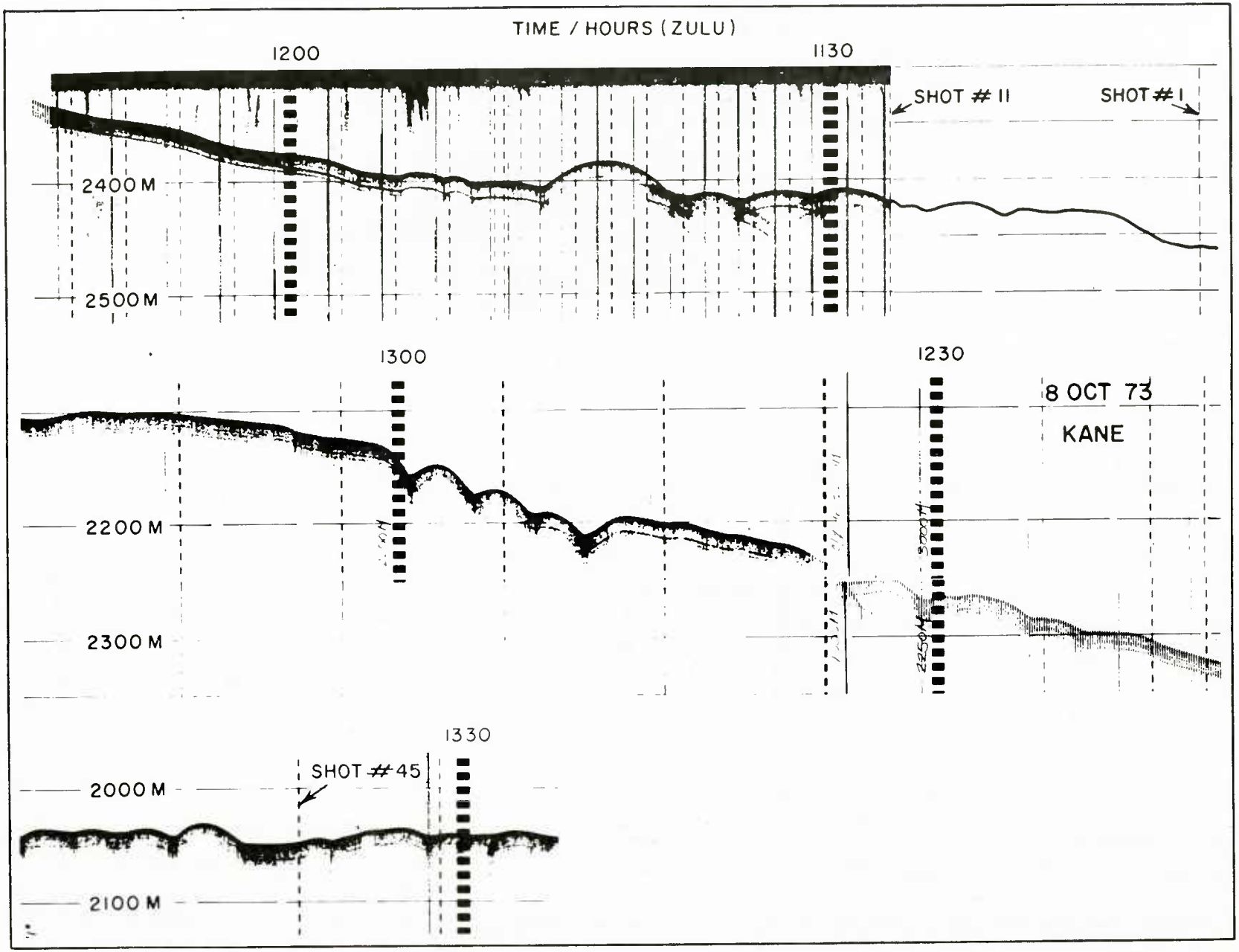

Figure 61. 3.5 kHz subbottom depth-recorder record along bomb run at station 8.

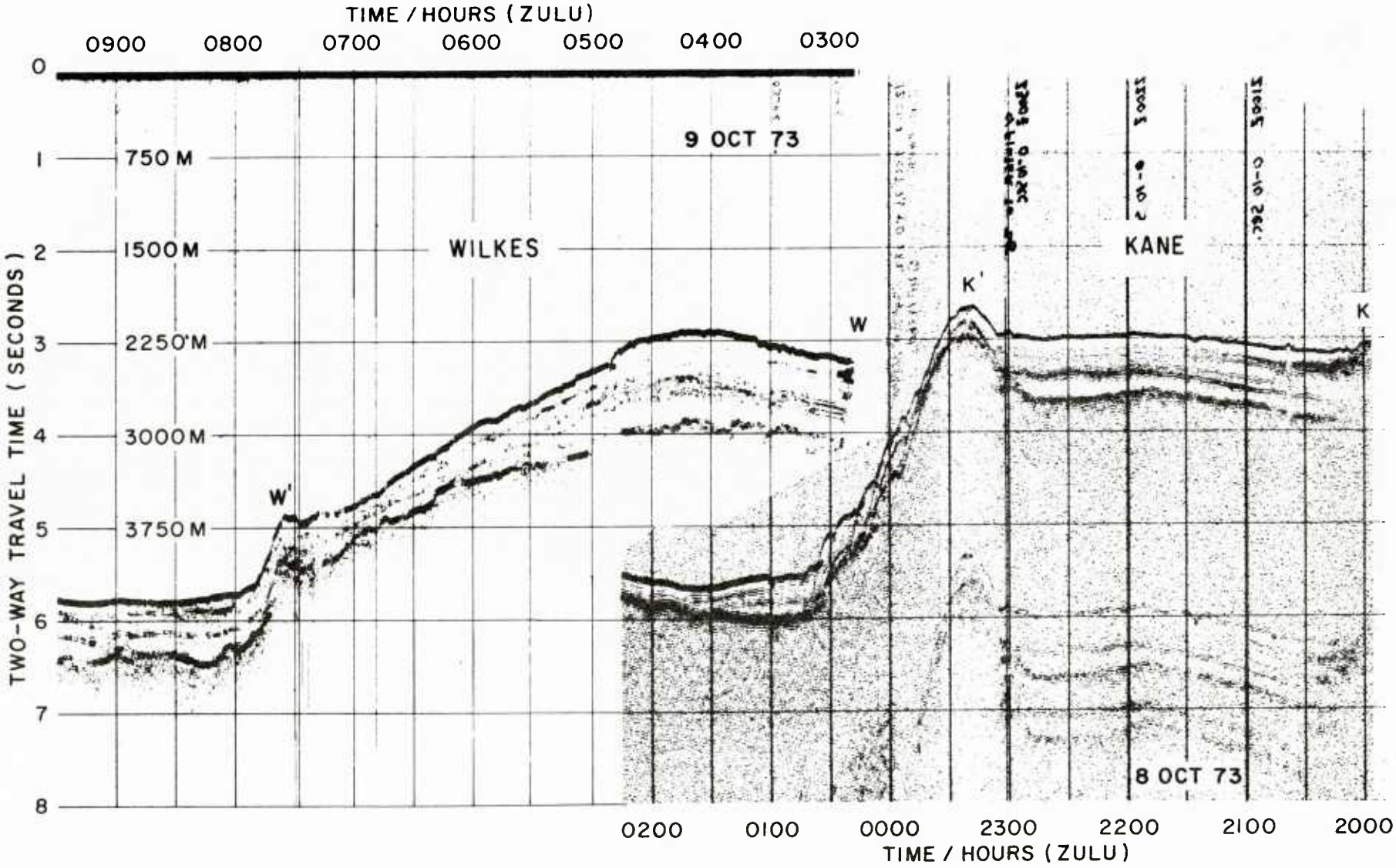

Figure 62. Seismic-profiler records near station 8.

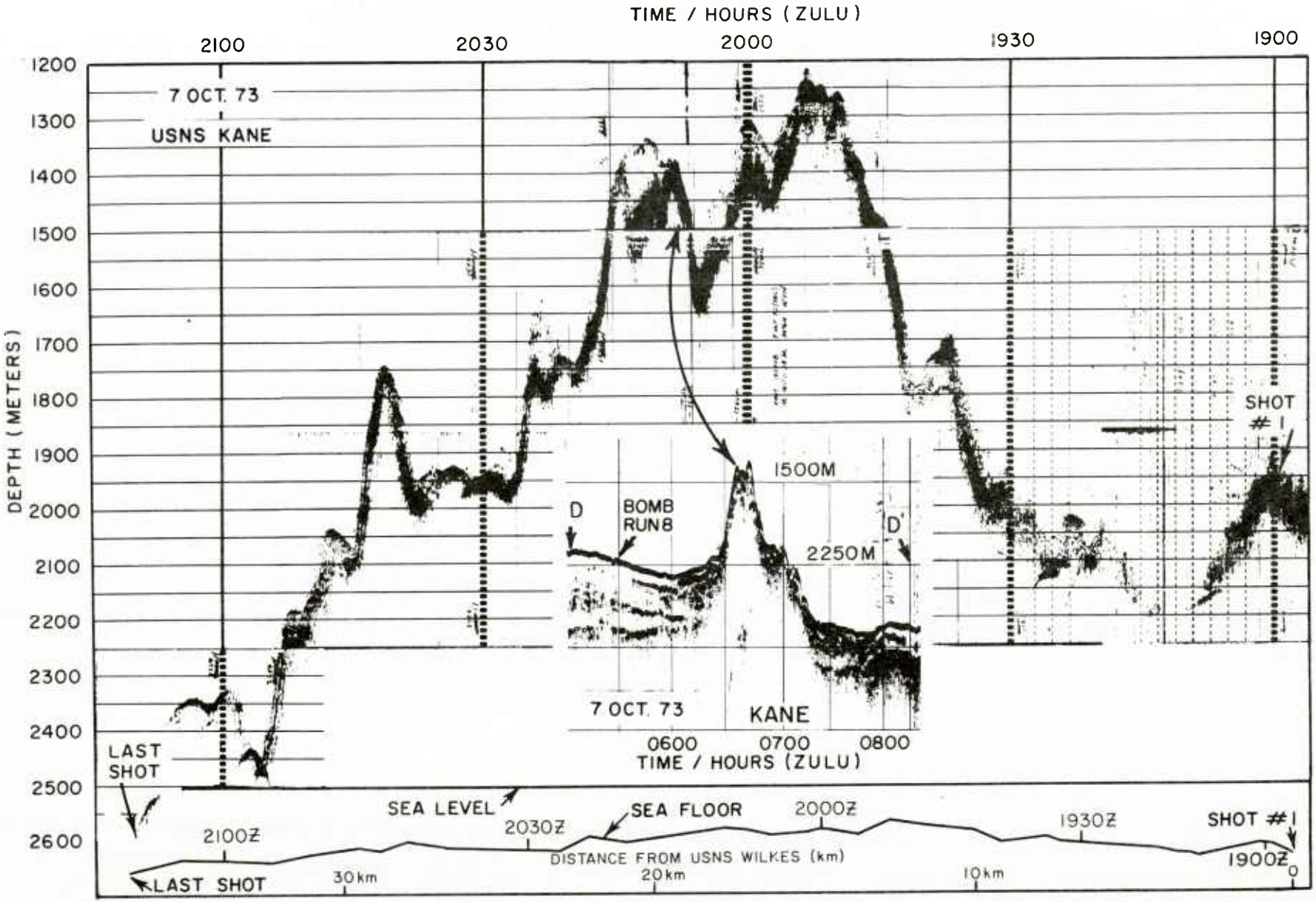

Figure 63. 3.5 kHz and seismic-profiler records at stations 7 and 8.

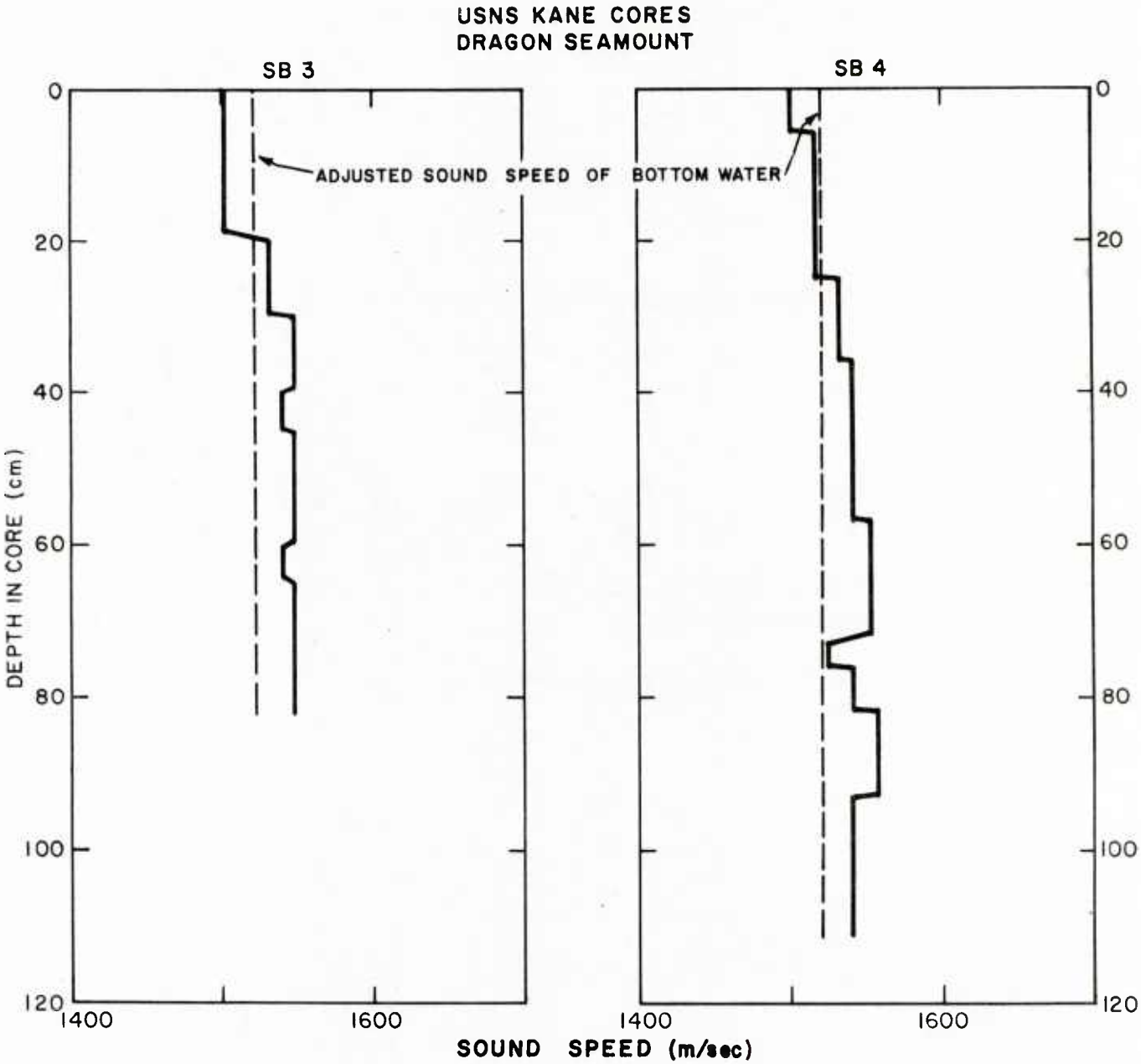

Figure 64. Sound-speed in cores taken at stations 7 and 8.

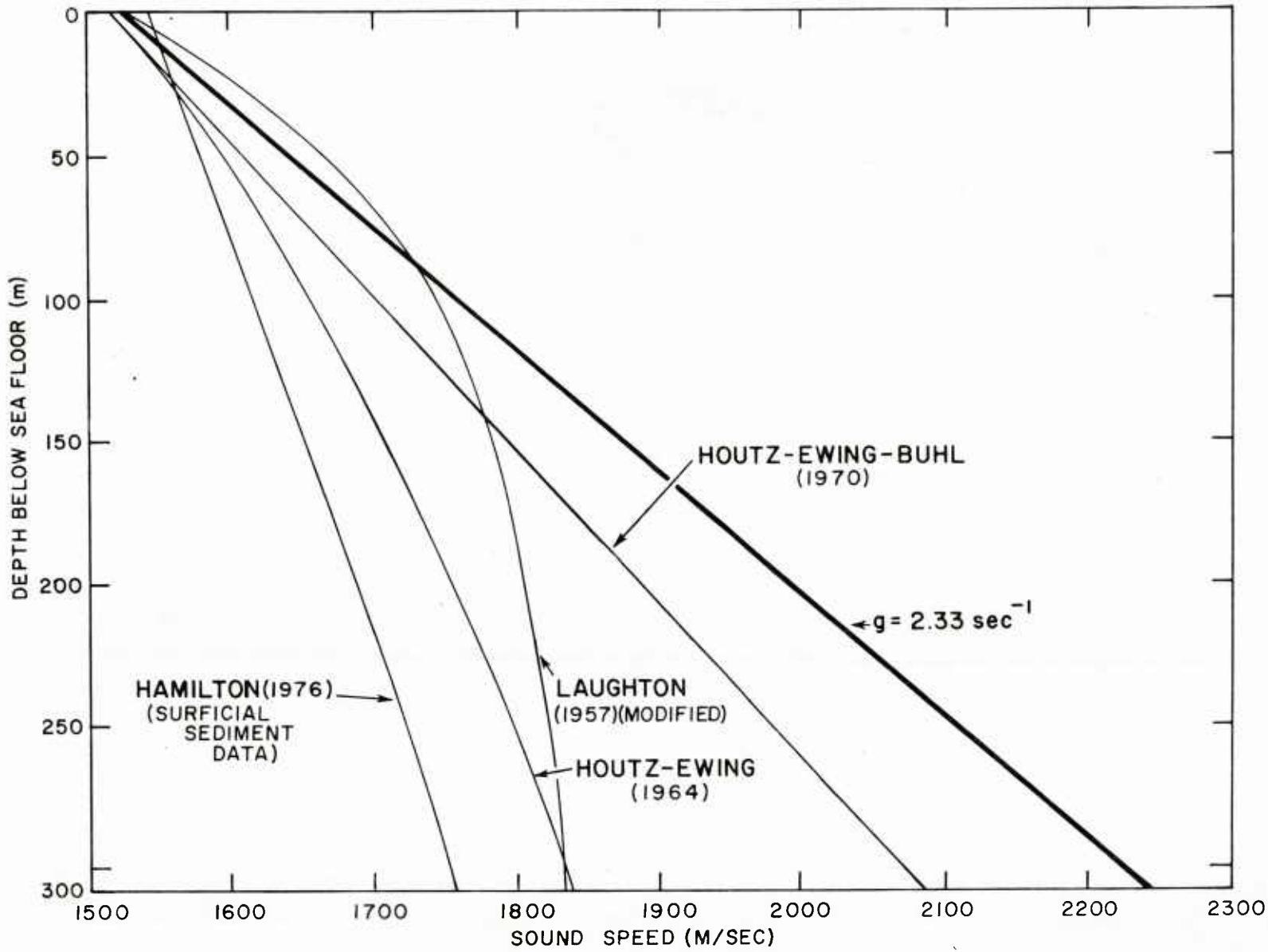

Figure 65. Predicted sediment sound-speed profiles at station 8.

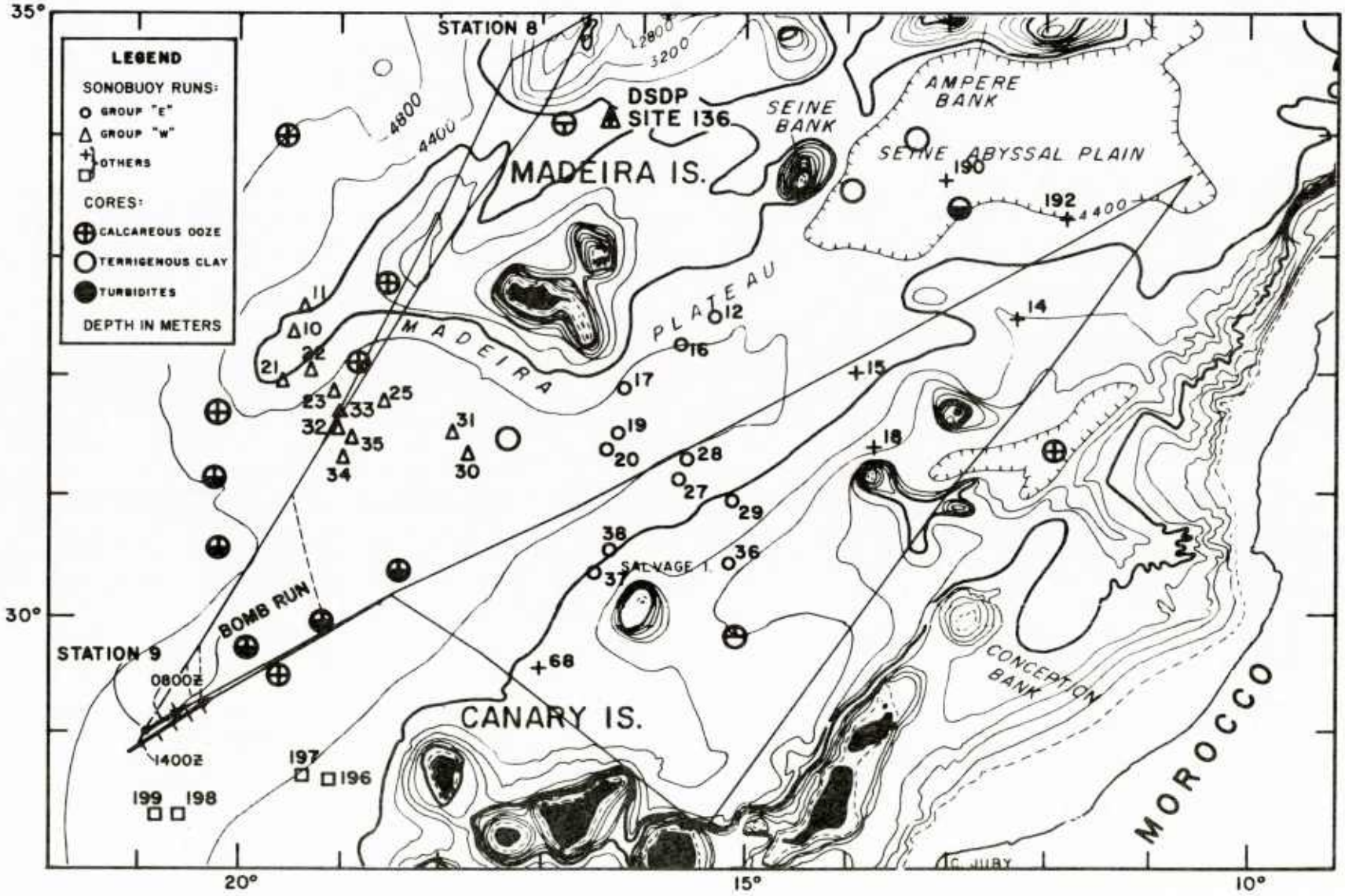

Figure 66. Area map for station 9 on the Lower Continental Rise south of Madeira.

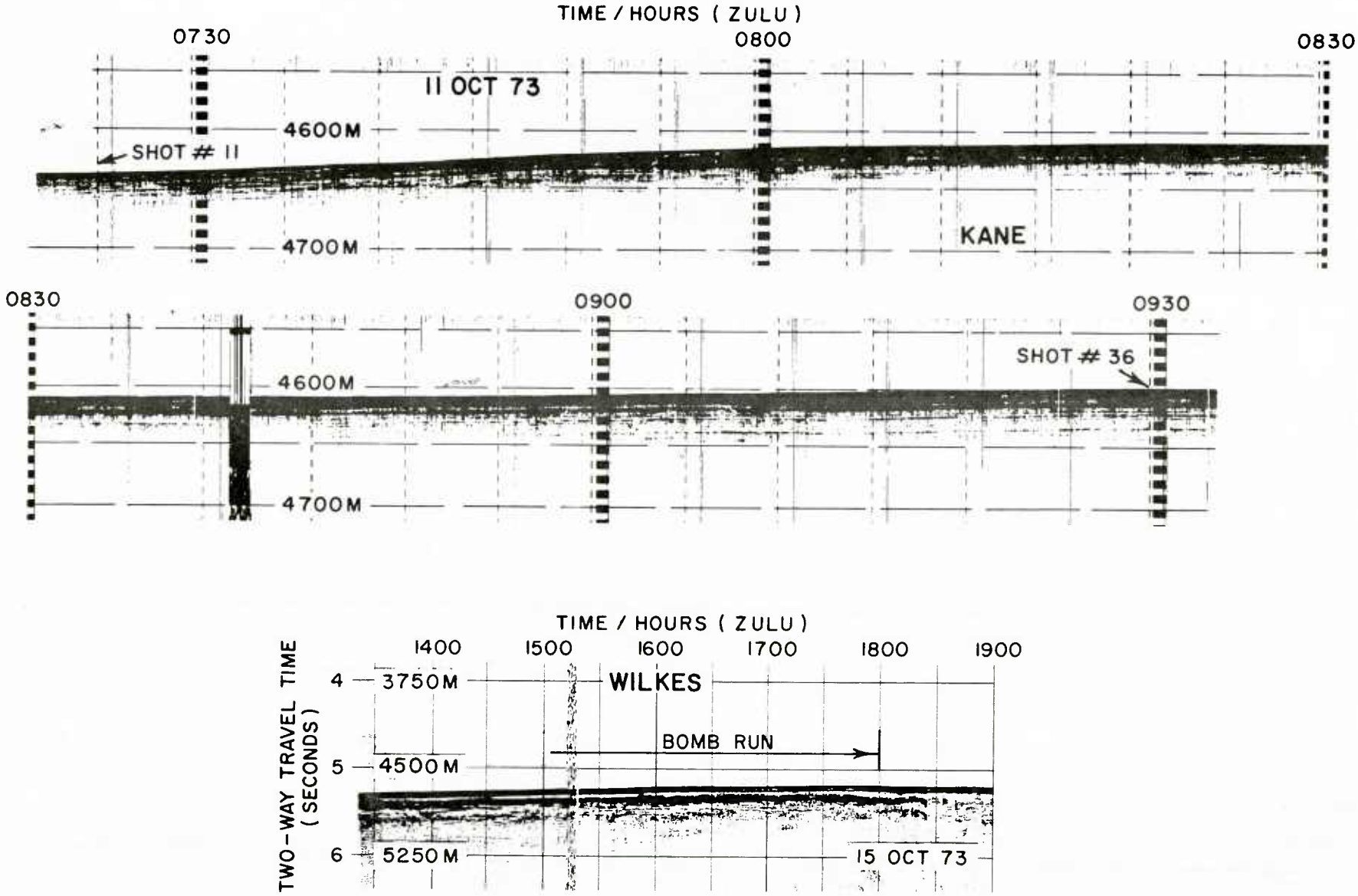

Figure 67. 3.5 kHz and seismic-profiler records along bomb run at station 9.

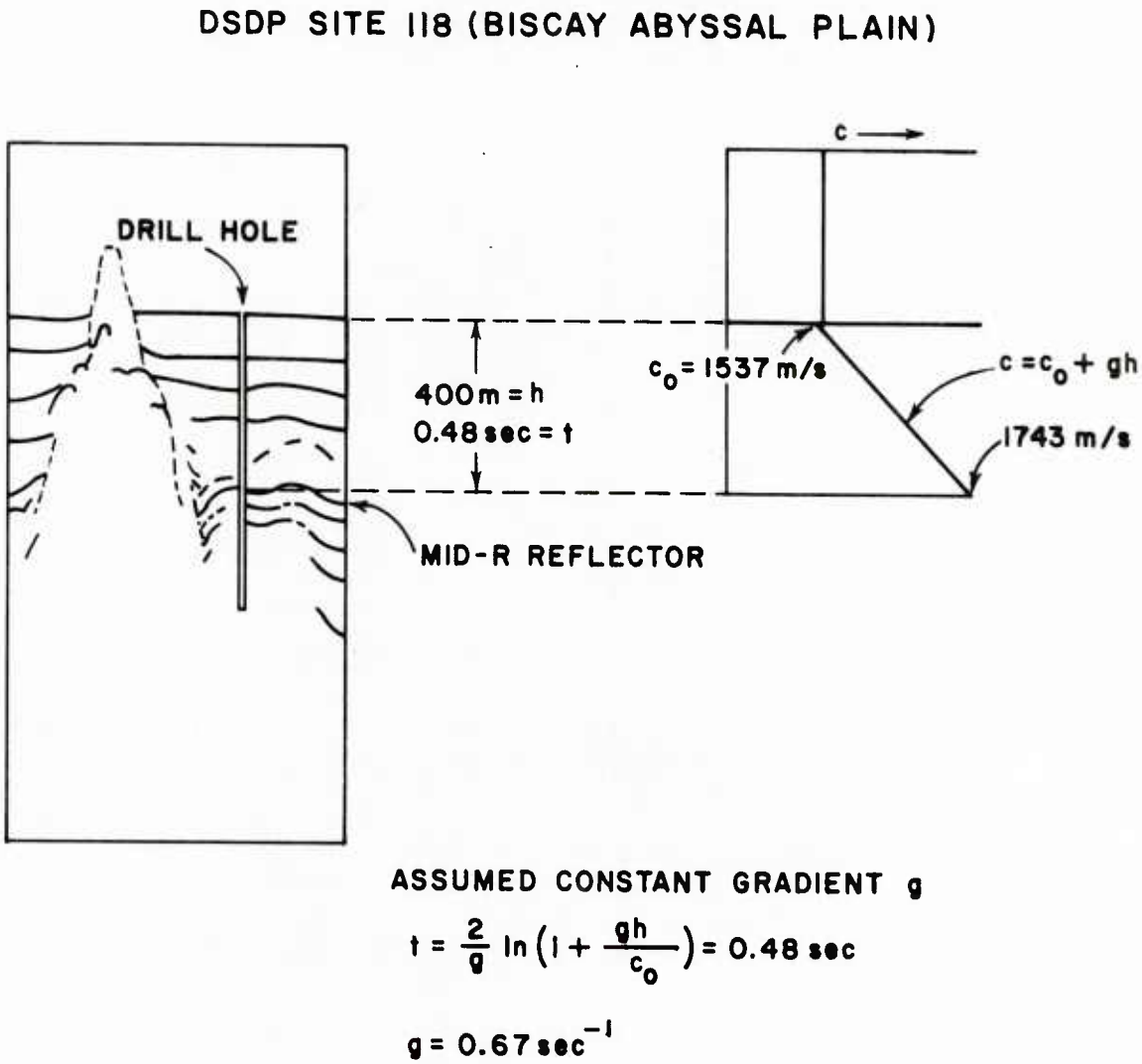

Figure 68. Sound-speed gradient at DSDP Site 118 determined with CRIC method.

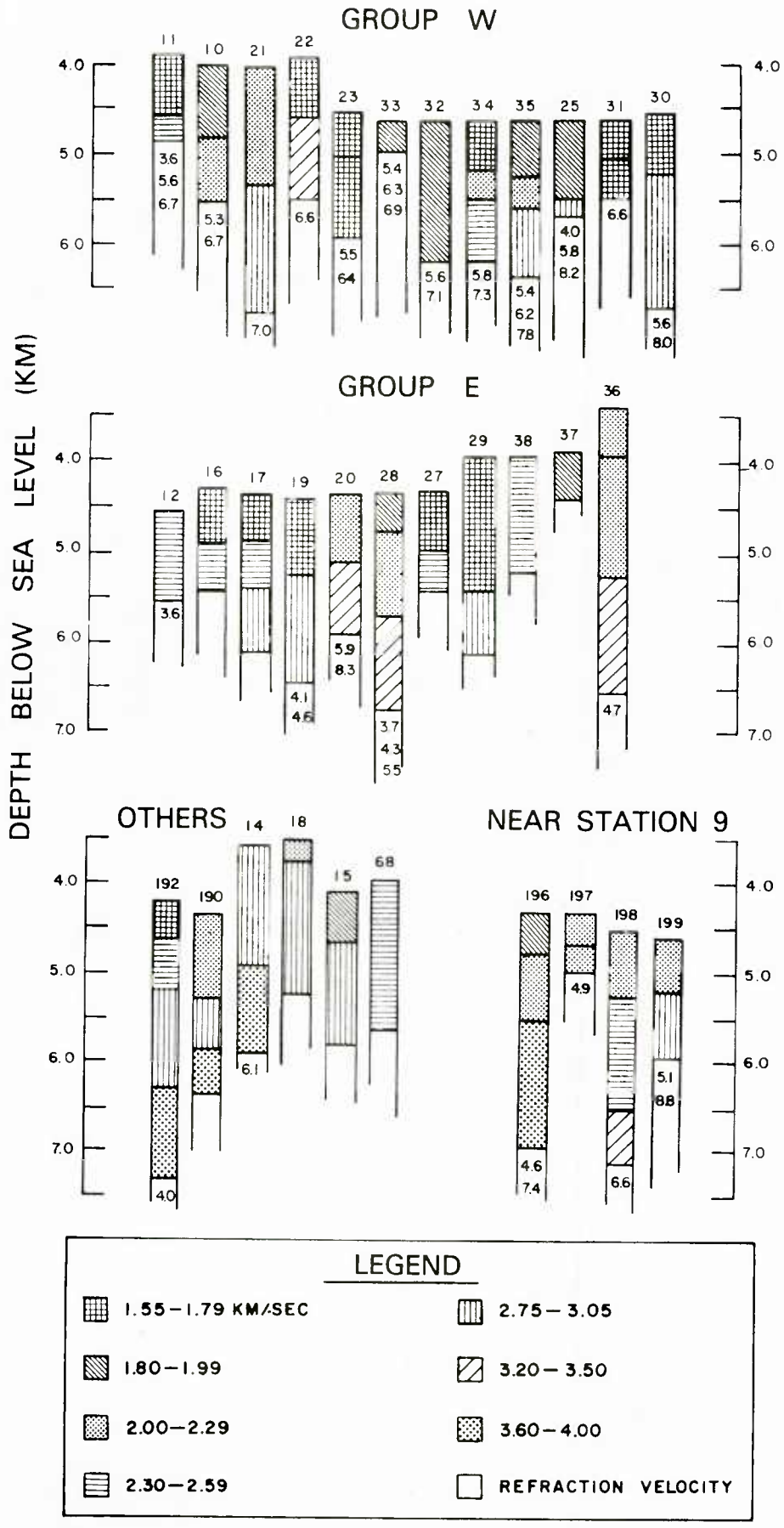

Figure 69. Results of sonobuoy stations off Northwest Africa.

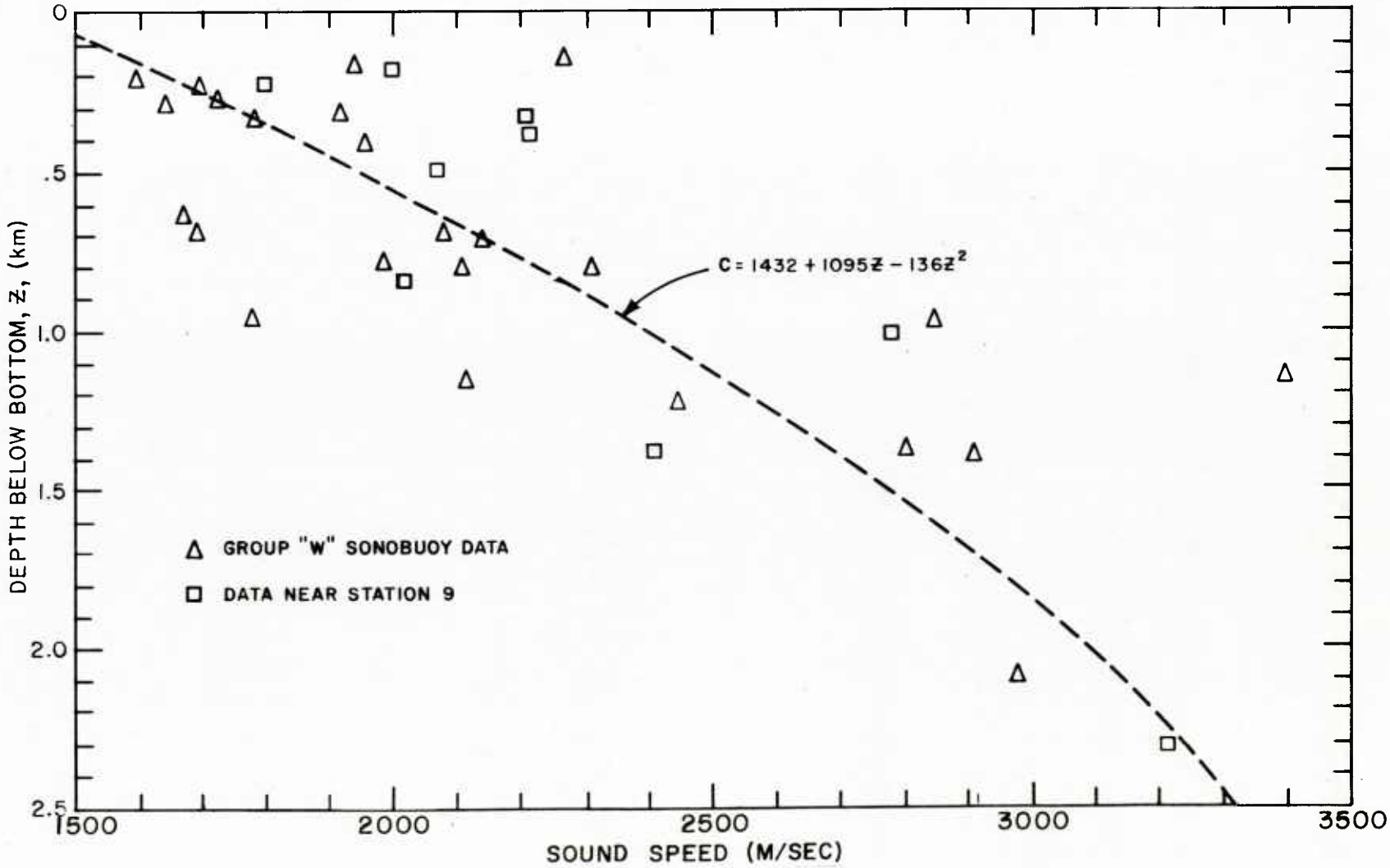

Figure 70. Sediment sound-speed profiles from wide-angle reflection data (Group W).

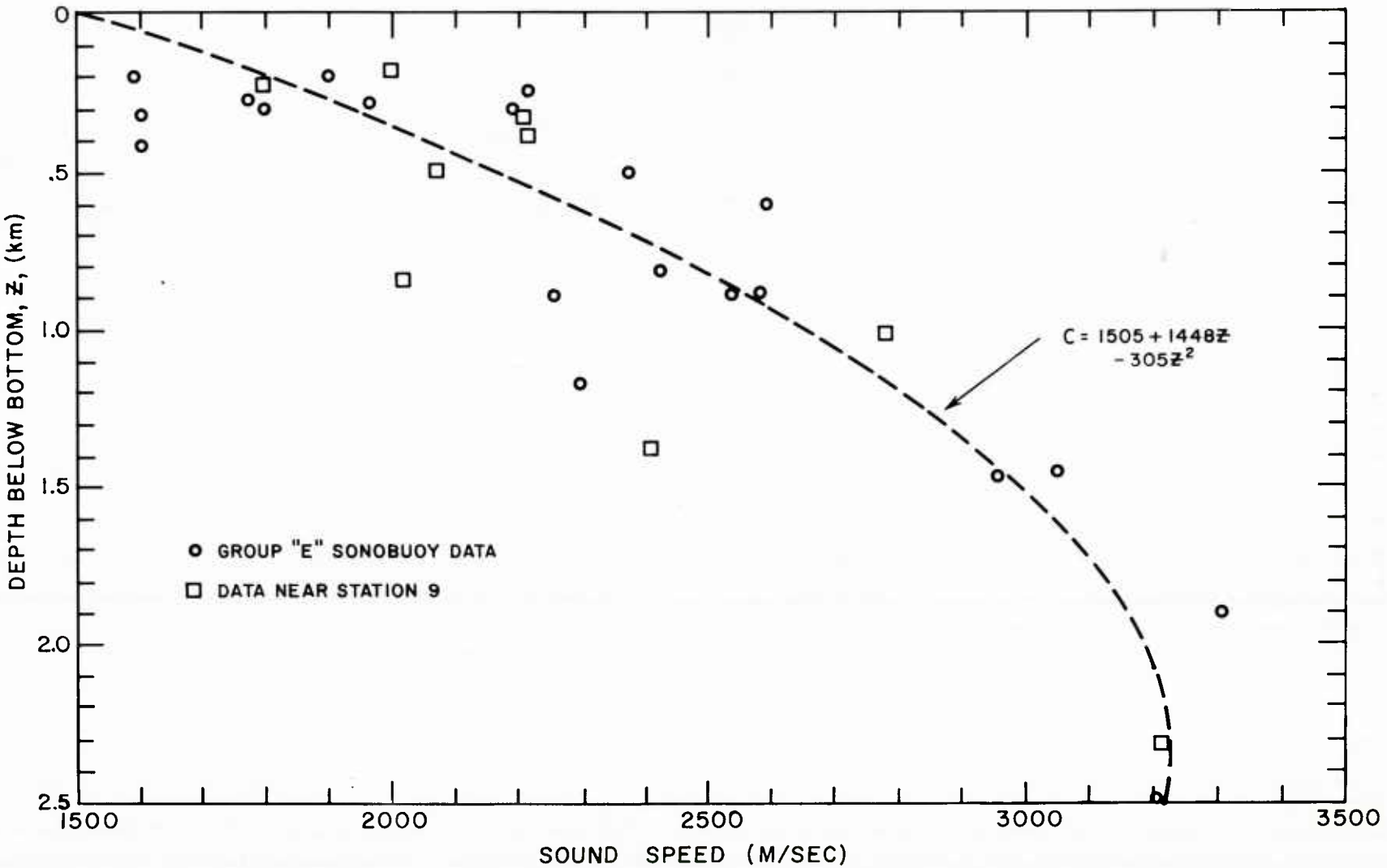

Figure 71. Sediment sound-speed profiles from wide-angle reflection data (Group E).

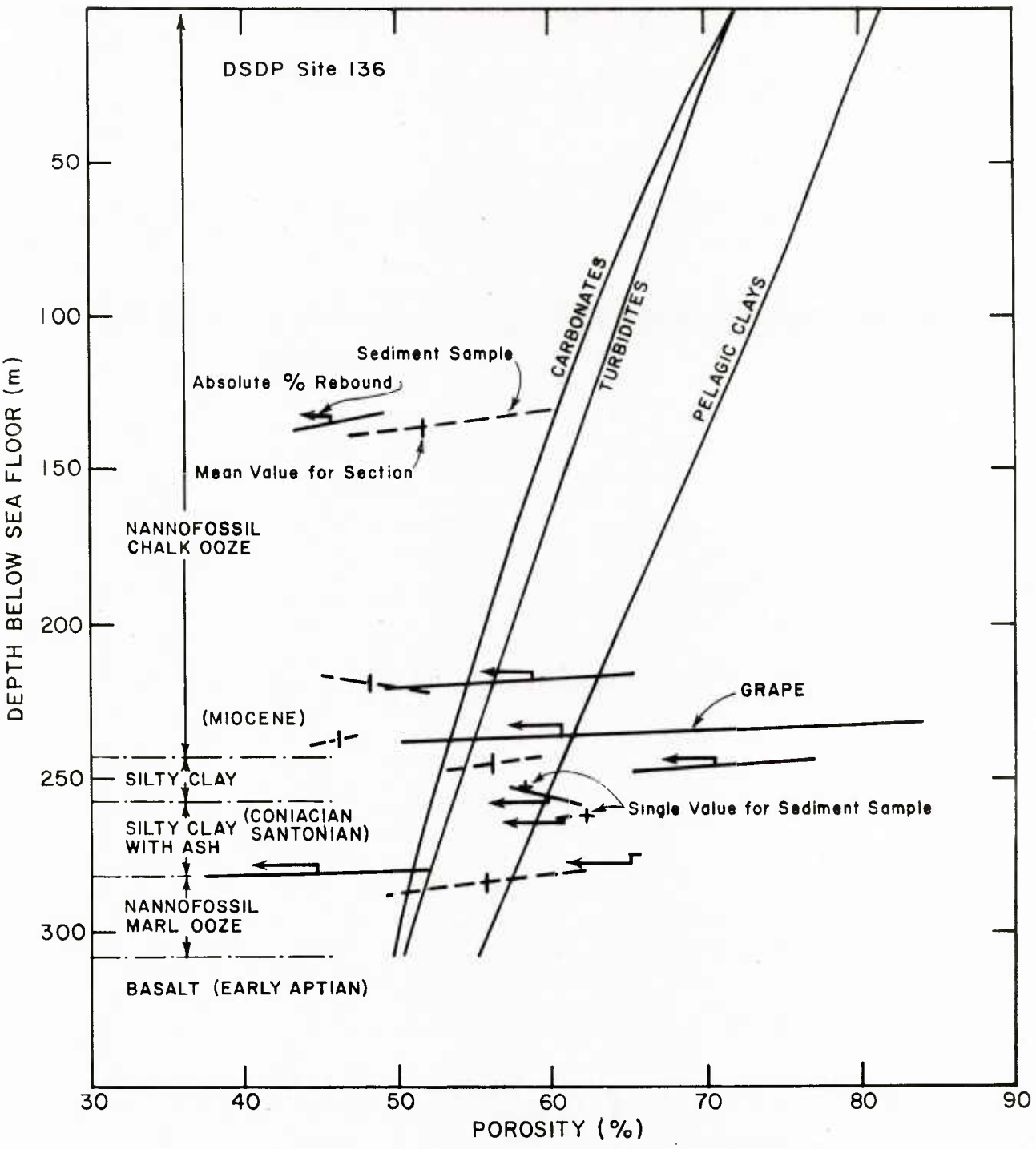

Figure 72. Sediment porosity values at DSDP Site 136.

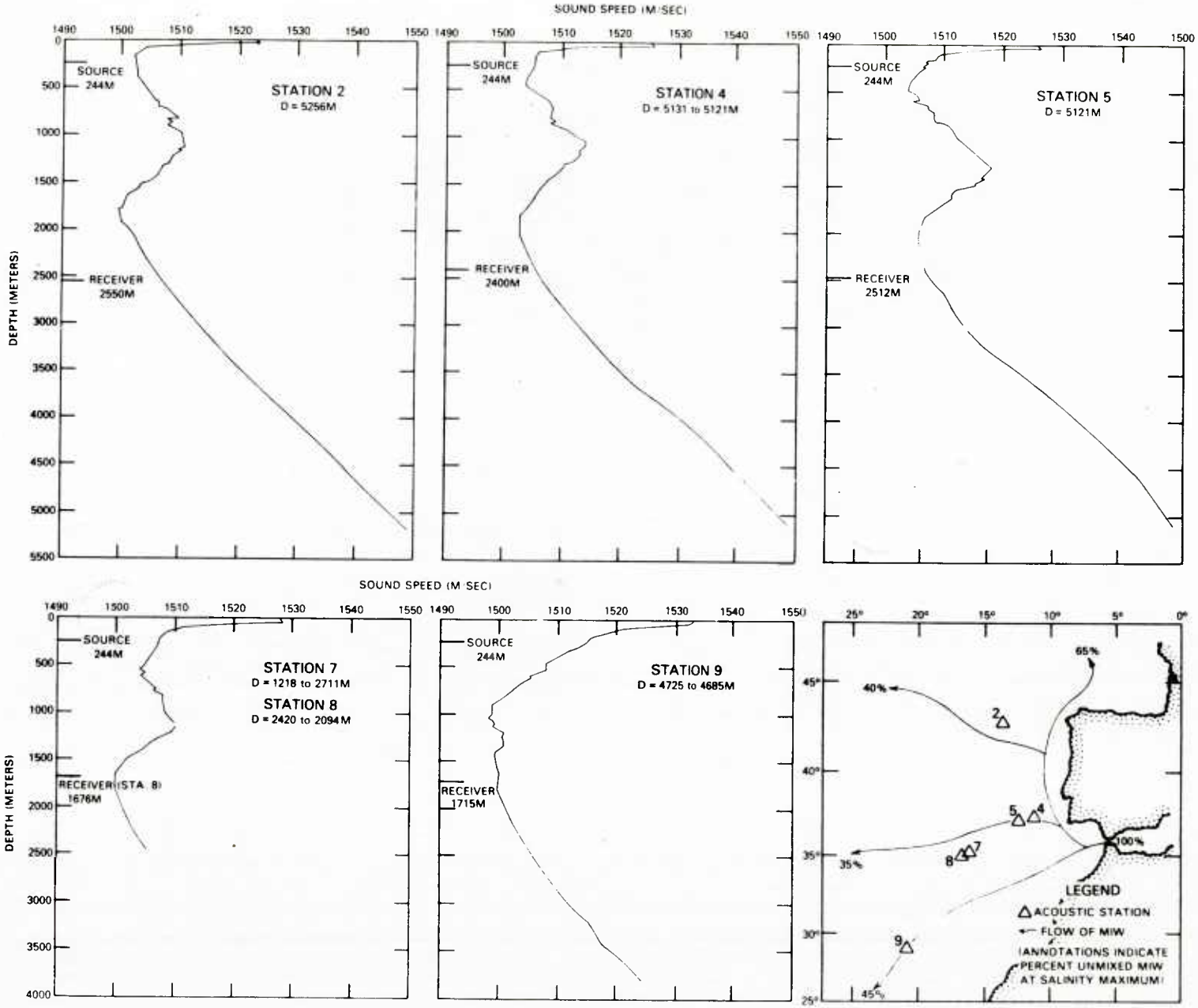

Figure 73. Water sound-speed profiles at acoustic stations.

Appendix A.
Tables of Formulas Used in Acoustical Analysis

Formulas given in Table 5 specify conditions to be satisfied for the validity of plane-wave approximations. The conditions are expressed in terms of computed parameters ε_k, ε_{rl}, and ε_t that must be small compared to one. The formulas were obtained from a calculation of reflectivity from a point source using the method of steepest descents following Brekhovskikh [38]. The formula for ε_t was obtained simply from the geometry of eigenrays connecting source and receiver.

The reflectivity calculation was applied only to singly reflected or refracted pulse arrivals in the context of a ray theoretical decomposition, and not to the total response from a continuous wave (CW) source. The condition on k was imposed in each case to assume that pulse arrivals were separated in time for a pulse bandwidth $\Delta\omega = kc$. Otherwise, a separate restriction on k was not required for the plane wave approxmation. Restrictions were found for products of the form kr^n where n = 1, 2, or 3, but these were automatically satisfied by the separate conditions on k and R. In the case of the pseudolinear halfspace, the restriction on k also satisfies requirements for the geometrical optics approximation (ray theory) for an observer at the top of the gradient halfspace (Brekhovskikh [38], pg. 206, eq. 16.39). When conditions for the plane-wave approximation are fulfilled, all pulse arrivals may be considered to arise from parallel rays at the same angle of incidence.

Table 6 gives numerical values for the quantities involved in the inequalities of Table 5. The ratios ε/R and ε/k represent the order of magnitude of the fractional error induced by neglect of non-plane-wave terms. These ratios are for worst case conditions at the extreme of the indicated angular interval. The error tends to drop off rapidly as the angle moves away from the end points of the interval; thus, much of the data corresponds to a better plane-wave approximation than indicated for the worst case conditions of Table 6.

The ratio ε_t/R is less than 0.1 in all cases and indicates a good plane-wave arrival time approximation. The other three ratios (ε_k, ε_{rl}, ε_{rh}) address all aspects of the plane approximation, including interpretation of pulse shapes, amplitudes, and arrival times. The conditions for which ε_k, ε_{rl}, and ε_{rh} are defined are sufficient for the validity of the plane-wave approximation. The condition on ε_t is thus, in some sense, a subset of these conditions and is far less restrictive. Correspondingly, the error term (ε_t) is much less than the more general error terms (ε_k, ε_{rl}, ε_{rh}).

The distinction between ε_t and ε_k, ε_{rl}, and ε_{rh} is important because the sound-speed parameters were extracted from the data on the basis of arrival time analysis. The ratio ε_t/R represents the plane wave error in arrival times; its smaller values suggest that good arrival-time accuracy is obtained in the plane-wave approximation, even though the total error is larger than desired in some cases. The larger values for ε_k, ε_{rl}, and ε_{rh} may be expected to signify greater error in determinations based on peak amplitudes such as in the estimation of attenuation coefficients.

Table 7 lists generalized formulas for ray path-lengths and travel times for layers with or without a turning point and for zero-gradient layers. Table 8 gives formulas for extracting sound-speed and layer thickness parameters by fitting straight lines to measured arrival time plots. Formulas for computing average attenuation are given in Table 9.

Table 5. Conditions to be satisfied for plane wave approximation

The symbols used in the table have the following meanings: r is the distance from the source-point image to the receiver; θ, θ_c, θ_r, are the grazing, critical grazing, and refracted grazing angles, respectively; k is the wave number ($2\pi/\lambda$); C is the sound speed in the water column, g is the sound speed gradient in the bottom; and h is the layer thickness. The column marked "grazing-angles" indicates that the inequality must be satisfied at either the highest or lowest grazing-angles used. The first three conditions for each model are sufficient to establish validity of the plane-wave approximation. The fourth inequality involving ε_t is sufficient for the accuracy of plane-wave arrival times and is less restrictive then the other three conditions.

Model	Requirements for plane wave approximation		Grazing-angles
Constant sound speed layer with totally reflecting bottom interface	$k \gg \varepsilon_k$	$\varepsilon_k = 1/(2h \sin\theta_r)$	low
	$r \gg \varepsilon_{rl}$	$\varepsilon_{rl} = 2h \sin^2\theta/(\sin^3\theta_r)$	low
	$r \gg \varepsilon_{rh}$	$\varepsilon_{rh} = h/4$	high
	$r \gg \varepsilon_t$	$\varepsilon_t = 2h \sin\theta \cos\theta_r/\sin\theta_r$	low
Pseudo-linear sound speed half space	$k \gg \varepsilon_k$	$\varepsilon_k = 3g/(2C \sin^3\theta_r)$	low
	$r \gg \varepsilon_{rl}$	$\varepsilon_{rl} = 2C \sin^2\theta/(g \sin\theta_r)$	low
	$r \gg \varepsilon_{rh}$	$\varepsilon_{rh} = 4C/g$	high
	$r \gg \varepsilon_t$	$\varepsilon_t = (C/g)\sin(2\theta_r)\sin\theta$	high

Table 6. Numerical values of the inequality conditions required for plane wave approximation

All quantities are defined in Table 5; angles are in degrees. The columns labeled θ give the range of grazing-angles over which the fractional errors ($\varepsilon/k, \varepsilon/R$) may be expected to be less than the values listed in the adjacent columns. The fractional errors give an order of magnitude measure of second-order terms in a power series expansion of the reflectivity in which the first-order term is the plane-wave contribution.

Sta.	Model	θ_c	ε_k/k	ε_{rl}/R	θ	ε_{rh}/R	θ	ε_t/R	θ
2	3	17.8	0.2	0.1	>22	0.5	<35	0.08	<35
4	1	19.4	0.1	0.1	>23	0.002	<90	0.02	>23
4	3	0	0.4	0.02	>15	0.3	<35	0.02	<35
5	3	13.9	0.4	0.1	>18	0.6	<35	0.08	<35
8	1	22.2	0.2	0.2	>26	0.004	<90	0.02	>26
9	1	19.4	0.1	0.1	>23	0.003	<90	0.02	>23

Table 7. Travel time and path-length formulas

Travel-time and path-length differences are t_n and S_n, respectively, between the first and nth arrivals. The incremental travel-time and path-length for arrival n in layer i is indicated by t_{ni}, S_{ni}, respectively. Corresponding quantities for a layer in which the ray has a turning point are given by t_{nT} and S_{nT} respectively; i.e., T is the index for the layer containing a turning point and is dependent on the grazing-angle θ.

$$t_n = \sum_{i=1}^{n-1} t_{ni} \qquad n-1 \leq T$$

$$t_{ni} = (2/3g_i)[\mathrm{Sin}^3\,\theta_{Ri} - (\mathrm{Sin}^2\,\theta_{Ri} - 2g_i\,h_i/C_{oi})^{3/2}] \qquad i \neq T,\ g_i \neq 0$$

$$t_{nt} = 2\,\mathrm{Sin}^3\,\theta_{RT}/(3\,v_{g_T})$$

$$t_{ni} = 2h_i\,\mathrm{Sin}\,\theta_{Ri}/C_{oi} \qquad g_i = 0$$

$$S_n = \sum_{i=1}^{n-1} S_{ni} \qquad n-1 \leq T$$

$$S_{ni} = (C_{oi}/g_i)\,[\mathrm{Sin}\,\theta_{Ri} - (v_i^{-2} - \mathrm{Cos}^2\,\theta_{Ri})^{1/2}/v_i + \mathrm{Cos}^2\,\theta_{Ri}\,\ln|(1 + \mathrm{Sin}\,\theta_{Ri})/[v_i^{-1} + (v_i^{-2} - \cos^2\,\theta_{Ri})^{1/2}]|] \qquad i \neq T,\ g_i \neq 0$$

$$S_{nt} = (C_{oT}/g_T)\,[\mathrm{Sin}\theta_{RT} + \mathrm{Cos}^2\,\theta_{RT}\,\ln|(1 + \mathrm{Sin}\theta_{RT})/\mathrm{Cos}\,\theta_{RT}|]$$

$$S_{ni} = 2h_i/\mathrm{Sin}\theta_{Ri} \qquad g_i = 0$$

$$1/v_i = [1 - 2g_ih_i/C_{oi}]^{1/2}$$

$$\mathrm{Cos}\,\theta_{Ri} = (C_{oi}/CW)\,\mathrm{Cos}\,\theta_o$$

$$C_{oi} = (CR_1\,CR_2\,\ldots\,CR_i)\,(v_1\,v_2\,\ldots\,v_{i-1})\,CW$$

$$0 \leq (C_{oT}/2g_T)\,[1 - (C_{oT}/CW)^2\,\mathrm{Cos}^2\theta_o] \leq h_T \qquad g_T \neq 0$$

Table 8. Formulas for evaluation of model parameters

The variable y is plotted versus x and a straight line is fitted. Model parameters are computed from the slope and x-intercept. For $i \neq T$ and $g_i \neq 0$, h_i is computed in terms of t_i.

Function to be plotted in the form: $y = a(x - x_{int})$	Parameter Extracted
Rayleigh Analysis	
$i = 1$ $y_1 = [\frac{1 - R_1}{1 + R_1} \text{ Sin } \theta_o]^2$	$DR = \lvert a \rvert^{1/2}$ $\frac{C_{oi}}{CW} = (x_{int})^{-1/2}$
Arrival Time Analysis	
$x = \text{Cos}^2 \theta_o$ $i = T$ $y = (\frac{3}{2} t_i)^{2/3}$	$C_{oi}/CW = (x_{int})^{-1/2}$ $g_i = (\lvert a \rvert x_{int})^{-3/2}$ $h_i \geq \frac{1}{2} CW \lvert a \rvert^{1/2} y$
$g_i = 0$ $y = (t_i)^2$	$C_{oi}/CW = (x_{int})^{-1/2}$ $h_i = \frac{CW}{2} \lvert a \rvert^{1/2}$

$i \neq T$, $g_i \neq 0$: C_{oi} and g_i are first determined at those angles for which $i = T$ using formulas above then

$$h_i = \frac{C_{oi}}{2g_i} [\text{Sin}^2 \theta_{Ri} - (\text{Sin}^3 \theta_{Ri} - \frac{3g_i t_i}{2})^{2/3}]$$

Table 9. Formulas for attenuation analysis

Formulas for attenuation analysis. The symbol κ_i represents the average attenuation coefficient in dB/m/kHz encountered by the ith arrival when i=T. Formulas for S_i are given in Table 7.

$$\kappa_i = \frac{746.2}{S_i} \left[1 - (1 + 0.36 \ln (1.2 P_i/T_i))^{1/2}\right]$$

$$T_i = (1 - R1^2) (1 - R_2{}^2) \ldots . (1 - R_{i-1}^2)$$

$$R_i = \frac{DR_i \text{ Sin } \theta_{i-1} - (1/CR_i) \text{ Sin } \theta R_i}{DR_i \text{ Sin } \theta_{i-1} + (1/CR_i) \text{ Sin } \theta R_i}$$

$$\text{Cos } \theta R_i = (C_{oi}/CW) \text{ Cos } \theta_o$$

$$\text{Cos } \theta_i = (C_i/CW) \text{ Cos } \theta_o$$

$$C_i = (CR_1 \; CR_2 \ldots . \; CR_i) \; (v_1 \; v_2 \ldots . \; v_i) \; CW$$

$$C_{oi} = C_i/v_i$$

P_i is the amplitude of the ith arrival of the unit impulse response, bandpass-filtered with a Gaussian-shaped filter spectrum with 3 dB down points at 43 and 87 Hz.

Appendix B.
Processed Acoustical Data and Analysis for Each Station

Station 2

In the low frequency traces of Figure 11, the dominant arrival seen at grazing angles of 35° and less is interpreted as a refracted arrival. The same type of arrival may also be seen in the expanded high-frequency traces of Figure 12 at grazing angles of 20.7° and less. Strong first-arrival pulses are seen which may contribute to low losses at high frequencies.

The bottom loss shown in Figures 13 and 14 is characterized at low frequencies by a low-loss region and a high-loss region. The angle at which the transition between the two behaviors occurs is the highest angle for which the strong low-frequency refracted arrival is observed. At frequencies above 100 Hz the transition is not as sharp because at high frequencies less energy is carried by the refracted arrival due to sediment attenuation along the refracted path. Nevertheless, the loss on the average increases slightly with grazing angle; no simple trend as a function of frequency is seen.

At high angles for which a refracted arrival is not observed, the loss at 100 Hz and below is on the order of 10 db, whereas at frequencies above 100 Hz, the loss is on tne order of 5 db with some significant fluctuation in the vicinity of 2000 Hz. This suggests that the sediments are better reflectors at high than at low frequencies, and is consistent with the strong reflectors observed in the high frequency impulse responses.

Strong fluctuation peaks are observed at low frequencies at angles around 25°. This is consistent with bottom loss predictions calculated for a gradient layer model. Accordingly, the loss increases slowly and smoothly with grazing angle until an angle is reached at which the refracted arrival is time-delayed by a half wavelength. At this angle, destructive interference produces the first large peak in the bottom loss. The fluctuation pattern then continues to all higher angles. In this data, the refracted arrival disappears at an angle just above the onset of the fluctuation pattern so that only the beginning part of the pattern is seen.

Further evidence for the interference hypothesis is seen in: (1) the strong peak at 24°, 80 Hz, and its companion at twice the frequency at 24°, 160 Hz; and (2) the small peak at 20°, 100 Hz, and its strong companion at 20°, 200 Hz. Differences in the magnitudes of the peaks may be due to an undersampling of the loss curves along the grazing angle axis.

The signal-to-noise ratio averaged over all angles for the 100 Hz one-third-octave frequency band was 29 dB.

The Rayleigh analysis shown in Figure 15 gives a density ratio DR=1.4 and a sound speed ratio CR=0.97. The low frequency arrival times were first analyzed as a single layer in Figure 16 giving g=0.8 sec^{-1}, CR=1.05, and h>280 m. Note that the data were plotted both under the assumption of a refracting layer and under the assumption of a reflecting layer. The refracting layer assumption provided a good linear fit, whereas the reflecting layer assumption did not.

Because the high frequency traces consisted primarily of two dominant arrivals at low angles, the analysis was extended to lower angles using arrival times measured from the well-resolved high frequency traces. As shown in Figure 17, the lowest angle arrivals could be interpreted as either a constant sound speed layer (CR_1=1.00, h_1=12 m) or a refracting layer (g_1=10 sec^{-1}, CR_1=0.96). The higher angle low-frequency arrivals were reinterpreted (Fig. 18) on the basis of Model 5 (g_2=0.8 sec^{-1}, CR_2=1.05, h_2 > 260 m) and Model 6 (g_2=0.8 sec^{-1},

Station 9

In the low-frequency impulse responses of Figure 41, the dominant penetrating arrival appears at grazing angles of 40.5° and less. At higher angles numerous smaller amplitude pulses are seen instead. The high-frequency traces of Figure 41 show that the dominant arrival is made up of a complex distribution of reflectors. The expanded high-frequency traces of Figure 42 show that the response is too complicated for a simple model at high frequencies.

The bottom loss at low frequencies (Fig. 43) changes gradually from low losses at low grazing-angles to high losses at high angles. At frequencies above 1 kHz, the loss curves (Fig. 44) tend to be flatter or somewhat concave downward with grazing-angle. At all angles and frequencies the curves tend to have superimposed strong oscillation patterns. The oscillation pattern at low frequencies and angles below 41° is derived from the interference between two dominant arrivals, and at higher angles between the first arrival and multiple arrivals at times greater than 100 msec. Unlike Station 8, at high frequencies there are numerous arrivals after the first. As a result, the bottom loss tends to smooth out at high angles and become more oscillatory at low angles. The signal-to-noise ratio averaged over all angles for the 100 Hz one-third-octave frequency band was 22 dB.

The Rayleigh analysis (DR=1.5, CR=0.97) was very precise as shown in Figure 45 by the close clustering of points about the straight-line fit. The arrival-time analysis (CR=1.06, h=80 m) in Figure 46 also produced a good fit on the basis of a reflecting layer. As in the case of Station 8 there is a large discrepancy between CR_R and CR_T, but again, this may represent sound-speed changes in the uppermost part of the sediment, which is not resolved in the arrival times of the low-frequency traces. The discrepancy was reduced by fitting Model 7 to the data (Fig. 47: $g=4.4$ sec^{-1}, $CR_1=0.97$, $h_1=29$ m, $CR_2=1.00$, $h_2=42$ m).

Station 7

The data from Station 7 is strikingly different from the rest. The impulse responses at both high and low frequencies (Figs. 48 and 49) are very random, i.e., the reflected pulses do not correlate from trace to trace. In order to show the long duration of the signals, the time scale in the figures has been compressed eight times that of the other stations. The expanded high-frequency traces show that the first arrivals are not well-defined. Note that some of the abrupt signal decays, such as seen in the traces for grazing angles 11.5-12.5° at 800 msec, are really an artifact of the processing. In these cases, the signal was not recorded or digitized for a sufficient length of time.

In general, the bottom-loss curves (Figs. 50 and 51) are nearly flat, but are uneven functions of grazing-angle at all frequencies and angles. The losses range primarily from 15 to 20 dB, sloping gently to lower losses at low angles and for low frequencies. At frequencies below 100 Hz the trend suggests a rapid decrease in the loss as the grazing-angle decreases below 10°.

The data are suggestive of scattering from a very rough surface with no detectable coherent component. This observation is consistent with the fact that this geophysical province was a rough, unsedimented, elongated seamount. Because of the lack of coherence, no modeling was attempted. It is interesting to note that the three standard deviation confidence limits on the bottom-loss curves collapse to a single curve, although the average signal-to-noise ratio at 100 Hz (29 dB) is not much better than, for example, Station 8 (27 dB). The reason is that the number of degrees of freedom is much greater because of signal duration. The greater signal duration results in higher frequency resolution and hence, more independent spectral estimates within a one-third-octave band. The small improvement in signal-to-noise ratio in comparison

with the other stations is attributed to the smaller dynamic range of the time spread signal. The attenuators or amplifiers were set to a higher gain to more fully utilize the available dynamic range of the tape-recorder. In effect this suppressed the tape-recorder noise floor to a lower level relative to the average signal level.

Appendix C.
Geological Analysis of Each Station

Comprehensive geological data analyses for each station site are presented in this appendix. The discussion of geological considerations common to several stations are deferred to Appendix D. Special emphasis is placed on the derivation of several possible sediment sound-speed profiles as determined from available geological data. The comparison with the profiles derived from the acoustic data analysis is shown in Figure 10.

Station locations are defined as the location of the anchored ship, USNS WILKES, during the reflectivity experiments. USNS KANE dropped SUS charges along a radial path called the bomb run. Seismic profiler and 3.5 kHz records taken along or near the bomb runs are reproduced here. The sound-speed profiles of the water column at the stations are illustrated in Appendix F.

Station 2

Station 2 was located near the northern boundary of the Iberian Abyssal Plain as shown in Figure 52. The plain is characterized by flat-lying, horizontally stratified sediments characteristic of abyssal plains. The sediments are not as thick as those in many abyssal plains, thus offering basement exposures in several places. Because of the thinner sediments, it was felt that this plain would offer geoacoustic properties different from the Tagus Abyssal Plain (Stations 4 and 5) or the Madeira lower continental rise (Station 9).

Geological Information

The boundaries of the Iberian Abyssal Plain are generally indicated in Figure 52 by the 5200 m contour on the west (roughly along 15°W) and by the 4400–4800 m contour on the east and south. The plain has a general slope from northeast to southwest with an average slope of 1:3600. Reynolds [46] compiled a geological analysis of the whole abyssal plain, emphasizing the area at Station 2. Much of the following information is taken from his report.

A seismic profiler record taken on a 1971 KANE cruise near Station 2 (Fig. 52) is shown in Figure 53; Station 2 corresponds to a position on the record near the break at 2300Z. The abyssal plain is characterized by several features visible on this profile. Between 0500 and 0700Z, a thick section of sediment exists as a transition zone between the fault-block to the west and the rough flat block relief of the continental margin to the east. This feature is observed all along the eastern boundary of the plain, varying between 5 and 40 m in width. In all cross sections of this feature, the surface is nearly smooth; in some, reflectors can be traced from the abyssal plain into this zone with no loss of continuity, while in other sections, continuity is broken.

Beneath the stratified flat-lying sediments, the very rough acoustic basement can be seen to the left (west) of 2300Z in Figure 53, varying between 0.8 and 2.0 sec two-way travel time below the sea floor. This roughness is characteristic of the basement throughout the abyssal plain as it rises to the west approaching the flanks of the Mid-Atlantic Ridge. At about 40°15'N the acoustic basement descends to the southeast with the overlying sediment forming a wedge of over 2.0 sec of thickness which increases to the southeast (see Fig. 52). An arc of sediment thicker than 1.0 sec extends from the southeastern corner of the plain along the eastern side and across the northern end of the plain. Sediment in the southwest corner and the west central part of the abyssal plain is generally less than one second thick and has many basement exposures. At a latitude of about 39°40'N, the basement emerges from the abyssal

plain to form an east-to-west topographic high along the southern edge of the Iberian Abyssal Plain.

Two main sedimentary units are apparent in the Iberian Abyssal Plain, and are separated by a prominent reflector that is continuous throughout the basin. The sedimentary unit above this reflector varies from a thickness of 0.3 sec in the northwest to greater than 1.0 sec in the east and southeast. The prominent reflector is flat-lying in the north, begins to dip to the southeast at about 42°N, and becomes less reflective until it is no longer discernible in the south. In many areas of the Iberian Abyssal Plain, the upper sedimentary unit (Unit 1) lies unconformably on the major reflector which marks the top of the underlying Unit 2 (Fig. 53). Both sedimentary units comprise interbedded layers of transparent (pelagic) and reflective (turbidite) layers; however, the upper unit is flat-lying, but the lower stratified unit is characterized by faulting and enough nonhorizontal orientation in the conformable reflectors to suggest tectonic deformation of this unit after deposition.

Within the upper unit are two distinct sections. The upper 0.2 sec (Section A) contains a sequence of highly reflective layers; weaker reflectors below give the lower section (B) a more transparent character. Section B is observed only in the northern part of the Iberian Basin. To the south, nearing the source of sediments at Nazare Canyon, reflectors of Section B gradually become more prominent, until at 42°N no distinction can be made between Sections A and B.

Available 3.5 kHz data were analyzed to determine the number of reflectors per meter, continuity of reflectors, dip, and depth of penetration. Analysis of 3.5 kHz data was hindered because the depth in the northern part of the abyssal plain and a portion of the southern part fall in the depth range where the return signal is gated to eliminate interference by the outgoing pulse. Because of the poor quality of the gated records, no 3.5 kHz record is presented for this station. Measurements made to determine the number of reflectors per meter for the remaining areas in the southern Iberian Basin, however, give a mean value of 0.297 with a range of 0.267-0.320 (3.37 m between reflectors, range 3.74-3.12). As discussed in Appendix D.2, this value indicates fewer reflectors per meter than actually exist.

Two core samples taken north of 42° in the plain consist of firm clay and firm silty clay, both with a carbonate content of 30-40%. Other coring attempts in the northern Iberian Abyssal Plain failed to penetrate the sea floor, but had highly compacted clay samples in the core cutters. The R/V VEMA (Lamont-Doherty) core taken near 41°N, 15°W shows several coarse-grained turbidite layers, 10-15 cm thick; a USNS KANE core at the plain's northern edge contained one 10 cm turbidite (Fig. 52). Core studies show that the pelagic material in the Iberian Basin consists of layers of foraminiferal lutite with moderate to moderately high calcium carbonate content. The turbidites are made up of terrigenous material and shallow water detritus derived from the western European land mass and continental shelf, grading upward from coarse-grained basal layers to fine-grained clay or silty clay. Contact of the turbidites with the layer below is very distinct, but the upper contact is imperceptible.

The sediments in the northern part of the Iberian Abyssal Plain are derived predominantly from the Bay of Biscay. Turbidity currents flowing across the Bay of Biscay are rejuvenated as they reach the steeper gradient of Theta Gap and flow southwestward into the Iberian Abyssal Plain [47]. Because of the great distance from its source, these turbidites would be expected to have fine-grained basal layers (silt to sandy silt).

Nazare Canyon, southeast of the plain, is the major supplier of turbidite sediment to the entire Iberian Abyssal Plain. Turbidite layers nearest this

source would be expected to have coarse-grained, poorly sorted basal units. Progressing away from the source, the turbidites should become thinner, finer grained, and better sorted. The increase in mean grain size close to the source area suggests that greater impedance contrasts should be found in the southeast portion of the plain. This is supported by 3.5 kHz and seismic records.

Laughton [48] states that the overspill of the Bay of Biscay did not start until the time represented by a horizontal layer 73 m below the sea bed. If Laughton's theory is correct, then almost all of the Iberian Abyssal Plain sediment other than about the upper 50-100 m was supplied by Nazare Canyon. However, Reynolds [46] notes evidence that a thicker portion of the sedimentary column is derived from the Biscay Abyssal Plain. Profiler records obtained west of Theta Gap and in the Biscay Abyssal Plain on other NAVOCEANO cruises suggest a continuity of the interface between Units 1 and 2 with a strong reflecting horizon in the Biscay Abyssal Plain. This horizon, identified as the mid-R reflector [49], was drilled at DSDP Site 118 in the Biscay Abyssal Plain (Fig. 52). On the profiler records, the sediments above the mid-R reflector look similar to Unit 1 sediments at Station 2. The sedimentary sequence above the mid-R reflector consists of a 250 m section of flat-lying, highly reflective turbidites overlying a 150 m thick section of weaker reflectors in nearly transparent sediment. These sections appear to correspond with Sections A and B, respectively, at Station 2. If Laughton's theory of the time of overspill into the Iberian Abysssal Plain is incorrect, then possibly the age of Unit 1 can be correlated with sediments above the mid-R reflector.

The seismic record near Station 2 in the Iberian Basin shows Section A to be 0.2 sec thick, or about two-thirds as thick as the upper section at Site 118. If the lower interface of Section A represents the onset of glaciation (2-3 mybp) when turbidity flows were greatly increased, then the sedimentation rate of this section, consisting of Pleistocene sediment, is about 5-8 cm/1000 yrs. This rate is about half that of the corresponding sediments at Site 118 in the Biscay Abyssal Plain. This lower rate is reasonable, since the northern Iberian Basin is far from turbidite sources both to the northeast and the southeast as compared to Site 118. Section B corresponds to the underlying, more transparent, sediments at Site 118 of Pliocene Age.

Sediment Surface Sound-Speed and Density

Sound-speed measurements made on the pelagic sections of several cores show a sediment to bottom water sound-speed ratio of 0.974. Based on the core and 3.5 kHz data, about 15 cm of reflective turbidite layers (i.e., the coarse-grained basal layers) with an average sound speed ratio of 1.100 (1700 m/sec) are estimated in the upper 5 m of sediment. Using these values, the average sediment to bottom water sound-speed ratio is about 0.977, with a sound-speed of 1515 m/sec. Using the same proportions with average densities of 1.5 and 1.8 g/cm^3 for the clay and the turbidites, respectively, the estimated average density is 1.51 g/cm^3.

Sound-Speed Profile

An estimate of a constant-gradient sound-speed profile for Station 2 is based on the assumption that the sediments are analogous to those at DSDP Site 118 in the Biscay Abyssal Plain. The method used (CRIC) and assumptions are discussed in Appendix E.2. The calculated average gradient is 0.67 sec^{-1} throughout the observed 0.48 sec thickness of sediments above the mid-R reflector. This value for an average gradient is the most accurate possible based on available geological and geophysical data.

Three other sound-speed profiles estimated in different ways for sediments at Station 2 are also shown in Figure 54.

All the profiles have been adjusted to the surface-sediment sound speed of 1515 m/sec. Each profile is drawn to a depth corresponding to the two-way travel time of 0.48 seconds.

Cernock [50] has measured the sound speed of clay sediments during consolidation tests in the laboratory (Appendix E.1). The sample used for the data presented in Figure 54 is from a core taken from an abyssal plain in the Gulf of Mexico near the continental rise.

The Houtz and Ewing [39] curve (Appendix E.3) is derived from data from sediments which include types similar to those found at Station 2, but are located in the western Atlantic.

Hamilton et al. [51] derived a sound-speed gradient for turbidite sediments using sonobuoy wide-angle reflection data (see Appendix E.4). The average gradient decreases with depth with an overall average value of 1.05 sec^{-1}.

In summary, four methods for estimating the sound-speed profile in sediments may be applicable to the northern Iberian Abyssal Plain. In deriving the sound-speed profile for Site 118 (assuming a similar profile at Station 2), the time/depth parameters are the only fixed data points. For simplicity, a constant gradient is assumed. However, the other three methods suggest decreasing gradients with depth. The two-way travel time to 400 m for Cernock's [50] profile and the constant-gradient profile are within 8 msec, which is within the error limits of the time measurement on the profiler record at Site 118. Although Cernock's model fits the observed parameters, insufficient work has been done in the shallow sediments to establish how to modify accurately the constant gradient model.

Attenuation

Actual measurements of mean grain size for cores in this area are not available. Based on the core data available, an estimated 3% of the core consists of 1700 m/sec velocity material. Referring to Hamilton's [52, 45] sound-speed and mean grain-size relationships, material with this sound speed has a grain size of about 3 ϕ. In Figure 3 of Reference [45], the value of the attenuation constant κ at $\phi = 3$ is 0.500 dB/m/kHz. The value of 0.500 may be a good average for the estimated 3% of coarse turbidite material in the cores. This value, averaged with the rest of the fine core material with $\kappa = 0.065$, gives a value of $\kappa = 0.078$ dB/m/kHz.

Stations 4 and 5

Stations 4 and 5 are located in the southern Tagus Abyssal Plain about 130 km apart (Fig. 55). These sites offer a thick sedimentary cover (up to 2 km) over the acoustic basement. Despite the relatively small separation of the two stations within a single geophysical province, sufficient contrast in geoacoustic parameters exists to justify bottom-reflectivity measurements at each site.

Geological Information

Ruddiman and Glover [53] studied core data and reflection records in the Tagus Abyssal Plain in order to define the geoacoustic parameters in the vicinity of Stations 4 and 5. The following information is taken from that report.

Sedimentary Composition and Structure

The sediment cores indicated in Figure 55 were taken by Ruddiman on USNS WILKES in October and November 1973.

The cores contained the two basic sediment types which have alternately been deposited in the basin: (1) fine-grained silty clays with moderate carbonate content (pelagic depositions accumulating at 2-3 cm/1000 yrs), and (2) well-sorted fine sand or silt grading upward through progressively finer grain sizes into silty clays. Duplaix et al. [54] have shown that the heavy fraction of the mineral sands and silt in Tagus Abyssal Plain cores are virtually

identical in mineralogical composition to the sands and silts found on the continental shelf of Portugal near the mouth of the Tagus River. The sediments on the shelf have been periodically and rapidly transported through two submarine canyons to the Tagus Abyssal Plain and deposited as turbidite layers.

Figures 56 and 57 show 3.5 kHz records taken during the bomb runs for Stations 4 and 5. Two tracks with seismic profiler coverage of the Tagus Abyssal Plain are shown in Figure 55. Although no tracklines actually traverse the length of the bomb runs, the profiles, shown in Figure 58, are representative of the sediment profile along both tracks. The two types of sediments collected in the cores represent the alternating transparent and reflective sequence necessary to produce the 3.5 kHz near-surface bottom reflections and the seismic-profile deep reflectors visible over the southern Tagus Abyssal Plain.

Ruddiman and Glover [53] studied in detail the reflectors in the cores and reflection records for comparison purposes. Their discussion is summarized in Appendix D.2. The number of reflectors per meter of sediment is about the same on the 3.5 kHz records throughout the whole Tagus Basin; the reflectors are often traceable for 40-80 km in the southern part of the plain, but are less continuous to the north. Groups of reflectors seen on the seismic records seem to be continuous throughout the entire Tagus Abyssal Plain. Characteristics of the 3.5 kHz records along the bomb runs can be described as follows.

Station 4: Poor penetration (averaging 20 m); one reflector continuously traceable throughout the run; thickening of layers near middle of the track; and a dip in reflectors up to 0.4 m/km toward the southern end. Station 5: Better penetration, averaging 30-35 m; good continuity of reflectors; dip toward middle of the trackline, averaging 0.1 m/km; and thickness between reflectors increasing to northeast at mean rates of 0.3%/km.

These dip and thickening measurements along the bomb runs are local two-dimensional trends superimposed on the general geometry of the abyssal plain, which has a general dip and thickening of the layers to the southeast. Thus, the deeper layers observed in the seismic records have greater dips (relative to the horizontal) than do the near-surface layers. As in the 3.5 kHz records, the deeper reflectors tend to dip toward the middle of the run for Station 5. The dips observed are summarized in Table 10.

Two major sedimentary units, each greater than 1.0 sec thickness, are visible in the seismic profiles. The deepest unit comprises interbedded reflectors and transparent layers in conformable sequences which are highly deformed. Evidently this unit represents an ancient episode of turbidite/pelagic deposition which was later deformed by tectonic activity.

The upper layer shows flat-laying, highly reflective turbidites with great regional continuity. This unit forms a

Table 10. Observed dips of reflectors at stations 4 and 5

Layer Depths	Dips Along Bomb Run: Station 4	Station 5	Regional Dip
Near Surface	0.1 m/km	0.1 m/km	0.2-0.3 m/km
0.4-0.5 sec (300-375 m)	0.5-0.8 m/km	1.1 m/km	1.1-1.6 m/km
0.8-0.9 sec (650-745 m)	1.1-1.6 m/km	3.2 m/km	2.2-3.2 m/km

southward thickening and dipping wedge of surprising geometric regularity. The thickness of this unit reaches maximum values of 1.2 sec (1050 m) in the southern Tagus Abyssal Plain and is roughly 1.0 sec (850 m) beneath acoustic Stations 4 and 5.

Age of Sediments

Extrapolating from core data, a Pleistocene sedimentation rate (combined pelagic and turbidite input) is 10 cm/1000 yrs. As Pleistocene sedimentation rates are generally about twice that of earlier rates, an average for the whole upper unit is estimated to be 5-10 cm/1000 yrs. Calculations show the age at the bottom of the upper 1000 m wedge of turbidites to be about 10-20 million years (my). The unconformity between the upper flat-lying turbidite wedge and the deformed lower turbidite unit is assumed to be a long hiatus which ended about 15 million years before the present (mybp) (based on findings on such hiatuses in a variety of DSDP sites [55, 56] in the eastern North Atlantic).

The deeper sediment layers are far more difficult to date. Magnetic anomaly dating shows that the age of the basement material of the basin from west to east is 100-120 my old, and 115 my for the region of Stations 4 and 5. Ruddiman and Glover [53] speculate that the lower deformed turbidite unit probably dated roughly 70-40 mybp and overlies a 200 m pelagic Cretaceous layer (aproximately 70-115 mybp).

As no DSDP holes have been drilled in the Tagus Basin, data were used from two sites with similar settings and sediments to estimate the ages and compositions of the major sedimentary sequences (Site 118 [49] in the Biscay Abyssal Plain [see Fig. 52] and Site 142 [57] in the Ceara Abyssal Plain in the equatorial Atlantic off Brazil). The uppermost sediment sequence at Site 118 is a 250 m sequence of Pleistocene (0-2 mybp) turbidites which have basal silts and sands, are interbedded with silty clays, and were deposited at a combined rate of 12.5 cm/1000 yrs. From 250 to 400 m, the sediment sequence consists of Pliocene (2-5 mybp) clays and silts deposited at rates of 5 cm/1000 yrs. The Biscay Abyssal Plain sediments thus serve as a good analogue to the upper portions of the Tagus wedge. At Site 142, the last 15 my of sediment comprise 700 m of alternating turbidite and pelagic material which was deposited at rates in excess of 10 cm/1000 yrs. The sediments from 400 to 700 m at Site 142 form a better analogue to the Tagus record than those at Site 118.

Sediment Surface Sound-Speed and Density

Sound-speeds were measured on cores taken by USNS WILKES (Fig. 59). The pelagic sediments have sound-speeds (adjusted to laboratory conditions) of about 1497 m/sec and densities of about 1.5 g/cm^3. The finer-grained upper portions of the turbidites have similar characteristics; they can be distinguished from pelagics by color and structure but are acoustically identical. Both types are acoustically transparent. The coarse-grained basal layers in the turbidites are acoustically reflective; they have velocities of 1650-1800 m/sec and densities of 1.8-1.9 g/cm^3. The basal turbidite layers can be considered simplistically as constant gradient layers: their bases form step-like, discontinuous increases of sound speed (from 1500 to 1700 m/sec) and density (from 1.5 to 1.9 g/cm^3) from the underlying pelagic layers, and their tops grade linearly into the sound speeds and densities of the upper turbidite sections, which are identical to the overlying pelagic layers. Based on core data, the mean thickness of reflective basal-turbidite layers is about 20 cm.

The mean intervening thickness of the low-speed transparent sediment is roughly 100 cm at Station 4, and 80 cm at Station 5. The average speed and density for the upper 5 m have been calculated for both stations using this information as shown in Table 11. The average sound

speeds listed in Table 11 have been corrected to in situ conditions.

Sound-Speed Profile

Sound-speed changes per unit depth through the sedimentary column near the acoustic stations in the Tagus Abyssal Plain are inferred through indirect means. This is accomplished by using relevant DSDP measurements of sound-speed in sediments with ages, lithology, and inferred state of compaction comparable to Tagus sediments.

Based on the study by Ruddiman and Glover [53] the sound-speed profile in the upper 200 m of the Tagus Abyssal Plain is assumed to be similar to that at Site 118 in the Biscay Abyssal Plain. Using the CRIC method described in Appendix E.2, the calculated gradient is 0.67 sec^{-1} for a 400 m section. As discussed in the appendix, the gradient in the upper 200 m is probably slightly higher. The curve is shown in Figure 54, Two curves are shown in Figure 10 for Stations 4 and 5. In addition to the Site 118 curve, Hamilton's [51] curve for abyssal plains, as discussed in Appendix E.4 for turbidite sediments, is shown. The two curves commence at the sediment interface with the sound-speed given in Table 11.

Attenuation

Grain-size measurements were taken on core W5 at Station 4 and core W4 at Station 5. The sampling interval was sufficient on W4 to provide a good estimate of mean grain size throughout the core. The closely spaced sound-speed measurements confirm the thoroughness of the grain-size sampling. On core W5, grain-size was not determined in the high sound-speed layers, so the same average grain-size as that in W4 was assumed. The percentages of basal turbidite and intervening layer thickness are the same as those used in Table 11. The attenuation determinations κ_G based on Hamilton's [45] relationships are shown in Table 12. Note that the effect on the average calculated attenuation due to the lower percentages of basal turbidities at Station 4 rather than at Station 5 is offset by the slightly finer grain-size at Station 5.

Station 8

The site for Station 8 offers a geologic setting quite different from that of the other stations. The site is located on a plateau contiguous to Dragon Seamount and removed from the continental margin. The locations of Station 8 and the bomb run are shown in Figure 60. The station

Table 11. Sound-speed ratio and density at stations 4 and 5

Station	Sediment Type	%	Sound-Speed m/sec (Ratio) Mean Value	Sound-Speed m/sec (Ratio) Average	Density g/cm^3 Mean Value	Density g/cm^3 Average
4	Basal Turbidite	16%	1600 (1.051)		1.7	
				1539 (0.994)		1.53
	Intervening Sediments	84%	1497 (0.984)		1.5	
5	Basal Turbidite	20%	1600 (1.051)		1.7	
				1542 (0.996)		1.54
	Intervening Sediments	80%	1497 (0.984)		1.5	

Table 12. Sound attenuation from cores at stations 4 and 5

Core	Sediment Type	%	Average Grain-Size ϕ	κ_G dB/m/kHz
W5 Station 4	Basal Turbidite	16	6.2	0.137
	Intervening	84	8.8	0.064
			Average	0.076
W4 Station 5	Basal Turbidite	20	6.2	0.137
	Intervening	80	9.1	0.062
			Average	0.077

is at a relatively shallow depth of about 2400 m. The run traverses a change of depth from 2460 to 2057 m. The sediments are sufficiently thick to provide acoustic propagation paths through the ocean floor, but lack the bathymetric smoothness found in the abyssal plains. As can be seen in the 3.5 kHz record shown in Figure 61, the topography has slight relief of about 25 m and maximum slopes of 3°. The site was chosen primarily because of the contrast in sediments with the deeper stations and also because of the slightly rough topography.

Geological Information

Sediment Thickness

Seismic records were obtained along two tracks nearly parallel to the bomb run (Fig. 60). The records shown in Figure 62 indicate that the sediment thickness is at least 0.7-1.0 sec two-way travel time over the entire bomb run. The deepest reflector observed along the KANE track is relatively smooth and has a sufficiently high acoustic impedance to mask any rough basement, whereas the basement roughness is more apparent on the WILKES track farther west. Diffuse, but strong, reflectors at the seismic frequencies are observed about two-thirds of the way down the sedimentary column.

The sediment thickness on the plateau is well-defined by other NAVOCEANO tracks traversing the area. The side of the plateau has a gentle slope to the northwest, with increasing slope continuing counter-clockwise around the periphery of the plateau. The blanket of sediments has continuity of thickness and appearance on traverses crossing the plateau to the northwest of Station 8. As the slope increases, the sediments thin to the extreme of no observable sediments on the southern side of the plateau, as revealed in a seismic profile record (not shown) on a traverse between Station 8 and Site 136 to the southeast. The ridge at point K' in Figures 60 and 62 is the southern boundary of thick sediments.

Sediment Composition

Sediments in the general vicinity of Station 8 are predominantly calcareous, and pelagic in origin. Linered Ewing cores, SB-3 and SB-4, were taken at Stations 7 and 8, respectively. Core SB-3 penetrated the entire sedimentary cover of only 82 cm. Although the sedimentary cover at Station 8 is thick, SB-4 only penetrated 112 cm despite the use of a 900 kgm (1 ton) weightstand, possibly because of the presence of at least one layer of coarse sediment. The grain size distribution was measured on two samples from each core. The sample at 22-28 cm depth in SB-4 reveals a coarse layer with 77% of the constituents in the sand

size (>0.063 mm). The other three samples in the two cores have sandy-silty clay. Both cores consist of predominantly foraminiferal ooze.

A Lamont-Doherty core, V30-193, taken 18 km north of Station 8 in a water depth of 2842 m (Fig. 60), consists predominantly of foraminiferal marl ooze in its 448 cm length. The carbonate content is moderate to high. The only detritus observed is negligible amounts of dark minerals and metamorphic rock fragments. Core V30-192 was taken 62 km northwest of Station 8 in a depth of 3808 m (north of the area of Fig. 60). At least 340 cm of sediment were obtained which consist also of predominantly carbonate sediments with negligible dark minerals.

The elevation of the site precludes recent turbidity-current deposition of terrigenous sediments from the continents. Any allochthonous recent sediments would be derived from turbidity flows off the Dragon Seamount (Station 7), from ice rafting, or from windblown detritus (including ash layers). The seamount turbidites would predominantly consist of pelagic sediments with some fragments of basaltic rock.

Volcanism

Uchipi et al. [58] report post-Miocene volcanism in Madeira and volcanism commencing in the Miocene up through the present in the Canary Islands. Evidence of volcanism can be seen in the 3.5 kHz and seismic-profiler records. A well-defined 3.5 kHz reflector at 14 m below the sea floor can be traced along the entire record in Figure 61. This reflector is observed on the tracks near Station 8 as far south as 32°50'N, and as far east as 16°W. This reflector may be an ash layer from very recent (0.5 mybp) volcanism.

Evidence of volcanism is also observed in the seismic-profiler record near the outcrop (Dragon Seamount). Intense heating of the sediments adjacent to the volcanic outcrop during the time of volcanism may have resulted in an increase in the acoustic impedance of the sediments (F. Bowles, pers. comm.). Sediments deposited after this event would have a lower acoustic impedance. Thus, this feature would appear as a buried reflector. An example of this feature is the opaque reflector, about 100 m below the surface at point W (at 3.3 sec) in Figure 62, which continues into Dragon Seamount to the right. This reflector is more clearly defined at 0540-0600Z and again at 0800Z on the seismic record in Figure 63. It was difficult to locate precisely the profiler records relative to the station and bomb run. However, the bottom-reflectivity data indicate a layer at 50 msec which could possibly correlate with this feature.

DSDP Site 136

The DSDP Site 136 is located in deep water (4139 m) 95 km south-southeast of Station 8 beyond the plateau on which the acoustic experiment was conducted (see Fig. 60). The sedimentary cover over basement is very thin--only 308 m. In fact, the short drilling distance through the sediments to the basement was one of the reasons for choosing the location of Site 136 [59].

The shallowest core taken in the Site 136 drill hole and the only one in the upper 215 m is in the 130 to 139 m interval. In this core no evidence of turbidites can be found. However, recent turbidites at the site cannot be ruled out and might have been sampled if the sampling density in the drill hole were greater. A 20 cm thick turbidite with low carbonate content was found 4 m down in core V27-162 taken about 55 km to the west. On the V-17 seismic-profiler record in the site report, there appears to be no topographic barrier which would prevent turbidite layers present at the site of core V27-162 from extending to Site 136. Whatever turbidite layers exist at Site 136 contribute little to the sediment thickness and consequently have little effect on the acoustic properties.

Despite the large differences in water depth and sedimentary thickness at Site 136 and Station 8, the composition of the sediments at the two locations is probably very similar. Strong reflecting horizons in the WILKES profiler record in Figure 62 may have been created by changes in pelagic sedimentation rates. Note that these horizons can be traced from the base of the plateau, past the obtrusion at W' and up the slope of the plateau, and at least the uppermost horizon is again visible approaching W'. This continuity suggests that the same deposition mechanism occurred over this area.

A summary of the sedimentary description for the DSDP Site is shown on the left of Figure 72. The upper 240 m of sediments at the site have moderate to high carbonate content, not unlike those samples obtained on the plateau near Station 8. Variations in sediment thickness occur along the base of the plateau. Hayes et al. [59] suggest that the thin sedimentary cover is due to erosion and nondeposition of sediment (major hiatuses are represented in the lithologic sections). Nevertheless, the evidence points to similar sediment composition in the upper 200 m at Site 136 and Station 8.

Sediment Surface Sound-Speed and Density

Sound-speeds were measured on cores SB-3 and SB-4. The sound-speed profiles shown in Figure 64 suggest a large gradient with depth, with only the upper few centimeters of core having a speed less than the sound-speed of the bottom water. However, SB-4 (taken at Station 8) is too short to safely extrapolate a gradient downward into the ocean floor. To estimate the average sound-speed of the upper 5 m of sediments, the assumption was made that the lower 4 m had the same sound-speed as the average speed of the lower 30 cm of the core. Using these values, the estimated adjusted sound-speed for the surface sediments is 1540 m/sec, with a sediment-to-bottom water sound-speed ratio of 1.013.

The measured values of wet density in the four samples were all very close to 1.60 g/cm^3.

Sound-Speed Profile

Based on the similarity in sediments at DSDP Site 136 and Station 8 as discussed in the geological section, the sound-speed profile at Station 8 can be represented by the estimated profile at Site 136. Due to the differences in water depth and temperature, the sound-speeds will be offset, especially near the surface, but the gradient will not change significantly.

The sound speed determined for Site 136 is a constant-gradient model with $g = 2.33\ sec^{-1}$. The data are limited and certain assumptions must be made (see Appendix E.2). Four other methods for estimating the sound-speed profile are presented here and are compared to support the validity of using the $g = 2.33\ sec^{-1}$ profile. The curves corresponding to all the sound-speed prediction methods are shown in Figure 65. These curves are based on in situ measurements and laboratory experiments.

Hamilton et al. [42] have recommended using Equation D from Houtz, Ewing, and Buhl [60] for estimating the sound-speed profile in pelagic sediments wherever in situ data are not available. The average sound speed for this profile is 1789 m/sec, with a standard deviation of 160 m/sec. In comparison, the average speed at Site 136 is 1867 m/sec, or only 78 m/sec higher. Therefore, Site 136 is not anomalously high when compared to some Pacific areas which have high-carbonate sediments. Details are given in Appendix E.4.

Houtz and Ewing [39] derived an equation from data covering a range of sediments which includes the gradient calculated for Site 136. The details used in developing the curve in Figure 65 are given in Appendix E.3.

Laughton [40] made laboratory measurements of sound-speed versus overburden

pressure. One of his samples taken from the North Atlantic in a water depth of 2577 m had a high carbonate content (54%). His values, modified in the upper 135 m, are presented in Figure 65. Further details and discussion are in Appendix E.1.

The lowest sound-speed profile in Figure 65 is based on surface sediment data from Hamilton's [52, 82] work as described in Appendix E.5. The results are extrapolated to buried compacted sediments by making adjustments to in situ conditions based on pressure and temperature corrections. Because the data are from surficial sediment samples, the profile is suspect, as explained in the appendix. The profile is presented with this caveat in mind. The details of the adjustments and relationships used are also discussed in the Appendix.

As seen in Figure 65, and confirmed by travel-time calculations, the four profiles derived from published data do not have sufficiently high sound-speeds to account for the time observed on the Site 136 profiler record. However, as discussed above, the comparatively high sound speed values of the g=2.33 sec^{-1} curve are not unreasonable in light of the published data. Difficulty in relating laboratory measurements to in situ conditions occurs because of the lack of understanding of how certain processes affect acoustic characteristics of sediments. Therefore, at present, techniques to determine in situ sound speed offer the best approach. Insufficient information is available at Site 136 to modify the constant-gradient profile derived using the CRIC method. Consistent with the general trend of a decreasing gradient with depth observed in the other profiles, the gradient value of 2.33 sec^{-1} would be a lower limit in the uppermost sediments and an upper limit in the deeper sediments. However, the average gradient is the best estimate when relating Site 136 to the upper 200 m of sediments at Station 8.

Attenuation

Grain size determined on samples from both cores taken at Stations 7 and 8 are shown in Table 13. Only one of four samples contained a substantial percentage of sand-sized particles. The values of attenuation are determined directly from Hamilton's [45] graph and a simple average is computed to determine the attenuation constant of κ = 0.25 dB/m/kHz. The small sampling may not be adequate, but with shallow carbonate deposits, large grain size is expected with a corresponding higher value of κ. Thus, the value of κ is the minimum that would be calculated by this method even with a greater sampling of size distribution.

Station 9

Station 9 is located on the lower continental rise west of North Africa on the eastern edge of the Cape Verde-Madeira Abyssal Plain in a water depth of about 4600 m. The almost featureless topography provides a site conducive to modeling. The bomb run for Station 9, shown in Figure 66, commences at 29°N, 20°50'W. The location provided the opportunity to conduct a long-range propagation experiment as indicated in the figure on the track to the northwest.

Geological Information

Several cores have been taken in this area by the Lamont-Doherty Geological Observatory. These samples are indicated

Table 13. Sound attenuation from cores at stations 7 and 8

Core	Sampling Interval	Sand-Silt-Clay	Mean Grain Size ϕ	κ_G db/m/kHz
SB-3	12-18 cm	27-22-51%	7.1	0.08
Station 7	22-28 cm	33-25-43%	6.6	0.10
SB-4	22-28 cm	77-10-12%	4.2	0.72
Station 8	64-72 cm	26-22-53%	7.2	0.09

in Figure 66. For the most part, cores in the area have carbonate sediments. Within these cores are layers characteristic of turbidites, but of carbonaceous rather than mineral composition. However, mineral (terrigenous) turbidites are observed in many cores as indicated in Figure 66 by the solid symbol. Because Africa is so highly arid and no major rivers empty into the Atlantic that far to the north, the major source of turbidites at the station is probably the Canary Islands, with a possible contribution from the Madeira Islands. Windblown quartz and clay minerals from Africa are also an important contribution to the sediments.

Sedimentation in this region is typical of abyssal plains, i.e., alternation of pelagics and turbidites, but topographically it lacks the flat character of abyssal plains. The seismic data, and on a more detailed scale, the 3.5 kHz data, show the surface to consist of irregular depth variations of 5 m amplitude. Regionally, the sea floor surface rises toward the east with a prominent change in topography occurring near the end of the long-range acoustic run. The records are shown in Figure 67.

The track approaching Station 9 from Station 8 and the track just beyond the end of the bomb run traverse a small double channel that is oriented NNW. Another channel with the same orientation is observed on both tracks; the crossing on the propagation run track is at 19°07'W. These channels are indicated by dashed lines in Figure 66. All the crossings show a channel relief of 5-10 m except the latter crossing which has a relief of 20 m. The channels are about 0.3 km wide on the southern KANE track crossing, but are not observed on the WILKES southern track, which is farther south and up-slope from the KANE track. Embley [61] has found evidence of debris flow deposits just southeast of the bomb run for this station. He has identified this type of deposit on the 3.5 kHz depth recorder as a thin lens lying on the ocean floor. This characteristic signature does not appear on the records in Figure 67. However, the NNW flow direction indicated by the channels coincides with the flow direction indicated by Embley.

The Canary Islands form a barrier along the coast of Africa, restricting the flow of turbidites to a path south of the islands in the vicinity of Station 9. Uchipi et al. [58] suggest that the whole region along the long-range propagation run obtained its major constituents of sediments prior to the formation of the Canary Islands by volcanic activity in the Oligocene.

Sediment Surface Sound-Speed and Density

An estimate of the surficial sediment sound-speed is based on the sediment type as estimated from cores in the area. The cores have a higher carbonate content than those at the other deep stations, but less than those at Station 8. The contribution of wind-blown clay particles is greater than at Station 8 farther north, but the clay content is less than that received from turbidity currents in the Tagus and Iberian Abyssal Plains. No sound-speed measurements were taken on cores from the area. By estimating an average type clay size particle distribution with a porosity of 70%, statistical relationships, such as in Anderson [62], can be used to predict average acoustic parameters. In this relationship, the carbonate content is not a factor. The predicted sediment-water sound-speed ratio and density for porosity of 70% are 0.984 and 1.52 gm/cm^3, respectively.

Sound-Speed Profile

Extensive sonobuoy data measured by Lamont-Doherty personnel in this area were made available by Robert Houtz; the locations of most are shown in Figure 66. The high density of stations (although no stations are on the acoustic measurement track) provides a method of estimating a sound-speed profile. This method entails the use of a statistical compilation of the sonobuoy data to

derive a gradient in the upper 200 m. The data and details of the method and assumptions are in Appendix E.4. The estimate of the gradient is 1.1 sec^{-1} with a standard deviation of about one-half this value.

Attenuation

In order to estimate the attenuation at Station 9, the mean grain size distribution must first be estimated. The core data suggest a greater preponderance of calcareous sediments than are found in the Tagus Abyssal Plain at Stations 4 and 5. Also, the sound-speed gradient at Station 9 is greater than at Stations 4 and 5. These two observations are self-consistent and further suggest a larger mean grain size at Station 9 than at the other abyssal plain stations, but not as high as observed at Station 8. Thus, without actual grain-size measurements, an estimated value of about 0.10 dB/m/kHz based on Hamilton [45] is proposed. Although very subjective, this value is consistent with an apparent relationship between estimates of the gradient and attenuation constant at the other stations.

Station 7

The site for Station 7 shown in Figure 60 provides a rough sea floor with essentially no sediments. Because of the high acoustic impedance of the ocean bottom, sound propagation paths in the bottom are not a consideration in analyzing the data. On the other hand, reverberation is very prominent. This type of bottom is acoustically representative of a significant portion of the ocean floor, which consists of the crest of the Mid-Oceanic Ridge or any other center of sea-floor spreading. The particular site was chosen because its location was within a reasonable vicinity of the cruise track plan.

Geological Information

The elongated basaltic outcrop which the bomb run traverses is called the Dragon Seamount. It rises to a minimum depth of 1200 m. The most detailed, published geophysical description of this site is reported by Laughton et al. [63]. The bathymetry of the Stations 7 and 8 vicinity, as illustrated in Figure 60, is primarily based on NAVOCEANO tracks, including surveys on the October 1973 cruises and other tracks and contours by Hayes et al. [59] as shown in the DSDP Site 136 report.

Because of the roughness of the track, 3.5 kHz records were not well-defined. The narrow beam 12 kHz record is shown in Figure 63 at one-half the scale used for the 3.5 kHz records of other stations. Along the bottom of the figure is a line drawing of the bathymetry used in the ray trace program with no vertical exaggeration. This line drawing is to assist the reader in visualizing the effects of the rough topography on ray paths with the true angles presented. The seismic profile section shown in the insert in Figure 63 is one crossing of the bomb run made on the survey by the WILKES.

Sediment Sound-Speed and Density

Core SB-3 taken in the outcrop area of Station 7 struck hard rock after penetrating less than a meter of sediment. The sediment consists of predominantly foraminiferal sandy clay. Sound-speed measurements were taken on this core aboard ship and are shown in Figure 64. The average adjusted sound-speed in the core is 1530 m/sec, giving a sediment-to-bottom water ratio of 1.005. Where this sedimentary cover does not exist, however, the igneous rock is in direct contact with the bottom water. Photographs taken by Laughton et al. [63] show steep slopes void of sediment. Fox et al. [64] measured the compressional sound-speeds of basalt samples taken from DSDP Site 136, 80 km south of the station. Measurements at 0.25 kb (equivalent to about 2500 m water depth) were 3880 m/sec, and the density was 2.5 g/cm^3. However, this sample is highly altered basalt, and Fox et al. [65] suggest that these values are considerably lower than relatively fresh and

unaltered basalt measured by others. For example, Christensen [66] measured 5100 m/sec at 0.20 kb on a water-saturated basalt sample with a density of 2.90 g/cm^3 from the Juan de Fuca Ridge. This measurement corresponds well with the average sound speed for the oceanic crust (Layer 2). Laughton et al. [63] report olivine basalt as the main rock dredged on Dragon Seamount. Using either density-sound speed set gives a very high reflection coefficient at the water-basalt interface of 0.7-0.8 (normal incidence bottom loss of 1.8-2.8 dB). The sediment covering is too thin to significantly affect the reflectivity at low frequencies over the bomb run track. A possible model may be a meter of sediment covering a few meters of weathered basalt over a core of unaltered basalt.

Appendix D.
Geological Aspects of Acoustic Parameters

Seafloor sediments contain features that create reflecting horizons, preferential acoustic propagation paths, and other spatial variations of acoustic parameters, all of which constitute the acoustical stratigraphy of the ocean floor. The ability to extrapolate the acoustical stratigraphy beyond areas of direct measurements requires understanding of the physical structure which influences it. We are still far from a thorough understanding because the correlation of the geological stratigraphy and acoustical stratigraphy is not simple. The objectives of this section are to: (1) emphasize sedimentary processes relevant to the acoustical stratigraphy at each station, (2) point out problems in the correlation of geological and acoustical stratigraphy, and (3) describe the acoustic parameters emphasized in this report and their methods of measurement.

Sedimentary Processes

A few predominant sedimentary processes have produced the primary types of sedimentary layers which affect the acoustic stratigraphy at the station locations in this report. Sediments emplaced by other processes may exist, but not to a significant degree. One such process is the precipitation of dissolved minerals in the water onto particles on the sea floor. An example is the formation of manganese nodules, which can be extensive enough to form manganese pavements. The more apparent sedimentary processes are discussed in the following paragraphs.

Pelagic Sediments

Pelagic sediments are formed by the deposition of the shells (tests) of fauna and flora which float in the ocean (plankta). The predominant test material of plankta is calcium carbonate or calcite. Coarse calcareous sediments consist predominantly of the tests of foraminifera, whereas the clay-size particles are tiny calcareous plates called coccoliths. Under proper environmental conditions, the calcareous sediments will partially or totally solidify to form chalk or limestone. Variation in these conditions and in sedimentation rates results in variations in the acoustic impedance of the pelagic sediments. In general, surface sediments have sound speeds less than the bottom water, with the sound speed increasing with depth of burial. Hamilton et al. [42] have observed that the sound speed increases more rapidly with depth of burial in sediments with high carbonate content than sediments with predominantly terrigenous clay. The sediments at Station 8 have high carbonate content with an implied higher sound-speed gradient than at the other stations. In water depths greater than 4000 m the carbonates tend to dissolve, inhibiting their contribution to the sediments. The degree of dissolution is dependent on the hydrostatic pressure and other parameters in the water which have fluctuated throughout geologic history, as well as the amount of carbonates available. (The reader is referred to Berger [67] for a discussion of the calcite compensation depth.)

In addition to the calcareous sources, silicoflagellates and diatoms, both algae, contribute silica constituents to the sediment. Since silicates do not dissolve in deep waters as readily as carbonates, the ratio of silica to calcite increases with water depth. Where siliceous sediments are dominant, they may change form from siliceous oozes to the denser form of chert with a much higher sound speed (about 3.6 km/sec). The formation of chert layers is not understood, although explanation relating their formation to volcanism have been suggested [67, 68]. Chert layers have been found in the DSDP sites, generally buried deeper than 250 m below the sea floor, although they have been cored as shallow as 100 m.

Generally, the layers have been determined to be older than Miocene (26 mybp). These layers are thin (about 5 cm), but several layers may occur together, thus creating a good reflector of sound over a large frequency range. Horizon A, an extensive, strong subbottom reflector observed in the northwestern Atlantic and correlative to horizons in the eastern Atlantic [58], has been drilled and correlates with several thin chert layers [69, 70]. The age of this layer is Eocene (50 mybp). Horizon A may therefore exist beneath the deep abyssal plains, but is masked by more recent sediments. The evidence indicates that chert layers are not necessarily time-synchronous, and that they may be more common than previously thought. The existence of chert as a reflector at any of the stations can not be ruled out.

Eolian Sediments

Eolian sediments are particles initially deposited on the ocean surface by the winds. One such type is ash that has been distributed over a broad area by wind during volcanism. Such ash layers may be only a few centimeters thick, or extremely thick as are found in the Mediterranean Sea basins. The layers are independent of water depth and type of surrounding sediment and create good sound reflectors. Several thin ash layers which are close together may form one reflecting horizon for a range of wavelengths of the impinging sound energy. Ash layers are the most likely cause of some of the reflectors seen near several of the stations. In particular, a rather shallow reflector at Station 8 is likely to be an ash layer.

Aside from ash, other land-derived debris is carried by the winds far out to sea and contributes to the sediments. This debris, even up to the silt-size, may be a significant constituent of the sediments west of the Sahara Desert, such as at Station 9. Windblown, clay-sized particles contribute in some degree to almost all the sediments in the world's oceans.

Gas Hydrates

A gas hydrate is a crystalline structure of water molecules in which gas molecules are physically trapped [71]. This formation produces a substantial increase in sound speed which, in turn, produces a strong reflecting horizon. Conditions under which this phenomenon occurs exist in the near-surface sediments; their geographical distribution is unknown although their presence at several locations has been verified. These hydrates leave no measurable evidence on bottom samples other than the expansion observed before a core sample is extruded from the coring tube. Because of the suspected widespread distribution, this feature may account for some of the reflectors observed at the stations.

Turbidites

Underwater flow mechanisms that contribute to the redistribution of sediments or emplacement of land-derived (terrigenous) deposits are: bottom contour currents, the nepheloid layer, debris flows (observed near Station 9), and turbidity currents. The last mechanism is the most obvious contributor of sediments at the stations.

The deposition of turbidite layers accounts for the thick sediments in the deep ocean basins' abyssal plains. These deposits are generally land-derived mineral material (predominantly quartz) mixed with shallow-water marine deposits of high carbonate content.

Turbidite currents are not restricted to the continental shelf, but can occur along any slope (such as that off an island). Material from rivers and the continental shelf piles up on the shelf until the deposit becomes unstable. A microearthquake can disturb the pile and trigger a down-slope flow of a mixture of the material and water. This turbid water builds up speed under the influence of gravity due to its excess density and low friction, and carries the shelf material down submarine canyons

along the continental slope into the deep ocean basins. Here, the material is deposited as the flow velocity decreases due to decrease of the downhill slope. The size of particles carried by the turbid water is a function of the velocity: the larger particles settle out first, and the finer particles later. The result is that during a turbidity flow, the first deposited particles are the largest. Thus, the larger particles are deposited in greater amounts at locations closer to the source. Turbidity flows tend to flatten the topography of the receiving basin thus producing the characteristic plain. The flatness is conducive to acoustic modeling; however, the complex layering complicates the models.

In a sedimentary column, the turbidite layer represents a rapid deposition which is interjected into the stream of continuous deposition of pelagic and eolian sediments. The turbidite layer may be represented in an idealized model by its grain-size distribution. Large grain-sized material is found at the base and gradually grades into smaller sized material at the top. The decrease in grain-size upward results from the decreasing velocity of the turbidity flow in time. The basal interface is sharply defined by the sudden increase in grain-size compared to that of the underlying sediments. At the top, however, the interface with the overlying sediments of similar grain-size is imperceptible. A common perturbation of the model is the diffusing of the sharp bottom interface by animal burrowing. A more complex grain-size profile than described here is observed at DSDP Site 118 northeast of Station 2 by Laughton et al. [49]. During periods of glaciation, the mean sea level is lowered due to the removal of water to the glaciers. This causes an increase in erosion which provides the source of turbidites. The glacial period commenced in the northern hemisphere about 3 mybp in the Pliocene. The peak of glacial intensity occurred about 0.4 mybp [72]. (The Pleistocene, often associated with the glacial period, began at 1.8 mybp.) Although four or five major glacial advances are observed on the continents, the deep-ocean paleontological record shows many fluctuations in the glacial cycle; each would have caused a variation in the turbidite activity. During periods of intense glaciation, less accumulation of pelagic sediments occurs between turbidity flows; thus, the percentage of large, grain-sized basal portions of turbidites in the sedimentary column represented by this period is greater.

Turbidity flows contributed to the bulk of the sediments at Station 2 in the Iberian Abyssal Plain and Stations 4 and 5 in the Tagus Abyssal Plain. The vertical sound-speed profile through a turbidite layer responds to the variation of density and mean grain-size in the layer. The sound-speed profile in the turbidites at Stations 4 and 5 is described in Appendix C. The number of turbidite layers influences the average sound speed of the sediments. The vertical spatial frequency can be inferred from seismic-profiler records as discussed in the following section.

Acoustic Reflectors and Geological Interfaces

The correlation between the geological and acoustical stratigraphy is not always apparent. This lack of correlation between acoustic and geological interfaces has often been observed in DSDP sites. Theoretical reasons for this phenomenon exist. Even in the simplest approach relating the acoustical stratigraphy to the geological stratigraphy, three limits must be considered. These limits involve the thickness of the interface zone, the thickness of a reflecting layer, and the separation of reflecting layers.

A reflecting interface occurs where an impedance contrast exists between two adjacent media. Maximum reflection occurs when the contrast occurs over a zone which is infinitesimal relative to the acoustic wavelength. On the other hand, no reflection occurs when the zone is infinite in length compared to a

wave-length. According to ray theory, this effect causes a refracting of the ray when the ray is oblique (i.e., if a speed change is involved rather than just a density change). Several conditions may exist which mask potential reflecting horizons. For example, slow changes in the sedimentary deposition process may create a wide interface zone even at wavelengths comparable to low frequency energy; at high-frequency wavelengths one may see the effects of burrowing by benthic creatures.

At normal incidence, peculiar phenomena occur on the reflecting of half-wavelength and quarter-wavelength layers. Brekhovskikh [38, pg. 55-56] offers a concise explanation of this phenomenon of a layer lying between media 1 and media 3 with impedance Z_i:

"The halfwave layer has no effect on the incident wave (as if the layer were absent), and the reflection coefficient is equal to the usual coefficient of reflection from the boundary between media 3 and 1 just as if they were in direct contact with one another. In particular, if media 3 and 1 have the same properties ($Z_3 = Z_1$), the reflection coefficient is zero."

This explanation is also true for an integral number of half-wavelength thicknesses. This limit may apply where turbidite layers alternate with pelagic layers. For the quarter-wavelength thick layer ($1/4\lambda$):

"Reflection at the boundary between any two media can be eliminated entirely by inserting a quarterwave layer between the two media, the layer having an impedance equal to the geometric mean of the impedances of the two media. A similar effect will be observed when the layer thickness is equal to $3/4\lambda$, $5/4\lambda$, etc."

The effect of the separation of layers can be thought of in terms of the layer thickness of the separating medium with the implications mentioned in the preceding paragraph. Another problem occurs with resolution if the spacing is so small that the returned pulse trains overlap. The chert or sandstone layers that would individually be transported to long acoustic wavelengths may appear as a single reflector if several are grouped together.

With additional mathematical terms, the above relationship can also be applied to oblique angles. These relationships are limits, rather than definite values for layer thicknesses, implying gradational effects.

Two kinds of seismic systems for recording travel time to subbottom layers were used consistently on the cruise: 3.5 kHz and the sparker (50-150 Hz). These systems display signals reflected at normal incidence from interfaces of contrasting acoustic impedance below the ocean floor as well as the water-sediment interface. The 3.5 kHz recorder is useful in defining reflectors in the upper 50 m of sediment. The sparker seismic records, on the other hand, are responsive to interfaces which affect low-frequency sound propagation and thus are closely related to the bottom-reflectivity measurements. Although the near-surface detail is lost due to the lower frequency and it has a more compressed time scale than the 3.5 kHz recorder, penetration is much greater--reaching to two seconds of two-way travel time, or about 2 km of sediment in the areas reported here. Since the sparker signal would interfere with the bottom-reflectivity experiment, it could not be operated during the experiment. The 3.5 kHz system, on the other hand, operating at a much higher frequency and at lower power with downward directivity, could be operated during the bottom-reflectivity run without interfering with the experiment.

Most of the reflectors seen on the seismic records are within the sedimentary column. Where penetration with the sparker system is sufficient, a strong reflector called basement is observed which generally correlates with oceanic layer "2". Basement has a compressional wave speed of at least 3 km/sec and consists of a high percentage of basalt

[73]. This layer was generated at the source of sea floor spreading, and, not being subjected to the erosional forces that exist on land, has roughness equivalent to that of the younger rough areas of the ocean floor such as the Mid-Atlantic Ridge. An example of this rough layer can be seen on some of the seismic-profile records in this report. The acoustic basement is defined as the bottom-most layer possible to observe on the profiler records. Acoustic basement may not be the same as basement in the geologic sense, but instead, may be the acoustic signature of a layer buried under unconsolidated sediments. In this case, a small amount of energy is transmitted to reflect off deeper interfaces which would have less impedance contrast; thus, the reflected energy would be imperceptible.

Subbottom depth recordings in abyssal plains characteristically display several reflecting horizons above the acoustic basement. One parameter which describes an aspect of the acoustical behavior of geological features in the sediments is the number of reflectors per meter. This parameter has been used in Table 3 to describe the 3.5 kHz subbottom records at each station.

The number of reflecting horizons observed in 3.5 kHz records and in the lower frequency seismic-profiler records, and the number of reflecting interfaces observed in deep-sea cores differ. In a study of the sediments at Stations 4 and 5 in the Tagus Abyssal Plain, Ruddiman and Glover [53] made a comparison of the number of reflectors per meter in the records and the cores. For resolution considerations, in comparing reflectors on the 3.5 kHz records to reflective layers in the cores, two adjustments must be made in the core data: first, turbidites spaced less than a quarter-wavelength (12 cm) apart were combined into a single reflector; second, layers appreciably less than a quarter wavelength thick were ignored. An average of roughly 0.75 reflectors/meter in the cores taken at acoustic Station 4 and 5 was calculated. In contrast, the underway 3.5 kHz data consistently recorded 0.25-0.40 reflectors per meter. Some of the loss may, of course, be cause by ship's motion and other masking effects due to noise. Thus, the near-surface Tagus Abyssal Plain sediments probably consist of two to three times as many individual major turbidites than are generally visible in the 3.5 kHz data.

To examine the resolution in seismic-profiler records, Ruddiman and Glover [53] counted the number of reflectors per depth of sediment on the records. Averages of 0.065-0.085 reflectors per meter were calculated in the upper 0.5-1.0 seconds (two-way travel time), or about 400-800 m on the profiles. This figure is roughly an order of magnitude fewer than the number of well-defined, thick turbidites observed in the cores, and a factor of four fewer reflectors per meter than are visible in the 3.5 kHz data. Each individual reflector observed on the sparker records must, therefore, be caused by groups of adjacent turbidites. Using the rough estimate of sparker resolution, as many as 10 major turbidite layers (and 5-10 more minor layers) may contribute to one individual seismic reflector.

Geoacoustic Parameters

Sediment Surface Density and Sound-Speed

The detection of horizons on the seismic recorders by normally incident acoustic waves is a function of the contrast in acoustic impedance of the medium at an interface. The impedance is a product of two measurable properties: density and compressional wave (sound) speed. The density is a commonly measured property on core samples and is the wet weight divided by the volume. Most near-surface sediments consist of clay-sized particles and have densities of about 1.5 g/cm^3, but can range from 1.2 to 1.6 g/cm^3. Higher densities are generally associated with silts or sands reaching an extreme of 2.6 g/cm^3 and above for nonporous material.

Fry and Raitt [74] described a method (using a receiver and source at the sea surface) of determining the sound-speed of ocean floor sediments where the speeds are less than that of the bottom water. Since then, new evidence indicates that low-speed sediments at the water-sediment interface are the rule rather than the exception in the deep ocean. Urick [75] considers a mixture of dispersed clay particles in sea water and describes the theoretical basis for a low-speed, clayey sediment. Because pelagic deposition is so common, and because the final settling particles of turbidity currents are commonly clay particles, the location of low sound-speed sediments is predictable. Often, the tops of cores taken in the deep ocean sediments are soupy, further supporting Urick's theory. The finest particle-sized, deep-water surface sediments--the oozes and clays--have sound speeds of about 0.985 of the sound speed of the ocean-bottom water at the water-sediment interface.

Sound-speed measurements have been made on linered cores from the upper 10 m of sediment by many investigators. A common method is to measure the time delay of a 400 kHz signal transmitted across the diameter of a core as compared to that through a distilled water sample in order to calculate the compressional wave speed of the sediment. The calculated speed is dependent on the laboratory conditions and needs to be corrected to a standard temperature for comparison with other measurements or to in situ temperature and pressure for absolute speed determinations. In this report, all sound-speeds have been adjusted to laboratory conditions of one atmosphere and 20°C for convenience in expressing the actual speeds without reference to in situ pressure and temperature. According to Wilson's equation [44], seawater sound-speed at these conditions is 1521.5-1522.5 m/sec for respective salinities of 34.68-35.46 parts per thousand. These salinity values are well within the range for ocean-bottom water in the northeast Atlantic [76]. Therefore, the adjusted sound-speed for the ocean-bottom water will be considered to be 1522 m/sec. Clays and oozes are approximately 1500 m/sec under the same conditions. Sediment sound-speed can also be expressed as the ratio of the sound-speed of sediment to that of the bottom water, which relieves the necessity of reference to a standard temperature.

The extensive collection of literature addressing the subject of relating measurable geologic parameters to sound-speed has been summarized by Hamilton [41]. Most of the studies are based on sediments from the upper few meters of the ocean floor; therefore, the statistical correlations observed apply to only surficial sediments. Hamilton emphasizes the need to use as much information as possible before relying on a general relationship. One commonly used relationship permits an estimate or prediction of sound-speed if the porosity is known. This is because the sound-speed is largely determined by the compressibilities of the pore-water and the solid material and the percentage of these two constituents. Hamilton separates sediments from abyssal hills, abyssal plains, and continental terraces and slopes in deriving the sound-speed-porosity relationships.

Other relationships can also be used in the prediction but with somewhat less reliability. Anderson [62] derived relationships using data from several oceans and showed that the highest degree of correlation exists with sound-speed and porosity as compared to sound-speed and other parameters such as mean grain size, carbonate content, or shear strength. The relationship between grain size and sound-speed is complicated by factors related to the sediment type and its effect on porosity. Surficial sediments of fine mean grain size normally consist of well-sorted clay particles. These sediments have high porosities due, in part, to the adsorbed water on the large surface area of clay minerals. On the other hand, sediments of larger mean grain size (silt-sand) are not well-sorted because the fine particles

fill the voids which exist in the packing of larger particles of uniform size. This results in a reduction in porosity. It therefore follows that an inverse relationship between grain size and porosity exist.

Calcareous sediments, however, do not follow this relationship. Clay-sized carbonate sediments consist of coccoliths, which are solid flat plates. Larger-sized calcite particles and silicate tests of radiolaria consist of hollow porous tests which permit a much higher porosity of the sediment than solid materials. Schreiber [77] observed that sediments with a grain size exceeding 0.008 mm median diameter* and consisting of radiolarian ooze or more than 50% carbonate content have much higher porosities than other sediments of the same grain size. She also shows how the high carbonate and radiolarian sediments deviate from the general sound speed-median diameter relationship, although this deviation is not as striking as the deviation from the median diameter-porosity relationship.

An interesting aspect of sound-speed is its relationship to density. Theoretically sound-speed decreases with increasing density. However, empirically it is higher in sediments of greater density. The associated decrease of the compressibility with an increase in density is the overriding factor which results in an actual increase in sound-speed. The additional factor of an increase of rigidity also increases the compressional wave velocity and adds a shear wave component. The latter, however, is probably negligible near the surface and is often, although perhaps erroneously, ignored in the intermediate depth sediments.

*The median and mean grain size are equivalent only if a symmetrical distribution of grain sizes based on weight exists. Horn et al. [78] states that the mean is a better measure of the distribution of sizes, and this description is now generally used when discussing sound speed of sediments.

Sound-Speed Profiles

A positive sound-speed gradient with depth in the upper sediments was first postulated by Hill [4] in 1952, and based on in situ experimental results. He derived a gradient of 2.5 sec^{-1} at a site in the Norwegian Sea. This value is high compared to gradients reported since then, but is comparable to our results. A gradient is also inferred from geological factors such as compaction, pressure, and temperature gradients in the sediments. Evidence from later work suggests that the gradient decreases with depth. In this report, several different methods are used to estimate the sound-speed profile in the upper 200 m of sediment. These methods are described in Appendix E.

Attenuation

The attenuation constant κ is the constant of proportionality relating attenuation α to frequency. Attenuation is defined as the loss of energy by absorption (dissipation due to heat) or other mechanisms, such as scattering, which are not attributed to geometric spreading. Hamilton [45] discusses physical factors which contribute to attenuation, such as particle angularity and composition. These factors are closely related to particle size distribution. Hamilton [45, 41] has summarized attenuation values in sediments determined by several investigators. From this compilation, he derived an empirical curve relating to mean grain size. This relationship is used in the present study to estimate the values of κ based on the mean grain size distribution as determined from core samples. Where core samples are not available, the mean grain size is estimated.

Appendix E.
Methods of Estimating Sediment Sound-Speed Profiles

Methods of estimating sediment sound-speed profiles are presented in detail in this appendix. The profiles were used in Appendix C for the acoustic stations. Some of the profiles were general in that they are derived from data at distant sites where a similar sediment type exists. On the other hand, other profiles have parameter values unique to a site not too distant from the acoustic stations. These profiles have been chosen as the best estimate for each station and are indicated by an arrow in Figure 10. The best estimate profile can be visually compared with the general profiles and the acoustically derived profile.

1. Laboratory Methods

In the reports of numerous laboratory experiments involving sea floor sediments, sound-speed measurements, high pressure, and compaction, only two sound-speed profiles applicable to sediments have been described (Laughton [40] and Cernock [50]). The authors of both reports have conducted laboratory experiments involving sound-speed vs. overburden pressure (as opposed to hydrostatic pressure alone) on unconsolidated sediment samples.

Laughton's [40] measurements included a sample with high carbonate content (54%) and a density of 1.59 g/cm^3 from the North Atlantic taken at a water depth of 2577 m. Because of the high carbonate content of the sediments at Station 8, his results are used to suggest how the profile of high-carbonate sediments may possibly appear. Hamilton [79] has made the conversions from pressure to depth in sediment for Laughton's globigerina ooze. Laughton used equipment designed for high pressures (up to 1024 kgm/cm^2) and measured only four values of sound-speed at pressures corresponding to depths of burial less than 400 m.

This includes the surface value of 1.62 m/sec and the values at 135, 260, and 360 m. Actual in situ values are expected to be higher than Laughton's computations because he had made no correction for a temperature gradient in the sediments. However, his surface value is 100 m/sec greater than the sediments at Station 8, thus, the actual profile is unrealistic in the near-surface area. Cernock [50] suggested that Laughton's initial values are too high because of his experimental procedure. Following this suggestion, Laughton's surface value is replaced by the surface-sediment sound-speed at Station 8. Laughton's values, with this modification, are represented by the curve in Figure 65.

Cernock [50] made measurements on a core sample 126 cm deep in an abyssal plain (water depth 3636 m) in the Gulf of Mexico. The sample is clay which has a low carbonate content (8%) and a density of 1.31 g/cm^3. The sound-speed ratio of his sample is the same as that reported for Station 2 (0.974). A correction of 26 m/sec is added to each of his calculations to correct for the difference in bottom-water sound-speed between the Gulf of Mexico station and Station 2 in the Iberian Abyssal Plain. The resulting curve is shown in Figure 54.

As pointed out by Cernock [50], results obtained by this method must be used with caution because of many unknowns. Laboratory experiments are performed over a short time period without the understanding of the chemical and physical effects which occur over geologic time. Also, present and past environmental conditions (pressure, temperature, and salinity) are unknown. In addition, laboratory measurements are made at frequencies on the order of 100 kHz, whereas in situ acoustic measurements were taken at frequencies on the order of 100 Hz.

2. CRIC Method

The CRIC method is useful in estimating the sound-speed profile in a section of sediments where the surface sound-speed ratio, CR, and the average or interval sound speed, IC, is known. In particular, this method is applicable to surface sections of DSDP sites where IC can be calculated by dividing the thickness of a sediment section by the travel time through the sediment. The section is bounded by acoustic reflectors which can be identified by the drilling process; e.g., the water interface on top and a sandstone layer or basalt at the bottom. The thickness is measured by the drilling depths at these interfaces, and the travel time is obtained from seismic profiler records. The sediment surface sound-speed c_o is often indirectly determined by measuring the sound-speed of a core sample in the laboratory. The ratio of the sediment sound-speed to that of the bottom water sound-speed CR can then be calculated from the laboratory measurements. The bottom water sound-speed c_B can be established from historical or in situ data. Thus,

$$c_o = CR \times c_B \qquad (1)$$

CR may be used from sediments at other locations if they are similar to those at the site.

The value of sound-speed as a function of depth z can be determined if a linear increase in sound-speed with depth is assumed. That is, a constant gradient g is assumed:

$$c(z) = c_o + gz \qquad (2)$$

The two-way travel time to depth z as observed on the profiler record is

$$t = (2/g)\ \ln(1 + gz/c_o) \qquad (3)$$

By reiteration, the value of g which satisfies Equation 3 can be calculated.

This method was used for determining the values of g at DSDP Sites 118 and 136. These values were used to estimate the sound-speed profiles at Stations 2, 4, 5, and 8.

The method is illustrated in Figure 68 where h, the thickness of the upper layer, is used instead of z. Other lines of evidence discussed in following sections indicate that the true sound-speed profile is not a constant gradient, but tends to have a decreasing gradient with depth. Therefore, the value of the constant gradient calculated by the CRIC method is the lower limit of the actual gradient in the upper part of the section, and the upper limit of the actual gradient in the lower part.

DSDP Site 118

Site 118 [49] is located in the Biscay Abyssal Plain (see Fig. 52). On the profiler records obtained at the site, a strong reflecting horizon called the mid-R reflector appears at 0.48 seconds two-way travel time below the ocean floor. The mid-R reflector was found to be several sandstone layers lithified from coarse turbidite layers in the depth interval from 400 to 450 m.

The in situ bottom temperature and salinity at Site 118 are 2.6° and 34.9 °/oo, respectively [76]. The corresponding bottom water sound-speed (c_B) at 4901 m is 1545 m/sec [44]. The value of CR is not available in the site report, but is available from an area of similar sediments. Based on Ruddiman and Glover's study [53], the Tagus Abyssal Plain is such an area. Using the ratio of sediment to bottom-water sound speed of 0.995 observed at Stations 4 and 5 in the Tagus Abyssal Plain, the calculated surface-sediment sound-speed at Site 118 is 1537 m/sec. The gradient g which satisfies Equation 3 using this value of c_o and the observed values of t (0.48 sec) and z (400 m) is 0.67 sec^{-1}. The sound-speed profile defined by Equation 2 using this value of g is used as the best estimate for Stations 4 and 5.

The value of g determined by the CRIC method at Site 118 is also estimated to be the value at Station 2 in the Iberian

Abyssal Plain. At Station 2, the source of sediments is more distant than at Site 118 or at Stations 4 and 5. This results in a smaller grain size in the basal turbidites in the northern Iberian Abyssal Plain, and is corroborated by the lower ratio of sediment to bottom-water sound-speed ratio (0.977 as compared to 0.995 in the Tagus Abyssal Plain). The smaller grain size suggests a respectively slower accumulation of sediments deposited by turbidites. Thus, sediments of a given age are less deeply buried at Station 2 than at Site 118. Hamilton et al. [42] measured gradients at different locations on the Bengal Fan, with different depths of burial to sediments of the same age. He observed that the gradients in the Bengal Fan are greater farther away from the source of sediments where the accumulation rates are less. He suggests that lithification increases with age with an accompanying increase in sound-speed. Therefore, sediments of a given age being less deeply buried at the distant stations account for the larger gradients. A similar argument might be used here to suggest that the gradient at Station 2 is higher than that at Site 118. However, the information is insufficient to support an adjustment to the value of 0.67 sec^{-1}.

DSDP Site 136

The CRIC method can also be applied to DSDP Site 136. The sediments at this site are discussed in Appendix C for Station 8. The value of c_o = 1530 m/sec (CR = 1.00) is assumed at Site 136. The basalt interface was drilled at 308 m. The corresponding two-way travel time observed on the profiler records from the DSDP report [59] is 0.33 sec. The value of g satisfying Equation 3 is 2.33 sec^{-1}.

The value of 2.33 sec^{-1} is considerably higher than those values estimated at the other stations. This value is a function of the assumed surface sound-speed C_o. However, the value of C_o is unlikely to be more than 30 m/sec in error. (This would allow for a low-speed bottom, CR=0.98, or a high-speed bottom as measured at Station 8, CR=1.013.) This amount of error does not significantly affect the determination of g: for C_o varying $\pm$ 30 m/sec, g varies $\pm$ 0.23 sec^{-1}.

Two possible sources of error are apparent in the DSDP data; neither is taken into account in this analysis: (a) The measured thickness of sediment, determined by the length of the drill cable, could be in error due to the uncertainty as to when the drill bit actually entered the ocean floor. This error probably is no greater than 5 m. (b) The seismic profile may not have been taken right at the core site--the topography of the basement is very rough and this could be in error. Or, the time read on the seismic profile may be in error. In considering this error, the site report states 0.33 sec to basement [59]. The pick may be a subjective or average estimate. In measuring the time scale of the record in Figure 3 of reference [59], it appears to be 0.37 sec. It is assumed, however, that the authors of the report had sufficient information to adequately define the travel time of 0.33 sec.

3. Seismic Refraction Method

Houtz and Ewing [39] developed a sound-speed-depth curve for unconsolidated sediments based on wide-angle reflection data. The data were obtained from the results of 60 seismic refraction profiles taken predominantly along the western North Atlantic continental rise and the Bermuda Rise. The geometry used in this technique is equivalent to that used in the present-day sonobuoy method. In five profiles, observed arrivals were interpreted as paths refracted in the sediments due to sound-speed gradients (i.e., turnaround rays). The average of the computed gradients is 1.85 sec^{-1}. In the same profiles, arrivals were observed which reflected from the base of the first sedimentary layer (validated by the $T^2 - X^2$ analysis). The calculated interval velocity implied a

decrease in the gradient from that calculated in the near-surface refracted arrival.

Houtz and Ewing [39] compiled 33 deep-water sedimentary sound-speeds calculated from the subbottom reflection curves on the refraction profiles. These values were plotted against the travel time in the sediment to the midpoint of the layer, where the midpoint time is one-half the interval time of the layer. By choosing a sound-speed function which provides a decreasing gradient with depth, sound-speed was derived as a function of time t in seconds:

$$C = 1520\ (1 + 8.75)^{1/5}\ \text{m/sec} \quad (4)$$

or expressed as a function of depth z in km:

$$C = 1520\ (1 + 6.91z)^{1/6}\ \text{m/sec} \quad (5)$$

Equation 5 is plotted in Figure 65. Equation 5 less 5 m/sec for a surface sound-speed correction is plotted in Figure 54.

4. Wide-Angle Reflection Method

Extensive wide-angle reflection profiles using the sonobuoy technique [80] provide average sound speeds for sedimentary layers in many ocean areas. We have used the results of this method in predicting possible sound-speed profiles at several of the stations.

Data for Turbidite Sediments

Hamilton et al. [51] have compiled data from 17 ocean areas with sediments formed mainly by turbidite deposition. The average gradient g is given by equation 6 where C_o is the sediment surface sound speed, and IC is the interval sound speed over the layer of thickness h:

$$g = 2\ (IC - C_o)/h \quad (6)$$

Equation 6 is an approximation because the value of IC is assumed to be identical to the value of sound speed at the midpoint of the layer. Hamilton et al. used the directly measurable parameter of travel time rather than the calculated thickness to compile average gradients. Their objective was to produce a simple means to estimate thickness from the travel time observed on a profiler record. They plotted the average gradient versus one-way travel time at increments of 0.1 sec. Results indicate a constant decrease of gradient with one-way travel time, t, as expressed by

$$g = 1.316 - 1.117t \quad (7)$$

The sound speed is given by

$$C = C_o + gh \quad (8)$$

where

$$h = C_o\ (e^{gt} - 1)/g \quad (9)$$

and using the value of g corresponding to t in Equation 7. By assuming a sediment surface sound speed of C_o = 1515.0 m/sec, the instantaneous sound-speed c has been plotted to produce the profile presented in Figure 54 for the Iberian Abyssal Plain. The profile is also shown in Figure 10 for Stations 4 and 5 in the Tagus Abyssal Plain.

Data for Highly Calcareous Sediments

Houtz, Ewing and Buhl [60] have compiled sonobuoy data collected in different areas of the Pacific Ocean. They plotted the interval sound speed of a layer against one-way travel time in seconds to the midpoint of the layer for all the valid data in each area. They derived an equation for each area by making a least squares fit of a polynomial for each set of data. One set of data is from pelagic sediments in the equatorial zone. Houtz et al. [60] noted the high sound-speed gradient for this set of data representing sediments of high carbonate content. Hamilton et al. [42] have recommended using the equation for this set of data for pelagic sediments anywhere in the world as a best estimate of sound-speed if there is no in situ data available. The sediments

at Station 8 are pelagic, with a high carbonate content. In following Hamilton's recommendation, this equation has been used in deriving a profile for Station 8.

The Houtz, Ewing, and Buhl [60] equation for sound-speed in the Pacific equatorial zone is:

$$C = 1521 + 2776t + 2931t^2 \text{ m/sec} \quad (10)$$

where t is the one-way travel time in seconds. (Their expression of sound speed versus depth [in their Table 2] is the best fit for data, but gives an interface sound-speed of 1600 m/sec.)

In order to use this data for the near-surface sound-speed profile, we have used the value of sound-speed from Equation 10 and the corresponding depth z from Equation 11 for the same value of one-way travel time. Equation 11 is an exact expression for depth z in terms of t derived by integration of Equation 10:

$$z = \int C\, dt = 1521t + 1388t^2 + 977t^3 \text{m} \quad (11)$$

Data for Station 9 Area

Many sonobuoy stations were taken on Lamont-Doherty cruises in the area of Station 9, as shown in Figure 66. The large variety of layer thicknesses with respective interval sound-speeds provides a data base to estimate an average sound-speed profile for the region. This type of information has been derived from sonobuoy data by Hamilton et al. [42] for several areas.

Twenty-three of the stations have been separated geographically into two groups as indicated in Figure 66: Group W (west) as denoted by triangles, and Group E (east) with circles. In addition, the four stations nearest Station 9 are grouped separately and are indicated by squares; all others are indicated by crosses. The layer thickness and interval speeds as well as deeper refraction speeds are shown for all the stations in Figure 69.

Groups E and W data are considered as two separate data bases to estimate a sound speed profile near Station 9. For all the layers in a group, the layer speed is plotted against the depth below seafloor to the midpoint of the layer. These plots are shown for Group W and Group E in Figures 70 and 71. A least-squares second-degree curve for speed as a function of depth of burial was computed and drawn on the figures.

In addition to the data base points, points for the layers determined from the sonobuoy stations near Station 9 are shown on both figures as squares. The curve for Group E appears to better represent the data points near Station 9 than does the curve for Group W. Therefore, the equation for this curve is used to define the function of speed with depth for this area:

$$C(z) = 1505 + 1448z - 305z^2 \text{ m/sec} \quad (12)$$

where z is in kilometers below sea floor, and C is sound-speed. The average gradient for the upper 200 m is $g = \Delta C/\Delta z = 1.39 \text{ sec}^{-1}$.

The in situ bottom-water sound-speed range over the range of water depth of all the sonobuoys is about 1515-1535 m/sec. This variation (due to differences in hydrostatic pressure) will affect the sound-speed in the unconsolidated sediments by the same amount. However, the variation is rather insignificant on the scale used in Figures 70 and 71. The value of the intercept for Group W is 1435 m/sec, which is obviously too low, whereas 1505 m/sec for Group E is within the range expected for clays.

The least-squares equation was recalculated using the data weighted according to the inverse of the standard error of each data point, and adding a heavily weighted (x20) surface sound-speed of 1520 m/sec. The effect of the weighted

data for either group was to decrease the near-surface gradient by less than 0.2 sec^{-1}. (The difference due to adding the heavily weighted surface sound speed is less than 0.1 sec^{-1}.)

A danger exists in extrapolating to the surface the sound speed versus depth curve determined predominantly by deeper layers. Laboratory experiments, such as by Laughton [40] (Fig. 65), show that the greatest increase of speed with overburden pressure due to depth of burial is in the near-surface sediments. Houtz and Ewing's [39] in situ experiments support this concept. Their data consist only of midlayer points to a maximum depth of 0.8 km. Below this depth a discontinuous increase in speed exists at the interface of unconsolidated sediments. As the method used to derive Equation 12 includes high-speed deeper layers in a model with a continuous sound-speed function, the gradient near the surface will be in error. If one could separate sound-speed determinations of the unconsolidated sediments in the sonobuoy data, the estimate would be more accurate.

An alternate method of calculating the gradient is used when considering only near-surface layers. Rather than estimating a sound-speed profile represented by a least-squares curve, only two points are determined. The upper point is the average water-sediment sound-speed value (1525 m/sec). The lower point has a sound-speed which is the average speed of all the layers considered. The depth at this point is the average of the midpoints of these layers. The gradient is then the difference in the two sound-speed values divided by the depth. This value of the gradient is about 0.9 times the value which satisfies the constant-gradient model with the same speed at the midpoint depth.

Two approaches to determine a gradient in the above manner are used here. In the first approach, layers with a midpoint depth less than a specific depth are assumed to consist only of unconsolidated sediments. The calculated average gradients using layers with midpoint depths less than 0.5 and 1.0 km are 1.1 and 1.2 sec^{-1}, respectively. In the second approach, layers with speeds less than a specified sound speed are assumed to consist of only unconsolidated sediments. The calculated average gradients using layers with speeds less than 2000 and 2300 m/sec are 0.8 and 1.2 sec^{-1}, respectively. The standard deviations of each of these four determinations are high, ranging from 0.6 to 0.9 sec^{-1}, which shows the variability of the sediment sound-speed profiles in this area. Throughout the DSDP reports, the reported sound-speeds for the unconsolidated sediments overlap. A similar difficulty arises in attempting to determine a critical depth which separates the unconsolidated and consolidated sediments. Nevertheless, the average of the four calculated gradients is about 1.1 sec^{-1}, which is less than one-half a standard deviation from each gradient value.

5. Surficial Sediment Data Method

A sequence of empirical and theoretical relationships are used to develop a sound-speed profile at the DSDP Site 136. Commencing with a semi-theoretical porosity-depth profile based on surficial sediment type, and applying an empirical porosity-sound-speed relationship also based on surficial sediment type, a sound-speed profile is derived which is then corrected for in situ pressure and temperature. The pressure and temperature corrections applied to sediments are those established for water. However, in order to estimate the temperature, an empirical relationship between temperature and porosity is used. Within this sequence of relationships are many implied assumptions which must be kept in mind when assessing the final results.

The DSDP report [59] provides some porosity data for Site 136. Porosity was measured by two methods on board the GLOMAR CHALLENGER on all the cores from

the drill hole: GRAPE (Gamma Ray Attenuation Porosity Evaluator) and a volumetric determination. The GRAPE method uses an average of 800 determinations per section to compute a single value for porosity, whereas the volumetric method determines one value for one sample of a section. The range of porosity values of all sections for each core by the these two methods are indicated in Figure 72. Because these measurements are made after the sample has suffered a release of overburden pressure from the in situ environment, a correction should be made to in situ conditions. This correction is shown by the length of the arrows from the mean of the GRAPE porosity range for each core. The correction adjusts the porosity to the in situ porosity based on depth of burial using the values determined by Hamilton [81].

Three theoretical curves by Hamilton [81] are presented in Figure 72 that show the relationship between porosity and depth of burial for carbonates, turbidites, or pelagic clays. The actual porosity measurements of the Site 136 cores vary considerably; therefore, these measurements cannot be used to justify the application of a particular curve. Because of the predominantly calcareous sediment at Site 136, the "carbonates" curve is used in determining a smooth porosity profile at the site. A sound-speed porosity relationship is used to transform this curve into a sound-speed-versus-depth curve.

Hamilton [52] derived curves representing sound-speed as a function of porosity for different types of sediments. His curve "T" is based on data derived from high carbonate content sediments found on the continental terrace. This set of data encompasses porosities of 35-80%. The sediments at Site 136 are probably similar in porosity and carbonate content to the sediments in Hamilton's data base. Hayes et al. [59] calculated a very high average sound speed of 1867 m/sec from the two-way travel time through the 308 m sediment column at Site 136. The high values are consistent with Hamilton's "T" curve. This curve is among the sound-speed porosity curves summarized by Anderson [62] and has the highest sound-speed values for the porosity range of 50-70%, i.e., the range expected at Site 136. Using the "T" curve, the porosity at each depth is used to estimate the sound-speed at that depth. However, the application of porosity relationships from surficial sediments to buried sediments presents a problem which is discussed later.

In determining the in situ sound-speeds for buried sediments, increases in temperature and hydrostatic pressure below the ocean floor must be considered. A common practice is to assume that the sound-speed of sediment varies with pressure and temperature to the same degree as does sea water, as defined by Wilson's equation given in Reference [44]. Considering only the hydrostatic pressure increase from the ocean floor (4169 m) to 308 m into the sediment (4477 m), the speed increases 5.5 m/sec.

To determine the in situ temperature below the sea floor, heat flow information must be considered. Bullard [82] suggests a general relationship between the thermal conductivity k of sediment and water content w:

$$k = (168 + 678\ w)^{-1}\ \text{cal/cm/sec/}^{o}\text{C} \qquad (13)$$

where w can be expressed in terms of the porosity n, water density ρ_w, and sediment grain density ρ_s:

$$w = [\rho_s/\rho_w\ (1/n-1) + 1]^{-1} \qquad (14)$$

The temperature at the lower boundary of the depth interval z_n is

$$T_n = -Q\Delta z_n/k + T_{n-1} \qquad (15)$$

where T_{n-1} is the temperature at the upper boundary of z_n, and Q is the heat flow. The average heat flow in this area is -1.06×10^{-6} cal/cm^2/sec [83], representing upward flow in the negative z direction, and the bottom temperature is 2.3°C [76]. Using $\rho_s = 2.7$ and $\rho_w = 1.05$ g/cm^{-3} in Equation 14 and the porosities obtained from the curve in Figure 72, the calculated in situ temperature increases with depth from 2.3°C at the ocean floor to 15.9°C at 308 m into the bottom. The resulting increase in sound-speed is 50.7 m/sec over the 308 m interval.

The above pressure and temperature effects have been applied in deriving the in situ profile. A problem exists, however, in using sound-speed-porosity relationships determined from sediments on the sea floor. Hamilton's [52] samples are all from the upper 30 cm of the sea floor. Indeed, most valid sound-speed measurements on ocean sediments are taken on surficial sediments. (In deep cores, such as the DSDP cores, the effect of the release of the overburden pressure presents a disturbance which has unknown effects in the sound-speed determinations.) Ocean-bottom clay samples which have not been previously buried have high porosities. When buried, the resulting compaction reduces the porosity. An uncompacted sample at the water-sediment interface with the same porosity will have larger grain size, and therefore will likely consist of carbonaceous or siliceous tests or quartz grain instead of clay minerals. The structural matrix is different as the mineralogy is different; therefore, the sound-speed of the surface sample would not necessarily be the same as that of the compacted clay of the same porosity. Thus, a problem exists in applying the sound speed-porosity relationships derived from surface sediment samples to buried sediments.

Appendix F.
Water-Column Sound-Speed Structure at Each Station

The sound-speed profile of the water column at each acoustic station was determined from data obtained with an SVSTD. The measurements were taken at each site immediately before or after the reflectivity experiment. The profiles for each station are shown in Figure 73. The variation of water depth along the bomb run is also noted.

The depths of the source and receiver for each station are shown on the respective profiles in Figure 73. The authors chose these depths prior to the cruise to obtain the optimum geometry (discussed in Sect. III) without consideration of the sound-speed profile. Near midwater receiver depths were used at all stations, except Station 7, where the receiver depth was the same as the shot depth.

Fenner and Bucca [84, 85] have described the water mass circulation and sound-speed profiles in the North Atlantic. The predominant structure of each profile is related to three oceanographic features: the surface layer, the intermediate water, and the deep water. The warm, saline water of the Gulf Stream/North Atlantic Current system produces the high sound-speed in the surface layer above a strong negative gradient common to all the stations. Below 2000 m, the North Atlantic Deep Water produces a characteristic positive gradient which varies only slightly between deep ocean basins. Interjected between these two water masses is the Mediterranean Intermediate Water (MIW) which flows out of the Straits of Gibraltar. This body of warm, highly saline water creates a sound-speed maximum which varies between 900 and 1200 m at our stations, and also causes the pronounced bichannel structure in the profiles. Consequently the deep sound-channel axis is depressed from about 1200 m to 2000 m in the presence of MIW.

The MIW flows preferentially along several routes as shown in the location chart in Figure 73. The extremely high sound speed at the maximum for Station 5 (about 1518 m/sec) indicates that this station lies on a preferential MIW flow-path. The sound-speed maximum for Station 4 is about 4 m/sec less than that for Station 5, reflecting a greater distance off the MIW flow-path. Sound-speed maxima for Stations 7 and 8 (about 1510 m/sec) indicate even further dilution of the MIW to the southwest. At Station 2, the sound-speed maximum of about 1510 m/sec indicates dilution of MIW to the northwest. Here, the depth and sound-speed at the upper channel axis are the minima encountered in our data due to the lower temperature at the northern location. At Station 9, the bichannel sound-speed structure has been compressed to an irregular structure around the depth of the deep sound-channel axis, as expected, in the region southwest of Madiera due to further dilution and sinking of the MIW. The 45% MIW concentration shown in Figure 73 southwest of Station 9 represents an anomalous condition (D. F. Fenner, pers. comm.).